KIT Scientific Report 7645

Colloid/nanoparticle formation and mobility in the context of deep geological nuclear waste disposal

(Project KOLLORADO-2; Final Report)

Florian Huber[1], Ulrich Noseck[2] & Thorsten Schäfer[1] (Eds.)

Authors:
M. Bouby[1], J. Brendlé[3], S. Büchner[1], G. Darbha[1], R. Götz[1], J. Flügge[2], W. Hauser[1], S. Heck[1], P. Hoess[1], F. Huber[1], B. Lanyon[4], U. Noseck[2], A. Pudewills[1], T. Schäfer[1], L. Truche[5]

[1]Karlsruhe Institut für Technologie (KIT), Institut für Nukleare Entsorgung (INE)

[2]Gesellschaft für Anlagen- und Reaktorsicherheit (GRS) mbH

[3]Fracture Systems Ltd

[4]Université de Haute Alsace (IS2M) CNRS-UMR

[5] Université de Lorraine (GeoRessources) CNRS-UMR

ANMERKUNG:

Die diesem Bericht zugrundeliegenden Arbeiten wurden mit Mitteln des Bundesministeriums für Wirtschaft und Technologie BMWi unter den Förderkennzeichen 02 E 10679 & 02 E 10669 gefördert. Die Verantwortung für den Inhalt dieser Veröffentlichung liegt alleine bei den Autoren.

List of content

List of figures

List of tables

1 Introduction

1.1 Scope of the work

In order to assess the relevance of colloidal influences on radionuclide transport for the long-term safety of a radioactive waste repository, the KOLLORADO-2 project integrates the results of in-vitro (geochemical), in-situ and in-silico (hydrogeological) studies. From the commonly considered set of necessary conditions (colloid presence/generation, their mobility and stability as well as the uptake of radionuclides and the irreversibility of this sorption process) required for a non-negligible impact of colloids on the pollutant propagation [1] the project focuses on the questions of

- colloid generation from compacted bentonite under low saline groundwater conditions (reference repository evolution in [2, 3]),
- nanoparticle mobility and
- radionuclide uptake/sorption mechanisms and the appropriate implementation of relevant data into a transport code.

Our results provide feedback for the design of future experiments. In particular the Grimsel Test Site Phase VI Project CFM (**C**olloid **F**ormation and **M**igration) aims towards lower flow rates similar to repository post-closure conditions in order to capture the slow desorption dynamics of tri- and tetravalent actinides from bentonite colloids and to better simulate repository relevant conditions of low ionic strength groundwater contact to the geo-engineered barrier (http://www.Grimsel.com/gts-phase-vi/cfm-section/cfm-introduction). The concomitant extended durations and the higher overhead in general necessitate a careful choice of parameters. Reactive transport modeling allows assessing the impact of various scenarios which are difficult or too expensive to realize under in-situ conditions. Finally yet importantly our results may serve as a basis for an appraisal of the implications of colloid presence in the vicinity of radioactive waste repositories in different deep geological host-rock formations. To evaluate the variance of groundwaters found in geological host rock formations on the significance of colloid/nanoparticle mobility studies conducted on granite from Äspö (Sweden) are also documented. The research leading to these results has received funding from the European Union's European Atomic Energy Community's (EURATOM) Seventh Framework Programme FP7/2007-2011 under grant agreement n° 269658 (CROCK project) and SKB, the Swedish Nuclear Fuel and Waste Management Company.

1.2 State of the art

Generation of energy by nuclear fission leads to the production of spent fuel elements which contain uranium, plutonium, fission products and the so-called “minor actinides” such as neptunium, americium and curium. The safe disposal of this highly toxic and radioactive waste demands its isolation from the biosphere for several hundred thousand years. Thus, the immobilization of long-lived radionuclides (actinides, activation and fission products) over a geological timescale is the primary aim of nuclear waste disposal. Storage in deep geological formations using a multi-barrier system is currently considered as the most feasible repository concept for high-level radioactive waste in the majority of nations worldwide [4, 5]. The multi-barrier system is composed of the following:

- the waste matrix itself consisting of the spent fuel and its container (technical barrier)
- the geotechnical barrier consisting of the backfill material; this report focuses solely on compacted bentonite, and
- the geological barrier (e.g., salt, granite, clay; this report focuses on crystalline host rocks).

For each of these barriers those processes have to be examined and described which potentially lead to the mobilization or immobilization of radionuclides. Beside transport a variety of geochemical processes can take place in the individual barriers (e.g., redox reactions, hydrolysis, sorption/desorption, dissolution/precipitation, colloid formation) and each has to be evaluated. The aim is to determine rates for the immobilization and/or mobilization of the radionuclides during transport through the individual barriers and from this it is possible to derive source terms for radionuclide release out of the barriers considering various scenarios. The combined source terms allow quantification of the potential release of long-lived radionuclides into the biosphere and hence provide a basis for a geochemically well-founded long-term safety analysis.

The engineered barrier system (EBS) of a deep geological repository for high-level nuclear waste foresees in most concepts [6, 7] the use of bentonite as buffer and backfill material. Bentonite clay has been found to be an appropriate material for the geotechnical barrier of the multi-barrier system due to its swelling properties [8, 9] inhibiting groundwater access to the waste canister and retarding radionuclide transport in form of dissolved and colloidal phases (safety functions “sorb radionuclides” and “filter colloids”, as defined by SKB [10]) away from the repository near field [11]. However, depending on the physico-chemical conditions (e.g., gas and water pressure, groundwater flow velocity) the bentonite barrier may also be eroded by colloid formation [4, 5, 12-18]. Bentonite colloid erosion has been reported to take place at the interface between the compacted bentonite buffer and granite [19, 20]. These results as well as laboratory bentonite erosion experiments [21] show a dependency of the colloid source term on ionic strength, pH, bentonite compaction and flow velocity. Under certain conditions, as e.g. imperfect backfilling and defects in plugs or fracturing radionuclide transport through the bentonite barrier may be rather quick. Speciation of radionuclides

in the groundwater/pore water mixing zone might control in such worst case scenarios the radionuclide mobility in the far-field [22]. The lately heavily discussed scenario of glacial water intrusion [11] estimates a high erosion of bentonite buffer due to the contact with glacial water of high pH and low salinity favoring the release of bentonite colloids/particles. In the framework of the Grimsel Test Site (GTS) Phase VI the international Colloid Formation and Migration (CFM) project with partners from Japan (JAEA, AIST and CRIEPI), Switzerland (NAGRA), Sweden (SKB), Finland (POSIVA), South Korea (KAERI), United States of America (US DOE) and Germany (BMWi, KIT-INE) investigate processes related to this bentonite erosion and the possible formation of colloids. The migration of bentonite colloids and associated radionuclides in the shearzone under investigation in CFM has been demonstrated in earlier studies [23-25].

Beside the formation/erosion of colloidal material of smectite origin also the neo-formation of colloids due to the geochemical gradients and oversaturation of mixing waters has to be considered. Colloid formation in chemically disturbed environments has been documented in a couple of cases. Acid mine drainage waters show the formation of colloids and the mobility of heavy metals is strongly associated with this colloidal phases [26, 27]. Studies with simulated tank waste solution (TWS) from the U.S. Department of Energy (DOE) Hanford Site (Washington State) showed that the maximum formation of mobile colloids occurred at the plume fronts with calcium carbonate as one of the dominant phases of the plume front colloids [28]. The authors identified the cation exchange process during infiltration of the high-Na^+ TWS solution, with complete replacement of exchangeable Ca^{2+}/Mg^{2+} from the sediment caused accumulation of these divalent cations at the moving plume front. Precipitation of supersaturated Ca^{2+}/Mg^{2+}- bearing minerals caused dramatic pH reduction at the plume front which triggered, in turn, precipitation of other minerals. Concerning the formation of aluminosilicate colloids laboratory studies have already demonstrated that these newly formed phases can have a significantly influence on the speciation of trivalent actinides [29].

Colloids are known to be ubiquitous in natural groundwaters and have been frequently discussed as potential carriers for radionuclides. Colloids show, in comparison with ionic species, a different migration behaviour: due to their comparatively larger size, charge and low diffusion coefficient the probability to penetrate into matrix pores of the host rock is lower and therefore they may be transported unretarded or in the fastest streamlines of the laminar flow field being faster than the average groundwater velocity monitored by dissolved conservative tracers. Thus, colloid bound contaminants such as radionuclides may interact to a lesser degree with the surface of the host rock minerals and can be transported over considerable distances. Transport of man-made nanoparticles as well as natural occurring radionuclides by colloids has been reported e.g. for the Nevada Test Site, USA [30, 31] and the Whiteshell Research Area, Canada [32].

However, colloids can also be retained by interaction with mineral surfaces or by agglomeration, sedimentation and filtration. All processes strongly depend on geochemical parameters, e.g., pH, ionic strength or colloid concentration. Therefore, the colloid stability is a key parameter for colloid facilitated transport. Dynamic light scattering (photon correlation spectroscopy; PCS) is frequently used to determine the coagulation rate and critical coagulation con-

centration (CCC) of various clay colloid suspensions [33-35]. Montmorillonite platelets are the major colloidal particles found to be mobilized from Febex bentonite. Due to their permanent negative face charge originating from isomorphous substitution and their pH dependent edge charge caused by broken tetrahedral and octrahedral sheets exposing silanol and aluminol groups [36, 37] three different modes of interactions can be distinguished: edge-face (EF), edge-edge (EE) and face-face (FF). In order to be able to predict montmorillonite colloid stability based on extended DLVO-theory [38, 39] the overall surface potential has to be separated into potentials and interaction modes associated with the edge and face geometry of the montmorillonite platelets and summing up hydration forces, born repulsion, electric double layer repulsion and London - van der Waals attraction. One suitable approach is the geometrical assumption made by Mahmood et al. [40] to calculate the total interaction energy by using a half-cylinder with the radius equal to half the thickness of the montmorillonite platelet.

In the **C**olloid and **R**adionuclide **R**etardation (CRR) experiment carried out at the Grimsel Test Site (GTS) the in situ migration behaviour of selected radionuclides and chemical radionuclide homologues in the presence and absence of bentonite colloids in a water-conducting shear zone was studied [23, 24]. Under fast flow conditions (~36 m/d) recovery of injected bentonite colloids was in the range of 50-100 %. Related laboratory experiments in granodiorite bore cores from the same site using carboxylated polystyrene (latex) colloids showed colloid recoveries ranging from 10 to nearly 50 % [41] under longer fracture residence times. Similarly low colloid recoveries with increasing residence time were found by other investigators [42]. The authors conclude that even under geochemical conditions where colloids are highly stabilized (low salinity, high pH) adsorption/filtration onto mineral surfaces may occur.

The extent of colloid adsorption on natural mineral surfaces may be influenced by, e.g., the chemical heterogeneity of the mineral surfaces, surface roughness, surface coatings, discrete surface charges (mineral edges and planes), mineral dissolution, the presence of dissolved ions or by matrix diffusion [43-48]. Degueldre et al. [49] carried out sorption experiments at pH 8 ($I = 10^{-2}$ M $NaClO_4$) with clay colloids and several single minerals (muscovite, biotite, quartz, feldspar) comprising the Grimsel granodiorite and observed considerable colloid adsorption. Alonso et al. [50] studied the interactions between gold colloids and a granite surface by μ-Particle Induced X-Ray Emission (μPIXE) to determine the amount of adsorbed colloids on different minerals under varying chemical conditions. These authors concluded that adsorption of colloids on rock surfaces is generally determined by electrostatic interactions. However, colloid adsorption was also detected under unfavorable (repulsive) colloid-fracture surface attachment conditions (e.g., alkaline pH). It was suggested that chemical effects may enhance colloid/rock interaction when favorable (attractive) electrostatic interaction does not exist. Furthermore, theoretical studies have been performed to calculate surface charge heterogeneity effects (e.g., [51]). These effects have also been experimentally evaluated, e.g. for Cu ion adsorption onto silica [52].

The issues mentioned above have been investigated in detail within the KOLLORADO-1 report [53] which gives a good overview of the state-of-the-art as basis of the KOLLORADO-2 project for the partners KIT-INE and GRS.

1.3 Aims and Approach

Laboratory program. The laboratory program conducted within the project KOLLORADO-2 aimed on deriving data on *(a) potential sources of colloid formation, (b) colloid- radionuclide interaction, (c) colloid attachment/retention mechanism and (d) the analysis of field migration experiments conducted at the GTS.* This will be elaborated in detail below:

To a): Concerning the formation of colloids at the interface between the bentonite buffer/backfill and the host rock formation two aspects are investigated in detail within the KOLLORADO-2 project:

- Colloid formation through colloidal release from the compacted bentonite as a function of contact water geochemistry, confining plate pore size, aperture distance and fluid velocity. The results are discussed in the light of the contact water composition changes and compared to the bentonite critical coagulation concentration (CCC) determined previously in batch-type coagulation studies (see chapter 2.1.3).

- Feasibility of the long-term in situ test (emplacement of a packer system with compacted bentonite rings in the MI shear zone at the GTS) concerning the radionuclide labeling and addition of structural substituted montmorillonite.

To b): Data sets of radionuclide desorption from montmorillonite colloids performed within the CRR project focused on short time scales capturing the fracture residence times of the in situ experiments. To gain knowledge about the long-term radionuclide-colloid-rock interaction the experimental program within KOLLORADO-2 focused on considerable longer time-scales (weeks to years) with two different approaches:

- Batch-type studies in the ternary system bentonite colloids – fracture filling material (FFM) and radionuclides (Am(III), Pu(IV), Th(IV), Np(V), U(VI) and Tc(VII)). Within this experimental program, synthetic Zn/Ni substituted montmorillonite was used. The results obtained are compared to Febex bentonite derived natural montmorillonite colloids.

- A similar batch-type approach using natural humic substances as a concurrence ligand to monitor desorption kinetics was used. Here, desorption was followed by asymmetrical flow-field-flow fractionation (AsFlFFF) coupled to ICP-MS.

- Indirect evidence of bentonite colloid metal sorption reversibility is also obtained from a number of field migration experiments under variation of flow velocity/residence time and desorption rates are determined and compared to the laboratory data.

To c): From the present status of knowledge, binding mechanisms of negatively charged colloids on negatively charged fracture mineral surfaces are not sufficiently understood. Under unfavorable (repulsive) electrostatic conditions it is not clear which interaction mechanisms

lead to colloid attachment. The work conducted within KOLLORADO-2 intended to answer this open question based on the following approach:

- Atomic Force Microscopy (AFM) colloid probe measurements under variable geochemical conditions and surface roughness to measure interaction forces between model colloid (carboxylated microspheres) and collector surfaces.

- Collector surfaces were varied starting with Si-waver material of defined surface roughness to single minerals usually found in crystalline rocks (mica, quartz, feldspar) to real mineral aggregates found on granite rock surfaces.

- Effect of field of view length (L) investigated using AFM resolution compared to vertical scanning interferometry (VSI) on the representative roughness parameters and attachment probability.

- Comparison of experimental results with theoretically calculated force curves based on DLVO theory in order to develop an approach to predict colloid-surface interaction.

- Upscaling of colloid-fracture surface interaction via macroscopic data derived from in situ migration experiments under variation of residence time in a natural water conducting fracture.

To d): The analysis of samples by HR-ICP-MS, LIBD/ s-curve LIBD, LSC and γ-spectrometry of the migration experiments performed at GTS in the framework of the CFM project was almost exclusively performed by KIT-INE. This included analysis of several homologues (Tb, Eu, Hf, Th) or radionuclides (Cs, Na, Ba, Am, Th, Pu, Np) and bentonite colloids. In addition, for the radionuclide migration test (CFM Run 12-02) the mobile LIBD system was transferred to the GTS for on-site colloid detection.

Modeling. One goal is to shed light on the multitude of different interaction forms and paths between radionuclides, colloids and the sediment matrix. Special interest was on the consequences of kinetically controlled adsorption and desorption processes and the influence of fracture geometry. A twofold approach was used:

(a) implementing a fracture geometry as realistic as possible by using µCT data into a 3D computational fluid dynamics (CFD) model investigating the effect on colloid/conservative tracer retention and

(b) macroscopic 1D/2D models using simplified geometry implementing sorption/desorption kinetics of colloids/radionuclides.

The RN colloid sorption/desorption and filtration parameters derived in the laboratory program by KIT-INE provide necessary input for transport calculations. Having calibrated the hydrogeological parameters with tracer data, the thus configured problem is then employed to make predictions for the migration of radionuclides and colloids, which are in turn compared to respective experiments in order to validate the models. During this project phase, a

number of field dipole experiments under differing flow conditions with homologues and colloids have been performed within the CFM project, providing the opportunity to particularly investigate the dependence of kinetically-controlled processes from the transport time. On that basis predicting calculations for first field experiments with radionuclides were carried out.

For the computer simulations a 2D as well as a 1D-transport code was used. This enables us to investigate the influence of dimensionality and complex flow fields on the form of the break through curve. In particular, we intend to separate these effects from matrix diffusion. To the end colloidal transport and sorption effects were integrated into the 2D version of the program r^3t. While the simulation of the CFM experiment in two dimensions leads to realistic run times, the computing demands of repository scale calculations force us to fall back on our 1D code TRAPIC [54, 55], which is currently further developed in order to consider colloid facilitated radionuclide transport in fractured media by a double porosity approach.

During the first phase of the CFM project, a series of tracer tests have been performed to evaluate suitable flow fields for the long-term in situ test within the fractured shear zone. The modeling work investigates also the long-term flow and the transport of tracers in the fractured shear zone at two different locations where in-situ colloid and radionuclides migration experiments are planned to take place. The calculations were carried out using the finite element code ADINA-F [56]. The main objectives of the numerical analyses are:

- Estimation of the flow and transport parameters from GTS hydraulic tests.
- Numerical simulations of conservative (Uranine/Amino-G) tracer tests to support the in situ measurements [1].
- The influence observation borehole extraction volume on the hydraulic conditions in the near-field of the compacted bentonite source.

1.4 List of publications within KOLLORADO-2

PhD thesis:

Seher, Holger (2011): The influence of colloids on the migration of radionuclides (in German). Ph.D., Universität Heidelberg.

Huber, Florian (2012): Impact of kinetics and flow path heterogeneity on nanoparticle/radionuclide migration (in English). Ph.D., Freie Universität Berlin.

Peer reviewed publications of INE in the framework of KOLLORADO-2:

1. Bouby, M.; Geckeis, H.; Lützenkirchen, J.; Mihai, S.; Schäfer, T., Interaction of bentonite colloids with Cs, Eu, Th and U in presence of humic acid: A flow field-flow fractionation study. *Geochim. Cosmochim. Acta* **2011,** *75*, (13), 3866-3880.

2. Darbha, G. K.; Fischer, C.; Michler, A.; Luetzenkirchen, J.; Schäfer, T.; Heberling, F.; Schild, D., Deposition of Latex Colloids at Rough Mineral Surfaces: An Analogue Study Using Nanopatterned Surfaces. *Langmuir* **2012,** *28*, (16), 6606-6617.

3. Darbha, G. K.; Schäfer, T.; Heberling, F.; Lüttge, A.; Fischer, C., Retention of Latex Colloids on Calcite as a Function of Surface Roughness and Topography. *Langmuir* **2010,** *26*, (7), 4743-4752.

4. Huber, F.; Enzmann, F.; Wenka, A.; Bouby, M.; Dentz, M.; Schäfer, T., Natural micro-scale heterogeneity induced solute and nanoparticle retardation in fractured crystalline rock. *J. Contam. Hydrol.* **2012,** *133*, 40-52.

5. Huber, F.; Kunze, P.; Geckeis, H.; Schäfer, T., Sorption reversibility kinetics in the ternary system radionuclide–bentonite colloids/nanoparticles–granite fracture filling material. *Appl. Geochem.* **2011,** *26*, (12), 2226-2237.

6. Bruggeman, C.; Maes, N.; Christiansen, B. C.; Stipp, S. L. S.; Breynaert, E.; Maes, A.; Regenspurg, S.; Malström, M. E.; Liu, X.; Grambow, B.; Schäfer, T., Redox-active phases and radionuclide equilibrium valence state in subsurface environments – New insights from 6th EC FP IP FUNMIG. *Appl. Geochem.* **2012,** *27*, (2), 404-413.

7. Schäfer, T.; Huber, F.; Seher, H.; Missana, T.; Alonso, U.; Kumke, M.; Eidner, S.; Claret, F.; Enzmann, F., Nanoparticles and their influence on radionuclide mobility in deep geological formations. *Appl. Geochem.* **2012,** *27*, (2), 390-403.

8. Darbha, G. K.; Fischer, C.; Luetzenkirchen, J.; Schäfer, T., Site-specific retention of colloids at rough rock surfaces *Environ. Sci. Technol.* **2012**, 46,(17), 9378-9387.

9. Huber, F.; Schild, D.; Vitova, T.; Rothe, J.; Kirsch, R.; Schäfer, T., U(VI) removal kinetics in presence of synthetic magnetite nanoparticles. *Geochim. Cosmochim. Acta* **2012**, 96, 154-173.

10. Fischer, C.; Michler, A.; Darbha, G. K.; Mike Kanbach; Schäfer, T., Deposition of mineral colloids on rough rock surfaces. *Am. J. Sci.* **2012**, 312, 885-906.

11. Filby, A.; Plaschke, M.; Geckeis, H., AFM force spectroscopy study of carboxylated latex colloids interacting with mineral surfaces. Colloids Surf. A **2012**, 414, 400-414.

Book chapters:

Geckeis, H.; Rabung, T.; Schäfer, T. (2011): Actinide - Nanoparticle interaction: generation, stability and mobility. In *Actinide Nanoparticle Research*, Kalmykov, S. N.; Denecke, M. A., Eds. Springer-Verlag: Berlin, Heidelberg, pp. 1-33.

Conference proceedings:

Flügge, J., Küntzel, M., Schäfer, T., Gaus, I., Noseck, U. (2010): Modeling colloid-bound radionuclide transport at the Grimsel test site. In: “Proceedings of the International Groundwater Symposium by IAHR”, Valencia, Spain, September 22-24, 2010.

2 Experimental Program

2.1 Laboratory program

2.1.1 The use of synthetic Zn-/Ni-labeled montmorillonite colloids as a natural bentonite marker

Abstract. Sorption reversibility kinetics for selected radionuclides (^{99}Tc(VII), ^{232}Th(IV), ^{233}U(VI), ^{237}Np(V), ^{242}Pu(IV) and ^{243}Am(III)) using synthetic montmorillonite colloids containing structurally bound Zn or Ni in the octahedral sheet in the presence of granodiorite fracture filling material from Grimsel (Switzerland) were examined in batch studies. The aim of the study is to compare the radionuclide sorption reversibility kinetics results obtained with the synthetic Zn-/Ni-montmorillonite to identical results already available using natural FEBEX bentonite derived colloids. The size distribution of the colloids mobilized from both synthetic montmorillonites is relatively comparable to the one obtained from the natural FEBEX bentonite. No colloidal attachment occurs over 10,000 h (~13 months) for both types of montmorillonite colloids on the fracture filling material. The tri- and tetravalent radionuclides (^{232}Th(IV), ^{242}Pu(IV) and ^{243}Am(III) are strongly colloidal associated initially in contrary to ^{99}Tc(VII), ^{233}U(VI) and ^{237}Np(V) which show no interaction with the bentonite colloids. In line with Eh-pH conditions prevailing in the experiments and thermodynamic considerations, the decrease in concentration of redox sensitive elements of ^{99}Tc(VII), ^{233}U(VI) and ^{237}Np(V) may be explained by a reduction into the lower oxidation state causing precipitation, sorption to the fracture filling material, possible formation of eigencolloids and/or even sorption to the bentonite colloids. Results for trivalent (^{243}Am(III)) and tetravalent radionuclides (^{232}Th(IV) and ^{242}Pu(IV)) obtained after ultracentrifugation show clearly lower concentrations. This demonstrates a radionuclide colloid association in good agreement with results obtained on natural FEBEX clay colloids (Huber et al., 2011). A slow radionuclide sorption reversibility is observed over 10,000 h for ^{232}Th(IV), ^{242}Pu(IV) and ^{243}Am(III) in qualitative agreement to the work on natural FEBEX colloids. This slower reversibility kinetics may be explained by the difference of the specific surface area with ~67 m^2/g for Ni-or Zn-montmorillonite colloids and ~33 m^2/g for natural FEBEX colloids, respectively. Based on the conceptual model that the driving force for the kinetically controlled radionuclide colloid desorption process and subsequent sorption to the FFM is the excess in surface area offered by the FFM, the observed desorption kinetics may likely be related to the different colloid/FFM surface area ratio.

Materials & Methods

Zn/Ni-montmorillonite synthesis and characterization. The Zn- and Ni-montmorillonite powders were synthesized using the procedure published by [57, 58]. The synthesis protocol is only briefly described here and the reader is referred to the original papers. Montmorillonite

containing Al and exclusively Zn/Ni as divalent elements in the octahedral sheet were synthesized in acidic and fluoride medium under mid-hydrothermal conditions (493 K, autogeneous pressure). A thorough characterization is provided by [57, 58] to which the reader is again referred for further information.

Zn/Ni-montmorillonite colloids characterization. In total, four Zn- and Ni-montmorillonite colloid suspensions were prepared in natural Grimsel groundwater (GGW), by repeating four time cycles of suspending, centrifugation for 30 min at 4000 rpm and re-suspending the separated solid in GGW. In case of the first Zn suspension, 250 mg Zn-montmorillonite powder has been equilibrated 10 days in 50 mL of GGW prior to the first step of centrifugation in order to achieve a high degree of delamination. The 3 others suspensions were equilibrated 3 days prior to centrifugation. In case of the Ni suspension, 1 g in 500 ml GGW has been equilibrated for 3 days. The final supernatants, containing either Zn- or Ni-Montmorillonite colloids, were taken as a colloid stock dispersions/solutions and stored in a refrigerator until both material analysis and experiments were performed.

Inductively coupled mass spectrometry (ICP-MS). The element concentration in the Zn- and Ni-Montmorillonite suspensions were determined by ICP-MS (Perkin Elmer ELAN 6000) after dilution by a factor of 50 in GGW. These samples are acidified with HNO_3 to pH 2 and immediately shaken before injection. An aliquot of each final suspension was ultracentrifuged at 90,000 rpm for 60 min in order to remove colloids subsequently analyzed for selected elements (Table 1).

Photon correlation spectroscopy (PCS). The electrophoretic mobility μ of the Zn- and Ni-montmorillonite colloids has been measured with the ZetaPlus system (Brookhaven Inc.) using the PALS Zeta Potential Analyzer Software (Version 3.13) setting the data acquisition criterion to a target residual of 0.02. The ζ-potentials measured in this study are calculated from electrophoretic mobility measurements using Smoluchowski's equation (Equation 1):

$$\zeta = \frac{\mu \cdot \eta}{\varepsilon_r \cdot \varepsilon_0} \qquad \text{(Equation 1)}$$

where ε_r is the relative permittivity of water [-], ε_0 the dielectric permittivity of vacuum [-] and η is the viscosity [Pa×s]. A complete description of this technique is provided by [59]. The coagulation rate of the Zn-/Ni-montmorillonite colloids is determined by photon correlation spectroscopy (PCS) using a ZetaPlus system (Brookhaven Inc.) [35]. The scattering light is measured perpendicular to the incident laser beam and the data evaluation is made by the instrument built-in software (Version 2.27). The hydrodynamic diameter (d_h) is calculated from the measured diffusion coefficient (D) by the Stokes-Einstein equation ((Equation 2) assuming spherical colloid geometry:

$$r_h = \frac{k_B \cdot T}{6 \cdot \pi \cdot \eta \cdot D} \qquad \text{(Equation 2)}$$

where k_B is the Boltzmann constant [J·K^{-1}], T the absolute temperature [K] and η is the viscosity of the fluid [Pa·s]. The stability ratio is calculated based on the expression given by (Equation 3) [35]:

$$W = \frac{[(dr_h/dt)_{t\to 0}/C]^{(f)}}{[(dr_h/dt)_{t\to 0}/C]} \qquad \text{(Equation 3)}$$

where W is the stability ratio [-], C the colloid concentration [mol/L] and the superscript (f) refers to measurements in the regime of fast solely diffusion controlled coagulation [33-35]. The region where fast diffusion controlled aggregation sets on is often called critical coagulation concentration (CCC). The advantage to determine colloid stability by means of W is the independency of the observation time used throughout the experiments [60] and that it is therefore possible to directly compare with published literature data. Prior to each coagulation experiment the colloid size of the suspension is checked directly in the cuvette. Afterwards, to start the coagulation process, the $CaCl_2$ electrolyte solution is added in a quantity to get the desired concentration. A measurement period of 10 s is combined to one data point by the software program. The measurement is stopped when the particle size has reached approx. 1000 nm.

Atomic Force Microscopy (AFM). Contact mode AFM imaging is performed using a Topomer TMX 2000 Explorer which is equipped with a cantilever oscillating hardware with possible oscillation frequencies ranging from 0 to 600 kHz. Probes with silicon tips (nominal radius of curvature, <10 nm; nominal spring constant, 48 N/m; nominal resonance frequency, 190 kHz) are mounted on a scanner with a maximum range of 2.2 µm in the x-y direction and 900 nm in the z direction. Imaging is performed on dried samples. The Zn-/Ni-montmorillonite colloids deposit was obtained by immersing a clean mica plate for 1 minute directly in the undiluted colloid suspensions. This method allows colloidal particle to adsorb from the solution to the mica surface and to avoid aggregates formation during drying in air [61].

Asymmetric Flow Field-Flow Fractionation (AsFlFFF) coupled to UV-Vis spectrophotometry and ICP-MS spectroscopy. The colloid stock suspensions were probed by Asymmetric Flow Field-Flow Fractionation (AsFlFFF) coupled to UV-Vis spectrophotometry and ICP-MS spectroscopy. The experimental equipment applied in this study has been detailed recently in [62-64]. The AsFlFFF system (HRFFF 10.000 AF4) is provided by Postnova Analytics (Landsberg, Germany). The accumulation wall consisted of an ultra-filtration membrane made of regenerated cellulose (cutoff 5 kDa, Postnova Analytics). The trapezoidal PTFE spacer, which delimits the area where the fractionation takes place, is 0.5 mm thick. In this study, the carrier solution consists of ultra-pure water adjusted to pH 9.3 by addition of ultra-pure NaOH 1 M (Merck). Colloid sizes are derived by calibration curves using a series of polystyrene sulfonate (PSS) reference standards (Polysciences, Eppelheim, Germany) with certified molecular weights (1.29, 4.4, 15.2, 29 and 81.8 kDa) and a series of carboxylated polystyrene

reference particles (Magsphere, USA) with certified sizes (24, 105, 207 and 510 nm). Mixtures were prepared just before injection into the carrier solution. Overloading effects which

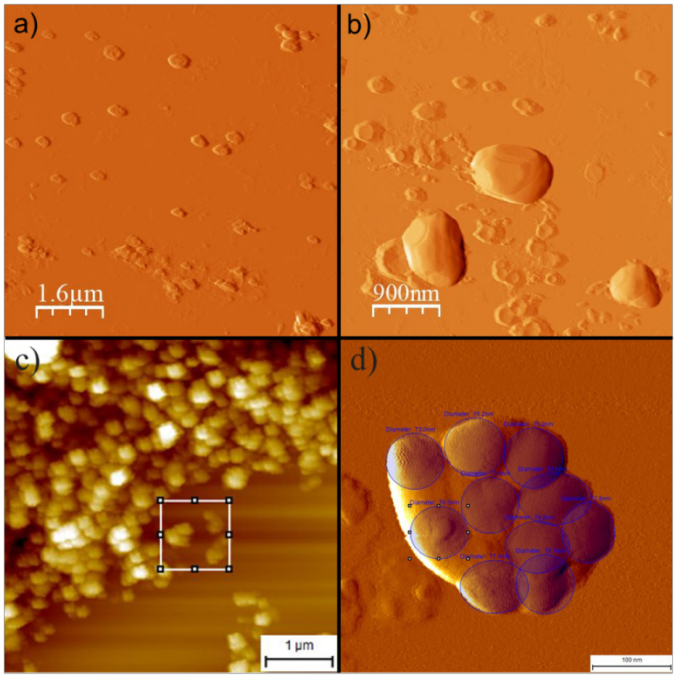

Figure 2.1: AFM pictures of the Zn- and Ni-montmorillonite colloids. a) and b) Zn-montmorillonite c) and d) Ni-montmorillonite.

have been frequently reported in the literature [65-67] have been checked by injecting 100 µL of a reference colloid mixture prepared at different concentrations. No shift of elution times was observed for PSS concentrations lower than 100 µg/L. Calibration methods for the quantitative evaluation of fractograms and their validation are described in detail in [68]. Briefly, measured intensities for the respective element of interest were normalized to the measured intensity of an internal standard ^{103}Rh. ^{103}Rh (50 µg/L) dissolved in 5% HNO3 (ultrapure) is admixed at constant flow to the channel effluent before entering the ICP-MS nebuliser. ICP-MS intensities are converted to masses (ng) for each element of interest. The mass versus elution time fractogram is then integrated in order to derive the total peak areas, which can then be attributed directly to the amount of given element in the respective colloidal fraction. This approach has been primarily adopted to correct for flow rate fluctuations observed with our AsFlFFF notably at the beginning of each fractionation run.

Laser-Induced Breakdown Detection (LIBD). The colloid concentration and number-weighted average colloid diameter is determined with a Laser-induced Breakdown Detection (LIBD) system [69, 70]. The sample solution is pumped through a quartz flow-through cell. A dielectric breakdown is produced in the focus region of a pulsed laser beam (Nd: YAG-laser, frequency: 15 Hz, wavelength: 532 nm). The laser pulse energy is varied. The laser pulse energy where the first breakdowns of the colloids can be detected is called breakdown threshold. The breakdown threshold is increasing with decreasing colloid size. The slope of the s-curve is increasing with increasing colloid concentration when the colloid size is kept constant. This

method is referred to as acoustic LIBD since the location of the breakdown event is done via acoustic location. The system is calibrated with polystyrene reference particles.

Fracture Filling Material characterization. The fracture filling material (FFM) applied in this study was obtained from the Grimsel Test site (GTS), Switzerland. The main rock type in this area is the so-called Grimsel "granodiorite" although from a petrologic point of view it should be classified as a granite [71]. Due to deformation ductile shear zones and soft fault gouges formed which have been reactivated later by brittle deformation causing thick fault gouge in the cm scale consisting mainly of phengite (smectites) and interbedded rock fragments [72, 73]. Prior to the experiments, the material was manually crushed, sieved and freeze dried under ambient conditions. A size fraction of 1-2 mm has been separated according to the experiments by [74] which has been characterized by scanning electron microscopy (SEM), energy dispersive x-ray microanalysis (EDX), specific surface area analysis (N_2-BET) and x-ray fluorescence analysis (XFR) (Table 2.1). It should be noted that although the material stems from the same location as the material used by [74] it represents a different batch.

Radionuclide cocktail characterization. The radionuclide cocktail used in the batch experiments was prepared after the same procedure as the cocktail used by [74]. Natural Grimsel groundwater (ph = 9.7, I = ~ 0.001 mM; see e.g. [74] for more details about the chemical composition of the natural Grimsel groundwater) which has been stored under anoxic conditions was spiked with either synthetic Zn- or Ni-montmorillonite colloids with a concentration of ~ 25 mg/L, respectively and subsequently with selected radionuclides. The whole preparation of the cocktails has been done in a glove box under Ar atmosphere. In accordance to the previous FEBEX bentonite experiments [74] the following radionuclides (in their respective oxidation states) have been applied: ^{99}Tc(VII), ^{232}Th(IV), ^{233}U(VI), ^{237}Np(V), ^{242}Pu(IV), and ^{243}Am(III). ^{242}Pu(IV) was added as ^{242}Pu(III) after electrochemical reduction and most likely totally transferred to ^{242}Pu(IV) by pH adjustment of the cocktail. Before the start of the experiments the cocktail was settled for 24 h. In Table 2.2 an overview of the RN applied in the experiments in conjunction with their concentrations are listed.

RN bentonite sorption reversibility experiments. All experiments were conducted at room temperature (~ 21°C) in a glove box under Ar atmosphere (< 1 ppm O2). A semi micro Ross electrode (81-03, Orion Co.) in combination with a digital pH meter (720A, Orion Co.). was used to measure pH in the samples. At least 4 commercial buffer solutions (Merck) were used to calibrate the set-up. Prior to the batch-type experiments the FFM material was contacted with fresh GGW in Zinsser vials (20 mL, HDPE) over a period of six weeks, exchanging the solution at least 5 times within this period. To monitor this equilibration process aliquots of the supernatant solution were taken for analysis. Duplicates of every sample were prepared with a solid to liquid ratio of 1:4 (4 g solid and 16 ml of solution). After this equilibration phase the supernatant was completely discarded from the vials and refilled with the radionuclide-colloid cocktail. First aliquots were taken 24h after addition of the radionuclide cocktail to the samples. The next aliquots were taken after 48 h, 120 h, 336 h, 504 h, 700 h, 1000 h and 3500 h,7500 h and 10000 h respectively. An aliquot of every sample (~ 4 ml) were transferred in ultracentrifugation vials using a syringe, sealed by welding inside the Ar glove box and subsequently ultracentrifuged (Beckman XL-90, rotor type 90Ti) at 90,000 rpm (cen-

trifugal force of about $5 \cdot 10^5$ g) for 90 min to remove colloid associated radionuclides. Afterwards aliquots of the supernatant were taken with a syringe and transferred to Zinsser vials and subsequently analyzed by ICP-MS. The ultracentrifugation procedure described above has been proven to be suitable to effectively remove bentonite colloids as well as RN (e.g.Th(IV), Pu(IV), etc.) "eigencolloids" from solution (Altmaier et al., 2004).

RN desorption experiments from FFM. Subsequently the samples were taking for the sorption reversibility experiments, the remaining RN containing solution of the sample vial was completely discarded and 8 ml of fresh GGW was added to the FFM material previously in contact with the RN cocktail in the Zinsser vials. The GGW was contacted for 7 days with the FFM to observe a possible desorption/remobilization process. After the contact time, aliquots were taken and analyzed by ICP-MS.

Results & Discussion

Zn/Ni-montmorillonite colloids characterization. The final concentrations of Na, Al, Fe, Zn and Ni in the prepared stock suspensions are listed in Table 2.1. Additionally. concentrations are given for ultracentrifuged samples to determine the colloidal concentration. Regarding the synthetic Zn-montmorillonite, Zn is found to be at 97 % in colloidal form and Al at 99.8 %. In case of Ni-montmorillonite, Al is indicated to be only ~50 % and Ni ~82 % in colloidal from, respectively. The pH decrease (~7.2) in the stock suspensions compared to the original GGW (~9.7) can be explained by a Na+-H+ exchange by the montmorillonite. The Zn/Ni-montmorillonite colloid concentration is determined via Al and Zn/Ni ICP-MS measurements taking into account the structural formula of Zn-/Ni-montmorillonite, respectively.

Table 2.1: Concentrations of Na, Al, Fe, Zn and Ni in both the Zn-montmorrilonite and Ni-montmorillonite colloid stock suspensions. Values are given both for UC and nUC samples.

Element	GGW (mg/L)	Zn-Mtm. (mg/L)	Zn-Mtm. (UC) (mg/L)	Ni-Mtm. (mg/L)	Ni-Mtm. (UC) (mg/L)
Na	0.56	15.5	15.5	17.1	17.4
Al	0.03	11.2	0.02	6.6	3.4
Fe	-	0.10	0.15	< d.l.	< d.l
Zn	0.004	9.28	0.28	2.59	2.43
Ni				1.9	0.34
pH	9.7	7.23	-	7.99	
Al/Zn		1.21	-		
Al/Ni				3.74	10

Photon correlation spectroscopy (PCS). The light scattering intensity for the measured suspensions lies above ~500k counts. The effective diameter (d_h) slightly increase over the 4

consecutive suspensions cycle. The average effective diameter is 260 nm with an average half-width of 132 nm recalculated from the polydispersivity index. The average ζ potential of the particle (zetaPlus, PALS system, Brookhaven Inc.) is found to be -32 ± 2 mV calculated by using Smoluchowski potential model (Equation 1). This value is slightly higher compared to FEBEX bentonite ζ potential (-40± 2 mV). Colloid stability analysis were performed by measuring the time dependent change of the effective diameter as a function of the $CaCl_2$ electrolyte concentration at pH 7.4. The fastest coagulation rate was observed at 0.83 mmol/L. Lowering the electrolyte concentration to 0.70 mmol/L does not imply a significant decrease in the measured coagulation rate within the analytical uncertainty. But, a significant drop occurs when the electrolyte concentration is furthermore lowered to 0.61 mmol/L. The similar Ca-CCC value found for FEBEX bentonite gives further confidence in the similar colloid stability between the natural and synthetic clay colloids.

The morphology of the bentonite colloids from the Zn stock suspension was imaged using contact mode AFM in air (Figure 2.1). It can be seen that the Zn-Montmorillonite colloids are spread out on the mica surface and most of the particles remain separate whereas a minor amount form aggregates on the mica surface. In Figure 2.1a and b, single particles are seen on the flat mica surface. Most of the single particles have a rather flat structure with diameters range from 70 to 300 nm and heights in the range from 15 to 40 nm (aspect ratio ~ 1/7). In contrast, the larger particles show an aspect ratio in the range of 4 (height 200 nm, diameter 800 nm) and might correspond to aggregates or stacks of montmorillonite platelets. Figure 2.1c shows the Ni-montmorillonite aggregates and in Figure 2.1d one of these aggregates is depicted in a detailed view. It can clearly be seen, that smaller particles (indicated with the blue circles) with values around 70nm forming the bigger aggregates. The roughness of the mica blank substrates was found to be lower than 0.1 nm root-mean-square (RMS) value, which is sufficiently low for a precise particle analysis. Particle diameters are calculated from the determined particle areas on the assumption that particles are disk-type shape. The lateral resolution of AFM is limited by the size and shape of the tip. For diameters range from 70 to 300 nm and heights in the range from 15 to 40 nm (aspect ratio ~ 1/7). In contrast, the larger particles show an aspect ratio in the range of 4 (height 200 nm, diameter 800 nm) and might correspond to aggregates or stacks of montmorillonite platelets. The roughness of the mica blank substrates was found to be lower than 0.1 nm root-mean-square (RMS) value, which is sufficiently low for a precise particle analysis. Particle diameters are calculated from the determined particle areas on the assumption that particles are disk-type shape. The lateral resolution of AFM is limited by the size and shape of the tip. For nanometric spherical particles (e.g., polystyrene nanospheres), lateral artifacts of more than 100% are found in the literature, whereas particle height is reproduced very exactly by AFM. However, the lateral tip artifact markedly depends on particle height, which has to be taken into account for the flat bentonite particles [59].

Table 2.2: Overview of the temporal concentration evolution of the batch reversibility experiments for the radionuclides applied.

Time	Al	Ni	Zn	^{99}Tc	^{232}Th	^{233}U	^{237}Np	^{242}Pu	^{243}Am
hours	mol/L	mol/L	mol/L	mol/L	mol/L	mol/L	mol/L	mol/L	mol/L
Zn-Montmorillonite (non UC samples)									
Colloid bound concentration [%]	-	-	-	< 1%	~100 %	< 10 %	< 1 %	> 75 %	> 82 %
0 (initial)	4.51×10^{-5}	6.76×10^{-8}	1.66×10^{-5}	8.95×10^{-9}	6.99×10^{-8}	3.74×10^{-7}	2.00×10^{-7}	1.12×10^{-8}	5.61×10^{-11}
24	5.27×10^{-4}	1.49×10^{-7}	1.45×10^{-5}	7.72×10^{-9}	5.60×10^{-8}	2.88×10^{-7}	1.44×10^{-7}	8.06×10^{-9}	6.08×10^{-11}
120	2.76×10^{-4}	1.58×10^{-8}	1.27×10^{-5}	8.20×10^{-9}	5.52×10^{-8}	2.55×10^{-7}	1.16×10^{-7}	7.63×10^{-9}	4.46×10^{-11}
336	3.03×10^{-4}	2.65×10^{-8}	1.65×10^{-5}	8.12×10^{-9}	5.312×10^{-8}	2.24×10^{-7}	8.93×10^{-8}	7.08×10^{-9}	5.11×10^{-11}
504	5.67×10^{-4}	3.01×10^{-8}	2.74×10^{-5}	9.72×10^{-9}	6.60×10^{-8}	2.40×10^{-7}	1.02×10^{-7}	8.63×10^{-9}	4.65×10^{-11}
700	6.20×10^{-4}	6.82-10^{-8}	2.00×10^{-5}	8.53×10^{-9}	6.43×10^{-8}	2.27×10^{-7}	9.98×10^{-8}	8.16×10^{-9}	2.73×10^{-11}
1000	5.57×10^{-4}	< d.l.	1.95×10^{-5}	8.46×10^{-9}	6.07×10^{-8}	2.31×10^{-7}	9.50×10^{-8}	7.13×10^{-9}	1.36×10^{-11}
3500	3.99×10^{-4}	< d.l.	1.84×10^{-5}	2.19×10^{-9}	5.30×10^{-8}	1.94×10^{-7}	9.91×10^{-8}	5.52×10^{-9}	1.12×10^{-11}
7500	3.62×10^{-5}	8.50×10^{-8}	1.23×10^{-5}	1.17×10^{-9}	3.21×10^{-8}	1.39×10^{-7}	5.173×10^{-8}	2.16×10^{-9}	< d.l.
10000	9.92×10^{-5}	1.79×10^{-7}	1.79×10^{-5}	4.54×10^{-10}	3.97×10^{-8}	1.90×10^{-7}	6.42×10^{-8}	3.36×10^{-9}	< d.l.
Ni-Montmorillonite (non UC samples)									
0 (initial)	6.56×10^{-5}	2.48×10^{-5}	7.05×10^{-7}	9.10×10^{-9}	7.43×10^{-8}	3.89×10^{-7}	2.08×10^{-7}	1.14×10^{-8}	7.05×10^{-11}
24	2.55×10^{-4}	1.93×10^{-5}	1.82×10^{-6}	8.70×10^{-9}	5.60×10^{-8}	2.83×10^{-7}	1.36×10^{-7}	7.26×10^{-9}	4.28×10^{-11}
120	3.41×10^{-4}	1.88×10^{-5}	1.26×10^{-6}	8.13×10^{-9}	5.90×10^{-8}	2.96×10^{-7}	1.40×10^{-7}	7.45×10^{-9}	3.78×10^{-11}
336	6.26×10^{-5}	2.65×10^{-5}	1.57×10^{-6}	8.02×10^{-9}	4.97×10^{-8}	2.34×10^{-7}	9.06×10^{-8}	6.14×10^{-9}	3.56×10^{-11}
504	4.86×10^{-4}	2.48×10^{-5}	< d.l.	9.70×10^{-9}	9.50×10^{-8}	2.70×10^{-7}	1.15×10^{-7}	7.51×10^{-9}	3.21×10^{-11}
700	4.05×10^{-4}	2.32×10^{-5}	< d.l.	8.78×10^{-9}	6.15×10^{-8}	2.66×10^{-7}	1.22×10^{-7}	7.019×10^{-9}	1.77×10^{-11}
1000	3.71×10^{-4}	1.69×10^{-5}	2.55×10^{-6}	7.54×10^{-9}	4.46×10^{-8}	2.66×10^{-7}	8.76×10^{-8}	4.34×10^{-9}	3.29×10^{-11}
3500	2.74×10^{-4}	2.28×10^{-5}	< d.l.	3.95×10^{-9}	5.42×10^{-8}	2.326×10^{-7}	8.90×10^{-8}	4.29×10^{-9}	1.77×10^{-11}
7500	3.31×10^{-5}	7.76×10^{-6}	6.88×10^{-7}	1.13×10^{-9}	1.62×10^{-8}	1.19×10^{-7}	2.92×10^{-8}	1.30×10^{-9}	< d.l.
10000	7.54×10^{-5}	$1.16\times^{10-5}$	1.19×10^{-6}	9.09×10^{-10}	3.29×10^{-8}	1.98×10^{-7}	5.89×10^{-8}	2.14×10^{-9}	< d.l.

A tip artifact (A) can be estimated by a simple geometrical approach, according to (Equation 4:

$$A = 2S = 2(2R_t \cdot h_p - h_p^2)^{0.5} \qquad \text{(Equation 4)}$$

where h_p is the particle height, R_t is radius of curvature of the AFM tip, and *S* the tip artifact on one side of the particle. The lateral tip artifact (*A*) is calculated individually for each particle where the height data (h_p) are determined by the grain analysis software. In the present case, all the particles have a diameter higher than the tip radius (10 nm according to the manufacturer specification), hence, a tip artifact between 20 and 30 nm is assumed depending on particle height. Particle diameters are corrected by these values of *A*. From the corrected particle diameters (d_p) and the average heights (h_p), a mean aspect ratio (h_p/d_p) of 0.08 is determined. This value is in fair agreement with an assumed aspect ratio of 1/10 for bentonite particles. To sum up, the Zn-Montmorillonite and the FEBEX bentonite colloids display the same morphology (i.e. platelet shape) and the same bimodal distribution with about the same diameter but not the same height. Roughly, the Zn-Montmorillonite colloids are 3 times higher than the FEBEX ones.

AsFlFFF measurements. AsFlFFF measurements have been performed on the Zn/Ni- montmorillonite colloidal stock suspensions obtained after the centrifugation steps. Figure 2.2 depicts the Al and Zn-fractogram obtained for the Zn-montmorillonite colloid stock suspension diluted by a factor of 10 in GGW prior to the injection for fractionation. Two colloidal fractions, with sizes at ~ 50-70 and 200 nm are observed with a rather broad size distribution. Elemental content in the colloidal fraction as determined from AsFlFFF measurements, are in mean: 9.8 mg/L colloidal Al and 5.9 mg/L colloidal Zn. The Al/Zn ratio was determined over the course of the double peak range and was found constant and equal to 2.0 ± 0.2. Elemental contents as determined from direct injection, are in mean: 10.00 mg/L Al and 8.04 mg/L Zn in stock solution. By comparing AsFlFFF and direct injection measurements, it is clear that Al is 100 % colloidal and that 73.5 % of Zn is in colloidal form. These conclusions are in perfect agreement with the Al-Zn measurements display in Table 2.1 and imply a very good sample recovery by AsFlFFF. In both cases, the Zn is very homogeneously correlated with the Al signal, which is greatly in favor of a Zn incorporation into the Al colloids or a homogeneous Zn sorption onto Al colloids. The Al to Zn mass ratio is constant over the entire peak range at a value of 1.9 – 2.0. It corresponds to a Al/Zn mol ratio of 4.86 which is in good agreement with the theoretical value (4.21) deduced from the Zn-montmorillonite structural formula. Results for the Ni-montmorillonite are additionally depicted in Figure 2.2. In contrast to the Zn-montmorillonite colloids, the Ni- montmorillonite colloidal fraction yields a monomodal distribution with a peak maximum position located at ~ 210 nm according to the size calibration with polystyrene particles. The Al/Ni mass ratios are determined to be 1.94 ± 0.59 corresponding to Al/Ni mol ratio of 4.3 which are in good agreement to the mol ratio determined for the Zn-montmorillonite colloids. Also, the sizes of the colloids extracted for both types of synthetic montmorillonite are quite close.

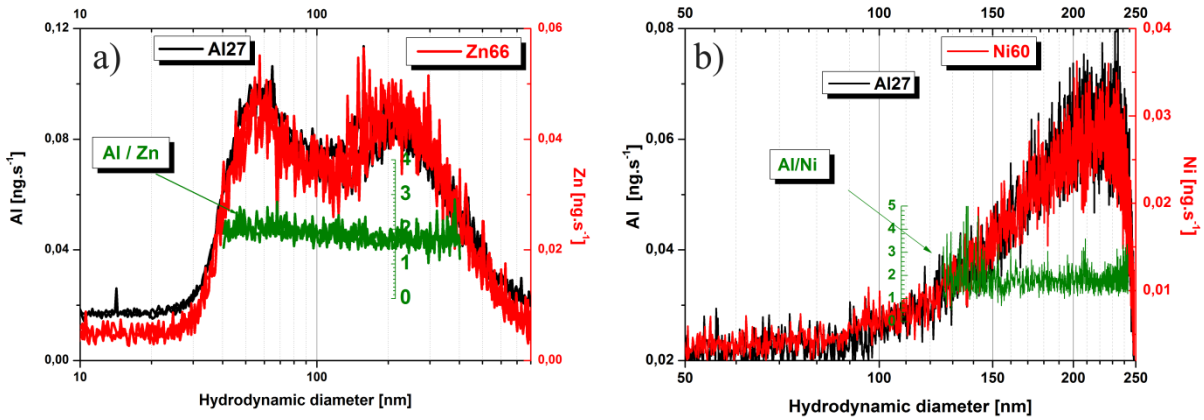

Figure 2.2: AsFlFFF fractograms for Zn- montmorillonite stock solution (left) and Ni-montmorillonite (right).

LIBD analysis. LIBD measurements have been performed on the Zn-montmorillonite stock suspension and corrected from the natural colloid background concentration of the Grimsel groundwater. Due to the high sensitivity of the LIBD, the Zn-Montmorillonite suspension has to be diluted with the Grimsel groundwater to a concentration of ~20 µg/L. Even at this low concentration, the breakdown probability lies close to the saturation of the method at 0.89 (89% of the laser pulses leads to a colloid breakdown). The mean colloid size of the bentonite particles in GGW is determined by evaluating the spatial distribution of the breakdown events relative to the calibration with polystyrene reference particles to values of 50 ± 10 nm. After correction for the different composition of polystyrene and smectites, this corresponds to diameters having a bimodal distribution of 40 nm and 200 nm .Taking into account the average density of 2.7 g/cm^3 for the Zn-Montmorillonite particles and a disk-like shape with 1/10 height-to-diameter proportion (aspect ratio), a mass concentration in a range of 10 mg/L can be calculated. This is only 10 % of the given concentration. However, one has to be careful applying the size calibration for the polystyrene particles directly to the Zn-montmorillonite colloids. The sensitivity for the Zn-montmorillonite particles is found to be significantly lower than for the polystyrene particles. This could be due to a very high ionization energy of the Zn-montmorillonite particles and a breakdown process of higher order than in the case of polystyrene particles. Hence, it appears that the reproducibility of the measurements at different concentrations of the suspension can vary of one order of magnitude. Further series of measurements at different dilution factors and with different suspensions are required to better understand the scatter of colloids concentrations values and to explain these discrepancies.

Fracture filling material (FFM) characterization. Scanning electron microscopy (SEM) of the Grimsel FFM grains show an angular morphology with rough heterogeneous grain surfaces (Figure 2.3). The sieved size fractions of 1-2 mm are validated by SEM. Energy dispersive x-ray microanalysis (EDX) spectra yield mainly k-feldspar, quartz and element signatures for sheet-silicates, most likely of biotite- and/or muscovite type.

The specific surface areas of the FFM was determined by BET N_2-adsorption. The samples were heated to 300°C and degassed for 6h. The determination of the surface was done via

multiple point analysis and a subsequent fit with the BET isotherm. In all BET measurements care was taken to have sufficient total surface (> 1 m^2) for reliable measurements. Specific surface area measurements (BET) yielded values of 0.26 m^2/g for the 1-2 mm size fraction, respectively. This values is higher compared to the 1-2 mm FFM size fraction used in the experiments by [74] with a specific surface area of 0.15 – 0.17 m^2/g. This difference may be attributed to artifacts from the sieving procedure and/or due to mineralogical differences between the different batches of the FFM.

Chemical rock composition analysis by x-ray fluorescence (XRF) has been conducted to determine the bulk major and trace elemental distribution in the fracture filling material (Table 3). As expected for a granodiorite, major elemental composition is dominated by SiO_2, Al_2O_3, K_2O and Fe_2O_3(tot) representing the main mineral elements quartz and k-feldspar/albite which is in accordance to the EDX analysis. The total iron content (3.43 wt% Fe_2O_3(tot) is comprised of 1.84 wt% FeO) which gives hint to minor oxidation effects through the separation and preparation of the FFM size fractions.

Table 2.3: Results of the XRF measurements.

SiO_2 (%)	Al_2O_3 (%)	Fe_2O_3(t) (%)	FeO (%)	MnO (%)	MgO (%)	CaO (%)	Na_2O (%)	K_2O (%)	TiO_2 (%)	P_2O_5 (%)	LOI (%)	Sum (%)
67.92	15.21	3.43	1.84	0.07	1.91	1.3	4.4	3.77	0.512	0.13	1.61	100.25

Ba (ppm)	Ce (ppm)	Co (ppm)	Cr (ppm)	Cu (ppm)	La (ppm)	Nb (ppm)	Ni (ppm)	Pb (ppm)	Rb (ppm)	Sr (ppm)	V (ppm)	Y (ppm)	Zn (ppm)	Zr (ppm)
758	87	5	11	0	40	23	7	9	200	171	39	45	64	289

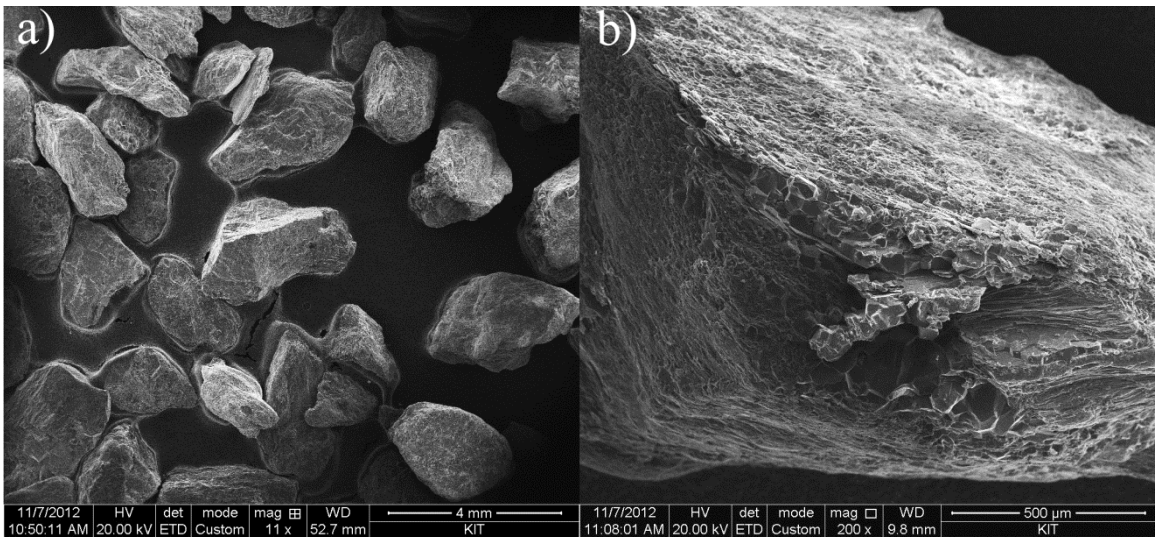

Figure 2.3: a) and b) SEM pictures fo the FFM.

Eh-pH-evolution. Eh and pH measurements have been conducted for every sample to monitor the contact time dependent evolution of pH and $Eh_{(SHE)}$ values. This was mandatory since the radionuclide cocktail included several redox sensitive radionuclides, i.e. $^{99}Tc(VII)$, $^{233}U(VI)$, $^{237}Np(V)$ and $^{242}Pu(IV)$. Details on the set-up and procedure of the pH and especially the Eh measurements are described in [74]. Nevertheless, it needs to be clearly stated that redox potential measurements may be coupled to high uncertainties especially in natural systems (see e.g. [75] and reference therein for general information on this issue). Figure 2.4 shows the pH-Eh evolution over the experimental duration for both sample series. The initial pH of the tracer cocktail (~9.7) slightly dropped in case of the samples after 24h to around 9.6 and 9.4 in case of the Zn- and Ni-Montmorillonite series, respectively most likely due to dissolution and/or ion-exchange processes of the fracture filling material. In the course of the experiments the pH values dropped further to final values of ~9.3 and ~9.2 for the Zn- and Ni-Montmorillonite, respectively after 10,000 h contact time. Regarding the evolution of the redox potential, both series show a pronounced decrease as a function of contact time starting from strongly oxidizing conditions after 24h (Eh_{SHE} = ~250 mV for Ni-Montmorillonite and ~350 mV for the Zn-Montmorillonite) to strongly reducing conditions after 10,000 h contact time (Eh_{SHE} = ~- 230 mV for Ni-Montmorillonite and ~- 240 mV for the Zn-Montmorillonite). These measured redox potentials are significantly lower than the values obtained in the laboratory by [74] but are in good agreement to in-situ Eh_{SHE} values obtained by [76] (Eh_{SHE} = < ~ -300 mV). The observed differences between the redox potentials obtained in this study and former results by [74] may be explained by a different batch of FFM and GGW, respectively.

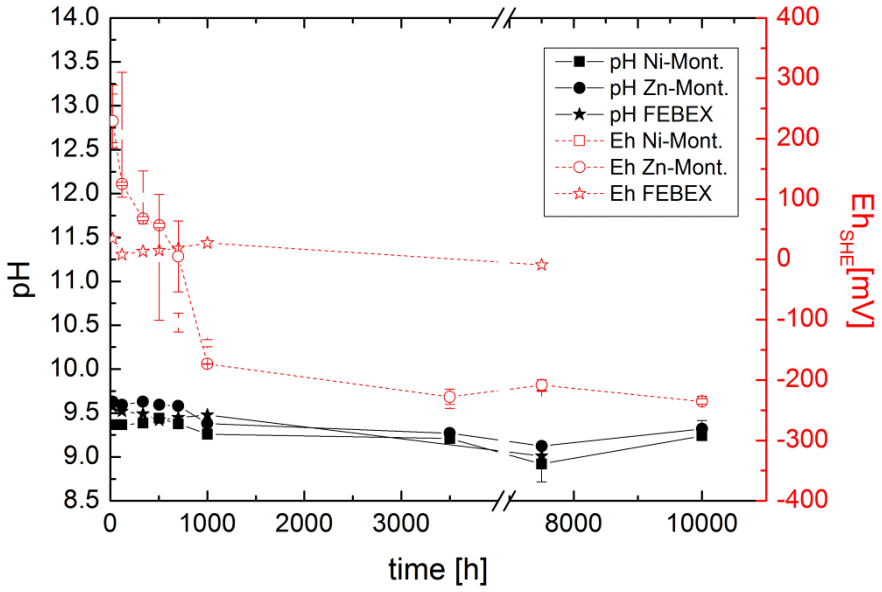

Figure 2.4: Eh and pH evolution of the Zn- and Ni-Montmorillonite of this study compared to similar experiments using Febex bentonite colloids [74].

Generally speaking, the discrepancies mentioned above between different laboratory studies and in-situ experiments reflect the low redox capacity of these systems making them extremely sensitive to intrusion of oxygen traces in the laboratory (glovebox < 1ppm O_2) and the uncertainties in measuring Eh values in groundwater.

Behavior of Zn- and Ni-montmorillonite colloids. Mandatory for the understanding of the results obtained for the different radiotracers is the colloid-fracture filling interaction over the experimental duration. It is obvious that a sorption of the colloids (and thus also the colloid associated radionuclides) onto the fracture filling material would bias the interpretation concerning colloid radionuclide sorption reversibility of these radionuclides. Thus, every sample was ultracentrifuged to assess the colloid-bond radionuclide concentration as well as the concentrations of the colloids as deduced from the Al, Zn and Ni ICP-MS signal. Results for Al, Zn and Ni concentrations of both series are depicted Figure 2.5 and listed in Table 2.2. Regarding Al, the non-ultracentrifuged samples scatter between ~6×10^{-4} M and ~3×10^{-5} M whereas the ultracentrifuged samples are in the range of ~1.5×10^{-5} M and ~2.5×10^{-6} M. This high scatter for both types of samples reflects the uncertainty accompanied in the analysis of the colloid concentration using the Al ICP-MS signal and in consequence the uncertainty in the determination of a possible attachment of the colloidal phase to the fracture filling material over the experimental duration. By comparison of the UC and the non-UC samples, a minimum colloid fraction of ~33% can be calculated for the Al. The data for Zn yield with values between ~3×10^{-5} M and ~1×10^{-5} M (~1.96 - 0.65 mg/L) in case of the non-UC samples show much less scatter than it was the case for Al. The Zn UC samples are at least one order of magnitude lower in concentration ranging between ~1×10^{-6} M and ~1×10^{-7} M. A colloidal fraction for Zn can be calculated to be at least 90%. The results for Ni are in close agreement with the Zn results in terms of only little scatter in the data for the non-UC samples. Values for the non-UC samples for Ni are between ~2×10^{-5} M and ~7×10^{-6} M (1.76 mg/L to 0.587 mg/L). Concerning the UC samples for Ni, values between ~2×10^{-6} M to ~3×10^{-8} M are observed. A minimum of ~80% can be derived for Ni as colloidal fraction by comparison of UC and non-UC samples, respectively. Generally speaking, the data for Zn and Ni clearly show the absence of colloid attachment to the FFM (or to the walls of the vials) since colloids

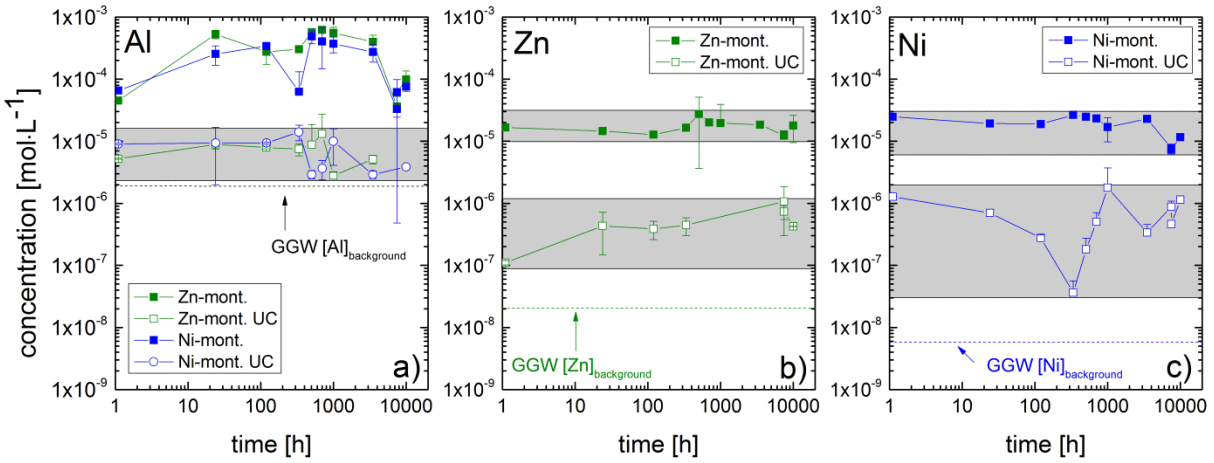

Figure 2.5: Temporal evolution of Al, Zn and Ni concentrations for both UC and non UC samples as markers for the colloids concentrations.

remain stable in solution over the whole experimental duration. Thus, the application of the synthetic Zn- and Ni-montmorillonite improves the reliability in the determination of the radio-

nuclide reversibility kinetics by circumventing the analytical uncertainties accompanied with the Al ICP MS signal as in previous studies [74].

^{232}Th(IV), ^{242}Pu(IV) and ^{243}Am(III). The results for the tri-and tetravalent radionuclides are shown in Figure 2.6a.-c. and Table 2.2, respectively. Generally speaking, by comparison of UC and non-UC samples both the formation of eigencolloids of ^{232}Th(IV) and ^{242}Pu(IV) due to their pronounced hydrolysis behavior and a strong clay colloid association or sorption of dissolved ^{232}Th(IV) and ^{242}Pu(IV) species is possible since the radionuclide concentrations before and after ultracentrifugation differ by at least one order of magnitude. Based on the macroscopic data presented no differentiation between a sorption of dissolved species to the bentonite colloids or the formation of eigencolloids which remain stable in solution or are associated to the clay colloids is feasible.

By comparison between UC and non UC samples, ^{232}Th(IV) shows the highest degree of colloidal association of all radionuclides applied in this study with ~96% and ~98% for the Ni- and Zn-montmorillonite, respectively indicating an identical behavior in terms of radionuclide colloid interaction. Th(IV) ultracentrifuged samples are at least on order of magnitude lower compared to the non-ultracentrifuged samples. ^{232}Th(VI) starts to show radionuclide desorption and subsequent removal from solution after ~ 3500 h contact time. At 10,000 h contact time a decrease of initially ~7×10^{-8} mol/L to ~3.5×10^{-8} mol/L (~50% removal from solution) in aqueous ^{232}Th(VI) concentration is detectable in case of the non-UC samples. No distinct difference in the reversibility behavior between the Zn- and the Ni-montmorillonite colloids is observed. The data indicate that the reversibility is still ongoing after 10,000 h thus no equilibrium state has been reached.

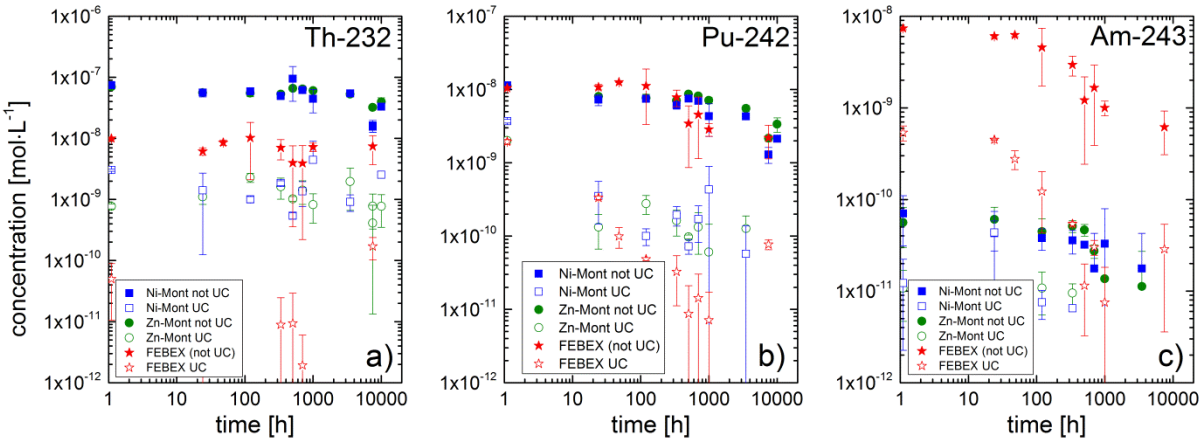

Figure 2.6: Time dependent evolution of radionuclide concentrations for a) Th-232, b) Pu-242 and c) Am-243. Values are given for both ultracentrifuged (UC) samples and for non ultracentrifuged (not UC) samples, respectively.

Regarding ^{242}Pu(IV), both sample series show an initial RN-colloid association with a higher amount of 82% for Zn-montmorillonite and 67% for Ni-montmorillonite, respectively, although lesser pronounced as ^{232}Th(IV). After ~1000 h, desorption of the ^{242}Pu(IV) off the colloidal phase is getting more pronounced for both series. After 10,000 h ~70% (in case of the Zn-montmorillonite) and ~ 81% (in case of Ni-montmorillonite) of the initial ^{242}Pu(IV) associated

to the colloidal phase are desorbed from the colloids and removed from the aqueous phase. Again, the data show no equilibrium state reached in terms of reversibility kinetics in both sample series at the end of the experiments.

Data for ^{243}Am(III) show a clear colloidal association with 83% and 81% in the case of Ni- and Zn-montmorillonite, respectively. A slight decrease in ^{243}Am(III) concentration for the non-UC samples is visible within the first 504 h and afterwards a steeper decrease occurs. One clearly has to state that the initial ^{243}Am(III) concentrations of ~7×10^{-11} M is rather low and therefore introduces more scatter in the data due to analytical uncertainties of the ICP-MS. Thus, the data from both series deviates slightly compared to each other and to ^{242}Pu(IV) and ^{232}Th(IV), respectively. The low starting concentration is also the reason why no ^{243}Am(III) was measureable in the UC samples after 336h due to the ICP-MS detection limit. In agreement to Pu(IV) and Th(IV) again no equilibrium state is reached after 10,000 h contact time.

^{99}Tc(VII), ^{233}U(VI) and ^{237}Np(V). Results for ^{99}Tc(VII) are shown in Figure 2.7 and in Table 2.2. By comparison between UC and non-UC samples it is obvious that ^{99}Tc(VII) is initially not colloidal associated since the aqueous concentrations are the same before and after the centrifugation procedure. The ^{99}Tc(VII) concentrations remain constant on the initial level until ~1000 h. Afterwards a drop in aqueous ^{99}Tc(VII) concentration is visible from initially ~1×10^{-8} M down to ~2.2×10^{-9} M (Zn) and ~3.9×10^{-9} M (Ni), respectively after 3500 h contact time. After 10,000 h both sample series are at least one order of magnitude lower (~4.5×10^{-10} M for Zn and ~9.1×10^{-10} for Ni) than at the start of the experiments. After 1000h a distinct difference between the UC and non-UC samples arises. That is, the initial Tc(VII) in the non-UC samples is reduced to Tc(IV) and shows a sorption kinetic to the fracture filling material. The reduction of the initial ^{99}Tc(VII) (pertechnetate) to ^{99}Tc(VI) is thermodynamically feasible after ~300 h contact time regarding the measured $Eh_{(SHE)}$ values of the samples depicted (as dashed line) in Figure 2.8a. It is well know that ^{99}Tc(IV) exhibits much lower solubility than ^{99}Tc(VII) (e.g. [77]), thus the formation of a ^{99}Tc(IV) phase and an attachment of ^{99}Tc(IV) to the bentonite colloids (in case of the UC samples) and/or to the FFM (in case of the nUC samples) seems reasonable to explain the results observed. Regarding the UC samples, after 3500h Tc concentrations are below the detection limit (~2×10^{-10} M) for both the Zn and Ni-Montmorillonite samples series. The differences between the UC and non-UC samples may be attributed to the association of a small fraction of Tc(IV) to the bentonite colloids and their removal via ultracentrifugation.

Regarding the results for ^{233}U(VI), a small portion of ^{233}U(VI) seems to be in colloidal form or attached to the synthetic bentonite colloids since the ^{233}U(VI) UC sample in the cocktail and after 24 h contact time in case of the Ni-Montmorillonite series shows a considerable lower concentration (Figure 2.7b). This difference only holds for these two samples of the Ni-Montmorillonite sample series and diminishes after 24h contact time which eventually may also be interpreted as an experimental or analytical artifact. In general, ^{233}U(VI) shows a slow removal kinetic until 3500 h contact times. For longer contact times, ^{233}U(VI) concentration both for UC and nUC samples decrease and a difference between both types of samples (UC and nUC) for both series seems to occur which may indicate a redox transformation to a

lower oxidation state (reduction of ^{233}U(VI) to ^{233}U(IV)) as it was observed for ^{99}Tc(VII)). Though, this difference between UC and nUC samples it not as pronounced as it was the case for ^{99}Tc(VII). Nevertheless, thermodynamic considerations (Figure 2.8b) clearly show the feasibility for a reduction of ^{233}U(VI) to ^{233}U(IV) based on experimentally measured $Eh_{(SHE)}$ values in the samples for both sample series.

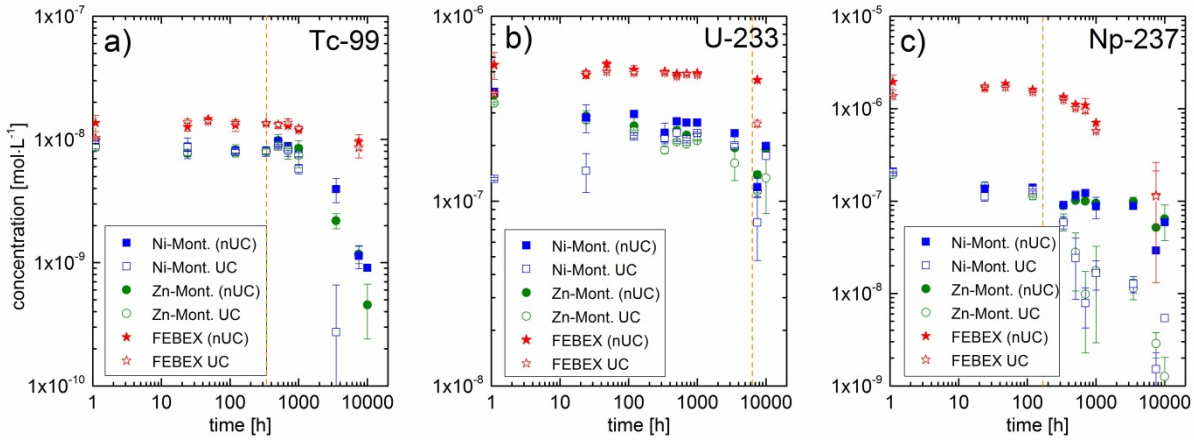

Figure 2.7: Time dependent evolution of radionuclide concentrations for a) Tc-99, b) U-233 and c) Np-237. Values are given for both ultracentrifuged (UC) samples and for non ultracentrifuged (not UC) samples, respectively. The orange dotted line indicates the time after a reduction of the radionuclide is thermodynamically feasible.

^{237}Np(V) results are depicted in Figure 2.7c and listed in Table 2.2. No initial colloid association with the synthetic Zn- and Ni-Montmorillonite is observed for ^{237}Np(V). With time, ^{237}Np(V) shows a slight decrease in concentration for both UC and non-UC samples. After 100 h contact time, differences are visible between UC and non-UC samples. The decrease in case of the ^{237}Np(V) concentration may again explained by the reduction to a lower oxidation state (Np)V) to Np(IV)) as it was the case for ^{99}Tc(VII) discussed above. This explanation may again be corroborated by Eh-pH conditions prevailing in the samples (Figure 2.4) making a reduction thermodynamically feasible after ~ 100 h contact time to the FFM. The reduced ^{237}Np(IV) subsequently shows a sorption kinetic to the FFM in the course of the experiment but seems to reach no equilibrium state after 10,000 h. The ^{237}Np(V) concentrations of the UC samples are lower compared to the non-UC samples indicating an attachment of reduced ^{237}Np(IV) to the synthetic Zn- and Ni-Montmorillonite colloids (~15% of the total Np present) which can be separated by ultracentrifugation.

Comparison to FEBEX bentonite results. To compare the results obtained in the study prevailing with previous experiments using Febex bentonite colloids, a desorption rate is fitted to the data using the following equation ((Equation 5) ([55]:

$$C(t) = C_0 \cdot e^{-k \cdot t} \qquad \text{(Equation 5)}$$

Where C(t) is the time dependent concentration in solution [mol/L], C_0 is the RN concentration in solution [mol/L], k = desorption rate [h^{-1}] and t is the time [h]. Table 2.4 lists all fitted desorption rates from the experiments in this study in conjunction to the desorption kinetics from the FEBEX experiments. The results from the FEBEX experiments revealed that ^{232}Th(IV) does not show a significant reversibility since only 1% of the initial ^{232}Th(IV) is removed after a contact time of 7500 h. Though, it has to be stated that this long-term value is likely to be attached with some uncertainty since the ^{232}Th(IV) concentration both after 500 h and 700 h already showed a decrease of ~18% of the initial ^{232}Th(IV) concentration (Figure 2.6). It cannot be ruled out that the increase for the data points at 1000 h and 7500 h may be resulting from the ultracentrifugation step and thus desorption kinetics may cannot be determined. The new results presented in this study for Zn-/Ni-montmorillonite show a significant reversibility for ^{232}Th(IV) for a contact time > 3500 h. Zn- and Ni-Montmorillonite show rather slow desorption rates of ~3.2×10^{-6} [h^{-1}] (Ni) and ~9.2×10^{-4} [h^{-1}] (Zn). Unfortunately, due to the scatter in the FEBEX ^{232}Th(IV) dataset it is not possible to fit a desorption rate.

Table 2.4: Reversibility kinetic rates for the tri- and tetravalent radionuclides in comparison to the results of the FEBEX experiments [74].

	$^{232Th(IV)}$(IV)	$^{242Pu(IV)}$(IV)	^{243}Am(III)
Syn. Zn-Montm.	0.00092 [h^{-1}]	0.00028 [h^{-1}]	0.0012 [h^{-1}]
Syn. Ni-Montm.	3.3×10^{-6} [h^{-1}]	0.00151 [h^{-1}]	0.0012 [h^{-1}]
FEBEX bentonite	not possible	0.00089 [h^{-1}]	0.0037 [h^{-1}]

Concerning ^{242}Pu(IV), a reversibility kinetics are both slower and faster than the results obtained using Febex bentonite colloids. Zn-montmorillonite (0.000235 [h^{-1}]) is slower than Ni-montmorillonite (0.00151 [h^{-1}]) whereas Febex reversibility kinetic (0.00089 [h^{-1}]) is in between . The quite high difference between the Zn-Mont. and Ni-Mont. series is clearly referred to the last data point of the Ni-Mont. series. After 7500h the absolute aqueous ^{242}Pu(IV) concentrations observed in this study are very similar to the FEBEX results. That is, the ^{242}Pu(IV) reversibility kinetics in both studies may not be as different as it was the case for ^{232}Th(IV). Regarding the uncertainties, one can state that the ^{242}Pu(IV) reversibility

kinetics should not be very different and are probably quite similar independent of the type of bentonite colloids used in both studies.

^{243}Am(III) exhibits a similar fast desorption with a rate of 0.0012 [h^{-1}] for both synthetic montmorillonite series. Though, compared to the ^{243}Am(III) desorption rate from the FEBEX bentonite experiments (0.0037 [h^{-1}]) it is ~3 times slower. Here, one has to point to the difference in the initial ^{243}Am(III) concentrations used in both studies which may has an influence on the reversibility kinetics. This issue needs to be studied more in detail to clarify a possible influence.

Generally speaking, the reversibility kinetics of the new synthetic montmorillonite series are slower compared to the FEBEX bentonite reversibility kinetics [74]. This observation may be explained by the differences in the ratio of the specific surface areas of the colloids and the FFM since the surface area of the colloids is in the order of 67 m^2/g while the FFM offers a surface area of 0.26 m^2/g giving a ratio of 38 ($TOT_{(BETFFM)}$ / $TOT_{(BETCOLL)}$; the TOT_{BET} is re-

ferred to the total BET per each Zinsser vial regarding the solid to solution ration (1:4; 4 g of FFM and 16 ml cocktail) and the concentration (total mass) of the montmorillonite colloids) which is smaller than the ratio by [74] (44 in case of the 1-2 mm size fraction) using FEBEX bentonite colloids with a lower specific surface area. The interaction between the tri- and tetravalent RN and the synthetic montmorillonite colloids is therefore either more strongly due to the formation of more stable sorption complexes at the surface of the colloids and/or the driving force of the surface area of the FFM compared to the surface area of the synthetic colloids is less pronounced.

Concerning the redox sensitive radionuclides ^{237}Np(V), ^{233}U(VI) and ^{99}Tc(VII), distinct difference arise compared to the FEBEX bentonite experiments. While a reduction of ^{237}Np(V) to ^{237}Np(IV) is thermodynamic feasible in both studies, a different behavior is visible. While in the FEBEX experiments no interaction of ^{237}Np(V) with the colloidal phase occurs, there may be an interaction with the synthetic montmorillonite colloids in the present experiments which seems obvious when comparing UC with nUC samples. It may be likely that the higher specific surface of the synthetic montmorillonite colloids (67 m^2/g) lead to an affinity of the ^{237}Np(V)) to sorb onto the colloidal phase and only to a lesser extent or with a slower kinetic to the FFM though one has to state that only ~15% of the Np present may be attached to the bentonite colloid whereas ~85% may sorb to the FFM.

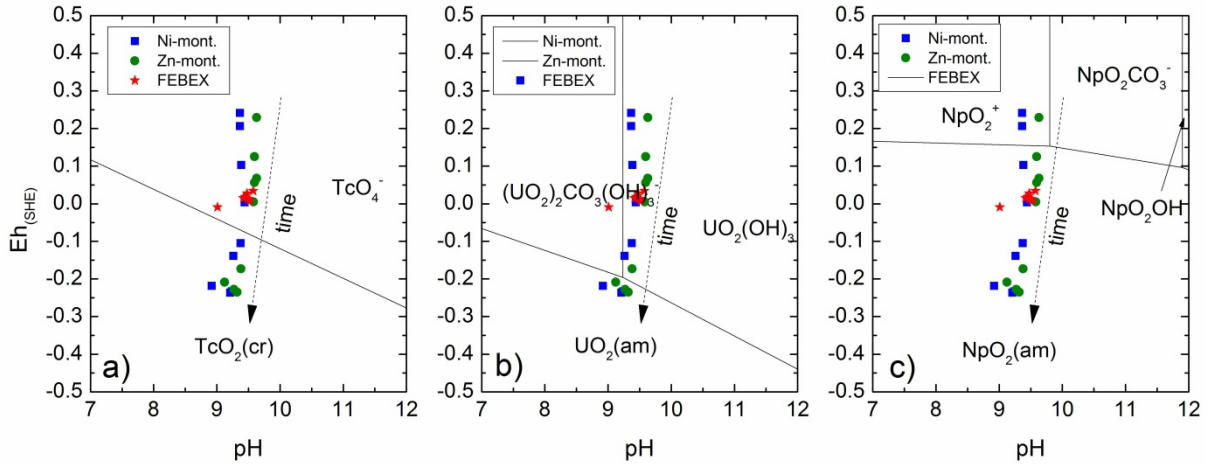

Figure 2.8: Eh-pH diagramm showing the experimentally measured values for the Ni- and Zn- Montmorillonite in comparison to the Febex bentonite experiments. a) Tc-99, b) U-233 and c) Np-237.

A similar behavior like in the case of ^{237}Np(V) is noticeable for ^{99}Tc(VII). Again, a reduction to a less soluble form (^{99}Tc(IV)) is thermodynamically feasible which is much more pronounced as in the FEBEX experiments [74] due to the more reducing conditions prevailing. The nUC samples show a pronounced decrease in concentration which has not been observed in the FEBEX experiments [74]. A possible explanation for this observation may be referred to the formation of a ^{99}Tc(IV) dissolved phase showing a sorption kinetic to the FFM and/or the formation and subsequent (kinetic) precipitation of a ^{99}Tc(IV) phase. Due to the macroscopic data only available no differentiation between both possible explanation can be drawn. Since the ^{99}Tc concentrations decrease also in the nUC samples and at the same time, the synthet-

ic montmorillonite colloids remain stable in solution, the explanation of the formation of ^{99}Tc(IV) eigencolloids which do not interact with the synthetic montmorillonite colloids and instead show a slow sorption kinetic or precipitation seems more likely.

^{233}U(VI) results of the study in hand are again in contrast to the FEBEX experimental results due to the more reducing conditions. After ~3500 h a decrease in both UC and nUC samples are detectable which was not observed in the FEBEX experiments [74]. Moreover, the degree of reduction is less pronounced compared to ^{99}Tc and ^{237}Np of the study prevailing, since the redox potentials of the samples measured are located near the borderline of reduction (Figure 2.8).

Generally speaking, it seems, that the FFM used in this study, though originating from the same location as the FFM of the FEBEX experiments, possess a higher redox capacity leading to considerably stronger reducing conditions (Figure 2.4).

FFM desorption experiments. To examine a possible desorption of FFM associated radionuclides sorbed during the sorption reversibility experiments, the FFM was contacted for 7 days with fresh GGW. Subsequently, the samples were probed by ICP-MS for their RN content. Figure 2.9 and shows results for all RN applied in the study.

Results for ^{242}Pu(IV) (Figure 2.9a) and ^{232}Th(IV) (Figure 2.9c) show an increase of desorption as function of contact times of the sorption reversibility samples. Since the amount of RN sorbed to the FFM increases with time (= longer contact times) in the reversibility kinetics experiments, the amount of RN potentially desorbing from the FFM may also increases with time since the initial (sorbed) RN concentration in the samples is higher. Thus it is expected that the RN desorption data are negatively correlated to the reversibility data which are additionally shown in Figure 2.9. In consequence, up to 20% of the sorbed ^{242}Pu(IV) fraction can be released after a contact time of 7 days.

In case of ^{232}Th(IV) an increase in concentration due to a mobilization of natural ^{232}Th(IV) out of the FFM cannot explain the increase of the reversibility samples at longer contact times since the contact time with the fresh GGW in the desorption experiments was the same for all samples thus the concentrations of natural Th in all samples should be very similar. In consequence, the increase in dissolved concentration may be referred to a desorption process.

^{243}Am(III) results are shown in Figure 2.9b for completeness, but due to the very low initial concentrations in the sorption reversibility experiments, the samples measured in the FFM desorption experiments are below the detection limit of the ICP-MS.

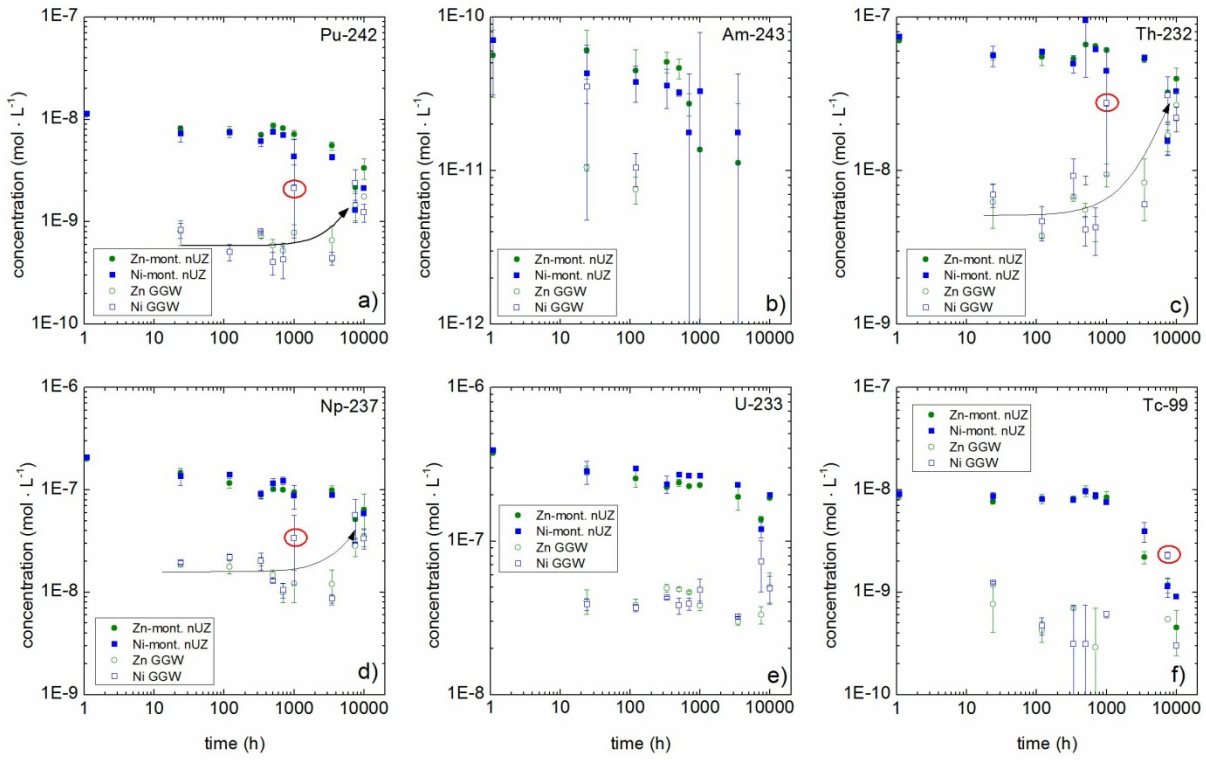

Figure 2.9: Results for the desoption experiments for all radionuclides applied.

Regarding the results of ^{237}Np(V) in Figure 2.9d, it can be seen, that the amount of RN desorbing from the FFM again increases for reversibility samples with longer contact times. This again inversely correlates to the reversibility experiments where Np shows a decrease in concentration due to either a sorption to the FFM or the precipitation of a Np(IV) phase ("eigencolloids"). Thus, there are several possible processes which could explain the remobilization of the Np. It can either be a desorption step of initially sorbed Np(V) or an oxidative dissolution process of Np(IV) to Np(V) due to the more positive redox potentials in the fresh GGW. The latter seems quite likely since the GGW used is the same as applied in the preparation of the RN cocktail for the sorption reversibility products. Thus, the redox potentials can be derived from the sorption reversibility experiments yielding values of ~150 mV (see Figure 2.4) which is positive enough to oxidize the Np(IV) to Np(V). Moreover, it is even likely that the redox potentials are higher, since the redox capacity of the material may already be depleted within the sorption reversibility experiments.

In contrast to the ^{237}Np results, U shows no increase in sorption, but stays constant at concentrations around 4×10^{-8} mol/L. This is in agreement to the sorption reversibility results where ^{233}U only shows a small decrease over the experimental duration. Thus, only little U is attached to the FFM surface which may potentially desorb.

^{99}Tc desorption results behave quite different to the ^{237}Np results, although both elements showed a pronounced decrease in concentration in the sorption reversibility experiments. Except for one data point for the sample at 7500 h contact time, there is no increase in desorption noticeable for ^{99}Tc. That is, the ^{99}Tc which was removed from solution within the

Table 2.5: Overview of the temporal evolution of various elements for both the Zn- and Ni-montmorillonite desorption experiments.

	Time	Al	st. dev.	Ni	st. dev.	Zn	st. dev.	^{99}Tc	st. dev.	^{232}Th	st. dev.	^{233}U	st. dev.	^{237}Np	st. dev.	^{242}Pu	st. dev.	^{243}Am	st. dev.
	hours	mol/l	mol/l	mol/l	mol/l	mol/l	mol/l	mol/l	mol/l	mol/l	mol/l	mol/l	mol/l	mol/l	mol/l	mol/l	mol/l	mol/l	mol/l
Ni-montmorillonite	24	1,17×10^{-04}	8,06×10^{-05}	2,06×10^{-06}	3,34×10^{-07}	7,03×10^{-07}	2,94×10^{-07}	1,24×10^{-09}	2,34×10^{-11}	6,95×10^{-09}	1,18×10^{-09}	3,87×10^{-08}	3,41×10^{-09}	1,95×10^{-08}	7,59×10^{-10}	8,29×10^{-10}	1,38×10^{-10}	3,52×10^{-11}	3,04×10^{-11}
	120	4,86×10^{-05}	2,00×10^{-06}	1,31×10^{-06}	2,20×10^{-07}	3,59×10^{-07}	1,06×10^{-09}	4,71×10^{-10}	9,12×10^{-11}	4,68×10^{-09}	1,19×10^{-09}	3,67×10^{-08}	2,09×10^{-09}	2,19×10^{-08}	1,62×10^{-09}	5,08×10^{-10}	9,10×10^{-11}	1,04×10^{-11}	2,54×10^{-12}
	336	4,25×10^{-04}	1,73×10^{-04}	2,34×10^{-06}	5,92×10^{-08}	< d.l.	< d.l.	3,12×10^{-10}	4,41×10^{-10}	9,26×10^{-09}	2,65×10^{-09}	4,28×10^{-08}	8,58×10^{-10}	2,02×10^{-08}	3,93×10^{-09}	8,07×10^{-10}	1,14×10^{-11}	< d.l.	< d.l.
	500	7,46×10^{-05}	2,33×10^{-05}	1,99×10^{-06}	1,37×10^{-07}	< d.l.	< d.l.	3,12×10^{-10}	4,41×10^{-10}	4,14×10^{-09}	9,02×10^{-10}	3,80×10^{-08}	4,66×10^{-09}	1,29×10^{-08}	5,42×10^{-10}	4,04×10^{-10}	1,04×10^{-10}	< d.l.	< d.l.
	700	5,63×10^{-05}	6,07×10^{-05}	1,62×10^{-06}	4,74×10^{-07}	< d.l.	< d.l.	< d.l.	< d.l.	4,27×10-09	1,46×10-09	3,90×10-08	3,55×10-09	1,05×10-08	1,75×10-09	4,28×10-10	1,49×10-10	< d.l.	< d.l.
	1000	1,07×10^{-03}	3,64×10^{-04}	8,94×10^{-06}	6,98×10^{-06}	7,75×10^{-07}	1,10×10^{-06}	6,10×10^{-10}	4,54×10^{-11}	2,74×10^{-08}	1,82×10^{-08}	4,79×10^{-08}	8,43×10^{-09}	3,40×10^{-08}	2,22×10^{-08}	2,14×10^{-09}	1,44×10^{-09}	< d.l.	< d.l.
	3500	1,52×10^{-04}	5,72×10^{-05}	2,18×10^{-06}	1,40×10^{-07}	< d.l.	< d.l.	< d.l.	< d.l.	6,03×10^{-09}	2,36×10^{-10}	3,23×10^{-08}	1,62×10^{-10}	8,67×10^{-09}	8,10×10^{-10}	4,42×10^{-10}	6,27×10^{-11}	< d.l.	< d.l.
	7500	3,16×10^{-04}	2,19×10^{-04}	1,45×10^{-05}	5,07×10^{-06}	1,03×10^{-06}	6,72×10^{-08}	2,30×10^{-09}	1,82×10^{-10}	3,09×10^{-08}	9,99×10^{-09}	7,35×10^{-08}	2,68×10^{-08}	5,66×10^{-08}	2,36×10^{-08}	2,40×10^{-09}	8,53×10^{-10}	< d.l.	< d.l.
	10000	1,65×10^{-04}	2,80×10^{-05}	6,47×10^{-06}	1,23×10^{-06}	4,51×10-^{07}	5,28×10^{-08}	3,03×10^{-10}	< d.l.	2,20×10^{-08}	4,08×10^{-09}	4,93×10^{-08}	9,88×10^{-09}	3,36×10^{-08}	7,16×10^{-09}	1,24×10^{-09}	2,50×10^{-10}	< d.l.	< d.l.
Zn-montmorillonite	24	4,87×10^{-05}	1,15×10^{-05}	5,01×10^{-08}	5,35×10^{-09}	1,39×10^{-06}	5,33×10^{-07}	7,70×10^{-10}	3,60×10-10	6,22×10^{-09}	1,99×10^{-09}	4,07×10^{-08}	7,31×10^{-09}	1,88×10^{-08}	1,03×10^{-09}	8,11×10^{-10}	2,22×10^{-10}	1,04×10^{-11}	5,09×10^{-13}
	120	4,39×10^{-05}	4,06×10^{-06}	2,69×10^{-08}	1,49×10^{-08}	9,70×10^{-07}	1,35×10^{-07}	4,22×10^{-10}	9,74×10-11	3,76×10^{-09}	1,40×10^{-10}	3,83×10^{-08}	3,73×10^{-09}	1,77×10^{-08}	2,64×10^{-09}	5,08×10^{-10}	1,99×10^{-11}	7,56×10^{-12}	1,53×10^{-12}
	336	3,37×10^{-04}	1,21×10^{-04}	< d.l.	< d.l.	1,62×10^{-06}	9,14×10^{-08}	7,03×10^{-10}	2,27×10-11	6,67×10^{-09}	3,47×10^{-10}	4,93×10^{-08}	2,90×10^{-09}	2,01×10^{-08}	1,95×10^{-09}	7,17×10^{-10}	2,05×10^{-11}	< d.l.	< d.l.
	500	1,13×10^{-04}	2,84×10^{-05}	< d.l.	< d.l.	< d.l.	< d.l.	< d.l.	< d.l.	5,54×10^{-09}	5,86×10^{-10}	4,84×10^{-08}	1,22×10^{-09}	1,47×10^{-08}	1,75×10^{-09}	5,87×10^{-10}	8,43×10^{-11}	< d.l.	< d.l.
	700	8,90×10^{-06}	1,78×10^{-06}	< d.l.	< d.l.	< d.l.	< d.l.	2,89×10^{-10}	4,09×10-10	4,24×10^{-09}	7,93×10^{-10}	4,64×10^{-08}	6,75×10^{-10}	1,00×10^{-08}	2,13×10^{-09}	5,23×10^{-10}	9,69×10^{-11}	< d.l.	< d.l.
	1000	8,33×10^{-04}	1,30×10^{-04}	1,73×10^{-08}	2,45×10^{-08}	2,14×10^{-06}	3,31×10^{-07}	< d.l.	< d.l.	9,42×10^{-09}	1,59×10^{-09}	3,80×10^{-08}	2,70×10^{-09}	1,21×10^{-08}	4,19×10^{-09}	7,84×10^{-10}	1,54×10^{-10}	< d.l.	< d.l.
	3500	3,97×10^{-04}	3,55×10^{-05}	< d.l.	< d.l.	2,24×10^{-06}	9,94×10^{-07}	< d.l.	< d.l.	8,32×10^{-09}	3,58×10^{-09}	2,98×10^{-08}	1,25×10^{-09}	1,20×10^{-08}	4,50×10^{-09}	6,59×10^{-10}	2,48×10^{-10}	< d.l.	< d.l.
	7500	1,45×10^{-04}	6,91×10^{-05}	1,14×10^{-06}		7,22×10^{-06}	6,73×10^{-07}	5,42×10^{-10}		1,69×10^{-08}	3,64×10^{-09}	3,31×10^{-08}	4,23×10^{-09}	2,82×10^{-08}	5,99×10^{-09}	1,46×10^{-09}	4,30×10^{-10}	< d.l.	< d.l.
	10000	2,44×10^{-04}	7,16×10^{-05}	2,58×10^{-07}	6,80×10^{-08}	6,45×10^{-06}	7,34×10^{-07}	< d.l.	< d.l.	2,66×10^{-08}	5,52×10^{-09}	5,02×10^{-08}	1,17×10^{-08}	3,49×10^{-08}	6,90×10^{-09}	1,77×10^{-09}	< d.l.	< d.l.	< d.l.

sorption reversibility experiments is not getting remobilized in the desorption experiments. Assuming the reduction of ^{99}Tc(VII) to a low soluble ^{99}Tc(IV) phase during the sorption reversibility process, it seems that the redox potentials of the fresh GGW applied in the FFM desorption processes is not able to oxidize the ^{99}Tc(IV) to ^{99}Tc(VII). It may be likely that although the redox potentials should be positive enough for an oxidation process to be feasible from a thermodynamically point of view, the transformation may have a slow kinetic or is even kinetically hindered to take place within the contact time of 7 days in the FFM desorption experiments.

Conclusions

To reduce the analytical uncertainties in determining bentonite colloid concentration both in in-situ field migration and laboratory column or batch experiments the application of synthetic Zn– and Ni-labeled montmorillonite colloids have been tested. Therefore, batch experiments on RN sorption reversibility kinetics in the presence of granite fracture filling material and Grimsel groundwater have been conducted identical to previous experiments using FEBEX bentonite colloids [74]. The tri-and tetravalent RN ^{232}Th(VI), ^{242}Pu(IV) and ^{243}Am(III) are strongly colloidal associated and show sorption reversibility. It seems that the reversibility kinetics are slower in case of the synthetic Zn- and Ni-montmorillonite colloids most likely due to the higher specific surface area (~ a factor of 2) compared to the FEBEX colloids and thus a stronger association to the colloids. Though, for ^{232}Th(IV) a very slow kinetic has been observed in the study prevailing whereas no kinetic rate is in [74] due to analytical uncertainties in the data. Identical to the FEBEX bentonite colloids study, ^{99}Tc(VIII), ^{233}U(VI) and ^{237}Np(V) are initially not attached to the synthetic Zn- and Ni-montmorillonite colloids. Though, regarding these RN, within the duration of the experiments differences arise compared to the results by [74] which are related to the Eh-pH conditions prevailing. A distinct drop in redox potentials are observed as a function of contact time to the FFM due to its bulk Fe^{2+} content which should govern the Eh conditions. These reducing conditions have not been observed in the study [74]. In consequence, the redox sensitive elements ^{99}Tc(VIII), ^{233}U(VI) and ^{237}Np(V) are prone to reduction processes in this study. ^{99}Tc(VIII) shows a decrease in concentration for both UC and non-UC samples for contact times > ~500 h due to the reduction to tetravalent ^{99}Tc and eventually an interaction in terms of sorption to the FFM (based on the non-UC samples) or precipitation of a sparingly soluble Tc(IV) phase. Besides, the nUC samples indicate an association to the colloids although ^{99}Tc could also form eigencolloids which are removed from solution by ultracentrifugation. The results of ^{99}Tc are very similar to the ^{237}Np(V) results. Again, a reduction of ^{237}Np(V) to ^{237}Np(IV) seems to occur since ^{237}Np displays a different behavior in the UC and nUC samples for contact times > ~ 300 h. It seems that ^{237}Np(IV) interacts with the colloidal phase or is forming eigencolloids which are removed by ultracentrifugation. The nUC samples show a much slower decrease in concentration indicating stabilized ^{237}Np(IV) colloids possibly due to an interaction with the montmorillonite colloids. ^{233}U(VI) shows a slow decrease in concentration over the whole experimental duration. This may be either due to a slow ^{233}U(VI) sorption and/or by a reduction to ^{233}U(IV) which is thermodynamically feasible under the Eh-pH conditions given after 3500 h contact time to the FFM. In contrast to ^{99}Tc(VII) and ^{237}Np(V), no clear difference be-

tween UC and nUC samples are detectable, thus no interaction with the synthetic colloidal phase seems to occur. To sum up, the synthetic Zn- and Ni-labeled montmorillonite colloids display a very similar behavior to the FEBEX bentonite colloids making them suitable as an admixture in e.g. field migration studies at the Grimsel Test Site in Switzerland in the frame of the Colloid Formation and Migration (CFM) Project. The use of the Zn and Ni ICP-MS signal significantly reduces the uncertainties coupled with the determination of the colloids concentration in solution, thus providing confidence in the reversibility results obtained. Moreover, the results of the study prevailing corroborate the findings [74] and highlight the influence of colloid specific surface area on the desorption behavior of attached radionuclides.

2.1.2 Interaction of bentonite colloids with Cs, Eu, Th and U in presence of humic acid: a Flow Field-Flow Fractionation study

Abstract. The interaction of Cs(I), Eu(III), Th(IV) and U(VI) with montmorillonite colloids was investigated in natural Grimsel Test Site groundwater over a 3 years period. The asymmetric flow field-flow fractionation combined with various detectors was applied to study size variations of colloids and to monitor colloid association of trace metals. The colloids suspended directly in the low ionic strength (I), slightly alkaline granitic groundwater (I = 10^{-3} mol/L, pH = 9.6) showed a gradual agglomeration with a size distribution shift from initially 10 - 200 nm to 50 - 400 nm within over 3 years. The Ca^{2+} concentration of 2.1×10^{-4} mol/L in the ground water is believed to be responsible for the slow agglomeration due to Ca^{2+} ion exchange against Li^{+} and Na^{+} at the permanently charged basal clay planes. Furthermore, the Ca^{2+} concentration lies close to the critical coagulation concentration (CCC) of 10^{-3} mol/L for clay colloids. Slow destabilization may delimit clay colloid migration in this specific groundwater over long time scales. Eu(III) and Th(IV) are found predominantly bound to clay colloids, while U(VI) prevails as the $UO_2(OH)_3^-$ complex and Cs(I) remains mainly as aquo-ion under our experimental conditions. Speciation calculations qualitatively represent the experimental data. A focus was set on the reversibility of metal ion-colloid binding. Addition of humic acid as a competing ligand induces rapid metal ion dissociation from clay colloids in the case of Eu(III) even after previous aging for about 3 years. Interestingly only partial dissociation occurs in the case of Th(IV). Experiments and calculations prove that the humate complexes dominate the speciation of all metal ions under given conditions. The partial irreversibility of clay bound Th(IV) is presently not understood but might play an important role for the colloid-mediated transport of polyvalent actinides over wide distances in natural groundwater.

Introduction. Colloid formation reactions play an important role notably for the solution chemistry of tri- and tetravalent actinides ([78] [79] [80]). Natural (ground) waters like granitic ones ([81]) contain colloidal matter like clay particles and natural organic matter such as humic and fulvic acids. Concentrations for inorganic colloids range from <0.1 to 18 mg/L [82]; [81]; [83]) and dissolved organic matter lies as well in the low mg/L concentration range [84]. ~~S~~such types of colloids attract strong interest in the context of nuclear waste disposal safety considerations as they influence aquatic radionuclide speciation and mobility under certain geochemical conditions. Beside various natural sources the bentonite of the engineered barrier system (EBS) may erode in contact with groundwater producing clay colloids [85]. Field ([86], [87]; [88]) and laboratory ([89]; [90]; [91]; [92]) studies have demonstrated the relevance of aquatic colloids as potential carriers for radionuclides under natural groundwater conditions. From the outcome of the Colloid and Radionuclide Retardation (CRR) project performed in the fractured crystalline rock at Nagra's Grimsel Test Site (GTS) in the central Swiss Alps ([93]) it is concluded that 1) clay colloid stability, which is strongly dependent on pH and salinity of the groundwater, is very high in the low ionic strength, high pH Grimsel Test Site groundwater ([85]) and 2) clay colloids significantly enhance the migration of tri- and tetravalent actinides.

Laboratory and field studies as cited above are often restricted to limited observation time scales. Geochemical equilibrium must not necessarily establish and slow colloid agglomeration kinetics might not be noticed. As a consequence the radionuclide mobilization effect of colloids might be less under low natural groundwater flow conditions and over the long term.

The present work focuses on this aspect by:

- a long term study (3 years) on clay colloid stability in Grimsel Test Site groundwater. The present work thus complements previous studies performed by Missana et al., ([85]) who investigated montmorillonite colloid stability over 5 months.

- a kinetic study on the interaction of bentonite colloids with the elements Cs(I), Eu(III), Th(IV) and U(VI) in the natural Grimsel Test Site groundwater over 3 years. The aim is to identify potential slow reactions modifying the extent of metal ion association to colloids.

- a study on metal ion desorption from colloids using humic acid as a competing ligand. Occasionally, 'irreversible' sorption onto colloids is discussed as relevant process which in turn may enhance contaminant mobility significantly (e.g. [94]). A well characterized colloidal humic acid is taken as it can be well separated from clay colloids by the analytical method applied in our study (see sections below). Our experiments aim at identifying kinetically hindered processes by dedicated experiments and speciation calculations on the basis of existing thermodynamic data.

Experiments were performed by application of the Asymmetric Flow Field-Flow Fractionation (AsFlFFF) coupled to several detectors such as an UV-Visible spectrophotometer and an ICP-Mass Spectrometer. This technique has been previously used to characterize clay and humic colloids ([59]; [68]) and to study their interaction with actinides or lanthanides as their chemical homologues ([95]; [96]). Actually, the AsFlFFF-ICP-MS experiments allowed the study of the evolution of metal ion - colloid systems over a time period of 3 years at trace element concentrations. Most spectroscopic techniques cannot be applied for element speciation under those conditions due to sensitivity constraints. A further goal of this study was, therefore, to examine the capabilities of this technique to gain insight into radionuclide and metal ion speciation in natural groundwater. Fractograms were inspected for variations in colloid size distribution reflecting colloid stability under given conditions and for the time dependent behavior of trace metal ions. Finally, experimental results were compared with the outcome of speciation calculations.

Materials & Methods

All the suspensions described hereafter have been prepared in the natural groundwater taken from Nagra's Grimsel Test Site (GTS), located at about 1730 m above the sea level under

a 450 m overburden of crystalline rock ([97]). The groundwater used as “solvent” was sampled under inert gas conditions in 50 L Teflon coated stainless steel barrels from borehole BOMI 87.010. The barrels were transferred directly to the laboratory. The chemical composition of the groundwater is characterized by a low ionic strength, low carbonate concentration and high pH ([98]; [96]).

FEBEX Bentonite. The original bentonite used in this work comes from the Cortijo de Archidona deposit (Spain). It is commonly called FEBEX bentonite ([99]). Natural bentonite was crushed and the resulting material sieved (size fraction < 63 µm). The final powder is then dispersed in the groundwater to obtain the clay colloids as described below.

Preparation of colloid suspensions according to [100]; [101]. A first suspension (S1) is prepared by placing 10 g of the sieved material (size fraction < 63 µm) in 1 L LiCl (1mol/L, prepared in Grimsel groundwater) during 4 days in order to achieve a high degree of delamination. After 4 days the suspension is distributed into centrifuge tubes. After the centrifugation step (at 4000 rpm during 35 min), the liquid is removed and the decanted solid is re-suspended by using an ultra-sonic bath in fresh Grimsel groundwater before being centrifuged again. In total, the Grimsel groundwater is exchanged three times. Soluble salts (like NaCl or $CaSO_4$) contained in the natural bentonite are removed during the washing procedure. At the end of the fourth centrifugation, the supernatant suspension constitutes the colloidal stock suspension (TS1). Concentrations of main cations such as Ca and Na in the suspension did not differ from those in the original groundwater. Due to the residual presence of Li cations from the delamination process, the clay colloids are considered to be partly in equilibrium with the groundwater environment.

Similarly, a second suspension (S2) is prepared by placing 10 g of the sieved material (size fraction < 63 µm) in 1 L Grimsel groundwater during 7 days. After 7 days the suspension is distributed into centrifuge tubes and centrifuged. The supernatant is then removed and replaced by fresh Grimsel groundwater. The solid is re-suspended by using an ultra-sonic bath. In total, the Grimsel groundwater is exchanged three times. At the end of the fourth centrifugation, the supernatant suspension constitutes the colloidal stock suspension (TS2). These clay colloids are expected to be in equilibrium with the groundwater environment.

The final suspensions have the following colloid concentrations: TS1: (1230 ± 30) mg/L and TS2: (180 ± 10) mg/L as deduced from the Al and Mg concentration measurements performed by ICP-MS. XRD analysis of those colloids showed the existence of mainly smectite clay particles. The resulting colloid concentration obtained for the TS2 stock suspension is ~7 times lower as compared to the suspension after treatment with Li^+. This shows the efficiency of the clay delamination process by homoionization with Li^+, in agreement with [102].

Preparation of metal ion stock solutions. A stock solution containing four elements representative for nuclear waste derived radionuclides occurring in four different valence states has been prepared from ICP-MS standard solution of Cs(I), Th(IV) (as chemical homologue to other tetravalent actinides Pu/Np/U(IV)), Eu(III) (as a chemical homologue for trivalent actinides Am/Cm/Pu(III)) and U(VI). The concentration of each element is at 1 mg/ml in 5 %

HNO_3; Specpure, Alfa Aesar. 100 µl aliquots of each solution are mixed and filled up to a total volume of 10 mL with ultra pure de-ionized water (MilliQ, Millipore). The resulting stock solution has a concentration of 10 mg/L for each element at pH ~1.3. For simplicity, this solution will be referred to as RN-cocktail hereafter.

Humic acid stock solution. The humic acid used is extracted from a natural deep groundwater (139 m depth) located at Gorleben in the Northern German Plain (Lower Saxony, GoHy-573). After isolation and purification, the elemental composition and the inorganic content of the final product (GoHy-HA-573) are determined [103]. To obtain a stock solution, a small amount of this product is dissolved in NaOH 0.1 mol/L (ultrapure, Merck) and then diluted with ultrapure deionized water (MilliQ plus, Millipore). The final pH is 9.4 ± 0.1. The dissolved organic carbon (DOC) content is measured with a TOC analyzer (TOC-5000, Shimadzu). The measured DOC of (258 ± 2) mg/L is converted to the humic acid concentration by considering the C-content of HA (59.3 ± 0.1 %). This leads to a value for the HA concentration of 435 mg/L. This solution is stored in the dark at 4°C in a fridge prior to use.

Batch experiments. All the solutions were prepared in a glove box under Ar-atmosphere (< 1 ppm O_2) using Grimsel groundwater (GGW), pH 9.6.

Sorption (kinetic) study over 3 years

Suspensions have been prepared in parallel and were analyzed after different contact times (CT): freshly prepared, 2 weeks, 3 months, 5 months, 7 months, 10 months, 1 year, 3 years. The different sets of batch samples are described hereafter.

- Set 1 or “HA”: dilution of the (GoHy-HA-573) stock solution down to 10 mg/L with GGW;

- Set 2 or “Clay”: dilution of the clay colloid stock suspension TS1 down to 20 mg/L with GGW;

- Set 3 or “HA-RN”: 10 mg/L GoHy-HA-573 + RN-cocktail with 10 µg/L of each spiked trace element in GGW;

- Set 4 or “Clay-RN”: 20 mg/L clay colloids (TS1) + RN-cocktail with 10 µg/L of each element in GGW;

- Set 5 or “Equil.”: 10 mg/L GoHy-HA-573 + 20 mg/L clay colloids (TS1) + RN-cocktail with 10 µg/L of each spiked trace element in GGW.

Cs, Eu, Th and U concentrations in the batch samples are 7.52×10^{-8} mol/L, 6.56×10^{-8} mol/L, 4.31×10^{-8} mol/L, and 4.20×10^{-8} mol/L, respectively.

Metal ion concentrations were measured by ICP-MS in the batch suspensions after their preparation (arithmetic mean of tree replicates) and in the sampling campaigns over 3 years, after dilution of an aliquot in 5 % HNO_3. Clay colloids dissolve at the low pH allowing then the measurement of Al as an indicator for the clay colloid concentration. No adsorption effects

have been observed on the walls of the 50 mL polyethylene tubes used as sample containers.

Reversibility study. Within batch experiments, the time dependence of RN desorption from HA and clay colloids is investigated. Suspensions Set 3 or “HA-RN” and Set 4 or “Clay-RN” were aged for periods of 1 day up to 3 years and clay colloids (Set 3) and humic acid (Set 4) were added subsequently. The evolution of the system is followed for desorption times (DT) ranging from 24 hours up to 3 years. The new batch systems containing both colloid types are then called Set 3 DT and Set 4 DT, respectively.

Fractionation: Asymmetrical Flow Field-Flow Fractionation (AsFlFFF) coupled to UV-Vis spectrophotometry and ICP-Mass spectrometry.

The general principle of the flow field-flow fractionation method is described in detail in [104]; [105]; [106].The experimental equipment applied in this study has been detailed in [68]. Only the main principle is recalled here. Size fractionation of colloids is carried out in a thin ribbon-like channel according to their diffusion coefficient. The carrier channel flow is laminar due to the small height of the spacer and transports colloidal components after their injection to the detectors under the action of a cross-flow perpendicular to the channel. This drives the particles towards the underlying channel wall consisting of an ultrafiltration membrane. The particles are then retained inside the channel while molecular and ionic species are able to permeate the membrane. The colloids diffuse back into the channel. In the so-called “normal” elution mode, the diffusion length is higher for smaller than for bigger colloids. Hence they reach faster stream lines in the laminar flow-field and are eluted prior to bigger particles with smaller diffusion coefficients. Colloids with sizes larger than around 800 nm (as reported by [107] for example) remain in faster flow stream lines for steric reasons and are thus eluted before smaller particles. In that case the AsFlFFF works in the “steric” elution mode.

The AsFlFFF system (HRFFF 10.000 AF4) is provided by Postnova Analytics (Landsberg, Germany). The accumulation wall consisted of an ultrafiltration membrane made of regenerated cellulose (cutoff 5 kDa, Postnova Analytics). The trapezoidal PTFE spacer which delimits the area where the fractionation takes place is 0.5 mm thick. In this study, the carrier solution consists of ultra pure water adjusted to pH 9.3 by addition of ultra pure NaOH 1 M (Merck). pH stability was checked by daily measurements (max. ~8 hours). The carrier solution was prepared and degassed prior to use by a vacuum degasser (HP 1100, Model G 1322A, Agilent, Waldbronn, Germany). Three additional on-line filters with a 100 nm pore size PTFE membrane are placed at the inlet ports of injection and laminar pump and between the module and the inlet port of the channel. A sample volume of 100 µL is injected via a Rheodyne injection valve. After fractionation, the effluent is directed through an UV detector (LambdaMax LC Modell 481, Waters, Milford, USA) for monitoring the organic component via both light absorption and scattering at a fixed laminar outflow rate of 0.8 mL/min while the cross flow rate varies linearly from 2.4 ml/min at the beginning (0 s) down to 0 ml/min after 30 min (1800 s). This corresponds to a starting value of 75 % of the total laminar inflow at the beginning down to 0 % at the end. In total, a fractogram is registered for 45 min (2700 s) which means that during the last 15 min (900 s), the system runs without crossflow allowing

theoretically the relaxation and the elution of all the remaining particles. For the analysis of inorganic component, the effluent is mixed via a T-piece with 6 % nitric acid containing 50 µg/L Rh as an internal standard and introduced into the ICP-Mass spectrometer (ELAN 6000, Perkin-Elmer, Germany) at a constant flow rate of 0.5 ml/min via a peristaltic pump (Minipuls3, Gilson, France). Two additional injection valves are installed: 1) one with a 100 µL loop is installed between the channel box and the UV-Vis detector and 2) one with a 130.4 µL loop is located in front of a T-piece (Omnifit) which admixes the acidic Rh-solution to the channel outflow before entering the ICP-MS nebulizer. Both additionally installed injection valves can be used to determine losses of sample constituents in the channel by injecting reference solutions.

Size determination. Colloid sizes are derived by calibration using a series of polystyrene sulfonate (PSS) reference standards (Polysciences, Eppelheim, Germany) with certified molecular weights (1.29, 4.4, 15.2, 29 and 81.8 kDa) and a series of carboxylated polystyrene reference particles (Magsphere,USA) with certified sizes (24, 105 , 207 , and 510 nm). Our system was calibrated up to 510 nm in the “normal” elution mode. Mixtures were prepared just before injection into the carrier solution. Overloading effects which have been frequently reported in the literature ([67]; [106], [66]) have been checked by injecting 100 µL of a reference colloid mixture prepared at different concentrations. No shift of elution times was observed for PSS concentrations below 100 µg/L.

Quantification of the fractograms and comparison with ultrafiltration. Calibration methods for the quantitative evaluation of fractograms and their validation are described in detail in ([68]). Briefly, measured intensities for the respective element of interest are normalized to the measured intensity of an internal standard Rh-103. Rh-103 (50 µg/L) dissolved in 5% HNO_3 (ultrapure) is admixed at constant flow to the channel effluent before entering the ICP-MS nebuliser. ICP-MS intensities are converted to masses (ng) for each analyte of interest. The mass versus elution time fractogram is then integrated in order to derive the total peak areas, which can then be attributed directly to the amount of given element in the respective colloidal fraction. This approach has been primarily adopted to correct for flow rate fluctuations observed with our AsFlFFF notably at the beginning of each fractionation run. Peak area determination is reproducible within less than 10 % uncertainty.

The quantified element content in the colloidal fraction is compared with parallel ultrafiltration experiments. Element concentrations are measured by ICP-MS in ultrafiltrates (ultrafiltration cartridges containing a polyethersulfone membrane with 1000 kDa cutoff corresponding to a pore size of ~17 nm according to ([108]), Pallfiltron, Germany) and in the total solution without filtration. The difference in concentrations is attributed to colloidal species.

Results & Discussion

The pH of all the different suspensions remains constant after solution preparation and lies in a range of 8.3-8.9. This is on average 1 pH unit lower than the initial Grimsel groundwater pH value due to the addition of a small amount of the RN-cocktail with very low pH (~1.3). The groundwater used for the experiments was not filtered. Naturally abundant colloidal particles

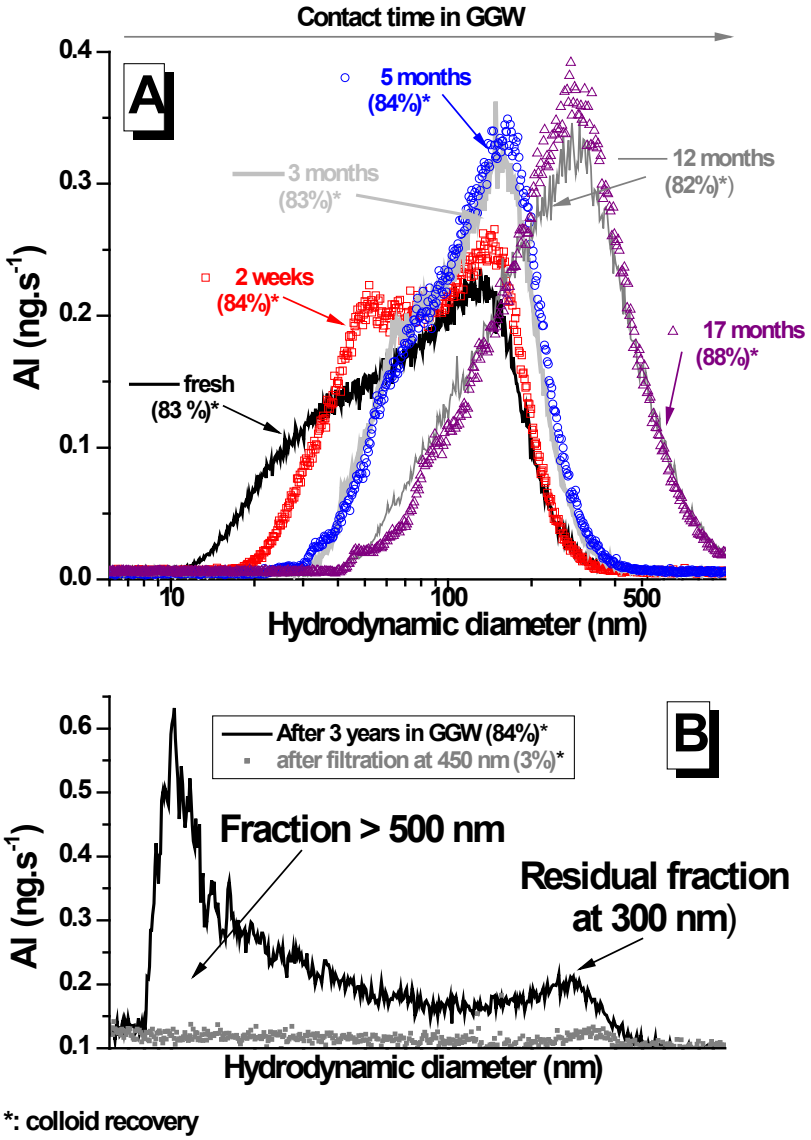

Figure 2.10: Evolution of Al-fractograms (representing bentonite colloids) over 3 years recorded after injection of Set 2 suspensions (with bentonite clay colloids initially Li^+-delaminated, TS1). The error for peak position reproducibility is less than 5%. The recoveries (values indicated in brackets) are reproducible within less than 10% uncertainty. These uncertainty ranges hold for all fractograms. A: The AsFlFFF works in the so-called normal mode where the smaller colloids are eluted prior to bigger ones. The calibration is valid up to 510 nm (see Text). B: The AsFlFFF works in the so-called steric mode where the bigger colloids (fraction > 500 nm) are eluted prior to smaller ones (residual fraction at 300 nm).

(SiO_2, phyllosilicates and Ca silicates) with sizes between 10 to 1000 nm exist at very low concentrations varying from 0.005 to 0.1 mg/L according to [81] and [109]. They could not be detected during repeated injections of the natural Grimsel groundwater into the AsFlFFF-ICP-MS system under our experimental conditions. Concentrations of those natural fine groundwater particles are by around 2 orders of magnitude lower than added clay and/or

humic colloids and are not believed to significantly influence metal ion speciation or to interfere significantly with the added colloids.

Study of clay colloid stability. Previous studies ([85]) suggest colloids being stable in the low ionic strength, high pH GGW. In order to determine the size distribution by AsFlFFF, we selected Al as an indicator element for the clay colloids (10.8 wt % of the clay mass) instead of Si, which is the main component of the bentonite ([99]). ICP-MS detection of Si is not sensitive due to a high background induced by the abrasion of the quartz torch. To check whether the Al fractograms reflect the clay colloids, the Al/Mg ratio was determined over the course of the peak and was found constant and equal to the expected value of 3.7 ± 0.2 (theoretical value: 3.68 ([99])). Fractograms of the set 2 suspensions containing 20 mg/L clay colloids (from TS1) in GGW, recorded over 3 years are presented on Figure 2.10A and Figure 2.10B. (84 ± 3) % of the injected Al mass are found in the elution band of the fractogram and correspond to the recovery of the clay colloids after fractionation for all analyses. The rest of the colloid mass (16 %) is obviously lost during fractionation and might be retained on the channel surfaces. A gradual agglomeration process is evidenced in Figure 2.10A after 18 months storage. The clay colloid size distribution varies from initially 10-200 nm to 50-400 nm during 18 months (Figure 2.10A). Measurements after 3 years (Figure 2.10B) reveal that slow agglomeration continues. Apparently, particles with sizes > 500 nm form and are eluted in the "steric" mode in the beginning of the fractogram. The large size of those early eluted colloids is confirmed by filtration through a membrane with 450 nm pore size. Injection of the filtrate into the channel resulted in a decrease of colloid recovery from 84 % to 3 % and only remaining colloids with a size around 300 nm are detected. The agglomeration phenomenon is reproducible and was observed as well in the other sets of samples containing bentonite colloids.

Missana et al. [85] dispersed the Na^+-homo-ionized FEBEX bentonite in deionized water resulting in a final ionic strength of 5×10^{-3} mol/L, for a pH value of 8.7 and an average colloidal size of (270 ± 50) nm as determined by photon correlation spectroscopy (PCS). SEM investigations showed that the dispersed colloids were in fact composed of aggregates. Those aggregates appeared to be stable for over 5 months and no size increase could be observed. In our work, the colloid suspension (S1) was originally homo-ionized with Li^+. At the end of the dispersion/centrifugation cycles, the Li^+ concentration was still 2.38×10^{-3} mol/L in the TS1 stock suspension. The further dilution of the clay colloid stock suspension (TS1) in GGW to 20 mg/L results in a final Li^+ concentration of 3.9×10^{-5} mol/L. We explain the observed agglomeration by the increase of the Ca^{2+} to Li^+ molar ratio in solution from 0.09 to 5.3 after the final dilution of the stock suspension TS1. Ca^{2+} (concentration in GGW: 2.1×10^{-4} mol/L) replaces Li^+ at the ion exchange sites of the clay platelet basal planes and as a consequence induces agglomeration. To confirm this hypothesis, a bentonite colloid stock suspension (TS2) has been prepared after suspending FEBEX bentonite powder directly in GGW (S2), without any previous Li^+ homo-ionization. Clay colloid preparation by performing dispersion/centrifugation cycles in GGW (TS2) results in the establishment of size distribution ranging from 50-500 nm centered at ~ 180 nm as determined by AsFlFFF-ICP-MS (Figure 2.11A, 'GGW'). The different behavior of TS1 and TS2 suspensions is shown in Figure 2.11. While

the initially Li^+ homo-ionized clay particles aggregate significantly during the first 4 months only a slight shift of the size distribution is observed for the clay suspension washed with groundwater only. The maximum of the size distribution increases slightly from 180 nm (colloid recovery after fractionation: ~74%) to about 200 nm. This could be an indication for ongoing colloid agglomeration, however, should be considered with caution with regard to analytical uncertainties. Nevertheless, analysis of an 8 years old FEBEX bentonite colloid suspension (20 mg/L) washed and prepared in Grimsel groundwater revealed again a slightly larger size maximum at 210 nm (colloid recovery: 66%). SEM analysis of those latter particles indicates the presence of aggregates. We have to note that the pH in this 8 years old solution decreased over time to 8.0. Despite experimental uncertainties, it appears that slow clay colloid aggregation occurs also for the non-Li^+-homo-ionized clay particles.

All results show slow clay agglomeration which is not finished after one year. At a first glance, this contradicts earlier studies ([85]; [93]) performed however over shorter time periods only and stating high colloid stability. Seher et al. [110] determined in recent experiments a critical coagulation concentration (CCC) of 1 10^{-3} mol/L for clay colloids prepared from FEBEX bentonite in $CaCl_2$ solutions. The CCC corresponds to the salt concentration where colloid agglomeration is purely diffusion limited and electrostatic repulsion becomes negligible. The CCC determined by [110] is just 5 times higher than the Ca-concentration in GGW. At lower Ca-concentrations (3.3 10^{-4} mol/L) a stability ratio W of ~ 100 is obtained at pH 9-10, i.e. only 1 of 100 colloid-colloid collisions leads to an agglomeration. For details on W determination see [111]. In our system containing Li^+ ions the destabilization effect due to Ca^{2+} ions obviously is enhanced due to the enrichment of Ca^{2+} at the clay basal planes via ion exchange.

In conclusion, the clay colloids undergo a continuous agglomeration process over long time periods in the natural GGW. The generally low ionic strength and high pH conditions of the GGW might thus not *per se* be sufficient to stabilize clay colloids for long time periods. Even under those conditions colloids might be prone to agglomeration and finally sedimentation. Further experiments are in progress to confirm this observation.

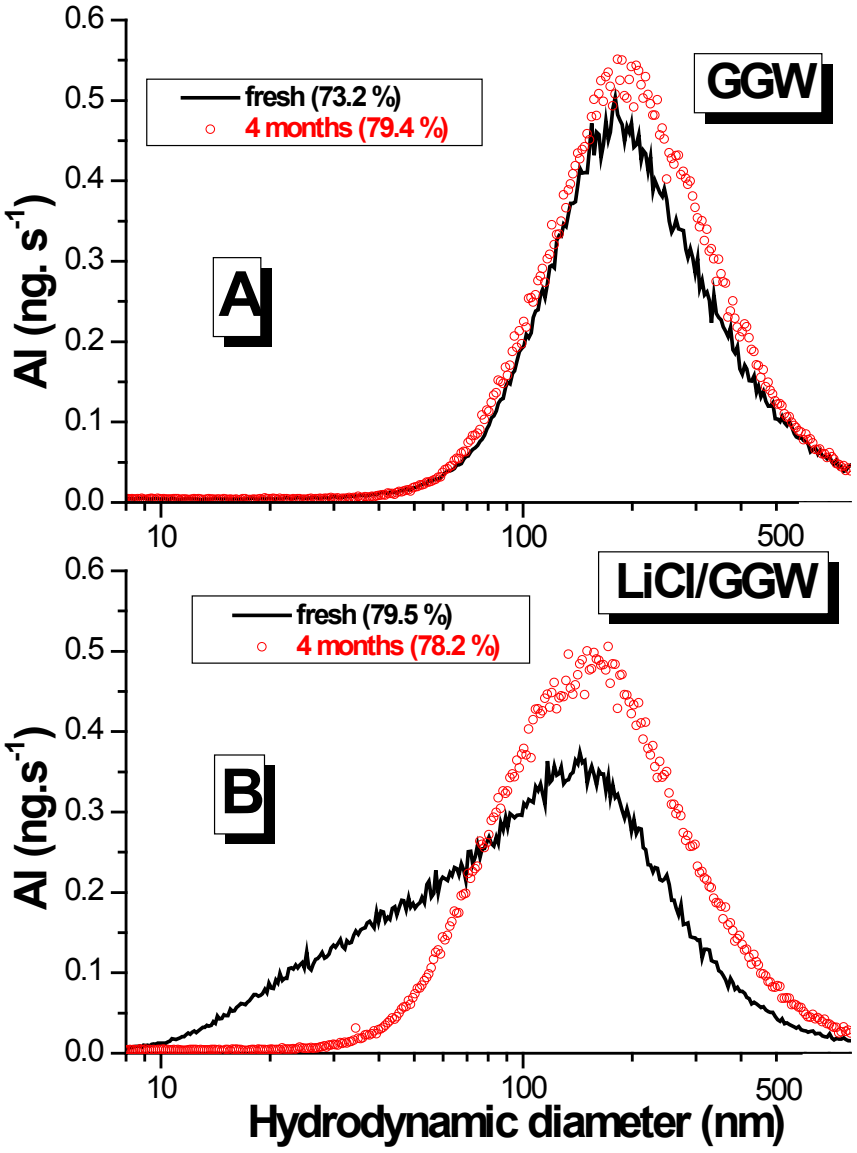

Figure 2.11: Comparison of the Al-fractogram evolution (representing bentonite colloids) over 4 months for batch samples of bentonite colloids prepared in Grimsel groundwater (GGW) directly (Figure 2.11A) or after an initial Li-homoinisation (LiCL/GGW) (Figure 2.11B). The values in brackets represent the Al recoveries determined from fractogram analysis.

Radionuclide-colloid interaction. The behavior of the radionuclides and radionuclide homologues Cs(I)-, Eu(III)-, Th(IV)-, and U(VI)-in the presence of 20 mg/L clay colloids has been followed by AsFlFFF-ICP-MS as a function of time. Figure 2.12A and Figure 2.12B shows the results obtained after injection of the set 4 suspensions investigated as a fresh sample, and after 2 weeks, 5 months, 17 months, 3 years.

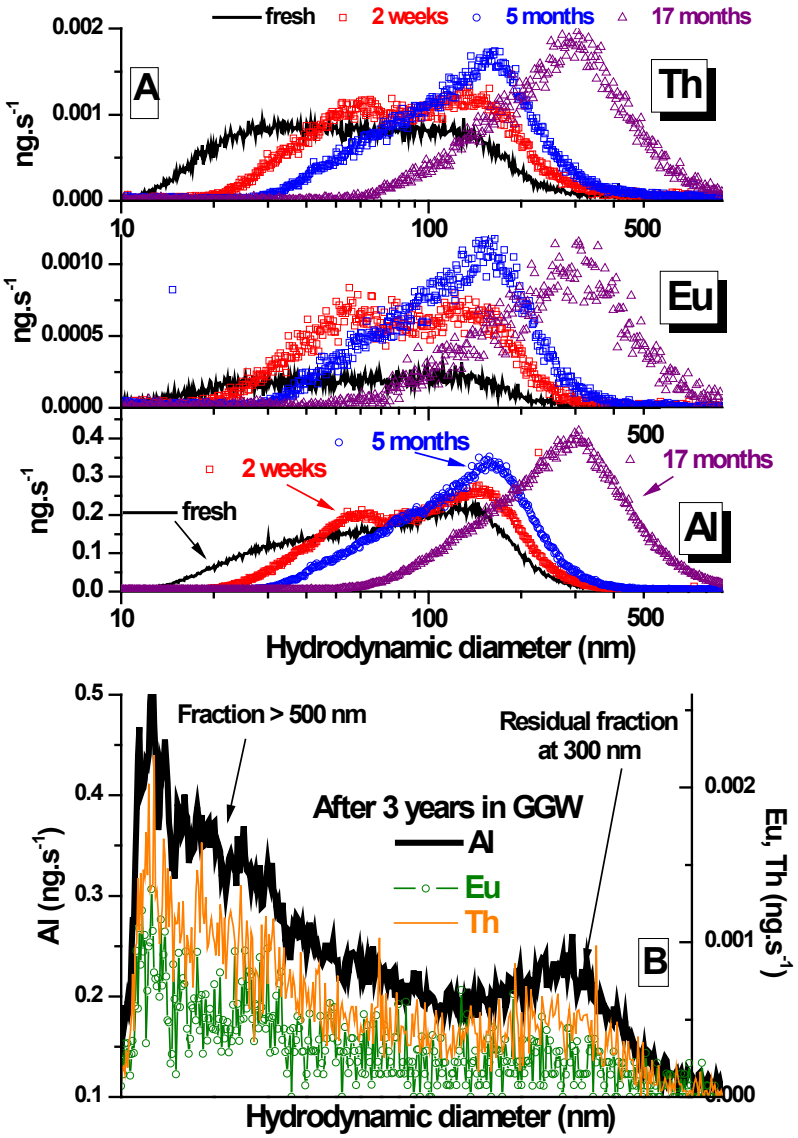

Figure 2.12: Interaction of Eu and Th with bentonite colloids followed over 3 years via the evolution of the Al-, Eu- and Th-fractograms recorded after injection of Set 4 suspensions. A: The AsFlFFF works in the so-called normal mode where the smaller colloids are eluted prior to bigger ones. The calibration is valid up to 510 nm (see Text). B: The AsFlFFF works in the so-called steric mode where the bigger colloids (fraction > 500 nm) are eluted prior to smaller ones (residual fraction at 300 nm).

Under the experimental conditions of this work, Cs(I) and U(VI) are hardly bound to the colloids and their signal in ICP-MS follows basically the background. Eu(III)- and Th(IV)-fractograms qualitatively follow the Al-fractograms indicating their attachment to clay colloids. As already discussed before, clay colloid agglomeration occurs in the same way as observed in the absence of metal ions (Figure 2.10A and Figure 2.10B). The close similarity of clay fractograms shown in Figure 2.10 and Figure 2.12 demonstrates the reproducibility of the AsFlFFF analysis. The sorption of Eu(III) and Th(IV) on colloids does not enhance the ag-

glomeration process. The different shapes of Th, Eu fractograms on the one hand and Al (i.e. clay) fractograms on the other hand suggest the preferred attachment of the polyvalent metal ions to smaller-sized colloids. We attribute this observation to a surface area effect: metal ions preferentially sorb to smaller colloids which have a higher specific surface area. It is well known that Th(IV) tends to form nano-sized polymeric (eigencolloid) species. According to our calculations (see below), the solution is potentially oversaturated with respect to amorphous Th (i.e. $ThO_{2,\ amorphous,\ fresh}$). AsFlFFF-ICP-MS analysis of groundwater spiked with the metal ions but without addition of colloids was not able to detect colloidal species. This does not mean that the eigencolloids do not exist as they could be sorbed onto the AsFlFFF membrane. Thus, we cannot exclude the possible initial formation of colloidal species after spiking, which may entail the attachment of these species to the clay particle surfaces.

In earlier studies we could demonstrate the reproducibility of the results obtained in fractionation experiments. Application of an appropriate calibration method as described in detail in [68] allowed the quantification of colloidal element fractions and their evolution in time (Figure 4) with in general an uncertainty < 10 %. Colloid bound element fractions are compared with the outcome of ultrafiltration experiments using 1000 kD filters (Figure 2.13).

Around (5 ± 1) % U(VI) was found colloid bound by AsFlFFF, whatever the colloid - metal ion contact time, which is confirmed by ultrafiltration results. The same is true for Cs(I), not shown in Figure 2.13 (data are almost congruent with those for U(VI)). These results are in agreement with previous ultracentrifugation experiments in the same system where 6 % of U(VI) and 8 % of Cs(I) were found to be clay colloids bound.

Up to 1 year, the Th(IV) recovery in the AsFlFFF effluent (90 ± 5 %) corresponds to the clay colloid recovery, showing its complete attachment to the colloids, which again is in agreement with ultrafiltration experiments performed after 1 year. Comparable colloid-borne association (84 %) was found for Pu(IV) using ultra centrifugation [93]. After one year, a slight decrease of the Th fraction associated to the clay colloids is observed. This behavior could be explained by partial Th desorption and formation of a carbonate complex due to intrusion of air traces into the glove box during long term storage, which could never be totally excluded.

Different results are found for the behavior of Eu(III). First, it appears that the colloid-borne Eu(III) fraction increases from 25 up to 60 % from the initial preparation of the sample (taken ~ 10 min after mixing) to the next sampling times. Analysis of the ultra-filtrate after one year indicates 97 % colloid-borne Eu(III) again in agreement with an earlier ultracentrifugation experiment ([93]) which resulted in 99 % colloid borne Am(III). We explain this behavior by the competitive Eu(III) sorption to the colloids and the cellulose ultrafiltration membrane in the AsFlFFF channel. Part of Eu(III) is thus believed to dissociate from the clay colloids and then being trapped by the membrane. This occurs most likely during the focusing step where colloids can have direct contact with the cellulose membrane surface. Nevertheless, it is presently too speculative to attribute the recovery increase between the two first measurements to an increase of the binding strength with time.

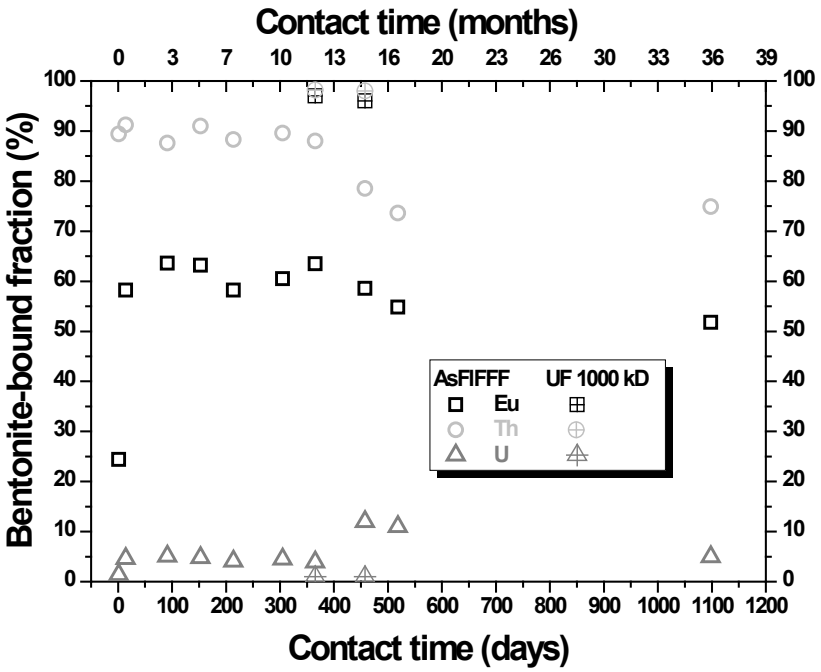

Figure 2.13: Fractions of U, Th and Eu bound to bentonite colloids (Set 4) determined from peak area analysis of fractograms as a function of the contact time (up to 3 years) in GGW and additional ultra filtration (UF) results (filtration at 1000 kDa). The values indicated are reproducible within less than 10% uncertainty.

It is clear that AsFlFFF represents an invasive speciation technique, where during fractionation chemical equilibrium can be disturbed. This is certainly the case for colloid borne Eu(III) where speciation is partially interfered by competitive sorption to the membrane. For the strongly colloid bound Th(IV) such processes appear to be less significant. The slight decrease of Th(IV) attachment to clay colloids by ~ 15% after 1 year as indicated by AsFlFFF is not yet clearly understood and requires further investigations.

The metal ion – colloid interaction as determined by AsFlFFF is compared with speciation calculations below.

Competition with humic acids. The impact of humic acid addition to metal ion bearing clay colloids is illustrated in Figure 2.14. The different colloidal fractions, humic acid or clay colloids, are clearly separated under the selected fractionation conditions. The humic acid (Go-Hy-HA-573) is identified by the UV-Vis absorbance signal recorded at 225 nm showing an asymmetrical size distribution centered at 0.9 nm which is not time-dependent.

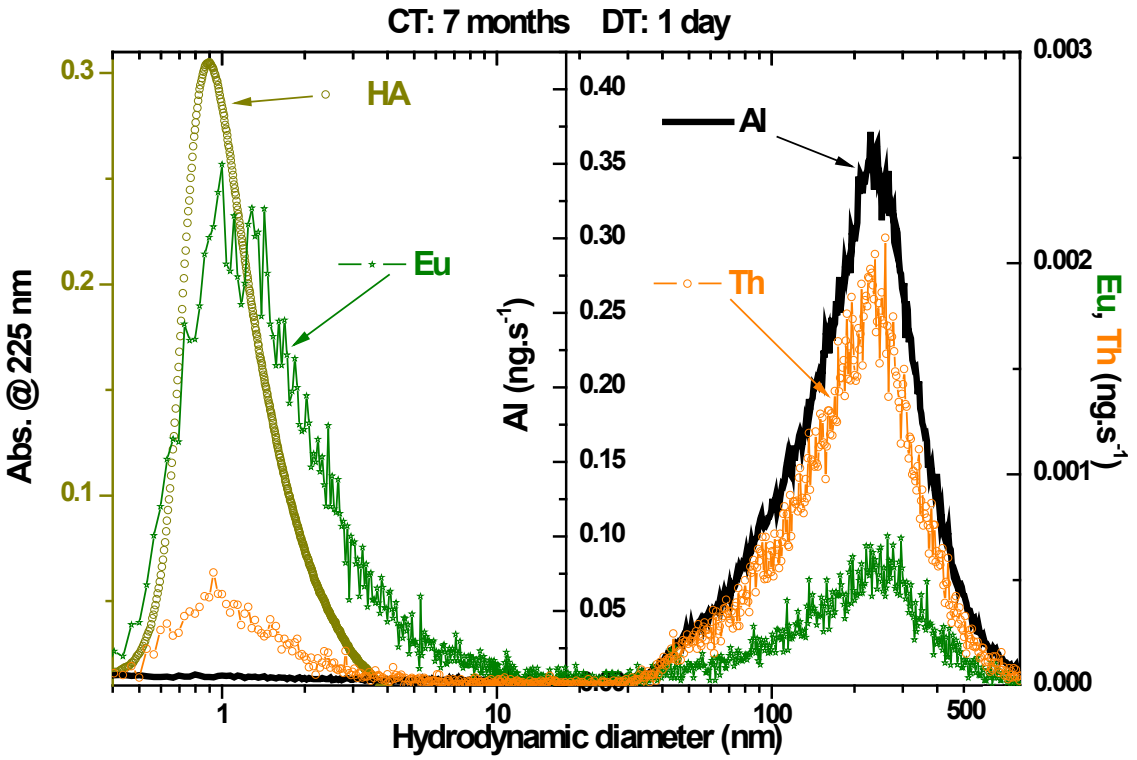

Figure 2.14: Example illustrating the influence of the humic acids (HA) addition (after 1 day) on the Eu and Th interaction with bentonite colloids contacted for a certain time (7 months) in GGW. The observation is made by measuring the Eu- and Th-fractograms and comparing them to the HA-fractogram (as obtained by the absorbance measurements at 225 nm) and Al-fractograms (representing bentonite colloids). DT: desorption time (after HA addition); CT: contact time (before HA addition). Sample analysis for Set4 DT.

As discussed earlier, Eu(III) and Th(IV) are initially completely clay colloid bound. The fractograms in Figure 2.14 show that addition of 10 mg/L humic acid induces partial dissociation of Eu(III) and Th(IV) from the clay particles even after only 1 day desorption time. With increasing desorption times, Eu(III) and Th(IV) association to humic acids is enhanced. The time dependent partitioning of metal ions between clay colloids and humic acid for all experiments observed by AsFlFFF and ultrafiltration (UF) over three years is plotted in Figure 2.15. In all experiments we observe desorption of Th(IV) and Eu(III) from the clay colloids almost irrespective of the previous contact time during the 3 years study. Eu(III) desorbs quite fast and finally is almost completely humic acid bound. Th(IV) desorbs slower and reaches a fraction of almost 50 % humate complexes after three years.

The results are compared with those obtained after simultaneous mixing of humic acid, bentonite colloids and RN-cocktail (set 5 or “Equil.”). Metal ion distribution does not vary in time in this system (Figure 2.15). The same is observed for experiments with suspensions of set 3 batches (“HA-RN”), in which bentonite colloids act as competitors for initially HA-bound metal ions. Furthermore, the result of these experiments resembles closely that obtained for the

"HA-RN" solution without bentonite colloids added. The combination of all these data clearly shows that for both Eu(III) and Th(IV) the chemical equilibrium is shifted towards the formation of humate complexes. This is also the case for UO_2^{2+}, where almost no surface attachment to clay colloids could be observed in all experiments.

The desorption experiments for Eu(III), therefore, show that bentonite colloids cannot compete with humic acid and the Eu sorption to bentonite colloids is fully reversible even after 3 years aging.

In contrast, Th(IV) appears to bind stronger to the clay colloids than Eu(III). The equilibrium distribution between humic acid and clay colloids is obviously not obtained within 3 years. In this case we observe a clear difference in the final Th(IV) speciation as a function of the addition sequence. Adding Th(IV) to the humic acid first and then clay colloids results in a clear predominance of Th(IV)-humate complexes, while the opposite mixing sequence yields a significant clay-colloid bound Th(IV) fraction (30 ± 5 %).

The metal ion/colloid speciation determined by AsFlFFF experimentally was compared with speciation calculations using existing thermodynamic data from the literature.

For the interaction of radionuclides with the clay surfaces, the model of Bradbury and Baeyens [112] was chosen. More precisely, their linear-free-energy relationship data for metal ion sorption to montmorillonite was used [112], based on hydrolysis constants published in the respective most recent NEA/OECD compilations ([113]; [114]). Site density values and CEC data for montmorillonite given by Bradbury and Baeyens are quite comparable to those determined by [115] for the clay in FEBEX bentonite. Therefore, we believe that the use of the data set of [112] is justified.

For the interaction of radionuclides with HA, the Nica-Donnan model [116] was applied. Complexation data are also in this case derived by relating the model parameters for the interaction of metal ions with humic acid to metal ion hydrolysis constants [116]. General model parameters are taken as recommended by Milne et al. Also in this case hydrolysis constants were taken from the most recent NEA/OECD compilations ([113]; [114]). This was the only way to allow for consistent application of the two models since metal hydrolysis constants used to derive complexation constants were not the same in both approaches. The calculations were done by using the ECOSAT program ([117]).

Furthermore, the Grimsel ground water components were considered in the calculations. This involved both the calculations for metal adsorption to the clay and the interaction with the HA. For example Al as a trivalent ion was present in significant amounts relative to the low concentrations of radionuclides, which is considered in the calculations. Aqueous speciation data for Al were taken from [118] while the parameters for the interactions with colloids and humic acid were obtained from the above cited papers using the linear-free-energy relationship equations published therein. The presence of DOC (1.2 ± 0.2 mg/L) in GGW was originally reported but the nature of this organic carbon has never been characterized and identified. Scoping calculations show that this quantity, if present as fulvic acid for example,

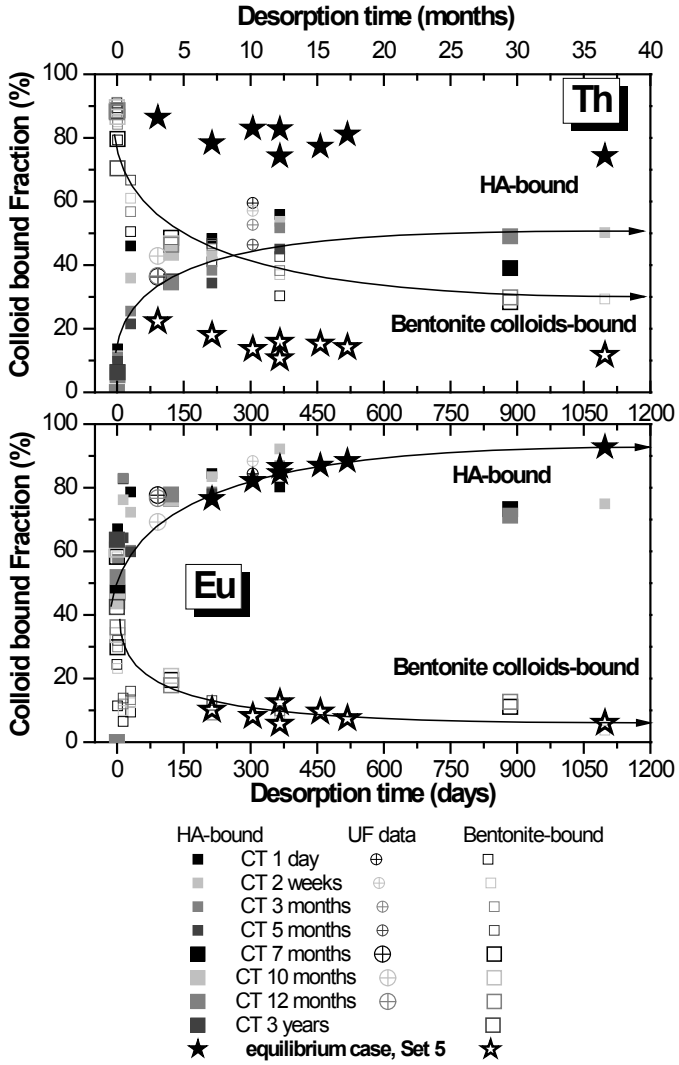

Figure 2.15: Evolution of Eu and Th partitioning between humic acid (HA) and bentonite colloids with time. Eu and Th have been aged with bentonite colloids before mixing during a certain time (CT: contact time) in GGW. The values represent the recoveries for Eu and Th as determined after analysis of Set 4 DT samples (HA acting as competing ligand). The values indicated are reproducible within less than 10% uncertainty. Full square symbols represent the fraction of elements desorbed from bentonite and bound to the competing humic acid. The open square symbols represent the fraction of elements remaining bound to the bentonite colloids. The crossed-symbols are additional ultra filtration data. The stars represent the partitioning between the two colloidal fractions for the so-called equilibrium system (Set 5). The curved arrows represent subjective envelopes.

would be sufficient to completely complex the radionuclides added to the GGW. However, such amounts of fulvic or humic acid should be detected by the AsFlFFF but this was not the case. Accordingly, speciation calculations were done without taking into account the background DOC in GGW.

Thermodynamic calculations. Auxiliary data were whenever possible taken from the NEA/OECD compilation books ([113]; [114]) to assure maximum consistency. Carbonate was treated as a component with a known total concentration, fixed at the concentration value of the Grimsel groundwater (2.8×10^{-4} mol/L) since the experiments were carried out in closed vials. Nevertheless, to test the sensitivity of the results due to variations of the carbonate concentration, it was varied from 5.7×10^{-5} mol/L to 5.7×10^{-4} mol/L.

Since all radionuclides/homologues were present simultaneously, the system was set-up as the complete multi-component system within ECOSAT [117]. The interaction of the HA with the clays was not considered because no type of interaction between them was experimentally observed. Calculations were done in the pH range 8.3 to 8.9 covering the experimental value of pH 8.6. This allowed an estimation of the sensitivity of the results due to slight variations of the pH. Since in such a multi-component system, not all relevant species (and therefore not all relevant thermodynamic data) are known, results have to be considered as approximations.

Speciation calculations were carried out on all the systems studied. In the first step, the speciation of the radionuclides in the GGW was calculated. The calculations showed that Th is potentially oversaturated with respect to the precipitation of amorphous $ThO_{2,\ amorphous,\ fresh}$ (containing ~ 81 % of the total Th) in the pH range considered.

Precipitation of thorium as described above is still thermodynamically expected when only bentonite colloids are present (Set 4). This allows for additional assumptions about the behavior of that system. Th could be present dissolved or precipitated just as in the absence of bentonite colloids. The precipitates could adhere to the bentonite colloids or surface precipitates could have formed on the bentonite colloids, so that part of the Th is eluted with the bentonite colloids in such a form.

The calculated speciation of Eu, U and Th in presence of 20 mg/L bentonite colloids is shown in Figure 2.16 (thin and dotted lines).

Negligible surface attachment of UO_2^{2+} to clay colloids is predicted in agreement with our experiments, dissolved $UO_2(OH)_3^-$ complexes prevail. Uptake of Eu is between 4 and 8 % in the considered pH range. Th uptake by clay colloids is between 3 and 10 % while the Th precipitate fraction is between 71 and 78 %. The adsorption model does not predict the experimentally found fraction of Eu and Th on bentonite colloids, both calculated fractions are lower. Nevertheless, for the Th, an agreement is found between the experimental and the calculated fraction by summing the calculated bentonite bound and precipitated values. Varying the carbonate concentration has a drastic effect on the Eu speciation results. An increase by a factor 2 (compared to the measured value in the GGW, i.e. 2.8×10^{-4} mol/L) reduces the calculated Eu fraction bound to bentonite by a factor 2 as well while a decrease by a factor 4 increases the calculated Eu fraction bound to bentonite by a factor 3. This might be one reason for the rather poor agreement between the experimental result and the calculated values. Our systems could be changed with respect to the total carbon content due to opening the vials in a carbon dioxide free atmosphere. It is also noteworthy that Bradbury and

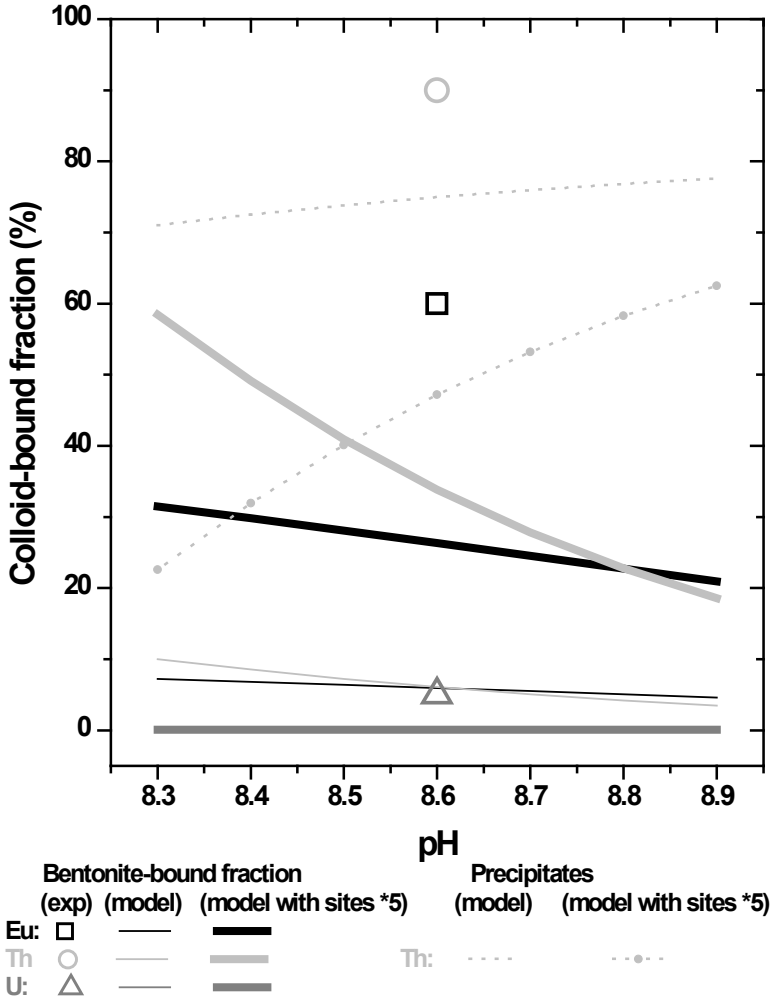

Figure 2.16: Calculated speciation distribution of Eu, Th and U between aqueous, bentonite colloids-bound fractions and precipitates as a function of pH, in the absence of humic acid, according to the thermodynamic model and data of Bradbury and Bayens (2005) (thin lines) or by increasing the total sites concentration by a factor 5 (thick lines), see text for details. The pH is varied to test its influence on the thermodynamic calculation. Experimental points from AsFlFFF analysis are added for direct comparison.

Baeyens considered the 0.5 µm size fraction of SWy1 Montmorillonite and determined a total edge sites density (≡ SOH) by titration of 8.2×10^{-2} mol/kg [119]. The AsFlFFF measurements indicate an initial FEBEX clay colloid size distribution ranging from only 10-200 nm with a maximum around 120 nm (Figure 3A). If we assume in a simplified approximation that the average particle diameter of the clay material used by Bradbury and Baeyens (and also by [115]) is about ~ 5 times larger than our colloidal fraction, we can also suppose that the total concentration of edge sites in our colloidal suspension scales by the same factor. The fact that the number of surface sites at clay platelets of course depends on particle size and surface area is well established (see e.g. [120]). By increasing the total site concentration by a

factor of 5 in our calculation (Figure 7, thick lines), the calculated Eu fraction increases but still remains below experimental observations. The calculated Th bentonite bound fraction increases (from 18 % and 60 %) while the calculated fraction of precipitated Th decreases accordingly. Speciation calculations clearly underpredict experimental observations with regard to Eu(III) and Th(IV) binding to clay colloids. One reason might be related to the experimentally observed preferential association of polyvalent metal ions to even smaller bentonite colloids offering higher specific surface area than assumed in our calculations. Another explanation could lie in variations of carbonate concentrations under our experimental conditions as compared to those originally present in the GGW. It is however tempting, even though somewhat speculative, to link the calculated oversaturation of Th(IV) with regard to precipitation of amorphous Th-hydroxide/oxide to the experimentally observed disequilibria of Th(IV) partitioning between clay colloids and humic acid.

In the pure organic matter system, the Nica-Donnan model ([116]) predicts complete uptake of both Eu and Th, while minor parts (< 10 %) of the uranyl species remain in solution. This agrees with our experimental results obtained by AsFlFFF for the data set 3. In the system containing both HA and clay colloids, Eu(III) is predicted to remain by less than 5 percent in aqueous solution. It is mainly bound to organic matter. This pattern is predicted to be even more pronounced for Th(IV), which should be 100 % organic matter bound according to the calculations. The calculations confirm that the speciation of Th, U and Eu is dominated by the respective humate complexes as demonstrated by the experiments with the analysis of the data set 5, “equil.”, considered as our equilibrium system (Figure 6).

The present experimental and calculated data agree with other reported results, which indicated that the metal ion / HA interaction inhibits at least partly the metal ion /mineral oxide sorption as for Am(III) onto silica [121], Eu(III) onto goethite or boehmite [122], Th(IV) onto hematite and silica ([123]; [124]; [125]), and Th(IV) and U(VI) onto hematite ([126]). In case of our experiments with Th(IV) it was shown that an equilibrium model is not adequate for describing the sorption-desorption process and the addition sequence was found to play a major role. Similar observations on disequilibria depending on addition sequences have been reported for other elements in various systems in presence of HA: U(VI) migrating through well characterized Clashach Sandstone matrix ([127]), Ni on kaolinite [128], Ni on HFO [129], Th on hematite [125], Zr and Hf on kaolinite and silica [130]. However, all these studies considered significantly shorter observation periods than three years. Explanations for observed kinetic effects are inter alia the transformation of initially adsorbed element to a less leachable surface precipitate [127] forming for example a metal hydroxide, a mixed layered double hydroxide (LDH) or a phyllosilicate phase within a matter of days or even less with a stabilization of the precipitate phase upon ageing [128]. Another explanation which can be found in literature is diffusion of metal ions into mineral pores or interlayer sites, finally retarding metal ion desorption from the mineral surface.

We presently do not understand the incomplete desorption of Th(IV) from clay colloids after humic acid addition and long contact times even though experiments and speciation calculations suggest that the equilibrium state clearly lies on the side of the HA-complex. However, the observation of different kinetic stabilities for Th(IV) and Eu(III) clay colloid species has

recently been confirmed by in-situ migration experiments performed at the Grimsel Test Site. Tetravalent elements sorbed to the bentonite colloids prior to the injection into a granitic fracture show a much higher recovery than colloid borne trivalent metal ions [131]. The above mentioned explanations discussed in the literature might be responsible for the finding. In our case possible precipitation or surface precipitation phenomena might explain the findings as discussed above. Further studies are underway to elucidate the mechanism of the observed slow reversibility/partial irreversibility of the Th(IV)-clay colloid binding.

Conclusions

- The flow field-flow fractionation method coupled to UV-Vis and ICP-MS detectors is a flexible colloid characterization method allowing the observation of the interaction between the metal ions present even in traces and colloids. This is relevant for natural ground water conditions where most spectroscopic techniques cannot be applied. Although chemical equilibria are disturbed by the nanoparticle separation and even if the interaction of samples with channel surfaces cannot be suppressed completely, the fractograms provide semi quantitative insight into the trace element partitioning in colloidal systems.

- The present study, performed over a 3 years period, suggests that the clay colloids undergo a continuous agglomeration process even in the natural GGW, where conditions were thought to be ideal for clay colloid stabilization. The water chemistry and mainly the Ca^{2+} concentration determine the colloid size distribution.

- The calculated distribution of U(VI), Th(IV) and Eu(III) qualitatively represent the experimental data. Eu(III) and Th(IV) were found to bind to clay colloids, while U(VI) and Cs(I) remain mainly dissolved in solution.

- The trivalent metal binding to clay colloids at slightly alkaline conditions of a granitic groundwater was found to be reversible. Part of Th(IV) could not be desorbed from the colloid surface even after contact times for about 3 years by humic acid addition, although the calculated and experimentally obtained equilibrium is clearly located at the side of the respective humate complex.

Further complementary studies have to be carried out to understand the kinetically hindered or partially irreversible desorption of Th from the clay colloids. A mechanistic explanation for this observation is not yet available, even though surface precipitation is indicated by calculations. Such type of ‘irreversible’ metal binding to colloids may enhance radionuclide transport as long as clay particles show a high colloidal stability. If colloids are unstable or prone to filtration in a given geological system, such processes may however also efficiently retard radionuclide migration. Further studies on the elucidation of the underlying mechanisms in colloidal systems are therefore of cardinal importance.

Acknowledgments

We thank Mr. Wolf from the GSF-National Research Center for environment and Health, Institute for groundwater Ecology, Neuherberg, Germany, for giving us 1g of the new isolated, purified and characterized GoHy-573 humic acid batch. CIEMAT is acknowledged for providing us with the FEBEX bentonite raw material.

Further details to the study presented in this chapter can be found in:

Bouby, M.; Geckeis, H.; Lützenkirchen, J.; Mihai, S.; Schäfer, T. (2011) *Interaction of bentonite colloids with Cs, Eu, Th and U in presence of humic acid: a Flow Field-Flow Fractionation study.* Geochimica and Cosmochimica Acta, 75(13), p3866-3880 and in the corresponding supplementary data file, http://dx.doi.org/10.1016/j.gca.2011.04.015.

2.1.3 Colloid generation at the compacted bentonite water interface

Abstract. Bentonite colloid generation was investigated under Grimsel groundwater using compacted Febex bentonite rings with identical dimensions to the planned CFM long-term in situ experiment and Grimsel groundwater as contact fluid. A water conducting feature was simulated by a parallel plate model with a 1 mm aperture. Colloid concentration and average colloid diameter was measured with Laser-induced Breakdown Detection (LIBD). Geochemical parameters (pH, electrical conductivity) as well as water chemistry was monitored. The swelling pressure induced a gel front penetrating max. 2.5 cm radial into the artificial fracture introducing a first colloid erosion peak, which leveled off after the final expansion state was reached. In a second phase after the chloride/sulfate inventory was released the colloid concentration increased again to plateau values of 6 – 15 mg/L (s-curve LIBD) until the termination of the experiments after eight months.

Materials & Methods

Material. In all experiments documented here smectite-rich Febex (full-scale engineered barrier experiment) bentonite from the deposit of Cabo de Gata, Almería (Spain) is used without any purification step [132]. The exchangeable cation composition was determined prior to the experiment to be 99 ± 2.1 meq·/100g. As contact water original Grimsel groundwater sampled from the MI shearzone in 50L Teflon coated Ar pre-flushed Al barrels is used.

Experimental setup. In order to mimic the contact zone of the CFM long-term in situ test to be started in November/December 2013 the geometry and chemical conditions of the laboratory experiments were chosen to be comparable to the in-situ test. Compacted bentonite rings were manufactured and provided by CIEMAT (Figure 2.17). The individual ring dimensions are 82mm outer diameter and 43mm inner diameter with an optimum dry density of 1.65 g/cm^3 resulting in a ring height of 25mm. In these compacted bentonite rings eight holes of 8mm diameter and 10mm depth are drilled to emplace glass ampules with a labeled bentonite slurry.

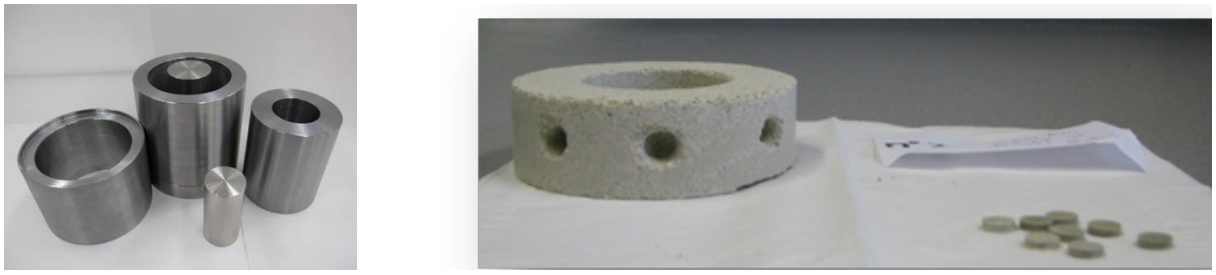

Figure 2.17: (left) Different molds manufactured by CIEMAT for compaction of bentonite rings. (right) Compacted bentonite ring (1.65 g·cm^{-3}) with 8mm drilled holes for emplacement of glass vials. In the lower right region of the image pellets of 2mm thickness are shown to close the pre-manufactured holes.

This procedure was necessary as tests to emplace directly the wet bentonite paste in the bore holes of the compacted bentonite ring induced a strong swelling pressure (Figure 2.18) with crack formation proliferating over a period of 25-60 min finally resulting in a disintegration of the bentonite ring. Due to the failure of the bentonite ring this preparation route was not continued and the alternative using glass ampules discussed and tested.

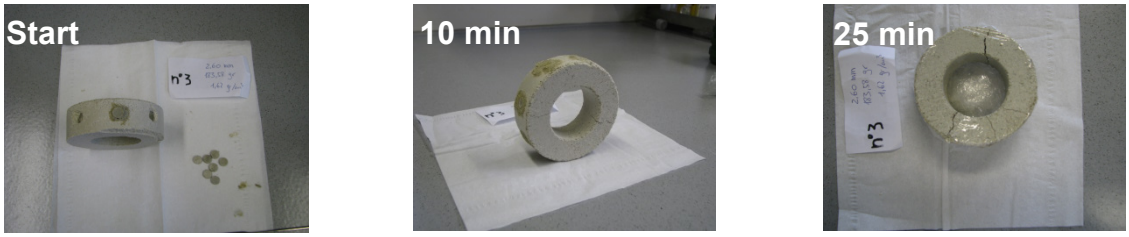

Figure 2.18: From left to right photo documentation of the direct emplacement of the bentonite slurry in ring #3 provided by CIEMAT. After 10 min contact time the first cracks due to the bentonite swelling pressure and the difference in water content were visible and after 25 min the bentonite ring disintegrated.

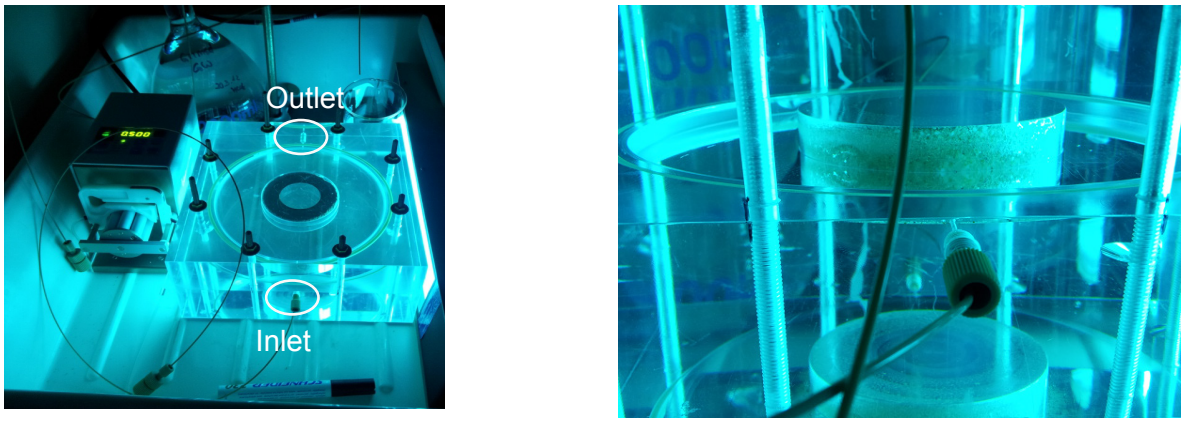

Figure 2.19: **(**left) Plexiglass experimental setup connected to a peristaltic pump delivering a constant Grimsel groundwater (GGW) flow of ~50 µL/min through the parallel plate model with 1 mm aperture. The bentonite ring with height 25 mm is confined through the plexiglas block and the inner part filled with a plexiglas rod. (right) Side view of the bentonite ring with the premanifactured holes emplaced with glass ampules covered with a bentonite pellet. Saturation starts from the direct contact to the water saturated artificial fracture.

Labeled bentonite in glass vials were prepared by inserting 300 mg paste (V/m = 1 ml/g) of synthetic Ni-montmorillonite provided by the group of Jocelyne Brendlé (University of Mulhouse), for details see [57]. Each bentonite paste containing vial was furthermore labeled with 10 mg Na-Fluorescein and 250 µg/L Eu, Tb, Hf and Th. To ease the breaking of the glass vials predetermined breaking points were engraved as lines.

The experimental set-up consists of two Plexiglas halves assembled to give a parallel plate system with 1mm aperture in the cylindrical form of 187 mm (Figure 2.19). A peristaltic pump is connected via Peek tubing to the Plexiglas block delivering a constant Grimsel groundwa-

ter (GGW) flow of ~50 µL/min through the parallel plate model. The bentonite ring with height 25mm is confined through the Plexiglas block and the inner cavity of the bentonite ring filled with a Plexiglas rod.

Analytical Methods. The colloid concentration and number-weighted average colloid diameter is determined with a Laser-induced Breakdown Detection (LIBD) system [109]. The sample solution is pumped through a silica flow-through cell. A dielectric breakdown is produced in the focus region of a pulsed laser beam (Nd: YAG-laser, Frequency: 15 Hz, Wavelength: 532 nm). The plasma generated by the breakdown event is monitored by a CCD-camera attached to an image-processing system. For details on the s-curve LIBD system it is referred to [69]. Both systems are calibrated with polystyrene reference particles.

Sample aliquots are taken to quantify the bentonite colloid concentration via ICP-MS Al-signal measurement. Additionally pH, Eh and temperature are measured to monitor changes in the electrolyte solutions. Na-Fluorescein measurements were performed using an Amico-Bowman Series 2 Spectrofluorometer (AB2).

Results and discussion

The time dependent swelling of the bentonite ring into the 1mm aperture in the Plexiglas experimental setup with the Febex bentonite ring (images taken under black-light, experiment MT4) is documented by digital imaging, see exemplarily Figure 2.20. In the upper image the bentonite ring is shown shortly after saturation of the 1mm aperture with GGW. In the lower left image the same bentonite ring is shown after eight months contact time in GGW showing the gel layer formation and swelling distance into the 1mm aperture. Even after eight months the location of the glass vials can be seen by an impression in the outer boundary of the gel layer (Figure 2.20).

The timely evolution of the swelling front into the aperture is shown exemplarily for one short-term experiment of 14 days (MT2) and one long-term experiment over a period of eight months (MT4). As can be clearly observed from Figure 2.21 the swelling starts after approximately one day and the radius of the bentonite ring increases from 4.1 cm by 1.9 - 2.4 cm to reach a maximum radius around 6 - 6.5 cm which corresponds to ~ 59% increase. The expansion of the compacted bentonite levels off after approximately ten days and remains constant over the experimental run time of max. 240 days.

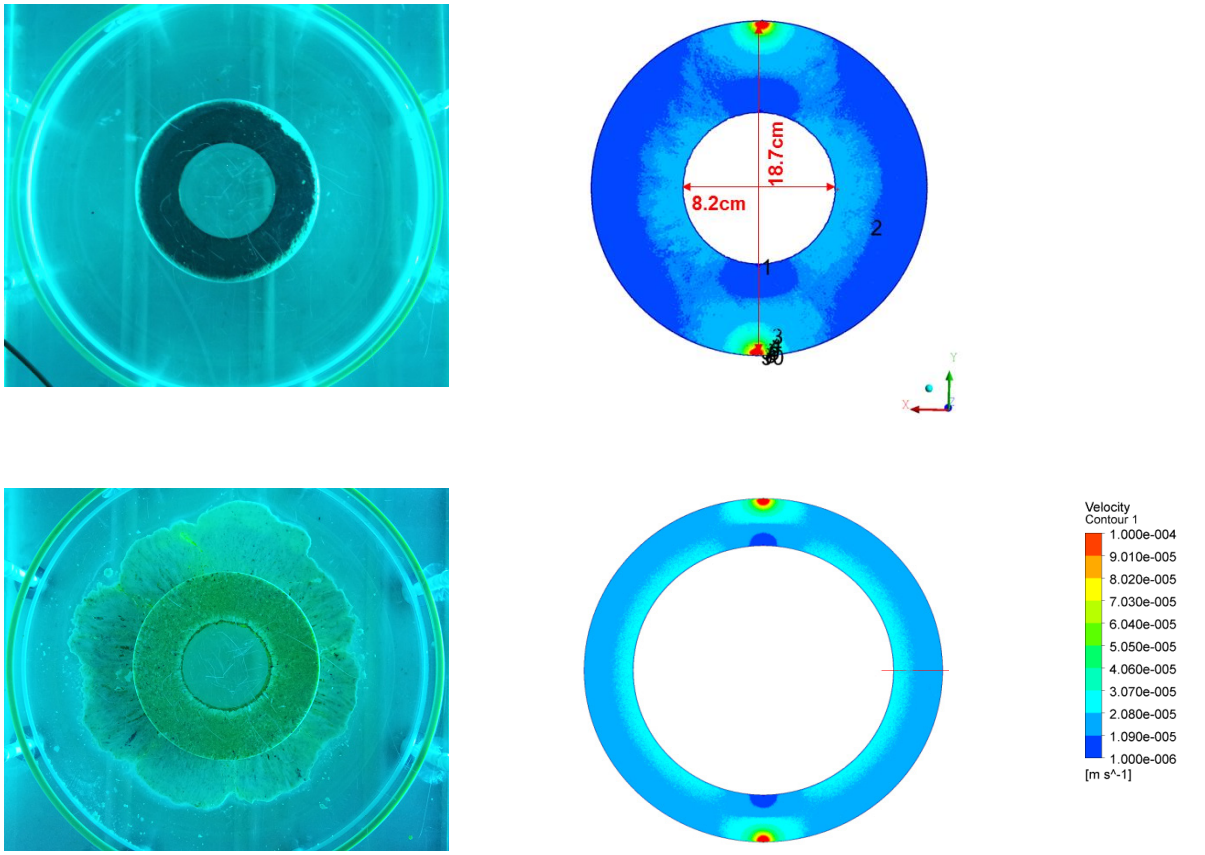

Figure 2.20: (left side) Plexiglas experimental setup with bentonite ring (images taken under black-light, experiment MT4). (Upper left) Bentonite ring shown shortly after saturation of the 1mm aperture with GGW. (Lower left) Bentonite ring shown after eight months contact time in GGW with the gel layer formed and swelling distance into the 1mm aperture. Green fluorescence indicated the release of Na-fluorescein from the crushed glass ampules (Upper right) Flow velocity distribution at the start of the experiment with a velocity range from $8 \cdot 10^{-6}$ m·s^{-1} to $1.8 \cdot 10^{-5}$ m·s^{-1}. (Lower right) Flow velocity distribution at the end of the experiment with a velocity range from $1.8 \cdot 10^{-5}$ m·s^{-1} to $2.3 \cdot 10^{-5}$ m·s^{-1}. The red line shows the cross section area taken for the velocity range given.

Based on the experimental set-up the constant flow rate of 50 µL/min adjusted by the peristaltic pump and the swelling of the bentonite source into the 1mm fracture the flow cross-section is changing in the course of the experiment. This geometry changes have been implemented in a simplified 3D computational fluid dynamics (CFD) model using Ansys Fluent [133] by simply changing the inner diameter of the model. The results show in the beginning of the experiment a velocity range from $8 \cdot 10^{-6}$ m/s to $1.8 \cdot 10^{-5}$ m/s with the higher fluid velocities occurring at the bentonite surface. At the end of the bentonite expansion phase a fluid velocity range from $1.8 \cdot 10^{-5}$ m/s to $2.3 \cdot 10^{-5}$ m/s is calculated again with a approximately 28% higher velocity at the interface to the bentonite ring.

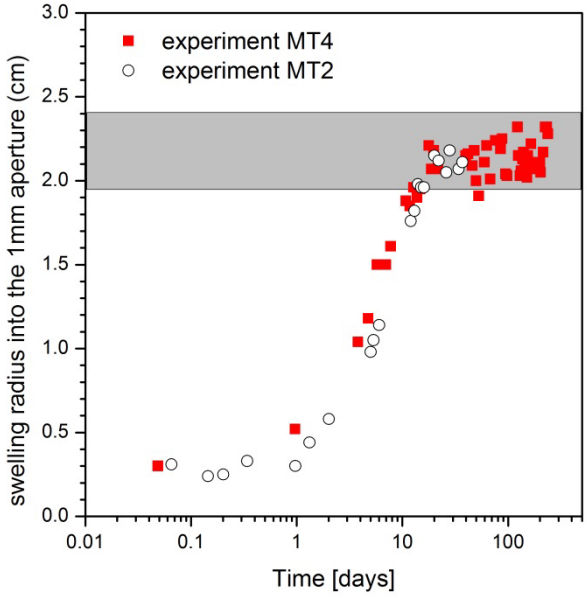

Figure 2.21: Time dependent Febex bentonite swelling/expansion into the 1mm aperture (parallel plate).

The colloid concentration released during the experiment was continuously monitored using (a) the optical LIBD system [109] and (b) the s-curve LIBD [70, 134]. In the initial swelling phase < 10 days a pronounced increase of colloid concentration was detected (see Figure 2.22) with a maximum of ~80 mg/L which declines to concentrations around 0.1 - 1 mg/L after ~10 days (when expansion maximum is reached). The colloid release remains constant until approx. 70 days contact time before the release rate continuously increases to concentration ranges of ~4 mg/L (optical detection, MOB1) and 6 – 15 mg/L (s-curve LIBD) reached after 120 days. Afterwards, the colloid release rate remains again constant until the termination of the experiment. The s-curve LIBD size distribution analysis (Figure 2.22) shows a release of a bimodal size distribution with one colloidal fraction in the size range 150 - 500 nm (yellow, dark yellow) and the other size fraction < 45nm (green, red, gray), the latter representing approximately 1 mg/L. The lower concentration range calculated based on the average colloid size detected by the optical LIBD system (ø 113 ± 22 nm in the time interval 120 to 200 days) indicates that mass calculations using the average colloid size and number concentration tend to underestimate the colloid mass at least in the bimodal size distribution found in the erosion experiments documented here. This is furthermore evidenced in samples measured by s-curve LIBD showing the absence of the larger size fraction (150-500nm) where very similar concentrations to the optical LIBD can be observed (Figure 2.22). From these laboratory experiments under Grimsel groundwater conditions based on the colloid concentration detected by LIBD after >120 days a bentonite mass loss of ~100 – 400 mg/a can be estimated, which is 0.5 – 2.2‰ per year of the total bentonite mass emplaced. This would lead to a complete bentonite ring erosion within a time frame of 460 to 1850 years.

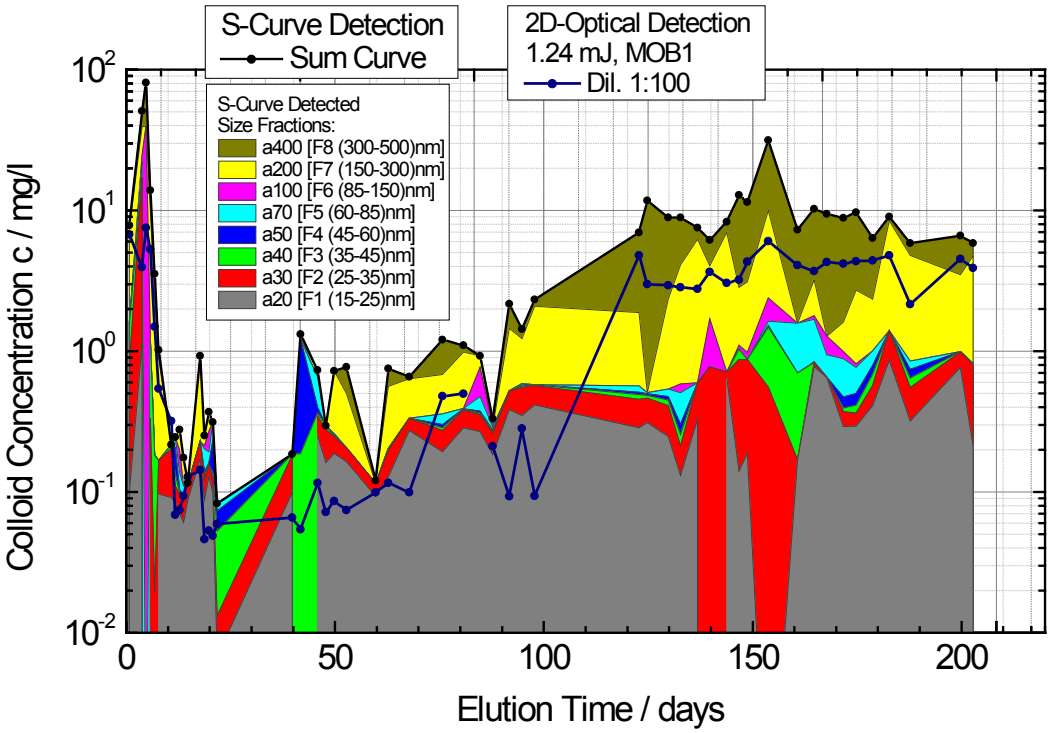

Figure 2.22: Time dependent colloid concentration measured by the acoustic LIBD (MOB1) and the s-curve LIBD released from the compacted Febex bentonite into the 1mm aperture under GGW conditions and a constant flow rate of 50µL/min.

Beside the colloid concentration also the water chemistry was monitored during the erosion experiments focusing on changes of the major cations/anions, but also to analyze the potential release of labeled Ni-montmorillonite, initial colloid associated trivalent and tetravalent elements as well as the conservative tracer Na-fluorescein.

It can clearly be seen from the fluorescence data given in Figure 2.23 that with the end of the bentonite swelling (indicated by an arrow) into the artificial fracture after approx. 15-20 days the fluorescence signal can be detected indicating a failure/cracking of the glass ampules. The fluorescence signal increases sharply to a plateau value after 20 days and remains at a median value of ~400 µg/L over the experimental duration. Taking the average flow rate of 45.82 µL·min^{-1} and the experimental duration of 237.75 days (total volume passed the bentonite ring of 15.69L GGW) a total released Na-fluorescein mass of 6.5 mg can be estimated which is ~8% of the total mass in the system.

Looking in detail to the concentration evolution of the anions chloride and sulfate a strong increase of the chloride signal can be detected which levels of and reaches background GGW values after approximately four months. Calculating the released chloride concentration as an integration of the peak observed leads to an estimated inventory of 62-69 mmol/kg bentonite which is considerably higher than the chloride inventory published by [135] of ~22 mmol/kg. The reasoning for the observed increase in sulfate concentration is the dissolution of accessory minerals as soluble sulphates (gypsum) and low soluble sulphates (barite, cel-

estite) present in the Febex bentonite with 0.14 ± 0.01 wt.% and 0.02 wt.% [135], respectively. However, the released sulfate concentration in experiment MT4 (Figure 2.23) taking into

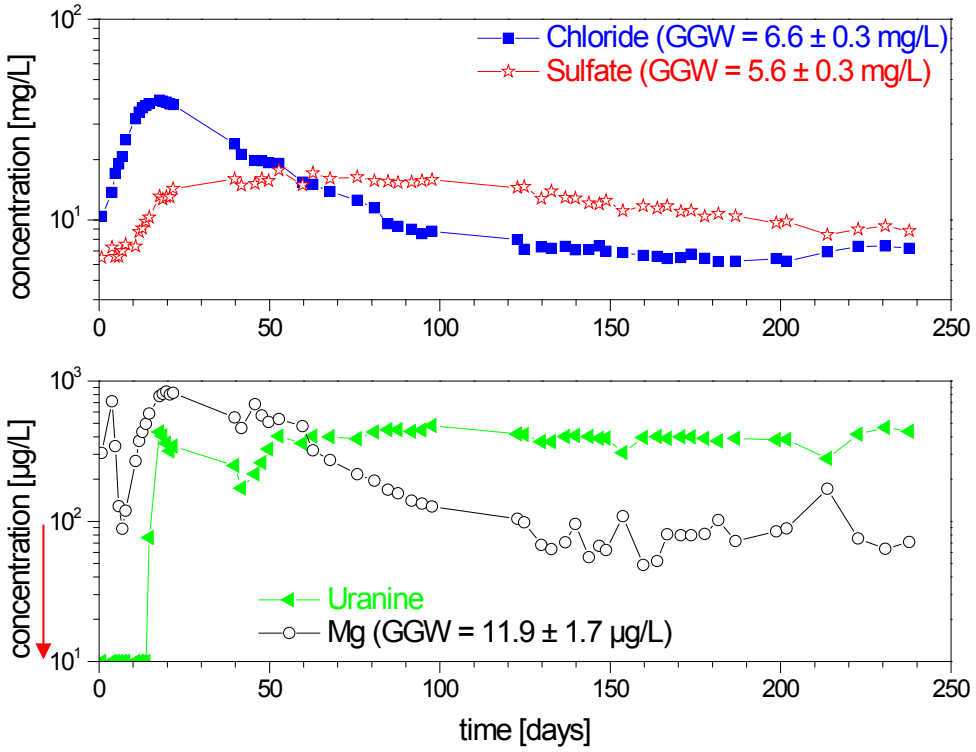

Figure 2.23: Time dependent concentration changes of selected anions (upper graph) and Mg as well as the conservative tracer Na-fluorescein (uranine).

account the GGW background concentration sums up to a total mass of ~4.1g sulfate resulting in a approximately ten times higher sulphate mineral inventory than expected based on literature data [135]. Beside the increase of the calcium concentration also the strontium concentration rises from 145-150 µg/L to values around 180-185 µg/L giving a hint to celestite dissolution (data not shown).

Based on the detected LIBD colloid concentration of approx. 10 mg/L having in mind 6 wt.% Ni in the synthetic montmorillonite structure [57] a maximum Ni concentration of 0.6 mg/L assuming pure Ni-montmorillonite release could be expected. The data measured for Ni in the eluat are within 2.5 ± 0.7 µg/L with one outlier of 76 µg/L. The results show that only a small portion of the released bentonite colloids originate from the glass ampules (Ni-montmorillonite). Having in mind 2 ng/mg Ni-montmorillonite colloid associated tri- and tetravalent elements (Eu, Tb, Hf and Th) and the max. concentration of 76 µg/L Ni-montmorillonite found this gives a max. expected concentration of the AN(III/IV) of 0.1-0.2 ng/L (0.1-0.2 ppt), which is clearly an analytical challenge and could not be detected in the course of this experiment using stable isotopes.

Conclusions

- These mock-up tests are performed to optimize the final design of the CFM long-term in situ study and show the general feasibility.

- Both, mechanical erosion due to the swelling into the artificial 1 mm fracture as well as chemical erosion evidenced by chemical long-term changes in contact water composition (chloride, sulfate) have been observed. The swelling pressure is sufficient to break the glass ampules filled with labeled synthetic Ni-montmorillonite, Na fluorescein and the sorbed tri- and tetravalent elements Tb, Eu, Hf and Th.

- Eroded bentonite concentrations determined under the adjusted flow velocity for the CFM experiment of 1.8 - $2.3 \cdot 10^{-5}$ m/s reach 6 – 15 mg/L with a bimodal size distribution of < 45 nm colloids and colloids in the size range of 150-500 nm.

- Concerning the labeling with glass ampules the contact area and released proportion of total colloid mass has to be taken into account concerning the detection limits of the analytics. Radioisotopes and pre-concentration methods (exchange resins in collaboration with Helsinki University) are currently tested in the laboratory for the CFM long-term in situ study.

2.1.4 Colloid – Mineral surface interactions (microscopic approach)

Abstract. Understanding the colloidal particle deposition mechanism at fluid-solid interfaces is important to address a variety of environmental and industrial processes. Colloids are ubiquitous in the subsurface environment (organics, inorganics, bacteria etc.) or in the context of hazardous waste disposal, colloids are generated when the groundwater is in contact with the geo-engineered barrier (bentonite clay). The colloids (or nanoparticles) characterized by their high surface to volume ratio, on which contaminants may be sorbed and subjected to the stability, these contaminant-sorbed-colloids can be transported to longer distances via micron-scaled-fractures to contaminate the nearby aquifers. During the migration of the colloids, they interact with the immobile rock and mineral surfaces. In general, most of the minerals and colloids in nature are negatively charged (unfavorable conditions). Under these conditions, the prediction of colloid retention efficiency unveils a larger deviation from experimental to theoretical models (colloid filtration theory) due to the non-inclusion of physical and chemical charge heterogeneity into predictive calculations. The current study emphasis the importance of surface heterogeneity and its role to retain colloidal particles onto surfaces under unfavorable conditions using vertical scanning interferometry (VSI) and atomic force microscopy (AFM) techniques. Since it is difficult to rationalize the impact of surface roughness to charge heterogeneity initial experimental studies were performed with silicon wafer substrates with varying roughness followed by rough host rock – granodiorite.

Materials & Methods

Characterization of Colloids. For colloid deposition experiments with silicon wafer substrates, carboxylate polystyrene latex colloids of size 0.3, 0.43, 1, 2 µm were purchased from Postnova Analytics (Landsberg, Germany). Zeta potentials and photon correlation spectroscopy (PCS) measurements of the colloids were obtained with a ZetaPlus (Zeta Potential Analyzer, Brookhaven Instruments Corporation, USA). The Smoluchowski equation was applied to convert electrophoretic mobility measurements of the colloids to zeta potentials[136]. The ζ potential measurements were performed at pH 5.5 in 10^{-2} M NaCl. The respective zeta potential values for 0.3, 0.43, 1, 2 µm were -52, -63, -45, -47 mV. The constant average diameters for the polydisperse colloid mixture(s) from the PCS measurements show that suspensions are stable for the duration of the experiments. For deposition experiments with granodiorite surface, colloids of 1 µm were used. The colloid concentration was adjusted to 48 x 10^6 particles/mL. The zeta- potential measurements (-32.4 ± 2 mV without Eu(III) addition, -26.6 ± 3 mV at 10^{-7} M Eu(III), -20.5 ± 2 mV at 5x10^{-7} M Eu(III), -15.8 ± 3.1 mV at 10^{-6} M Eu(III)) implicate negative charge at pH = 5 in 10^{-3} M NaCl for all conditions. Simultaneous PCS measurements showed that the colloids were stable over the designed experimental time of 60 min.

Surface topography analysis and quantification of colloidal deposition. Silicon wafers with (100) orientation were purchased from AMO GmbH, Aachen, Germany Figure 2.24.

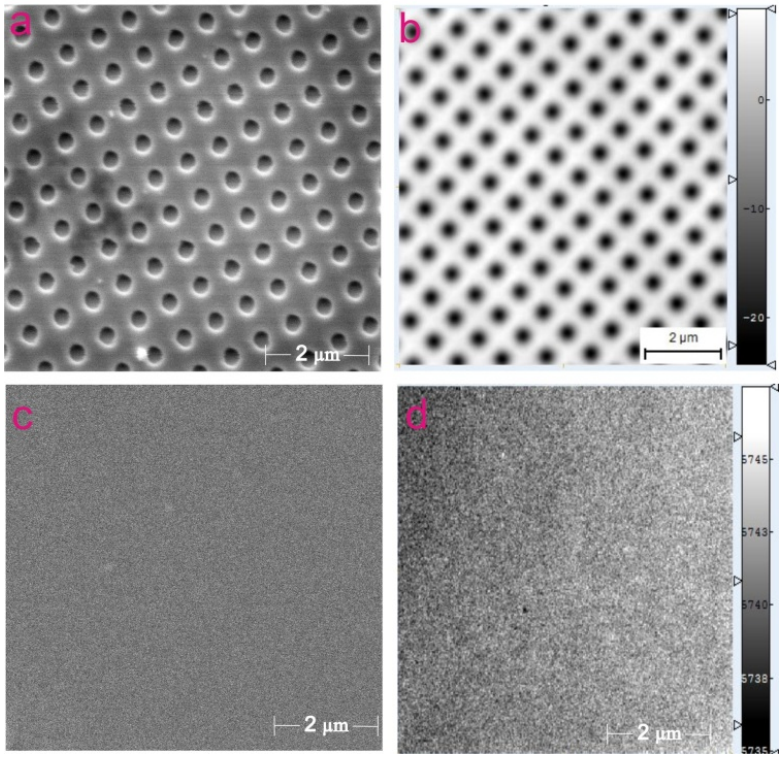

Figure 2.24: Rough and smooth silicon wafer surface data from SEM and Vertical Scanning Interferometry. a:rough SEM, b: rough VSI, c: smooth SEM, d: smooth VSI.

The silicon topography for the rough substrate consists of a regular pit pattern (pit diameter=400 nm, pit spacing=400 nm, pit depth=100 nm) and the smooth substrate was without holes. Wafers were cleaned by consecutive sonication in acetone and isopropanol followed by piranha acid. After a thorough rinsing in water, before the wafers were used as substrates for colloid deposition experiments they were left in air for complete oxidation for 5 to 7 days. For surface functionalization with APTES (Aldrich, USA), the substrates were cleaned with piranha acid and rinsed with water. Subsequently, they were dried under a flow of pure nitrogen. The dry substrates were then immersed in a 10% APTES in methanol solution for 60 min followed by thorough rinsing in methanol and again dried under flow of nitrogen [137]. A thickness of ~0.9 nm and ~0.6 nm for SiO_2 and APTES layers was measured using XPS. Mg K_α (1253.6 eV) x-ray excitation was applied, the angle (electron analyzer - surface normal) was 20°, the solid angle of analyzer acceptance ±2°, analysis area 2 mm of diameter. The SiO_2 film thickness was calculated from the elemental Si 2p line intensities assigned to SiO_2 and Si^0 after Shirley background subtraction. These values were in agreement with that reported in literature [137, 138]. Typical dimensions of each silicon sample were 4 mm x 4 mm x 0.68 mm. AFM force volume measurements performed (Bruker Dimension 3100 atomic force microscope, equipped with a nanoscope IV controller) reveal the uniform surface charge distribution without any heterogeneity (Figure 2.25).

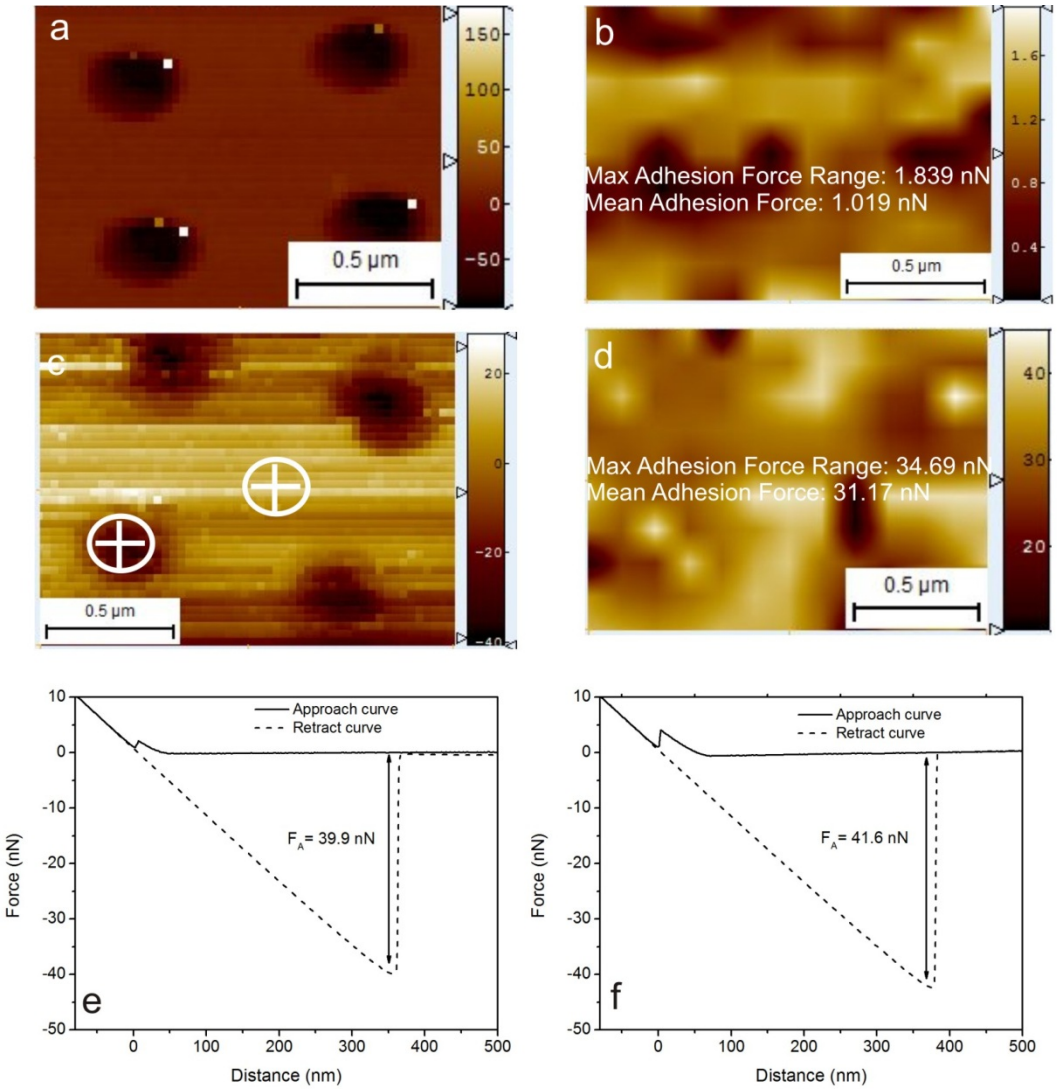

Figure 2.25: a: Topography image obtained during force-volume measurements on the silicon wafer obtained using a silica tip, b: represents corresponding maximum adhesion force mapping for silica tip, c: Topography image obtained during force-volume measurements on the silicon wafer obtained using a 1 µm polystyrene colloid, d: represents corresponding maximum adhesion force mapping for 1 µm colloid, e & f: force-distance curves inside hole and on the flat surface (marked with circle in figure c).

The characterization and quantification of surface topography of collector surfaces was carried out with a ZeMapper vertical scanning interferometry (VSI), manufactured by Zemetrics Inc., Tucson, AZ. Vertical resolution of the instrument was < 1 nm [139]. Test measurements using a calibration sample showed that objects of a lateral dimension of at least 0.15 µm are detectable on the here applied surface structure at highest magnification (100x1.6, field of view 93 µm x 93 µm, virtual pixel length 45 nm). White light mode was implemented for all measurements. Three-dimensional datasets obtained by VSI were applied for detailed particle deposition characterization and quantification using Scanning Probe Image Processing (SPIP) software by Image Metrology. For natural quartz surfaces, the approach of converged roughness parameters [140] was applied for the comparison of roughness differences.

The root-mean-square roughness (*Rq*) was employed to describe the surface roughness of the substrate. *Rq* is an amplitude parameter and is used to describe the dispersion of the height distribution (Equation 6). It is the sample standard deviation and describes the deviation of measured surface sites from the mean or another reference surface, for example, a "zero" (unreacted) plane. For calculation of *Rq* the surface is considered as a set of *N* profiles. Each profile has a number of M points.

$$Rq = \sqrt{\frac{1}{MN}\sum_{k=0}^{M-1}\sum_{i=0}^{N-1}[z(x_{k,}y_i)]^2} \qquad \text{(Equation 6)}$$

The parameter *R10* is the average height of the five highest local maximums plus the average height of the five lowest local minimums (Equation 7):

$$R10 = \frac{\sum_{i=1}^{5}|z_{pi}| + \sum_{i=1}^{5}|z_{vi}|}{5} \qquad \text{(Equation 7)}$$

The parameter *F* expresses the ratio between the measured surface area, F_m, and the area of the flat xy plane, which is the sampling area and is given as (Equation 8)

$$F = \frac{F_m}{F_0} \qquad \text{(Equation 8)}$$

For a totally flat surface, the total and geometrical surface area and the sampling area are the same (*F*=1).

The parameter *Rt* is the height difference between the highest and lowest pixel in the image (Equation 9).

$$Rt = z_{max} - z_{min} \qquad \text{(Equation 9)}$$

For the current approach, as surfaces with defined topography were applied, *Rq* is the characteristic representation factor for sum of size, depth and distance between pits.

The colloid deposition flux, *J ((*Equation 10*)* and colloid deposition efficiency, was determined from the (Equation 7) [141].

$$J = \frac{\left({}^{N}/_{A}\right)}{T * C_0} \qquad \text{(Equation 10)}$$

Where *N* is the number of colloids; *A* is the scan area; *T* is time in seconds; C_0 is initial colloid concentration.

For granodiorite, finding the optimal representative scan area (or length (*L*), since the considered area is always a square) for particle quantification is essential especially on rough surfaces. The analysis of "*L*" is performed using the approach of *converged* roughness parameters. Surface maps from VSI data showed constant values for the number of particles adsorbed normalized to the scan area (for 60 min reaction time) and the root mean square roughness (*Rq*) values for higher scan-areas (Figure 2.26). For smaller surface sections, larger deviations were observed between the colloidal deposition flux and roughness values. However, a scan area of ~90,000 µm^2 (L = 300 µm) was considered to provide reproducible results for deposition analysis. Hence, all the data for particle quantification was obtained at L = 300 µm.

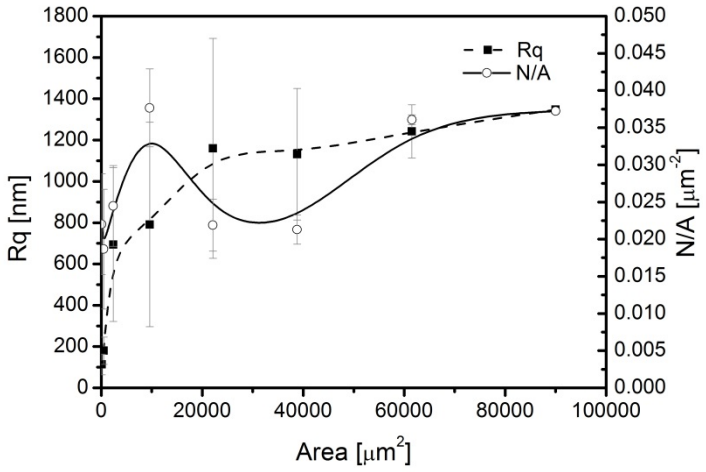

Figure 2.26: Average RMS roughness (Rq) and number of particles adsorbed normalized over scan area (N/A) are shown as a function of scan size area.

Using SPIP software, the VSI data sets are processed for optimized plane correction followed by application of a "particle analysis tool (within the software)" to quantify colloid concentrations. The kinetics of colloid deposition were determined by calculating the dimensionless Sherwood number [142] ((Equation 11):

$$Sh = \frac{Ja_p}{C_0 D_\infty} \qquad \text{(Equation 11)}$$

where a_p is the radius of the particle, C_0 is the bulk colloidal concentration, D_∞ is the bulk diffusion coefficient, and J is deposition flux ((Equation 12):

$$J = \frac{N}{TA} \qquad \text{(Equation 12)}$$

where N represents number of deposited colloids, T is time in sec, and A is area under consideration.

Deposition experiments. All the experiments were performed at room temperature (~22 ^oC) and at pH~5. The specific conductivity of the water was 0.054 µS/cm. The colloidal deposition experiments on silicon substrates were conducted in a rectangular parallel-plate channel fluid cell made of Teflon (Figure 2.27). The inner dimensions of the cell were 60 mm x 10 mm x 3.4 mm. The substrate was oriented parallel to the flow direction. After use, the particle suspension was discarded. For comparison and in order to quantify the influence of half pores on the substrate surface, the colloid deposition experiments were conducted for both plane and rough substrates.

For deposition experiments on granodiorite, a stock solution of Eu(III) (ICP standard) and the remaining chemicals (NaCl, NaOH, CH_3COOH) were purchased from Merck, Germany and used without further purification steps. Speciation predominance diagrams for varying Eu concentrations (at atmospheric CO_2 conditions, $pCO_2=10^{-3.5}$) were calculated using Medusa software developed by Puigdomenech [143]. Based on these results, Eu exists in its ionic form as Eu(III) below pH 5.6 and at high pH (>6) Eu precipitates as carbonate. Hence, all adsorption experiments were maintained at pH of 5 using acetic acid. Adding acetic acid to the suspension does not affect the sorption behavior of Eu.[144, 145] The amount of of Eu(III) sorbed onto colloids and granodiorite was obtained through ICP-MS. At 10^{-6} M, 10% and 13% of total Eu(III) was sorbed onto the colloids and to the granodiorite sample.

The sorption experiments were conducted in a circular, open-channel fluid cell made of Teflon. The inner diameter of the cell was 30 mm and the height was 12 mm. Reaction time was 60 min. The mineral surfaces were oriented parallel to the flow direction. After use, the particle suspension was discarded. The volumetric flow rate in the cell was 0.02 mL/min with an average flow velocity of 4.7 x 10^{-7} m/sec. The Reynolds (Re=0.014) and Peclet numbers (Pe=0.000032) indicate that the flow is laminar and diffusion dominated.

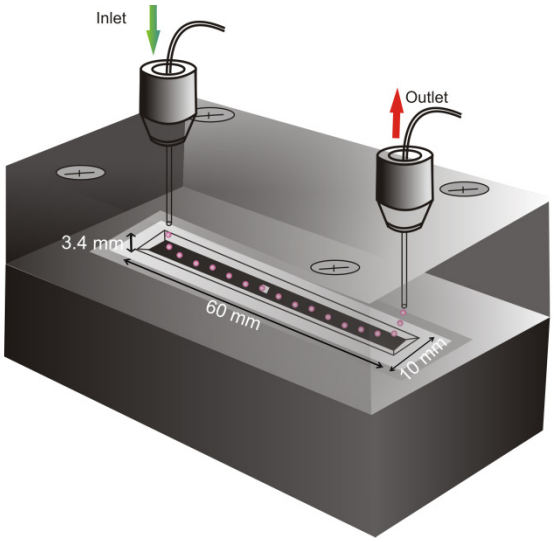

Figure 2.27: Schematic diagram of the flow cell.

Granodiorite sample preparation and characterization. The granodiorite is from GTS, Grimsel, Switzerland. Granodiorite samples were equilibrated with 10^{-3} M NaCl at pH 5 in the flow through cell until constant pH outflow conditions were established, usually taking 2 hours. The granodiorite is composed of quartz (15%), plagioclase (28%), K-feldspar (7%), biotite (41%), Muscovite (4%) and Clay minerals (0-1%) by volume [146, 147]. Samples of approx. 1 x 1 x 0.4 cm^3 were used for the experiments. The mineral samples were polished with SiC powder (Theodor Erich, Hamburg, Germany) (29.2 ± 1.5 µm) followed by Diamond powder (Struers, Willich, Germany) (6.5 ± 1 µm). Again, VSI was applied for both the characterization of surface topography and the quantification of colloid deposition. The ζ of granodiorite surface was determined by streaming potential measurements using a SurPASS apparatus with gap cell at ionic strength of 10^{-3} M NaCl solution at pH 5.The polished samples were used for sorption and as well as for streaming potential studies.

Surface topography and porosity analysis of granodiorite. Again, VSI Rock surface topography was quantified using vertical scanning interferometry (VSI) [148]. Vertical resolution of surface maps is about 1 nm. Except for the detailed height profile variation to study site-specific retention of colloids (see discussion) where blue light (phase shift mode of VSI) was used for scanning to reduce the noise and improve vertical resolution down to < 1 nm, white light mode was applied for all the measurements. The obtained data sets were applied for detailed mineral/rock surface analysis topography characterization using Scanning Probe Image Processing (SPIP) software by Image Metrology. For colloid number quantification, data sets obtained with the 50x objective (L = 300 µm) were used. The surface roughness parameters *Rq, Rt, R10, F* were calculated for quantitative characterization of surface topography. The concept of *converged* surface roughness parameters was applied [140]. It is referred to the SI for details on the calculation of surface roughness and topography analysis. The granodiorite surface porosity refers to the portion of volume below the mean surface height and is obtained from the height profile histogram.

Granodiorite surface topography, roughness, and porosity. The granodiorite surface roughness and topography were analyzed using the approach of *converged* roughness parameters (see also previous section) [140, 148]. For this purpose, the surface was scanned across various scan lengths, L (1490, 749, 300, 200, 100, 50, 25 µm). Respective calculated roughness results, *Rq,* were plotted against *L* (Figure 2.28). For every scan length, roughness data from 50 subsets were calculated. Based on this analysis as well as on petrographic results, it was found that the surfaces can be characterized by four types of topographies (Figure 2.28, upper section) where surface roughness *Rq* ranges over one order of magnitude:

(1) smooth surface, of large single crystals (mainly feldspar with flat intragranular pores, minor quartz single crystals),

(2) a mixture of portions of the smooth surface of large crystals (type 1) plus smaller adjacent crystals (mainly feldspar and quartz) as well as respective intergranular pores,

(3) surface topography of small crystals (mainly quartz and feldspar) and intergranular pores of size range similar to crystal size,

(4) surface topography of mainly sheet silicate aggregates, some small feldspar and quartz crystals, as well as half-pores with depth 5 – 8 µm.

Overall, *Rq* at L = 300 µm for granodiorite surface samples shows a broad range with mean *Rq* = 1100 ± 300 nm (Table 2.6). This is much higher than the surface roughness of single mineral grains of granodiorite (*Rq* < 500 nm) and underlines the major impact of intergranular pores on the resulting high surface roughness of granodiorite.

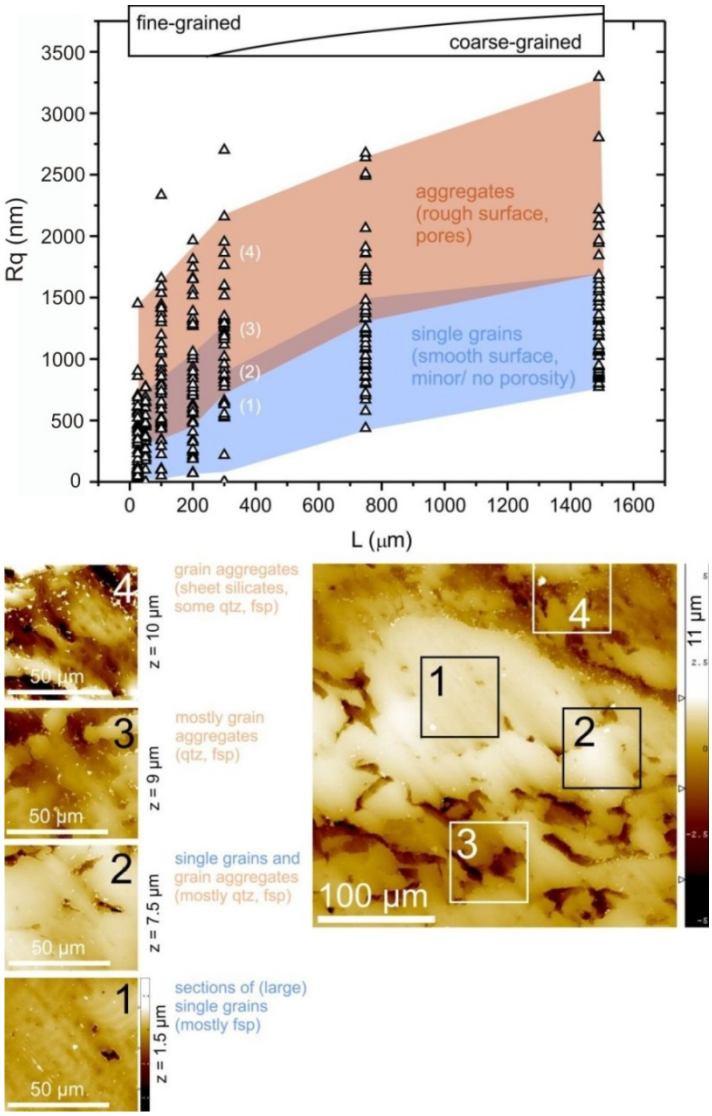

Figure 2.28: Root-mean-square roughness (Rq) as a function of field-of-view length (L) of granodiorite sample and classification into four types (1-4) of distinct topographies, red-colored text indicates rough surfaces portions, blue-colored text indicates relatively smooth surface portions.

Table 2.6: Characterization of topography of granodiorite surface by mean roughness parameters.

	Mean Root-mean-square roughness Rq [nm]	Mean roughness depth Rt [nm]	Mean Ten-point-height R10 [nm]	Mean roughness factor F [-]	Mean half-pore volume µm^3	Mean pore diameter µm	Mean pore density µm^{-2}
Granodiorite	1100 ± 300	13400 ± 1600	13000 ± 1600	46 ± 29	16000 ± 11000	33 ± 19	0.006 ± 0.002

Results and Discussion

Colloid retention on Silicon wafer substrate

Influence of surface roughness on colloid deposition:

The data of colloid deposition flux for varying colloid diameter at constant flow velocity on silica substrate with holes (rough surface) and smooth surface under favorable (APTES coated layer) and unfavorable (SiO_2 layer) conditions are presented in Figure 2.29.

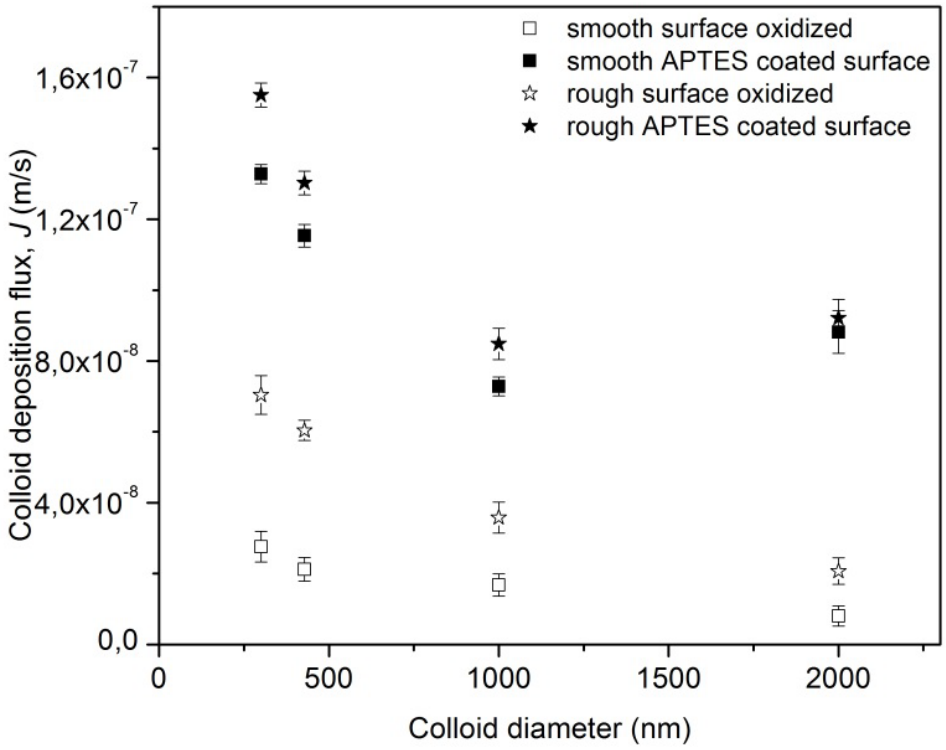

Figure 2.29: Comparison of colloid deposition flux of carboxylated latex colloids of different sizes at constant fluid velocity (1.3 x 10^{-5} m/s) for smooth and rough surfaces. The influence of surface roughness on particle retention is smaller for larger colloids and under unfavorable conditions.

Favorable conditions (APTES coated surfaces):

Regardless of particle diameter, the colloid deposition flux is always higher for an APTES coated surfaces (favorable) compared to a silicon oxide surfaces (unfavorable). For an 0.3 µm colloid it results in a ratio of ~ 4.8. This is because of the electrostatic forces of attraction between the positively charged silica surface (exposed amino groups) and the high negative surface charge of latex colloids [142]. The resulting high colloid deposition rate is attributed to an increase in range and magnitude of the attractive double layer interactions. The particle deposition in the absence of energy barrier showed initial decrement with the size followed

by increase. Moreover, in the absence of an energy barrier, for colloidal particles the gravitational force is not an important factor [149]. The observed minimum deposition flux corresponded to 1 µm colloids with a minor difference that of 2 µm. The slight increment in J for colloids with d = 2 µm vs. d = 1 µm could be attributed to the stronger electrostatic forces of attraction with size of particle [149]. The 0.3 µm colloids experienced the highest difference in J for smooth (average Rq=1.6 ± 0.3 nm) vs. rough (average Rq=18.2 ± 0.4 nm) substrate deposition and the value decreased with an increase in particle size. Thus, it can be noticed that the effect of surface roughness is more pronounced for smaller colloids compared to larger colloids. The particles beyond 1 µm did not experience any influence of surface roughness.

Unfavorable conditions:

In general, silicon substrates covered by a SiO_2 layer show a decrease of colloid deposition compared to APTES coated surfaces because of the electrical double layer repulsions. Similar to the previously reported favorable conditions, both effects were again observed: The rough surface shows generally higher deposition rates and, secondly, the deposition is more effective for smaller particles. A 2.8 and 2.73 times increased colloidal deposition for a rough vs. smooth surface was observed for 0.3 and 0.43 µm colloids. This was the highest observed ratio compared to a factor of 2.1 for 1 µm or 2.4 for 2 µm colloid. As DLVO theory predicts, the height of the energy barrier is proportional to the size of the particles approaching the interfaces. For a fixed surface potential of particles and surface, the surface potentials control the magnitude of the double-layer interaction energy and, thus, may have an effect on the particle deposition rates [149, 150]. This explains the reason for the decrease of J with increasing colloid size under unfavorable conditions.

Generally, as a particle approaches to a rough surface, the repulsive energy barrier height is reduced. This is because of the effectively larger separation distance between a spherical particle and a rough vs. smooth surface [151]. Therefore rough surfaces are more favorable for particle deposition [152, 153]. According to previous studies, the influence of roughness is important under unfavorable conditions [142, 146]. As reported in literature, the deposition under repulsive EDL is attributed to colloid association with substrate via secondary energy minima and hence CFT is not applicable [141]. It is evident that electrostatic and acid–base interactions decay more rapidly than vdW interactions and hence the surface roughness promotes colloidal adhesion irrespective of the chemical properties of substrate material [154]. We interpret therefore the difference in J found (compared to J for favorable conditions) as a combined effect of charge and roughness. Numerical simulations by Hoek et al. also indicate that for rough surfaces the interaction energy barrier height is primarily determined by the zeta potentials of the surfaces [152, 154]. The efficiency of roughness-governed particle retention seems to be at maximum in the presence of an energy barrier. Therefore we performed the below discussed systematic experimental approach by varying particle size and fluid flow velocity to predict particle retention at rough vs. smooth surface in the presence of energy barrier.

Impact of particle size variation and fluid flow velocity variation on particle retention at given rough vs. smooth surface topography:

The systematic study of colloidal particle deposition under varying flow rates at smooth vs rough SiO_2 substrates (Figure 2.30) showed independent deposition behavior with respect to substrate roughness. In the presence of energy barrier, at all fluid velocities, both smooth and rough surfaces exhibited a dependent colloid deposition behavior with a maximum deposition for 0.3 µm colloid. Moreover, independently of the applied fluid velocity the rate of deposition fluxes were high for rough vs. smooth. From smooth to rough the deposition rate for smaller colloids (0.3 and 0.43 µm) is increased by factor of approx. 2.66 compared to bigger colloids (1 and 2 µm) by factor of 1.2 to 2 times. This shows the dependency of colloid deposition on ratio between sizes of colloid to that of roughness value. As the ratio increases, the effective surface contact area with the substrate increases, therefore less effect of roughness is seen by the particle.

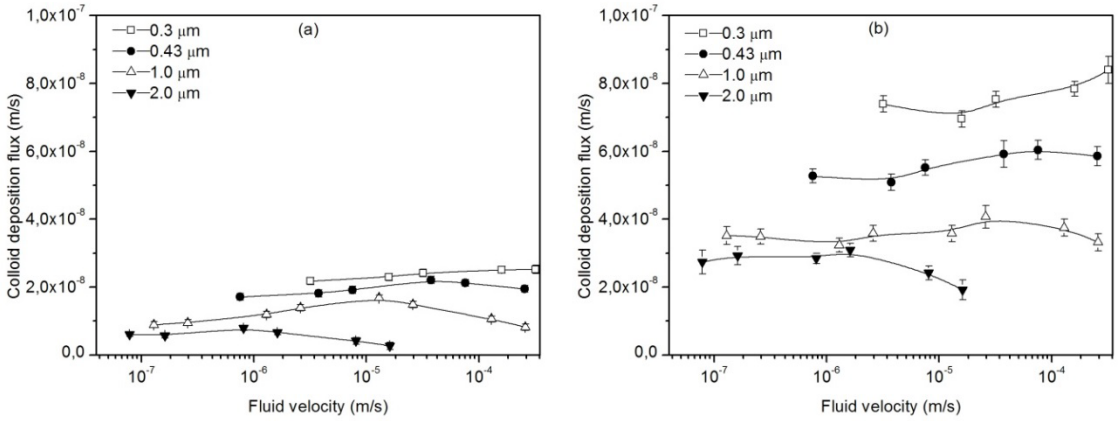

Figure 2.30: Colloid deposition flux at smooth (a) and rough (b) oxidized silicon wafer substrates. For smooth surfaces, beyond a critical velocity (for 1 µm it is 10^{-5} m/s) the rate of colloidal deposition decreased with an increase in colloid size and fluid velocity. While, under applied hydrodynamic torque at high flow velocities roughness of the substrate retains colloids onto surface (for 1 µm it is 5 x 10^{-5} m/s).

For colloids of all sizes, both kind of substrates exhibit increased colloid deposition fluxes with initial increment in the fluid velocity. For a smooth surface, beyond a critical velocity based on the size of the colloid, the detachment mechanism starts. The tendency to release or transport the larger colloids was initiated at lower velocities compared to smaller colloid fraction. The 0.3 and 0.43 µm colloids are stable to retain on surface even at high fluid velocities (<5 x 10^{-5} m/s) while 1 and 2 µm colloids can sustain up to 10^{-5} and 10^{-6} m/s. This shows that the colloids deposited in the secondary minima are subjected to remove from the surface under the influence of hydrodynamic force [141, 155, 156]. The electrostatic and vdW interactions decay with colloid-surface separation distance at distinct rates, at small separation distances (primary minimum, ~0.4 nm) vdW attraction may greatly dominate, at intermediate distances where particles tend to deposit electrostatic forces play role and at very large distances (secondary minimum, ~5-10 nm) vdW attraction may slightly dominate. Hence, col-

loids that are attached in the secondary minima are weakly associated with the solid phase. On the other hand, in case of rough substrate, under the implemented velocities, no influence of hydrodynamic torque on 0.3 and 0.43 µm was observed. Pertaining to greater restraining torque these colloids retained even at $>10^{-4}$ m/s fluid velocity. The larger colloid fraction, 1 and 2 µm colloids detached from the surface beyond 10^{-4} and 5 x 10^{-6} m/s irrespective of the influence of substrate roughness. This shows their fewer tendencies for surface roughness. Because of the maintained balance between adhesion force over applied torque, it is worth noticing that these velocities are higher at smooth surfaces. Our results are supported by the recent calculations from Shen et al.,[157] where they predicted the attachment efficiency of a colloid doesn't change until it reaches a critical velocity which is a function of ionic strength, surface properties of colloids and substrate. Also, a colloid with lower diameter attains critical velocity at higher flow conditions compared to a colloid with higher diameter.

Particle retention mechanisms:

According to fundamental studies reported in the literature [158], when a particle interacts with the substrate, different mechanisms may play a role either for attachment or detachment, such as rolling, dragging, lifting (Figure 2.31). As reported from the literature, rolling plays an important role to remove from surface under laminar flow conditions. Rolling can be initiated on any particle independent of its size even at smallest flow rates (i.e., at lowest Reynolds numbers) adopted in the current system [159]. In order that a particle to be removed from the surface, the hydrodynamic torque applied on the particle must exceed that of the adhesion torque [160]. Burdick et al. reported that the liver arm for the applied torque decreased with increasing size of surface roughness. Unlike a smooth surface, a rough surface can change the point around which the rolling occurs, hence for a rough surface a larger applied torque is required to remove a particle from the surface [161].

The hydrodynamic and adhesive forces will have a big impact on that section of the collector surface where retention occurs, and that colloids that collide with a collector may roll along the surface until they come to a region that is chemically and hydrodynamically favorable for deposition [158, 160]. In the current case, as similar chemical conditions were maintained, rolling is initiated even at low flow velocities. Retention of 0.3 µm particles that can be imbedded into holes is preferable pertaining to higher straining compared to any larger colloid sizes . With an increasing colloid size the restraining torque acting on the particles decreases. Simultaneously the fluid drag force increases which results in lower colloid retention.

The physical forces acting on the particle are dependent on the flow conditions near the particle-substrate interface. The drag force (F_D) effectively acts on the attached particles at a height of $1.4\,r_c$ ((Equation 13) [158]. An increase in particle size will result in an increasing applied torque with vertical velocity gradient on the surface of substrate and may lead to an excessive fluid drag. The larger contact area of the colloid with increasing diameter disables the effect of surface roughness. This means that the impact of surface roughness on colloidal retention is caused by the effective contact area at the interface. Under unfavorable conditions, the particles are deposited in the secondary minimum, the depth of secondary minima

increases with particle size, due to high Van der Waals forces. Simultaneous excess fluid drag (T_{app}) may lead the particle to remove from surface.

$$T_{applied} = 1.4 r_c F_D \quad \text{(Equation 13)}$$

Where the drag force F_D is given as:

$$F_D = 10.205 \pi \mu \left(\frac{\partial V}{\partial r}\right) r_c^2 \quad \text{(Equation 14)}$$

$$T_{adhesive} = F_A l_x \quad \text{(Equation 15)}$$

Where r_c radius of colloid; F_D, drag force; F_A, force of adhesion acting on a liver arm l_x (calculated according to [156]). Here l_x is radius of the colloid-surface contact area which is calculated according to the Johnson, Kendall, and Robers theory. At secondary minimum as there is no direct contact between colloid and surface, the value of l_x is given as

$$l_x = \left(\frac{F_A r_c}{4K}\right)^{1/3} \quad \text{(Equation 16)}$$

Here *(*(Equation 16*) K* is the composite Young's modulus and employed a value of *K* = 1.332 x 10^8 N m^{-2} based on the Fore-volume data collected from AFM for polystyrene colloid-silicon wafer collector in 10^{-2}M NaCl solution. This is one order of magnitude lower than the system where polystyrene colloids-glass bead collectors were considered [162].

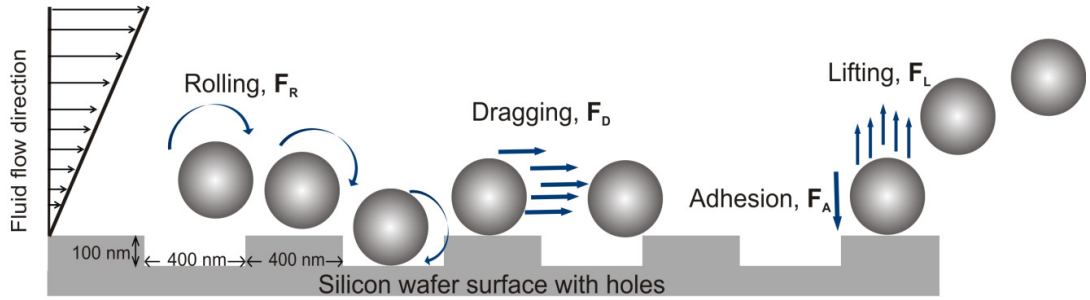

Figure 2.31: Schematic profile diagram to visualize the common forces at a fluid-solid body interface. As an example, a particle with d = 0.3 µm is shown at the structured surface applied for the study reported here.

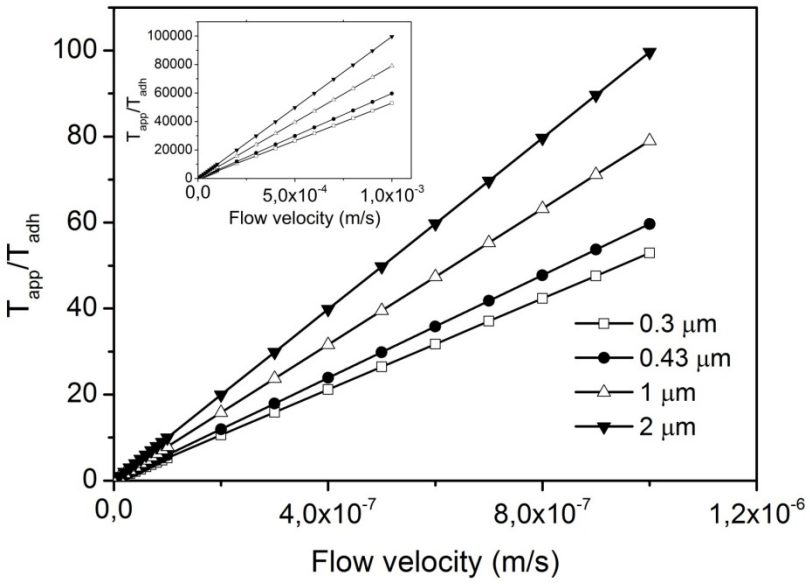

Figure 2.32: The ratio of T_{app}/T_{adh} at a smooth surface under varying flow rates for all colloid sizes applied in this study. The high probability of particle removal can be predicted when $T_{app}>>T_{adh}$.

Considering the DLVO interaction energy profile between a colloid and a plate, Gregory's superposition approximations was employed to calculate the adhesive force (F_A) that acts on attached colloids [163]. The value of F_A was estimated as Φ_{min}/h, where Φ_{min} is the absolute value of the secondary minimum interaction energy, and h is the separation distance between the colloid and the substrate. The calculation from DLVO interaction energy profile resulted in Φ_{min} of -0.54, -0.72, -1.89, -3.73 kT for the 0.3, 0.43, 1, 2 µm colloids. The obtained value was used to estimate the applied and adhesion (resisting) torque acting on colloids in the secondary minimum using equations 6 and 7. It can be interpreted from Figure 2.32 that with an increment in fluid velocity the ratio T_{app}/T_{adh} increases at a higher rate with size of particle. As the substrate employed here has constant Rq, with an increase in size of colloid the ratio Rq/r_c determines the colloid deposition efficiency. For the smaller colloid fraction (0.3 and 0.43 µm) the ratio is higher due to an effective contact area with the substrate compared to the larger colloid fraction (1 and 2 µm). It is worth noticing that, for all particles, though at lower velocities (10^{-6} to 10^{-7} m/s) higher ratios of T_{app}/T_{adh} (5 to 99) can be observed, experimentally no impact on particle deposition efficiency was observed (Figure 2.32).

Table 2.7 represents the comparison between calculated and observed fluid velocities around which the particle detachment is expected. A minimum ratio T_{app}/T_{adh} of >15900 is needed for a 0.3 µm to remove from the rough surface which is the highest observed value for the whole system. The impact of surface roughness can be directly seen by an increase of the ratio from T_{app}/T_{adh} (smooth vs rough). In perspective of flow in groundwater systems, it can be interpreted that for a colloid size fraction of ≤ 2 µm where flow velocities are ≤0.26 m/d colloid filtration is the dominant mechanism.

Table 2.7: The observed detachment velocities for all size colloids for smooth vs. rough substrates. At these velocities, the respective ratio T_{app}/T_{adh} is provided.

Diameter of colloid [µm]	Approx. detachment flow velocity for rough surface [m/s]	T_{app}/T_{adh} (rough)	Approx. detachment flow velocity for smooth surface [m/s]	T_{app}/T_{adh} (smooth)
0.3	>3 x 10^{-4} (or ~26 m/d)	15900	>10^{-4}	5290
0.43	>10^{-4} (or ~8.6 m/d)	5970	>2 x 10^{-5}	1190
1	>7 x 10^{-5} (or ~6 m/d)	5530	>10^{-5}	790
2	>3 x 10^{-6} (or ~0.26 m/d)	299	>10^{-6}	99.6

Colloid retention on Granodiorite substrate

Impact of surface roughness and Eu(III) concentration on colloid deposition efficiency

An increase in both roughness (Rq) and Eu(III) concentration increased the colloid deposition efficiency on granodiorite surface (Figure 2.33). A broad roughness range of Rq = 100-2000 nm has been investigated. Smooth mineral grains, crystal aggregates, and intergranular pore space contribute to this roughness range (see classification, Figure 2.28). In the absence of Eu(III), a Sh range of three orders of magnitude, from about 0.002 to 0.25, has been detected. A positive correlation between Sh and surface roughness Rq has been found (Figure 2.33). An increase in Sh by a factor of 2.7 from zero to 10^{-6} M Eu(III) (at Rq ~ 1100 nm) was observed (Figure 2.33a). The highest particle deposition density was detected for sections of surface type 4 (sheet silicates plus intergranular pores, Figure 2.28).

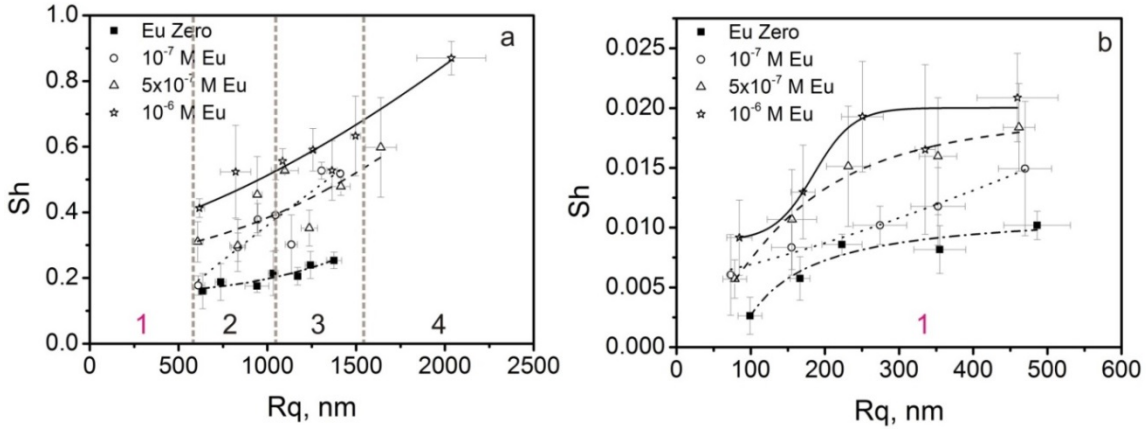

Figure 2.33: Deposition of polystyrene colloids on Grimsel Granodiorite surfaces as a function of surface roughness and Eu(III) concentration. Data in diagram (a) were collected at surfaces (300 µm x 300 µm) with roughness range of Rq = 500 to 2000 nm. Data in diagram (b) result from experiments using surface sections (50 µm x 50 µm) with remarkably lower roughness range (Rq < 500 nm). Numbers 1 to 4 represent the corresponding classification of the surface types from Figure **2.28**.

Figure 2.28 shows the inhomogeneity of surface topography of a natural rock, classified by surface types (1) to (4). For larger surface sections with only few but large variations in height, the quantitative contribution of flat surface sections to the overall surface roughness (Rq) is suppressed. To overcome this limitation of surface amplitude parameter analysis, the concept of converged roughness parameters has been applied [140]. Applying this concept and in order to get a deconvolution of scale-depending roughness contributions, we analyzed surface sections of 50 µm x 50 µm and compared it to the large sections (300 µm x 300 µm, Figure 2.33b vs. Figure 2.33a). This analysis revealed, that the overall variation of both, Rq and Sh is remarkably high. This is owing to two main contributors to surface roughness: rough surface sections with pores yielded high retention efficiency (high Sh, Figure 2.33a) and comparatively smooth surfaces with almost no pores yielded low retention efficiency (low Sh, Figure 2.33b). The total impact of Eu(III) concentration variation on particle retention at smooth surfaces is however similar to the results found for rough surfaces. For flat surfaces

(Figure 2.33b), an increase in Sh by a factor of 2.2 owing to the increase in concentration from zero to 10^{-6} M Eu(III) (at Rq ~ 450 nm, large single-crystal surface) was observed. In the absence of Eu(III), however, from L = 50 µm (at Rq = 450 nm) to L = 300 µm (at Rq = 1100 nm) an increase in Sh by a factor of ~24 was observed owing to increase in roughness (Figure 2.33b vs. Figure 2.33a). Overall, the large variation in deposition efficiency is predominantly influenced by roughness variations. At rough rock surfaces, roughness and Eu(III) concentration variations act in tandem, but the major variations in Sh are governed by topography variations.

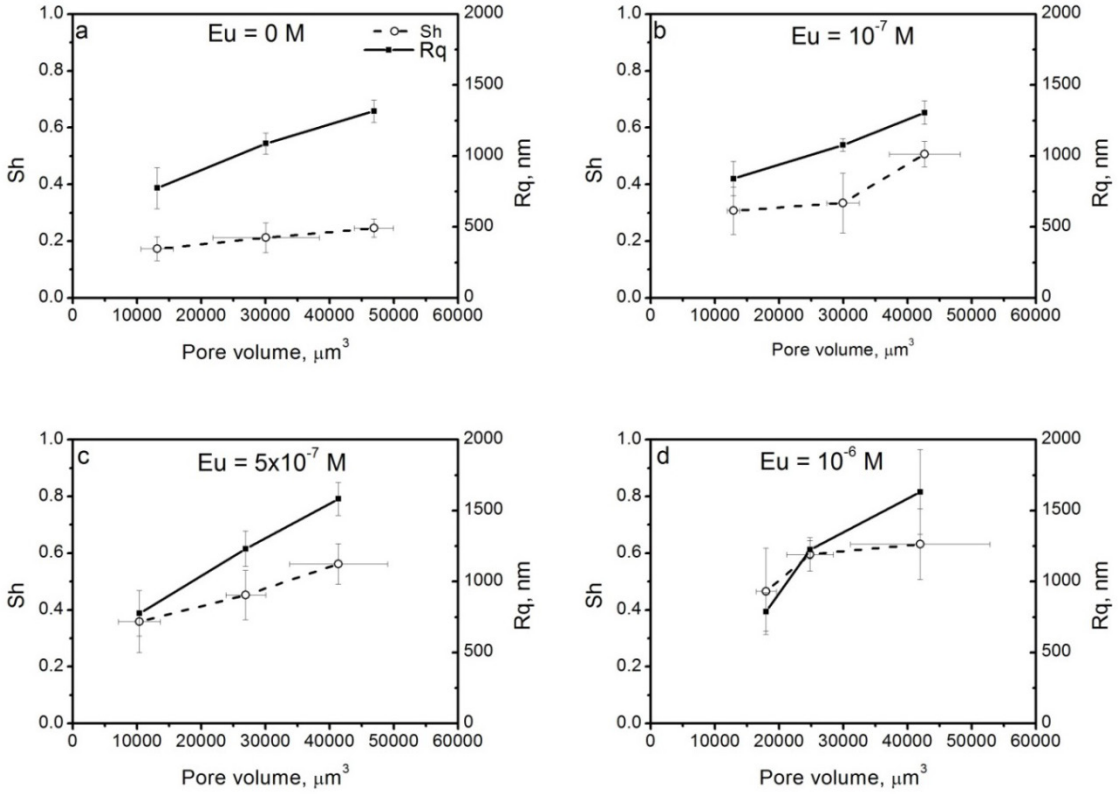

Figure 2.34: Colloid deposition flux (*Sh*) and surface roughness (*Rq*) of granodiorite collector material (size: 300 µm x 300 µm) as a function of (half-) pore volume of the surface at a) no Eu(III) b) 10^{-7} M Eu(III) c) $5x10^{-7}$ M Eu(III) d) 10^{-6} M Eu(III).

Effect of porosity on colloidal particle deposition processes

The majority of colloidal retention is influenced by surface sites at pore walls. Pores in this rock do exist in-between crystals (intergranular porosity) as well as within crystals (intragranular porosity). The impact of porosity on colloid sorption was identified by plotting *Sh* and *Rq* vs. pore volume (Figure 2.34). Here, pore volume (portion of void volume below the plane surface) is estimated from the frequency height profile histograms of the data sets obtained for each concentration of Eu(III). A clear correlation between pore volume to *Sh* and *Rq* observed in all cases suggests the colloid sorption influenced by roughness from pore space geometry of the surface. An increase in porosity results in enhancement of colloid sorption for [Eu(III)] ≤ $5x10^{-7}$ M. However, the site-specific retention of particles, identified in compari-

son of data from Figure 2.33a vs. Figure 2.33b is not visible from a simple porosity analysis. Therefore, the sole information about porosity variation is not able to predict quantitatively the overall range and spatial distribution of retention efficiency of rock surfaces.

Smooth surface vs. porous volume with rough surface sections

The observed sorption behavior of colloids on granodiorite suggests a characteristic variability in surface roughness: The tendency to sorb colloids at pore walls between grain aggregates is remarkably higher compared to smooth mineral surface sections, see Figure 2.33a (rough surface with pores) vs. Figure 2.33b (smooth surface, almost no pores). This was further investigated using porosity data and surface-specific *Sh* data, measured at surface sections with well-defined porosity. The ratio of *Sh* from pore walls to *Sh* from smooth surface portions is shown as a function of surface-normalized porosity (void volume/material volume), Figure 2.35. The data show an increase in retention efficiency as a function of porosity. This effect is more pronounced at low [Eu(III)] concentrations. At high [Eu(III)], sorption of colloids is independent of pore volume. This is due to the sorption of Eu(III) to smooth surface portions where *Shss* dominates Sh_{PV} value.

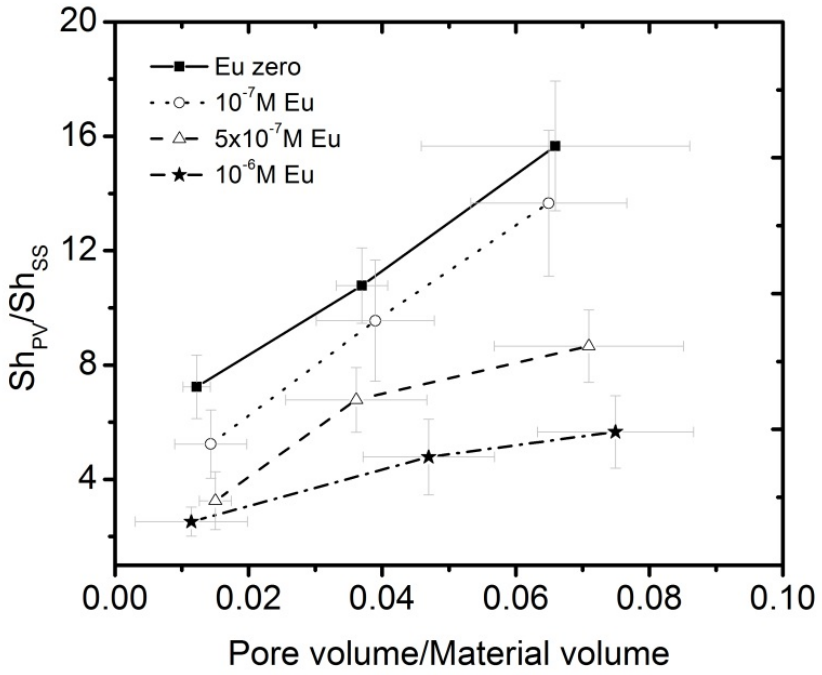

Figure 2.35: Ratio of colloid deposition in porous volume (Sh_{PV}) to smooth surface (Sh_{SS}) versus ratio of pore volume to material volume.

The results of our experimental approach suggest a combination of both variation in Eu(III) concentration as well as variation in surface roughness and topography that governs quantitatively the colloid retention efficiency of rock surfaces.

Eu(III) concentration variations are able to modify the electrostatic repulsion potential of the particle-collector system, based on well-known DLVO theory. Confirmed by zeta-potential measurements, an increase in Eu(III) concentration increased the potential of the colloids (from -32.4 ± 2 mV at zero Eu(III) to -15.8 ± 3.1 mV at 10^{-6} M Eu(III)) which strongly lowers electrostatic repulsions at the interface. At pH = 5, the granodiorite surface is negatively charged. This is predicted from other studies about single mineral surface charge, where the isoelectric point (IEP) for these minerals is (in decreasing order): feldspars~5[164-167] >biotite~3 [168, 169] >granite~2.1 [146] >quartz~2 [165, 166, 170]. The rock surface, a complex mixture of these minerals that exposed a randomly oriented combination of crystal surfaces of all of these minerals was analyzed for its surface potential . At pH = 5 and at 0 M Eu, the measured ζ-potential for granodiorite surface was -38 ± 3 mV, which indicates unfavorable conditions for particle deposition.

Generally, the quantitative impact of roughness variations on colloidal retention at rock surfaces is still subject of experimental investigation [171-173] and developing theoretical approaches [151, 174]. Several experimental studies showed already, that surface roughness of simple mineral surface structures [175] or artificial material surfaces [176] plays an important role under unfavorable electrostatic conditions to increase particle retention efficiency. Roughness is in particular important when the overall DLVO interaction energy between interacting surfaces is reduced [175], because this increases the interfacial interactions owing to physical heterogeneity. For a particle to deposit onto the surface, it should overcome the repulsive energy barrier at primary or secondary minimum [158]. For [Eu(III)] = 0 M, electrostatic repulsions cause a significant energy barrier to colloid retention in the primary minimum (264 kT, SI). Because colloid sorption is still observed for [Eu(III)] = 0 M (colloids and mineral surfaces are highly negatively charged), secondary minimum interaction is more plausible (-21 kT) [177, 178]. When a particle is deposited in secondary minimum, colloid removal mechanisms such as rolling, sliding, and reversible retention of colloids may play a significant role in terms of trapping as well as re-mobilization [161, 179, 180]. However, as [Eu(III)] increases and surface charge of granodiorite become less negative (-28.3 ± 3 mV at 10^{-7} M, -25 ± 3 mV at $5x10^{-7}$ M and -20 ± 2 mV at 10^{-6} M Eu), colloid deposition in the primary minimum is probable. It is known from previous reports, that the binding efficiency of negatively charged colloids can be enhanced by formation of polyvalent cation bridges between colloids and mineral surfaces [181]. Considering the model calculations by Duffadar et.al. [182], the colloid deposition in our study is mainly influenced by nanometer-sized heterogeneities on the granodiorite surface due to the random distribution of cationic patches from the sorption of Eu(III). The complex mineralogical structure of granodiorite at intergranular pore walls also results in surface chemical and charge heterogeneity. When Eu(III) is added to the suspension, it adsorbs partially to colloids as well as to the granodiorite surface (at 10^{-6} M Eu(III), 10% and 13% of total Eu(III) sorbs to colloids and to the granodiorite surface, respectively). Assuming complete sorption of Eu(III) to the collector surface results in $85.7x10^{14}$ adsorption sites/cm^2. Under the implemented flow conditions, even at 10^{-6}M Eu(III), only $7.22x10^{14}$ sites/cm^2 are available. Hence, a patch-wise distribution of Eu(III) on the surface is expected. Therefore, fluctuations in patch density of sorbed Eu(III) yield a local variation of

resulting electrostatic forces towards the particle and result in selective attraction to overcome the interaction energy barrier.

It has been found that the highest density of colloid deposition on granodiorite surface was at porous sections characterized by grain aggregates and grain boundaries (i.e., intergranular porosity). Intragranular porosity was of minor importance for increased retention efficiency. More specifically, it was observed that the colloid deposition was enhanced at the pore walls (Figure 2.36). The wall sections with their characteristic asperities (Figure 2.28) at intergrown sheet silicates or other silicate aggregates were identified as favorable sites for particle-collector interaction. In contrast, a lower colloid deposition density was observed at single and large feldspar or quartz grains with minor or no asperities. This is according to previous studies were a positive correlation between surface roughness and particle retention has been found, e.g., for retention of iron oxide particles at rough rock surfaces [183, 184].

Additionally to the already discussed local variations of DLVO interaction potential at rough surfaces, another explanation of the contrast in retention at rough surfaces is provided by gradients in hydrodynamic forces at rough surfaces [160, 161]. An increase in [Eu] results in the enhancement of the ratio between adhesion torque to applied (resultant) torque T_{adh}/T_{app}. More specifically, the velocity gradient along the surface of substrate increases with increase in distance from the surface, implying hydrodynamic shear forces acting on the mineral substrate are at maximum on colloids and reach a minimum along half-pores, i.e. the rear stagnation point [160]. Rolling, with the larger moment arm [185], is the dominant mechanism of detachment under laminar flow conditions. Since the colloid may be subject to the rolling mechanism [161] it is finally trapped at the location with lowest drag forces [157]. In case of porous rock surfaces this is in pores at pore walls. The deposited colloids in such low-flow zones are hydrodynamically disconnected (immobile regions) [186]. This provides higher collision frequencies due to increased residence time and finally results in enhanced colloid retention. Comparative results from Filby et. al., [147] who reported that bentonite colloids in the presence of Eu(III) were deposited preferentially at granodiorite cavities relative to the entire surface, are in agreement with current observations. Numerical simulations from Boutt et.al. [187] suggested the presence of such “trapping zones” that cause zones of fluid recirculation induced by surface roughness in the micrometer scale.

Additionally to hydrodynamic explanations, previous studies suggested that sub-micron-sized asperities, similar to structures present at the investigated rock surface play an important role in reducing the effective contact area of colloids during adhesion [188]. The walls along the pits with high step density (i.e. protrusion density) which act as positive asperities [188] (see also Figure 2.36d) are able to reduce the electrostatic repulsive barrier at the interface and may initiate the contact [189]. These protrusions with mean height = 0.5 ± 0.3 µm are 2 to 4 times smaller than the colloid diameter and diminish locally the electrostatic repulsion. Consequently, van der Waals forces do dominate the DLVO interaction when the colloid is approaching the surface. When the particle approaches the pore wall, the asperities act as steric barriers and prevent further rolling over the surface by increasing the hydrodynamic drag

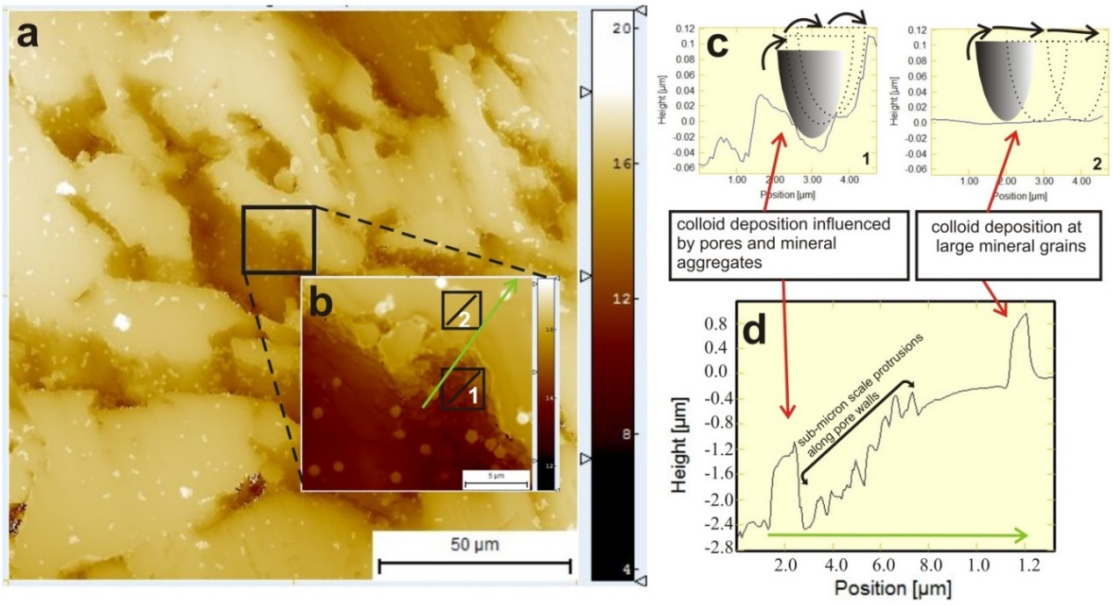

Figure 2.36: (a) Visualization of sites of preferred particle retention at rough granodiorite surface. (a) Map rendered from VSI data shows both flat surface sections and pores; (b) inset shows preferred particle deposition at the pore-walls; (c) profiles along the highlighted lines in boxes (1 & 2 of fig.b): profile (1) illustrates the trapping of colloidal particles owing to sub-micron surface asperities at pore walls; profile (2) illustrates the absence of protrusions that results in minimal restraining torque along the surface and prevents adhesion by roll-over mechanism (d) height profile (see location in (b), green line) showing examples of sites occupied by adsorbed colloids at pore walls submicron-sized asperities.

required for detachment (Figure 2.36c-1) [162]. This influence of surface asperities together with locally attractive regions on the surface due to positively charged patches (caused by the adsorption of Eu(III)) have a pronounced effect in causing frequent surface contact of the particle [182]. The interaction energy is significantly attenuated by an increase in the ratio of particle to asperity size [151]. Our study showed that the colloid sorption is clearly favored at surface sections with high density of small asperities (density (D) = 2.6 ± 0.55 μm^{-1}, asperity diameter (ϕ) = 0.6 ± 0.2 µm, height (h)= 0.4 ± 0.1 µm) in contrast to surface sections with larger asperities and lower asperity density (D = 1.2 ± 0.6 μm^{-1}, ϕ = 1.4 ± 0.4 µm, h = 0.6 ± 0.2 µm). This is also according to previously made conclusions that at lower density asperities, where colloids are embedded in-between of protrusions they do encounter a larger repulsive DLVO interaction energy due to the higher contact area [151, 152]. Hence, these zones are unfavorable for colloid attachment. The absence of such protrusions on, smooth large feldspar and quartz grains leads to an enhanced drag force over adhesion force [161, 162, 180, 190]. This explains the comparatively lower colloid retention efficiency at those surfaces (Figure 2.36c-2). Occasionally, due to small-scaled chemical inhomogeneities, an accumulation of colloidal particles was observed on smooth mineral surfaces, and, inversely, a few regions with high surface roughness show minor or no colloid deposition [191].

Conclusions

The Silicon wafer samples possessing surface structures in the submicron scale has a significant effect on colloidal deposition under unfavorable conditions rather when surfaces are oppositely charged. Under unfavorable conditions, the deposition efficiency at rough surfaces is increased at least by a factor of 2.7 in case of 0.3 and 0.43 µm and 1.2 & 1.8 for 1 and 2 µm colloids compared to smooth surfaces of the same surface charge. The impact of roughness on retention is especially important for small particles. This may explain differences in retention efficiency of mineral colloids in the environment as a function of particle size. Rolling is the fundamental transport mechanism at surfaces to trap preferentially smaller colloids. This results in a high deposition flux over a broad range of fluid velocities. For both smooth and rough collector surfaces the deposition flux increases with fluid velocity. Beyond a critical velocity, however, the particles detach from surface. Due to higher restraining torque acting at rough collector surfaces, this critical velocity is higher at rough surfaces. The increase in polydispersity results in lower deposition efficiency. The electro-hydrodynamic blocking (shadow effect) is more efficient at higher polydispersity as well as when the Peclet number is close to 1.

The present study showed the relevance of granodiorite mineral surface topography for colloidal transition pathways under unfavorable electrostatic conditions. Given the scale of surface asperities and well quantified surface heterogeneities, it can be concluded that surface roughness is the critical factor in determining favorable, versus less favorable, sections for colloid deposition on complex mineral surfaces. The results presented suggest that a mixture of several mechanisms, such as local DLVO potential variation as well as local fluid dynamics are involved in the complex behavior of colloid retention increase at rough rock surface sections. We conclude that coupling of both the current microscopic approach that enhanced the clear understanding of colloid deposition at complex rough mineral surfaces at larger scan areas and the nanoscopic AFM investigations (for example: force-volume analysis) are the promising step toward the fundamental understanding.

Further details to the study presented in this chapter can be found in:

Gopala Krishna Darbha*, Cornelius Fischer, Johannes Luetzenkirchen, Thorsten Schäfer *“Site-specific retention of colloids at rough rock surfaces”.* Environmental Science & Technology. 46, 9378, 2012.

Gopala Krishna Darbha*, Cornelius Fischer, Alex Michler, Johannes Luetzenkirchen, Thorsten Schäfer, Frank Heberling and Dieter Schild *“Deposition of Latex Colloids at Rough Mineral Surfaces: An Analog Study using Nanopatterned Surfaces”.* Langmuir, 28, 6606, 2012.

Fischer, C.; Michler, A.; Darbha, G. K.*; Mike Kanbach; Schäfer, T., *“Deposition of mineral colloids on rough rock surfaces”.* Am. J. Schi. 2012, 312, 885-906, 2012.

2.2 Field experiments at Grimsel Test Site (GTS)

2.2.1 The Colloid Formation and Migration (CFM) project: Background and project organisation

The Colloid Formation and Migration (CFM) project is conducted in the framework of Phase VI of the research program of the Grimsel Test Site (GTS). GTS Phase VI runs from 2004 to 2013 and is dedicated to repository-relevant (i.e. large-scale, long-term) in-situ experiments. An extension of Phase VI until 2018 is under discussion.

The CFM project is the current project in a series of experiments conducted within the Radionuclide Retardation Programme of the GTS since 1984. Phase 1 began in 2004 and ended early in 2008. The main tasks were preparatory studies concerning in-situ boundary conditions, predictive modeling and supporting laboratory programs.

Experiment aims and boundary conditions

The aims of the CFM long-term colloid project are listed in Table 2.8.

Table 2.8: CFM project aims and approaches.

Aim	How it is addressed in the CFM project
Examine colloid generation rates and mechanisms at the engineered barrier system (EBS) – host rock boundary under in-situ conditions	Laboratory (e.g. Bentflow and mock-up tests) and in-situ test
Evaluate the long-distance migration behaviour of EBS-derived colloids in a water-conducting feature in a repository-relevant flow system (i.e. with a very low flowrate/water flux)	Colloid tracer tests and monitoring of release from in-situ test
Study the long-term geochemical behaviour (mobility, mineralisation, colloid formation etc.) of radionuclides at the EBS-host rock boundary	Laboratory tests (including mock-ups) and monitoring of in-situ test near field
Examine reversibility of radionuclide uptake onto colloids	Laboratory, possibly mock-ups
Gain experience in long-term monitoring of radionuclide/colloid propagation near a repository	Design, development, implementation and “post-mortem” examination of in-situ test monitoring system
Apply the results to improve repository performance assessments, optimise EBS design and contribute to the "monitoring" debate	

History of field activities for site selection, characterization and preparation from 2005 on:

The field activities conducted in Phase 1 of the CFM experiment focused on site selection, site characterization and site preparation. Colloid transport in a water-conducting feature is expected to take place in an advective flow regime. At the onset of Phase 1 it was clear, therefore, that the key element for the selection of a suitable site at GTS for the CFM experiment was the availability of a water-conducting feature with a well characterized natural flow field. The migration (MI) shear zone at tunnel position AU96 met many expectations. As the focus structure of earlier MI, EP (Excavation project) and CRR (Colloid and Radionuclide Retardation) experiments, it had been studied already and instrumentation was in place. Numerous hydro- and tracer tests had been conducted, some with active tracers which required the temporary transformation of the AU gallery into a radiation controlled zone. The MI shear zone is an almost two dimensional feature extending from the KWO (Kraftwerke Oberhasli AG) access tunnel towards the VE gallery.

An early task of the CFM Phase 1 site characterization was the investigation of the tunnel surface of the roughly 7 m marked by the MI shear zone (tunnel coordinates AU93 to AU100). Focus was on (i) detailed mapping of major structural features like ductile shear zones, brittle fractures and fault gouge and (ii) hydrological investigations in terms of localizing major water inflow points and measuring the groundwater flow rates of these features.

Figure 2.37 shows the result of the geological mapping of the MI shear zone. The main foliation in the granodiorite is defined by biotite and feldspars which are aligned in parallel to each other. The shear zone was originally formed by ductile deformation. In a later stage of alpine deformation and following uplift, the shear zone was reactivated. In this brittle deformation phase, cohesionless fault gouge material formed along discrete fracture planes. The complete MI shear zone is represented by 3 steep (>70°) shear planes striking WSW-ENE. They are hydraulically connected and represent a complex water conducting feature. The transmissivity of the shear zone was found to be, in general, between 10^{-8} and 10^{-6} m^2 s^{-1} with very low transmissivity parts where transmissivity is $<10^{-10}$ m^2 m^{-1}.

The main shear plane in the northern part of the mapped zone shows a high degree of brittle deformation overprinting the older ductile features. This main shear plane is also characterized by distinct inflow points where surface packers have been installed (red circles in Figure 2.37). These inflow points are openings of up to 10 mm in width and deliver continuous water inflow into the tunnel. The water conducting features tend to be filled with fault gouge. More detail on the deformation history and fracture geometry is found in [192]. The results of the mineralogical analyses and investigations of the chemical composition of discharging groundwater from the MI shear zone are found in [193].

The hydraulic characterization of the test site could build on tests from the existing boreholes and results from earlier MI, EP and CRR activities. Figure 2.38 shows the test site in a 3D block model with the MI shear zone and boreholes at the onset of Phase 2 of the CFM project. The 86 mm boreholes are equipped with inflatable multi-packer systems isolating the MI shear zone interval in each borehole. The isolated intervals are equipped with pressure lines allowing permanent monitoring of groundwater pressure in the MI shear zone as well as flow lines for hydro- and tracer testing.

Preliminary hydraulic tests were conducted at the CFM site in March 2005. Hydraulic testing focused on the MI shear zone with the intention to estimate the shear-zone transmissivities T and to provide data for numeric modeling. Other objectives of the field campaign were to document 'static' interval pressures, to measure the natural inflow into the tunnel from the so-called Pinkel and Kalotte inflow points and to assess the impact of the sealed boreholes. The 2-day hydraulic testing campaign confirmed the heterogeneous properties of the MI shear zone. For the majority of the investigated shear-zone intervals, the estimated T values vary between $6 \cdot 10^{-8}$ m^2 s^{-1} and $1.4 \cdot 10^{-6}$ m^2 s^{-1}. The measured hydraulic heads vary within 12.8 m. Interference reactions were recorded in all but two monitored boreholes. Further results are provided in [193].

Preparation of the test site started with cleaning the rock surface using sandblasting and pressure washing. The cleaning campaign allowed detailed geological mapping and detection of the major inflow points which were then equipped with surface packers (Figure 2.37 for locations). The next step involved sealing the shear planes and, eventually, the entire tunnel surface over a 6 m stretch with special cements and resins. Tunnel inflow continued to be monitored throughout these activities. Pressures have also been recorded continuously since March 2005 in the packed off borehole intervals in the MI shear zone. The pressure records show responses to tests of the sealing quality, renewed sealing activities, pressure conditions created for tracer tests etc.

Two tracer tests were performed after the resin sealing (but prior to establishing low gradient flow fields) within the MI shear zone using uranine (Na-fluorescein) doped water. #1 was the first tracer test performed after the shear zone was sealed in the second half of 2005. The sealing was a requirement to achieve lower hydraulic gradients. Tracer Test Run #2 was performed in January 2006 after a fissure near the Pinkel surface packer was sealed and the shear zone pressures had recovered and stabilized. The objectives of the tracer tests were to obtain advective travel times, assess the recovered tracer and estimate the dispersion parameters in the shear zone flow field from boreholes to the tunnel surface packer intervals when the shear zone was sealed but allowed to freely flow from surface packers.

Two boreholes, CFM 06.001 and CFM 06.002, were drilled and equipped for testing and observation in August 2006 (Figure 2.38). In particular the hydraulic modeling results showed the boreholes could fill existing data gaps. An inspection with a borehole camera was carried out in both boreholes. The camera logs confirmed the position of the shear zone and identified lamprophyre intrusions in the core of CFM 06.001, whereas in CFM 06.002 no clear fractures were observed, except a water outflow point at the borehole end (6.85 m). Some weeks later, borehole CFM 06.002 was extended to penetrate the shear zone. Both boreholes were equipped with packer systems and saturated.

By the time of the 3rd CFM Project Meeting in May 2006 it was apparent that the status of the sealing of the MI shear zone did not fulfill the requirements for the in-situ experiment. The hydraulic gradients within the MI shear zone towards the AU tunnel were too steep. It was decided to install a 5 m long steel mechanical tunnel packer (referred to as mega-packer or sub-mountain packer) to resist higher pressures in the MI shear zone. The annular space

between the tunnel wall and the packer can be pressurized to support the resin sealing. In February 2007 the mega-packer and the new boreholes were instrumented and connected to the GeoMonitor II automatic data acquisition system (DAS).

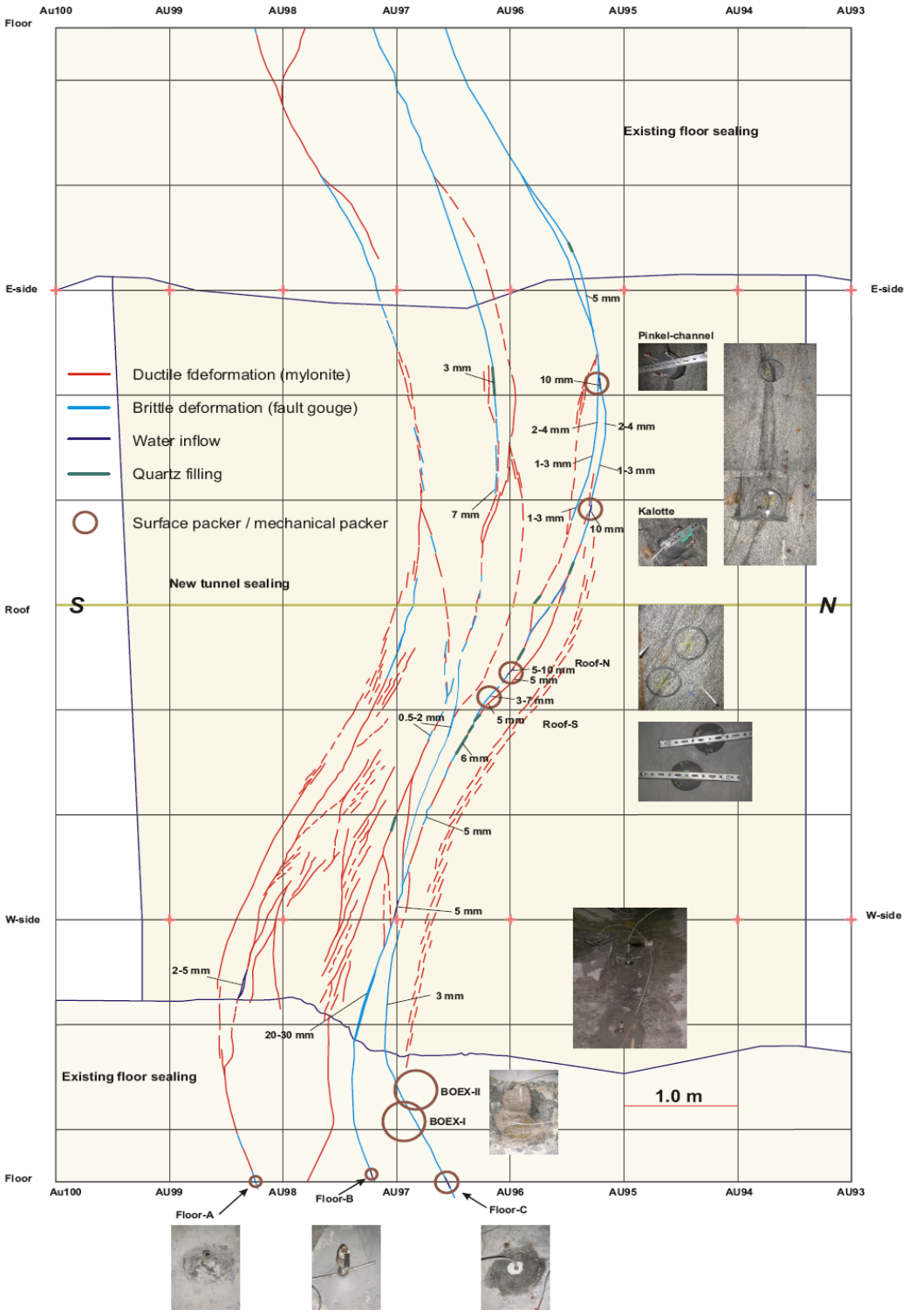

Figure 2.37: Detailed geological mapping of the MI shear zone between tunnel meters AU93 and AU100 with surface-packer locations [193].

In the immediate area around the tunnel intersection, the MI shear zone is effectively isolated and does not intersect any other large scale structure. At a greater distance it is believed that

the shear zone intersects the lamprophyre that crosses the tunnel at about tunnel meter AU73 close to the site of the LTD (Long Term Diffusion) monopole experiment (over-cored in 2010). The local transmissivity of the shear zone around borehole CFM 06.001 (~10^{-9} m^2 s^{-1}) is slightly lower than the average of the CFM/MI zone (between 10^{-8} and 10^{-6} m^2 s^{-1}). The hydraulic properties of the lamprophyre and observed pressure interferences with the MI shear zone were analyzed in [194].

Throughout 2007, a series of five tracer tests (Tracer Test Runs 07-01 to 07-05) was conducted with dyed water to further evaluate the flow field for the colloid migration experiment. Homologue Tracer Test 08-01 was carried out in January 2008 and followed by companion Tracer Test Run 08-02 with uranine injection in February into approximately the same flow field. It had been decided that the conservative tracer might cause complexation and so the test needed to be performed separately. The flow field selected was similar (in terms of outflow from the shear zone) to that used in Tracer Test Run 07-01. The results from runs 08-01 and 08-02 are discussed in more detail in a later section.

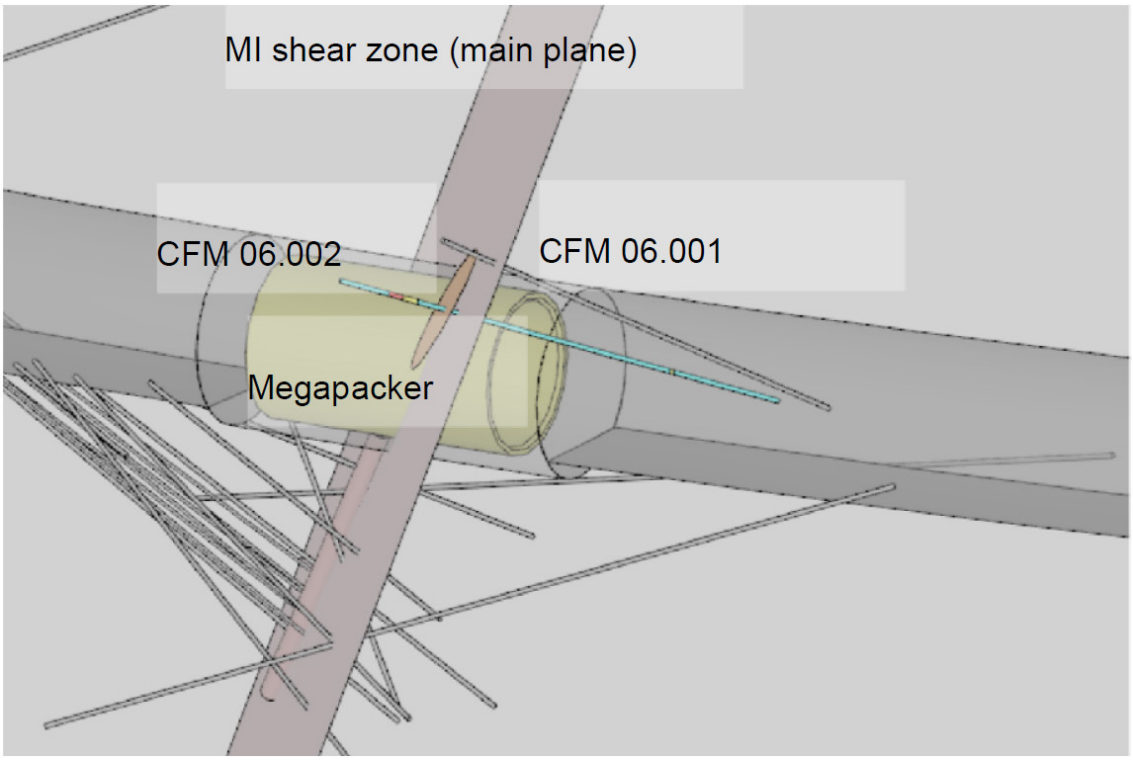

Figure 2.38: Schematic of the site of the CFM in-situ experiment. Boreholes CFM 06.001 and CFM 06.002 were drilled in 2006. They are shown in the foreground (CFM 06.002 coloured by lithology). The location of the main plane of the shear zone is also shown, as is the main flowing feature in borehole CFM 06.002. The other boreholes are from previous investigations.

One of the three key objectives for 2008/2009 was the development and demonstration of an adequate and robust sealing system suitable for the performance of a long-term in-situ test. Since the beginning of the project in 2004, numerous considerations eventually resulted in the implementation of three increasingly complex sealing concepts. It was recognized at the

beginning of Phase 2 that further improvements would be necessary. Eventually, the 5 m long steel liner of the mega-packer installed in Phase 1 was left in place while the cement-filled Bullflex packers on each end were replaced with inflatable rubber packers. The new system was put into operation in September 2009 and provided reliable sealing over a range of conditions with no indication of significant leakage over the first few months of observation.

The second key objective concerned the characterization of borehole CFM 06.002 and the key feature in it as a possible emplacement location for the bentonite source for the in-situ test. For this, the lithological and structural features were analyzed with an optical borehole scan, core mapping and an impression packer survey. A hydraulic screening test campaign with test intervals in borehole CFM 06.002 and monitoring intervals in this and neighboring boreholes supported the hydrogeological characterization of the MI shear zone. The highest transmissivities were associated with the borehole section between 6.40 and 7.10 m which contains a single fracture identified in the core (), images and the impression packer data. The design of the final borehole instrumentation was optimized accordingly. Interval 2 of the triple packer system installed in May 2009 covers this 0.7 m section and was equipped with a PEEK (Polyetheretherketon) dummy to reduce its volume.

The results from Tracer Test Run 09-01 demonstrated that the interval around the candidate feature is suitable for the in-situ test. The attributes include:

- There is a well-characterized distinct flow feature in interval 2 (6.40 – 7.10 m).
- The feature is well connected to flow paths in the shear zone (cross-hole tests and tracer).
- The flow rate through the borehole interval under suitable boundary conditions (out-flow from Pinkel surface packer) is consistent with the target range for the in-situ test.
- The location is suitable for post-test over-coring.

While the suitability of the ‘single fracture’ or ‘distinct flow feature’ in borehole CFM 06.002 became apparent, there were discrepancies with respect to its exact location in the borehole from the different investigation methods. All conceivable explanations considered, it appeared most sensible at the time to define the position of the key feature in terms of a depth range which accounts for the recognized uncertainty inherent in the depth information. For further planning purposes the depth of the key feature was considered to be 6.70 – 6.85 m from the borehole mouth (Figure 2.39).

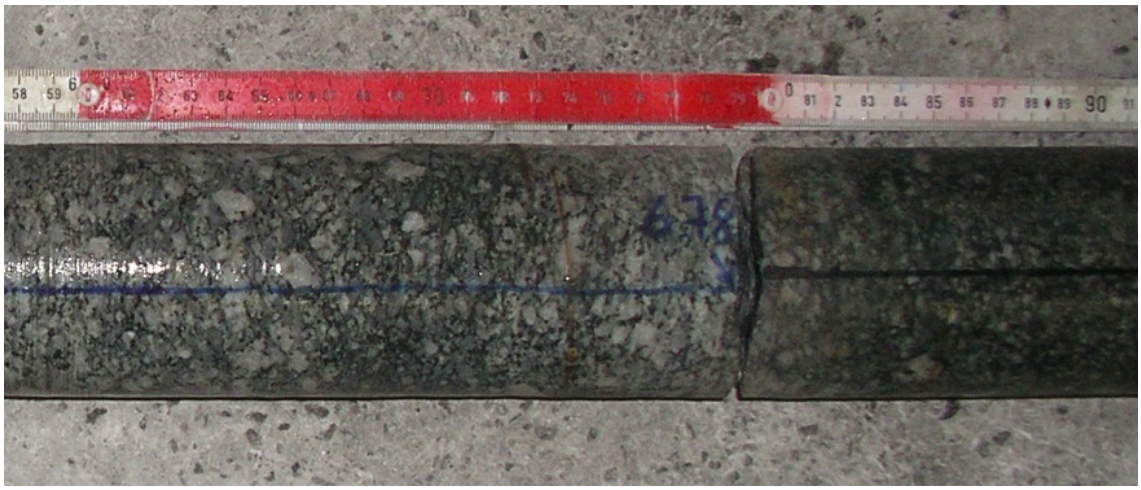

Figure 2.39: Photograph of the core section from borehole CFM 06.002 showing the fracture plane at a depth of 6.78 m. To account for localisation difficulties the key feature is generally considered to be in the depth range of 6.70 – 6.85 m.

The third key objective related to the development of instrumentation for monitoring groundwater chemistry and tracer testing. The surface equipment at the CFM site was augmented in November 2009 with two chemistry cabinets. Although their flexible configurations facilitate tracer testing, they are designed also for the long-term sampling and monitoring purposes required for both migration tests and the long-term in-situ test. At the end of 2009, the field setup at the CFM site included 20 monitoring intervals in twelve boreholes, seven surface or short borehole packers at the intersection of the MI shear zone and the AU tunnel, and injection and extraction groundwater monitoring systems.

Tracer Test Runs 10-01 to 10-04 were performed in 2010 with homologues, colloids and conservative tracers. All were conducted as point dilution tests with recirculation of tracer in interval 2 of borehole CFM 06.002 and extraction from the Pinkel surface packer. The suitability of this dipole for the long-term in-situ test could be confirmed. The tracer tests provided field data on colloid and homologue transport at longer timescales than previously achieved in controlled conditions.

Tracer Test run 10-01 was a homologue/colloid tracer test performed at 50 ml min-1 extraction from the Pinkel.

Tracer Test Run 10-03 was a homologue/colloid tracer test performed at a low extraction from the Pinkel of 10.3 ml min-1. Although homologues and colloids were identified at the Pinkel an anomalous loss of Uranine was detected.

The three monitoring boreholes CFM 11.001, CFM 11.002 and CFM 11.003 were drilled, surveyed, core mapped and equipped with triple packer systems. They are in close proximity (~4 cm) and parallel to borehole CFM 06.002 because of the intention to use them for colloid and radionuclide monitoring at small distances from the source, and for resin injection and stabilization of the key feature in the target shear zone before over-coring will take place.

After drilling these monitoring boreholes, Tracer Test Runs 11-01 and 11-02 demonstrated that a low flow velocity zone was present around CFM 06.002-i2 resulting in very little “dilution flow” through the interval necessitating a change to a dipole configuration for future tracer tests from this interval. Only a very small injection rate (0.33 ml min-1) was necessary and this rate was used for Tracer Test Runs 12-01 & 12-02, the confirmation/preparatory conservative tracer test and the Radionuclide/colloid migration test.

During Tracer Test Runs 11-01&2 it was also established that at low gradients Uranine showed anomalous losses compared to the tracer Amino-G Acid (AGA). The process causing these losses is not understood although it has been suggested that it is associated with low pH conditions in the injection interval. From Tracer Test Run 11-01 onwards AGA has been used as the primary conservative tracer. Tests with Eosin (from Tracer Test Run 12-04 on) have showed similar behavior to Uranine.

Tracer Test Run 12-01 was a preparatory conservative tracer test to confirm the setup for the subsequent Radionuclide/colloid test run 12-02.

Following Tracer Test Run 12-02 a series of conservative tracer dipole tests (Tracer Test Runs 12-03,4,5,6 and 13-02,3) was performed in the CRR area of the shear zone utilizing boreholes BOMI 87.008, BOMI 87,010, CRR 99002 and CRR0.0.003. The aim was to select a suitable dipole for a 2nd RN test and determine the feasibility of performing tracer migration tests in parallel with the long term in situ test. As part of the preparation for such tests packer systems in these boreholes were replaced with systems suitable for future migration tests incorporating low-volume PEEK interval completions.

Tracer Test Runs 11-03 and 13-01 focused on demonstrating the feasibility of very low flow rate sampling of water from around CFM 06.002-i2 from the near-field monitoring boreholes CFM 11.001,2,3. These tracer tests also provided information on the small-scale heterogeneity around CFM 06.002-i2.

Table 2.9 lists the tracer tests performed within the CFM Project from 2007 to 2013.

Table 2.9: Field tracer tests performed within the framework of CFM 2005-2013.

Tracer Test Run	Test Type	Injection BC	Injection	Shear Zone Extraction	SZ flow (ml/min)	Additional Extraction	Comment
05-01	Conservative	Injection	BOMI 87.010i2	Pinkel/fissure	573		Test prior to sealing
06-01	Conservative	Injection	BOCRR00.003i2	Pinkel	602		Test prior to sealing
07-01	Conservative	Injection	CFM06.002i1	Pinkel	164.7		Evaluation of 06.002
07-02	Conservative	Injection	BOMI 87.010i2	Pinkel	119		Repeat 05-01 low outflow
07-03	Conservative	Injection	BOCRR00.003I2	BOMI87.010i2	75	Slight leakage	Dipole selection tests
07-04	Conservative	Injection	BOMI87.010i2	Pinkel	109		Dipole selection tests
07-05	Conservative	Injection	BOMI87.008i2	BOMI87.010i2	110		Dipole selection tests
08-01	Homologue/colloid	Point Dilution	CFM06.002i1	Pinkel	160		Sections 3-5
08-02	Conservative	Point Dilution	CFM06.002i1	Pinkel	160		Sections 3-5
09-01	Conservative	Point Dilution	CFM06.002i2	Pinkel	52		Preparation for 10-01
10-01	Homologue/colloid	Point Dilution	CFM06.002i2	Pinkel	48		Sections 3-5
10-02	Conservative	Point Dilution	CFM06.002i2	Pinkel	10.4		Preparation for 10-03
10-03	Homologue/colloid	Point Dilution	CFM06.002i2	Pinkel	10.1		Sections 3-5
	Homologue/colloid	Point Dilution	CFM06.002i2	BOMI87.010i2	10.3		Additional extraction
10-04	Conservative	Point Dilution	CFM06.002i2	Pinkel	25.15		Higher outflow test
11-01	Homologue/colloid	Point Dilution	CFM06.002i2	Pinkel	10.3		Repeat of 10-03 with AGA

Table 2.9**:** (continued): Field tracer tests performed within the framework of CFM 2005-20113.

Tracer Test Run	Test Type	Injection BC	Injection	Shear Zone Extraction	SZ flow (ml/min)	Additional Extraction	Comment
11-02	Conservative	Point Dilution	CFM06.002i2	Pinkel	25.15		Repeat with higher outflow
11-02	Conservative	Injection	CFM06.002i2	Pinkel	25.15		Test of injection
11-03	Conservative	Point Dilution	CFM06.002i2	Pinkel	25.15	CFM11.001i2	Sampling feasibility test
	Conservative	Point Dilution	CFM06.002i2	Pinkel	25.15	CFM11.002i2	
	Conservative	Point Dilution	CFM06.002i2	Pinkel	25.15	CFM11.003i2	
	Conservative	Injection	CFM06.002i2	Pinkel	25.15		Test of low rate injection
12-01	Conservative	Injection	CFM06.002i2	Pinkel	25.15		
12-01	Conservative	Injection	CFM06.002i2	Pinkel	25.15		
12-02	RN/Colloid	Injection	CFM06.002i2	Pinkel	25.15		Sections 3-5
12-03	Conservative	Injection	BOCRR00.003i2	Pinkel	25.15		Dipole feasibility tests
12-04	Conservative	Injection	BOCRR00.003i2	Pinkel	25.15	BOMI87.010i2	
12-05	Conservative	Injection	BOCRR00.003i2	Pinkel	25.15	BOMI87.010i2	
12-06	Conservative	Injection	BOMI87.008i2	Pinkel	25.15	BOMI87.010i2	
13-01	Conservative	Point Dilution	CFM06.002i2	Pinkel	25.15	CFM11.002i2	Sampling feasibility test
13-02	Conservative	Injection	BOCRR99.002i2	Pinkel	25.15	BOMI87.010i2	Dipole feasibility tests
13-03	Conservative	Injection	BOCRR99.002i2	Pinkel	25.15	BOMI87.010i2	

2.2.2 New in-situ field experiments at Grimsel Test Site (GTS) within Kollorado-2

Abstract. The influence of colloidal/nano-scale phases on the radionuclide (RNs) solubility and migration behavior is still one of the uncertainties in repository safety assessment. In this chapter we report on the progress concerning the colloid migration under near natural hydraulic conditions at the Grimsel Test Site. These experiments on the demonstration of colloid mobility under defined hydraulic conditions are of paramount importance to judge later on the potential bentonite erosion and colloid formation in the long-term in situ test.

Materials & Methods

Within the Colloid Formation and Migration (CFM) project at the Grimsel Test Site (GTS, Switzerland) a huge geo-technical effort has been carried out to isolate hydraulically a shear-zone from the artificially introduced hydraulic gradient due to the tunnel construction. The construction is a combination of polymer resin impregnation of the tunnel surface and a steel torus to seal the tunnel surface. The steel tube with reinforcement rings is sealed at both ends with rubber based hydraulic “donut” packers and the annulus between resin and steel ring is filled and pressurized with water to counteract the hydrostatic pressure of the water conducting feature giving mechanical support to the resin. Natural outflow points of the MI shear zone localized prior to the construction were sealed by surface packer systems. This design gives the opportunity to regulate outflow and thereby adjust the flow velocity and gradient in the fracture. Currently, a very stable gradient of ~60 mm over a dipole length of 6m resulting (~1%) is established over months.

A number of tracer injection experiments are performed to optimize the experimental setup and injection procedure and to clearly document to the regulator the overall control of the system:

1) Conservative tracer tests using fluorescence dyes (Uranine, Amino-G) and

2) So-called “homologue” tracer tests performed by injecting a suspension of Febex bentonite colloids associated Eu, Tb, Hf in addition to the conservative tracer.

After these experiments, a license request was submitted end 2011 and the license was granted in January 2012 by the Swiss regulatory (BAG) to perform the first radionuclide tracer test under these low-flow conditions. Only the radionuclide tracer test Run 12-02 will be presented in detail, for other experiments, see e.g. [195].

RN Injection cocktail preparation. The injection cocktail of 2.25L spiked Grimsel groundwater was prepared at INE in an argon glove box and transferred to GTS in a lead shielded sample container (Swagelok). Based on the ICP-MS measurements a total colloid concentration of 101.4 ± 2.5 mg/L montmorillonite clay colloids were used, whereas 8.9 ± 0.4mg/L were present as synthetic montmorillonite with structural incorporated Ni. For details on the structural characterization of the Ni- montmorillonite phyllosilicate, see [57]. The rest of the colloids consisted of Febex bentonite derived montmorillonite colloids, similar to the ones injected within the CRR project [23, 24]. The total mass injected based on the Al or Ni signal

was 23,339-25,663 µg or 1,090-1,119 µg, respectively. Separate analysis of the colloids by optical Laser Induced Breakdown Detection (LIBD, apparatus MOB2) revealed a colloid concentration of 137.2 mg/L and an average colloid size based on a calibration using spherical polystyrene particles of 104 ± 8nm. The injected masses of colloids and conservative tracer are listed in Table 2.10.

Table 2.10: Composition of tracer cocktail Run 12-02 concerning colloid concentration and conservative tracer. Background electrolyte is original Grimsel groundwater.

Tracer	Total injected mass	Detection method
Colloids (Febex + Ni-montm.)	228.2 ± 5.6 mg	ICP-MS
Ni-montm. colloids	20.0 ± 0.9 mg	ICP-MS
Colloids (Febex + Ni-montm.) **Al-signal**	23.3 – 25.6 mg	ICP-MS
Ni-montm. colloids **Ni-signal**	1.09 - 1.12 mg	ICP-MS
Colloids (Febex + Ni-montm.)	308.7 ± 15.4* mg	LIBD
Conservative tracer (Amino-G)	3.70 ± 0.02 mg	Fluorescence

*5% uncertainty assumed.

Beside the colloids and the conservative tracer Amino-G (1646 ± 8 ppb) the radioisotopes as listed in Table 2.11 were injected. The trivalent and tetravalent actinides were quantitatively associated with the colloids present as well as Cs, whereas Np(V) and Na are not bentonite colloid bond.

Table 2.11: Composition of tracer cocktail Run 12-02 given in mol/L and total activity as well as the colloid associated fraction in the cocktail. Background electrolyte is original Grimsel groundwater.

Tracer	concentration (mol/L) / total activity	colloid association (min-max values)*
^{22}Na	1.0-1.1·10^{-10} / (1.17 MBq)	0 - 3.5 %
^{133}Ba	6.8-7.0·10^{-10} / (1.97 MBq)	24 – 34 %
^{137}Cs	7.9-8.0·10^{-10} / (785 kBq)	97 – 98 %
^{232}Th	5.3-5.6·10^{-9} / (8 mBq)	94 – 97 %
^{237}Np	9.3-9.4·10^{-9} / (119 Bq)	0 - 1 %
^{243}Am	7.0-7.4·10^{-11} / (290 Bq)	99 – 100%
^{242}Pu	3.0-3.2·10^{-9} / (190 Bq)	99 – 100%

* Colloid separation was performed by ultracentrifugation at 90,000 rpm (ca. 5x10^{5}g) for 60min.

The injection of the radionuclide bentonite colloid cocktail was performed through borehole CFM 06.002-i2 into the MI shearzone and the water extracted under a constant flow rate of approx. 25 mL/min from the “Pinkel” surface packer (dipole distance 6.08 m). The tracer cocktail was re- circulated in the injection loop to monitor the fluorescence decrease of the conservative tracer (Amino-G; 7 amino-1,3-naphtalene disulfonic acid) and therefore providing an injection function for consequent transport modeling (Figure 2.40).

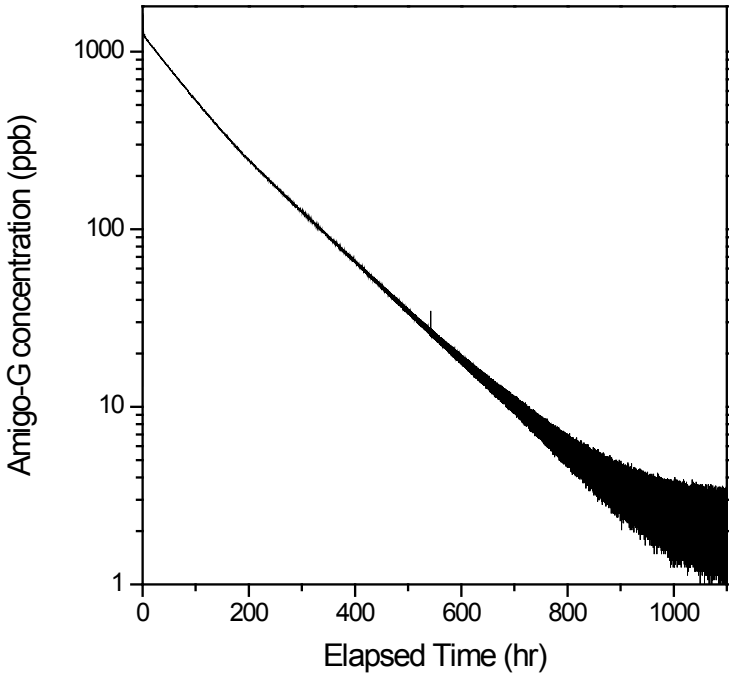

Figure 2.40: Fluorescence signal of the conservative tracer (Amino-G) in the injection loop during Run 12-02 providing an injection function for consequent transport modeling.

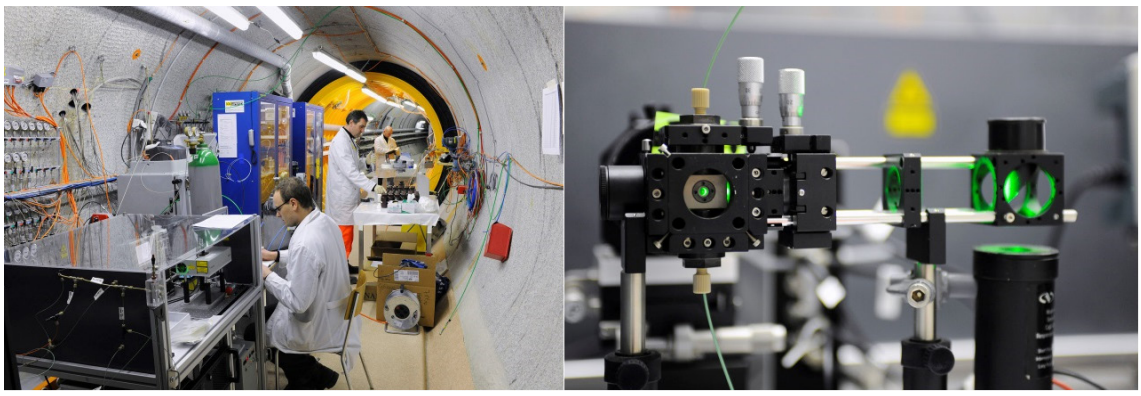

Figure 2.41: Pictures of the experimental set-up during Run 12-02. Mobile LIBD-system in the experimental tunnel of the Grimsel Test Site (GTS) with megapacker system in the back (left) and zoom in on LIBD system showing the flow-through cuvette installed directly in-line to the outflow of the “Pinkel” surface packer (right).

It has been shown through prior migration tests that the local transmissivity of borehole CFM 06.002 is very heterogeneous and under the low flow conditions established an almost stagnant zone around the borehole exists. Therefore, in Run 12-02 an injection with 0.33mL/min during recirculation has been used. For on-site colloid analysis a LIBD system similar to the one used in the CRR experiments [4] was transferred to Grimsel and installed in-line at the

"Pinkel" outlet to directly monitor the mobile colloid fraction throughout the experiment (Figure 2.41).

Results & Discussion

Conservative tracer. The conservative tracer Amino-G was recovered quantitatively both by on site inline and off-site fluorescence detection. In both, the on-line and off-site Amino-G fluorescence data periodic up- and downturns on top of the breakthrough curve (BTC) could be observed, with a periodicity similar to the earth tides showing again the low gradient established in the migration shear zone within the CFM project. From the concentration maxima in the BTC a dilution factor via dispersion of ~137 could be determined.

Colloid tracer. The clay colloid recovery (integration until 34.7 days) determined by the on-site LIBD measurements was quantified to be ~48 % taking into account the LIBD determined mass injected (Figure 2.44 and Table 2.12). In comparison, the HR-ICP-MS provided 44-49 % recovery by analyzing the Al-signal for a background Al concentration of 28 ppb in the Grimsel groundwater and 56-61 % for a background Al concentration of 25 ppb, respectively. All three colloid breakthrough curves are presented in Figure 2.42 together with the conservative tracer Amino-G.

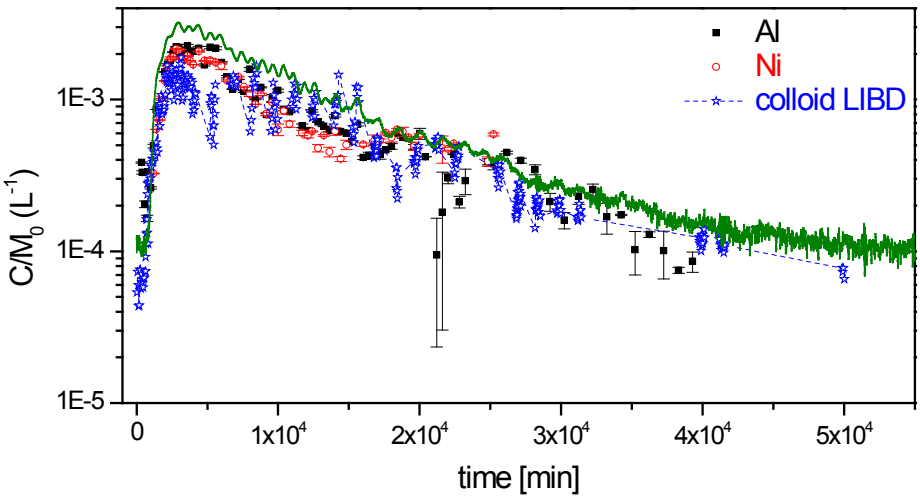

Figure 2.42: Colloid breakthrough curves of Run 12-02 measured by LIBD and HR-ICP-MS taking the montmorillonite structural elements Al and Ni.

Both, the rising edge of the BTC and the tailing is in good agreement between the different measurement methods applied. However, the on-site LIBD measurements with a higher sampling frequency seems to resolve at least partly the tidal effects seen in the conservative tracer. Especially quantification of the colloid recovery based on the Al signal is very sensi-

tive to the background Al signal from the groundwater in the MI shearzone. Fluctuations of 3 ppb in the groundwater content can lead to changes in recovery of more than 10 % based on the long tailing (water volume). The issue of background monitoring of natural fluctuations becomes especially important with respect to the interpretation of the bentonite erosion in the planned long-term in situ experiment. To judge the potential influence of an artificial colloid mobilization throughout the radionuclide migration experiment the Al/Ni ratio was taken as an indicator. For the injected clay colloids the Al/Ni ratio = 21.6 ± 0.3, whereas in the effluent samples the Al/Ni ratio determined by linear regression for all samples Ni could be detected in the BTC is 22.0 ± 2.0 (Figure 2.43).

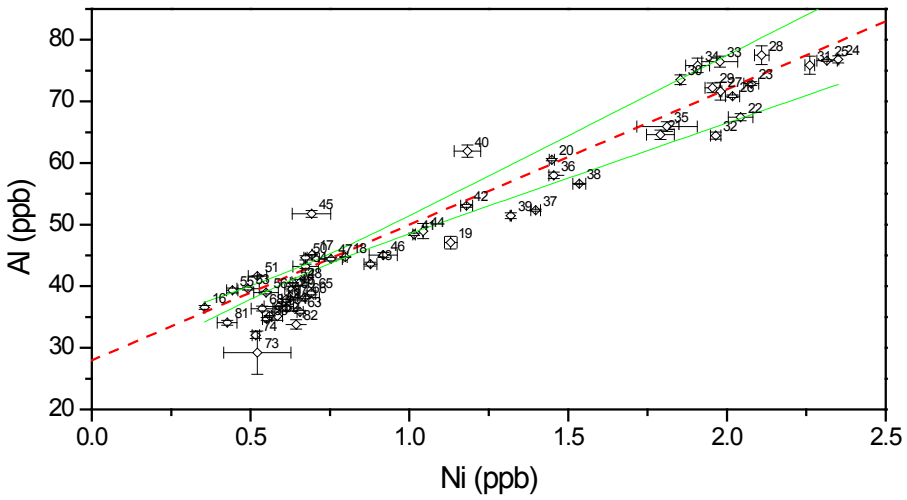

Figure 2.43: HR-ICP-MS data of Al plotted against Ni from samples of the Run 12-02. Beside the linear regression given an average Ni/Al ratio of 22.0 ± 2.0 the 95% confidence intervalls are given.

Based on this comparison a significant mobilization of Al containing colloidal phases from the shearzone or during the cocktail injection through an induced pressure gradient as frequently discussed and observed in [196, 197] can be undoubtly excluded. In addition, closely looking on the y-axis intersection of the correlation fit one can deduce that the background Al concentration is close to 28 ppb. The Al/Ni ratio observed excludes the possibility of a preferential filtration or significant dissolution of the used synthetic Ni- montmorillonite giving further evidence in the suitability of this material as a colloid marker also to be used in the long-term in situ experiment to be started end 2013.

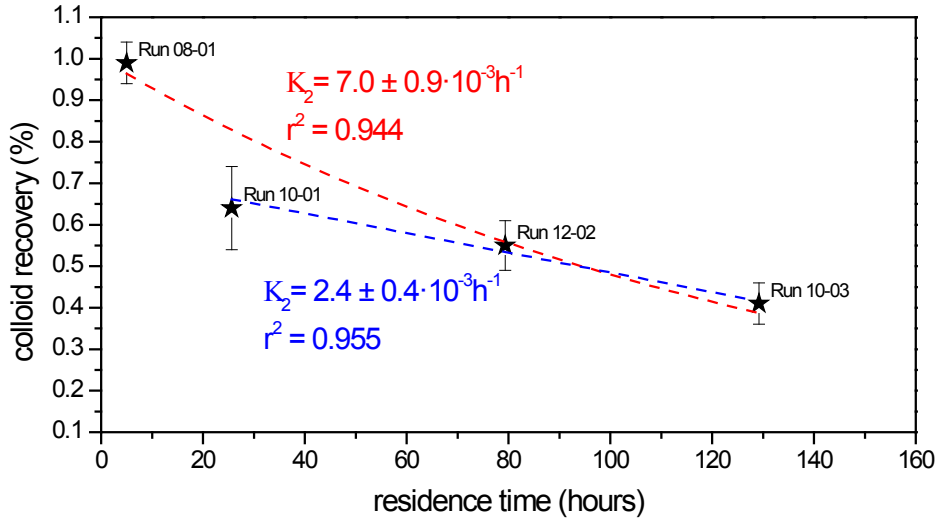

Figure 2.44: Exponential fit to the colloid recoveries determined in various colloid migration experiments performed in the MI shearzone (same dipole geometry).

Furthermore, based on the colloid migration experiments performed so far in the same dipole of the MI shearzone (Run 08-01, Run 10-01, Run 10-03 and Run 12-02) under variation of the fracture residence time a filtration rate K_2 of 7.0 ± 0.9·10^{-3} h^{-1} can be estimated (Figure 2.44). This value is lower than the value of 2·10^{-2} h^{-1} estimated by filtration theory in [198]. Looking in detail on the colloid recovery data of Figure 2.44 a bi-exponential fit might be more suited, as the filtration rate is faster under high flow velocity (low residence time) compared to the long-term experiments. A linear fit of the long-term experiments Run 10-01 to 12-02 reveals a colloid filtration rate of K_2 of 2.4 ± 0.4·10^{-3} h^{-1} almost an order of magnitude lower than predicted in [198]. The observed discrepancy with a overprediction of colloid filtration, respectively the attachment factor, compared to experimental results was also observed by [199] for 40nm colloids and improved in a new collector efficiency equation that has to be tested for the Grimsel system and the results obtained within the KOLLORADO-II project.

The ^{22}Na, ^{137}Cs and ^{133}Ba case. Analysis of the weakly sorbing tracers by γ-spectrometry performed by PSI-LES and KIT-INE showed very good conformity and revealed recoveries for ^{22}Na, ^{137}Cs and ^{133}Ba of 64 %, 10 % and 1 %, respectively (Figure 2.45). These data are confirmed in addition by analysis of sample aliquots taken from the waste tanks, where the complete eluted water volume of 4100L covering the experimental duration of 114 days was collected (Table 2.12). For ^{137}Cs and ^{133}Ba the quantified recovery between the integration of the BTC based on the samples taken for laboratory analysis and the analysis of the total recovered extraction volume is in good agreement, whereas for the ^{22}Na recovery a significant higher recovery of 74.9 % from the waste tank could be quantified. Taken into account the measurement of 0.2007 ± 0.0249 Bq/mL ^{22}Na in the last sample analyzed (sample #96) this discrepancy clearly arises from the fact, that the full BTC is not covered by the samples analyzed. For ^{137}Cs and ^{133}Ba no activity could be detected from sample #64 and sample #43, respectively showing that here the full BTC was covered analytically.

Based on the observed recovery of 8.4-10 % for ^{137}Cs tailing into account the initial quantitative association to montmorillonite colloids the sorption is clearly reversible [200]. If full reversibility is on hand cannot be conclusively judged based on Run 12-02 and additional experiments under higher residence time would be needed.

Table 2.12: Composition of tracer cocktail Run 12-02 given in mol/L and total activity as well as the colloid associated fraction in the cocktail. Background electrolyte is original Grimsel groundwater.

Colloid/ Tracer	Recovery	Sample region/ time
Colloids		
LIBD on site	48%	up to 34.7d
Al signal	44 - 49%[§] 56 - 61%[$]	Sample 1-96 (27.3d)
Ni signal	51 - 52%	Sample 1-96 (27.3d)
Amino-G	100% (in line)	Sample 1-96 (27.3.d)
^{22}Na	64% (75.9%)*	Sample 1-96 (27.3.d)
^{133}Ba	1% (0.6%)*	Sample 1-96 (27.3.d)
^{137}Cs	10% (8.4%)*	Sample 1-96 (27.3.d)
^{232}Th	not quantified	Sample 1-96 (27.3d)
^{237}Np	4-5%	Sample 1-96 (27.3d)
^{243}Am	21-22%	Sample 1-96 (27.3d)
^{242}Pu	30-35%	Sample 1-96 (27.3d)

* The data given in brackets was determined by analysis of the waste tanks (4100L total extracted volume, 114 days experimental duration).

[§] Background Aluminium- signal of 28 ppb assumed. [$] Background Aluminium- signal of 25 ppb assumed.

The ^{232}Th, ^{237}Np, ^{243}Am and ^{242}Pu case. All injected radionuclides including the strongly sorbing tri- and tetravalent actinides could be detected in the effluent. For the initial quantitatively colloid associated actinides Am(III) and Pu(IV) a recovery of 20-21% and 30-35%, respectively, could be quantified. Np recovery is significantly reduced to ~4-5 % in comparison to the CRR experiment of 82 ± 4 % [23], which hints to a kinetic controlled Np(V) reduction observed through the increased residence time in Run 12-02. Assuming equilibrium conditions reached within Run 12-02 concerning Np redox speciation the recovery can be used to estimate via the Pourbaix diagram shown in Figure 2.47 the in-situ redox conditions prevailing during the experiment. Based on the recovery of 4-5% a maximum $Eh_{(SHE)}$ of -120mV could be predicted, which is lower than the value of -70 mV taken by [201] for thermodynamic calculations in the Grimsel groundwater and lower than the value of -88 mV calculated for a oxidation of Fe(II) contained in biotite to $Fe(OH)_3(s)$, but considerable higher than the Eh value of -377mV for the SO_4^{2-}/HS^- couple [201] determining the in-situ redox conditions.

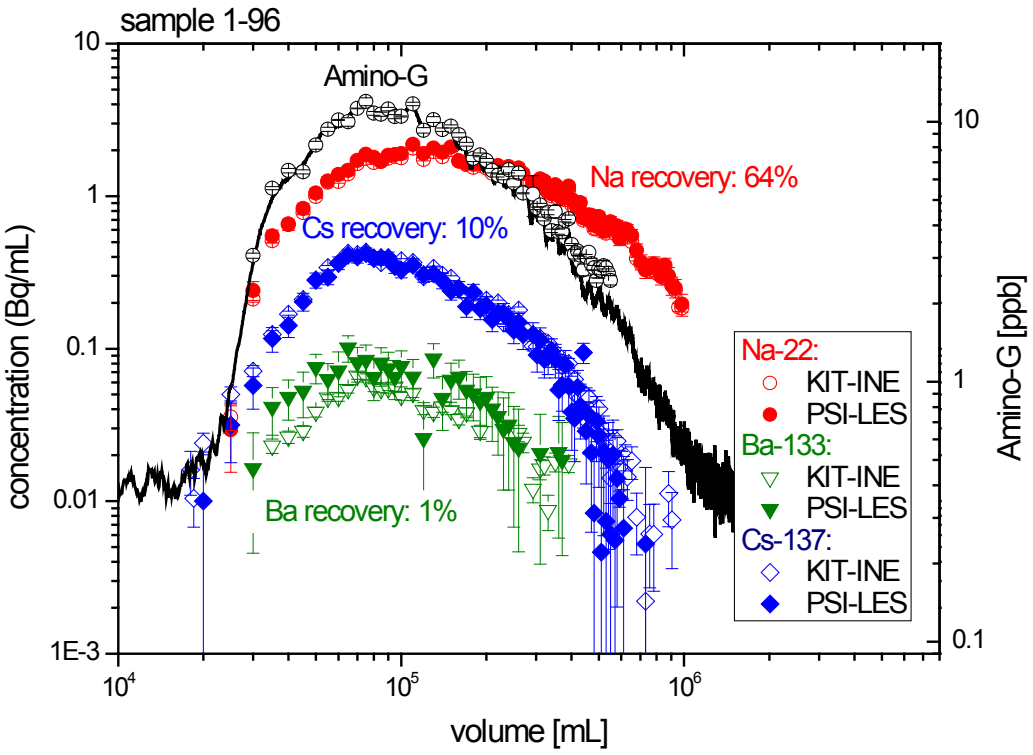

Figure 2.45: Breakthrough curves of conservative tracer Amino-G; solid black line on-site flourescence monitor data and open black circles INE off site fluorescence measurements using an Amico-Bowman Series II spectrofluorimeter (AB2). Gamma- spectrometry data from PSI-LES and INE for Na-22, Ba-133 and Cs-137 are inserted and recovery is given

Based on the long-term monitoring data at the CFM site via flow through cells $Eh_{(SHE)}$ < -200 mV seems to be a realistic approximation. However, based on the very low Fe concentrations of ~$3 \cdot 10^{-9}$ M it is questionable what potential is detected by the redox electrode. The rising edge of the Th breakthrough curve is very similar to the one measured for Pu and the peak maximum obtained definitely higher in comparison to Pu, indicating slower sorption reversibility and therefore higher recovery (Figure 2.48). However, precise recovery calculations cannot be made, as the data scatter in the tailing would results in recoveries > 100%. The exact reason for this scatter is currently not understood and a challenge for the next experiments planned.

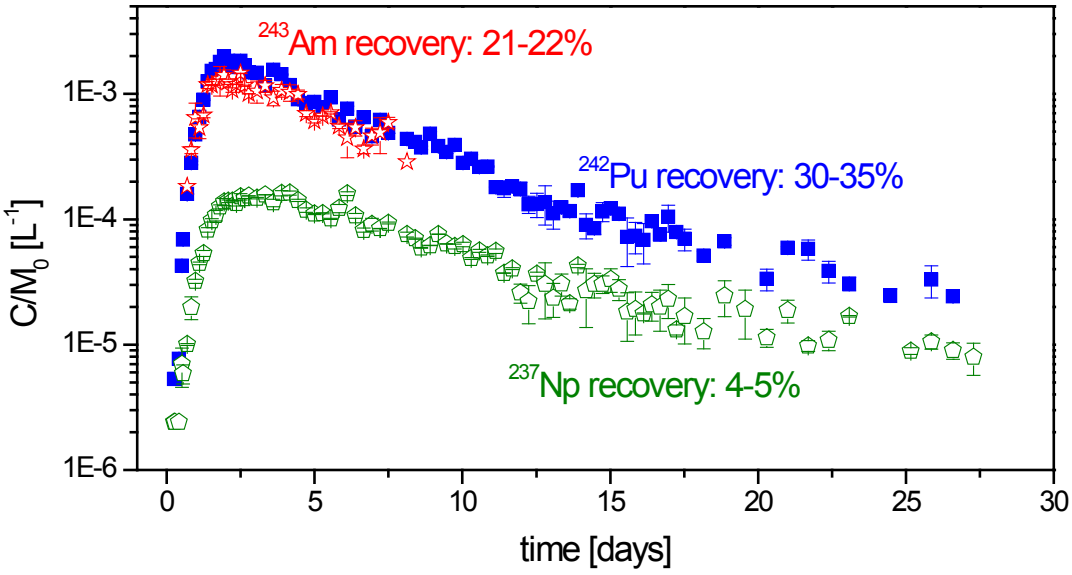

Figure 2.46: Breakthrough curve of the colloid-associated trivalent ^{243}Am(III) and the tetravalent ^{242}Pu(IV). ^{237}Np is additional shown, which was injected in the pentavalent state. All data is normalized to the injected mass M_0 for comparison and recovery is given.

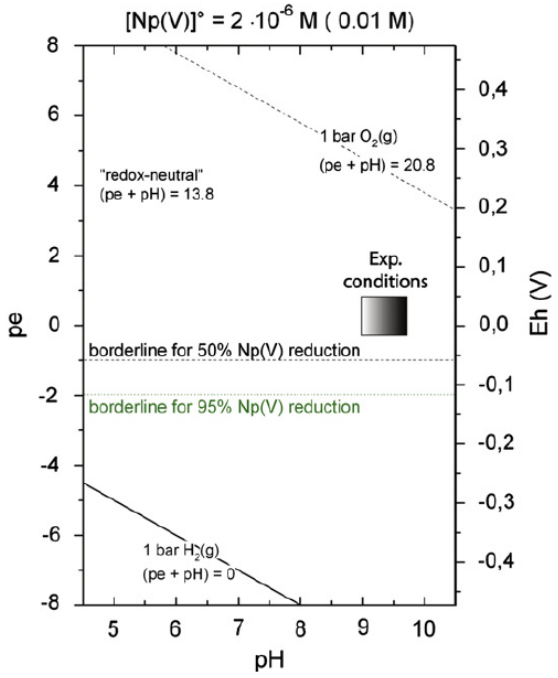

Figure 2.47: Neptunium Pourbaix diagram showing the pH indepent borderline (pH 5.5 to 10.5) of 50% Np(V) reduction and 95% Np(V) reduction. As square experimental conditions of laboratory batch experiments are shown. Graph adapted from Huber et al. [202].

In summary, earlier field colloid migration tests at the GTS conducted within the CRR (Colloid and Radionuclide Retention) experiment were limited by relatively short residence times and high flow velocity of the tracer in the fracture [1,2]. CFM field migration experiments have been conducted throughout the period from 2008 to 2012 reducing successively the flow velocity to near-natural flow conditions and therefore establishing higher tracer residence times in order to quantify retention/sorption reversibility of colloid-bound radionuclides. The results showed a surprisingly high recovery of both the bentonite colloids and the colloid associated tri- and tetravalent elements, not expected from previous experiments conducted within the CRR project in the same shear zone. The data of Run 12-02 clearly show the mobility of bentonite derived montmorillonite colloids under near-natural flow conditions in the MI shear zone of the Grimsel Test Site.

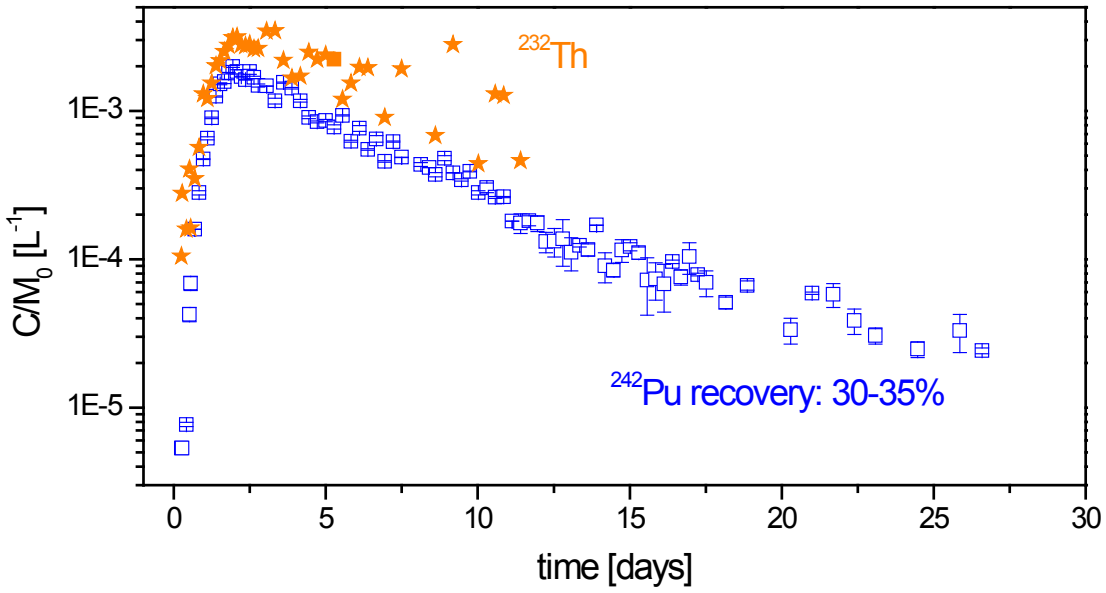

Figure 2.48: Breakthrough curve of the colloid-associated tetravalent actinides ^{232}Th and ^{242}Pu (for comparison). All data is normalized to the injected mass M_0 for comparison and recovery is given for Pu.

Size distribution analysis by LIBD and SPC showed for all experiments no size fractionation effect in the colloid breakthrough. This lack of size exclusion phenomena in combination with high colloid recovery indicates a broad channel („highway“) as flow path for the CFM experiments. Overall, the CRR and CFM project results obtained so far clearly demonstrate the sensitivity of colloid transport on flow path geometry/heterogeneity of the fracture/shear zone and demonstrate the slow desorption of bentonite colloid bound metal ions especially for the tetravalent elements.

Conclusions

The following conclusions can be drawn:

- Control of the hydraulic system has allowed to further decrease in gradients and consequent increase in travel time.
- The established flow velocity and gradient in the MI shear zone is more relevant to post-closure situation with 1% gradient and ~10^{-5} m/s flow velocity while maintaining high recovery.
- The In situ colloid/homologue tracer tests demonstrate:
    - Radionuclide/homologue colloid associated transport over increasing residence time detectable in the MI shearzone, which is a proof of concept for the planned long-term in situ test monitoring bentonite erosion.
    - Radionuclide/Homologue recovery is lower for trivalent actinides compared to tetravalent actinides and in turn the sorption reversibility faster for An(III) compared to An(IV).
    - Overall, the bentonite colloid sorption reversibility kinetics are faster in the in-situ experiments than observed in batch type studies.
    - Redox reactions faster compared to lab batch-type studies, which is a clear result from the more reducing redox conditions established in-situ.
- The megapacker sealing system works well and is ready for the long-term in-situ experiment.

Further details to the study presented in this chapter can be found in:

Geckeis, H.; Rabung, T.; Schäfer, T. (2011): Actinide - *Nanoparticle interaction: generation, stability and mobility.* In *Actinide Nanoparticle Research*, Kalmykov, S. N.; Denecke, M. A., Eds. Springer-Verlag: Berlin, Heidelberg, pp. 1-33.

Schäfer, T.; Seher, H.; Hauser, W.; Walther, C.; Degueldre, C.; Yamada, M.; Suzuki, M.; Missana, T.; Alonso, U.; Trick, T.; Blechschmidt, I., "*The Colloid Formation and Migration (CFM) project at the Grimsel Test Site (Switzerland): Results from the homologue tests. Geochim"*. Cosmochim. Acta 2009, 73, (13), A1168-A1168.

Schäfer, T.; M. Lagos; W. Hauser; S. Heck; F. Huber; M. Bouby; H. Geckeis; C. Degueldre; M. Yamada; M. Suzuki; S. Wold, K. Kontar; I. Blechschmidt, "*Pu, Np, Am transport under near-natural flow conditions at the Grimsel Test Site (Switzerland)"*. Environmental Science & Technology (to be submitted).

3 Modeling

The objectives of flow and transport modeling are manifold. Modeling of the flow field and the transport of ideal tracers aims at understanding the flow conditions in the Grimsel shear zone and the impact of the different dipoles on the flow field. Further, predictions about the impact of reduced flow conditions – as planned in future homologue tests – are possible. Flow and transport modeling of a well characterized fracture in a bore core aims in understanding of the effect of heterogeneities on flow field and transport of tracers. Finally, the application of transport models including kinetically-controlled sorption reactions to describe the interaction between radionuclides, colloids and sediment matrix yields – based on the results from the experimental program – in understanding the impact of the different processes on the shape of the break-through curves and on the recovery of the radionuclide tracers. It furthermore contributes to the qualification of the codes and sets the basis for calculations with regard to the long-term safety of deep geological repositories.

3.1 CFM hydraulics and transport modeling

3.1.1 Numerical modeling of groundwater flow and solute transport through a shear zone at the Grimsel Test Site

Abstract. The Colloid Formation and Migration (CFM) project aims to investigate and quantify the impact of colloids on the transport of radionuclides in a fracture taking into account the repository relevant spatial and temporal conditions. The in situ experiment is located in the Grimsel underground laboratory in Switzerland [193]. In the second phase of this project, different tracer tests with uranine and/or amino-G as conservative tracers were performed. Prior to the tracer tests, the experimental tunnel was equipped with a new 3m-diameter surface packer system. The scope of this packer was to avoid uncontrolled flow rates towards the open tunnel, to reduce the hydraulic gradient in the shear zone and to achieve longer tracer travel times. At this stage of the project, the development of simple numerical models using the measured regional hydraulic head data were performed. The results obtained provide a fairly consistent picture of the pathway around the CFM and contributed significantly for further model simulations.

The objectives of the actual numerical modeling are to analyze the conservative tracer data to identify hydraulic and transport processes and effective parameters and also to use the modeling results to predict the outcome of a hot tracer test performed in the same geometry and hydraulic conditions.

In this contribution a series of tracer tests was simulated numerically. It was assumed that the groundwater flow and the solute transport take place in fractures filled with fault gouges,

and the shear zone at the test location is plane which allows a two dimensional approach for the model geometry. The mathematical model is based on the Darcy's law for groundwater flow and the advection-dispersion equations for solute transport with a linear sorption in the fracture material. However, the model represents a planar confined porous media with a constant porosity and an anisotropic permeability. The analyses were performed with the ADINA-F finite element code [56]. A comparison of the transport model results and test data is presented as breakthrough curves at the extraction holes where the tracers concentration is plotted versus time. The overall agreement of model results and experiment data is reasonable and should provide a useful assessment of the accuracy of the final test model.

Material and Methods

Simulation of the conservative tracer tests 09-01 and 10-01

After the improvement of the CFM-mega-packer and the installation of the new injection and extraction flow monitoring system the tracer tests 09.01 and 10.01 were performed between the borehole CFM 06.002 (injection point) and the Pinkel surface packer (extraction point). The boundary conditions for the both tests were:

- Tracer injection in CDM 0602i2 borehole;
- Extraction from Pinkel surface packer;
- Following through recirculation and zero net injection in the borehole CDM 0602 i2.

The aims of these analyses are to calibrate the existing model and determine its effective hydraulic and transport parameters and to determine the suitability of the shear zone interval for the planned long-term in situ test. For model calculation it was assumed that the groundwater flow and the solute transport take place in fractures filled with fault gouges, the shear zone at the test location is plane which allows a two dimensional approach for the model geometry.

The layout of the two tests is shown schematically in Figure 3.1. The distance between injection and extraction borehole is about 6.08 m and both tests were performed in recirculation flow rate of 45-50 ml/min to provide a comparison with the transport conditions similar to those when a bentonite source will be emplaced. The tests parameters are listed below in Table 3.1. The detailed description is provided in the experimental report [203].

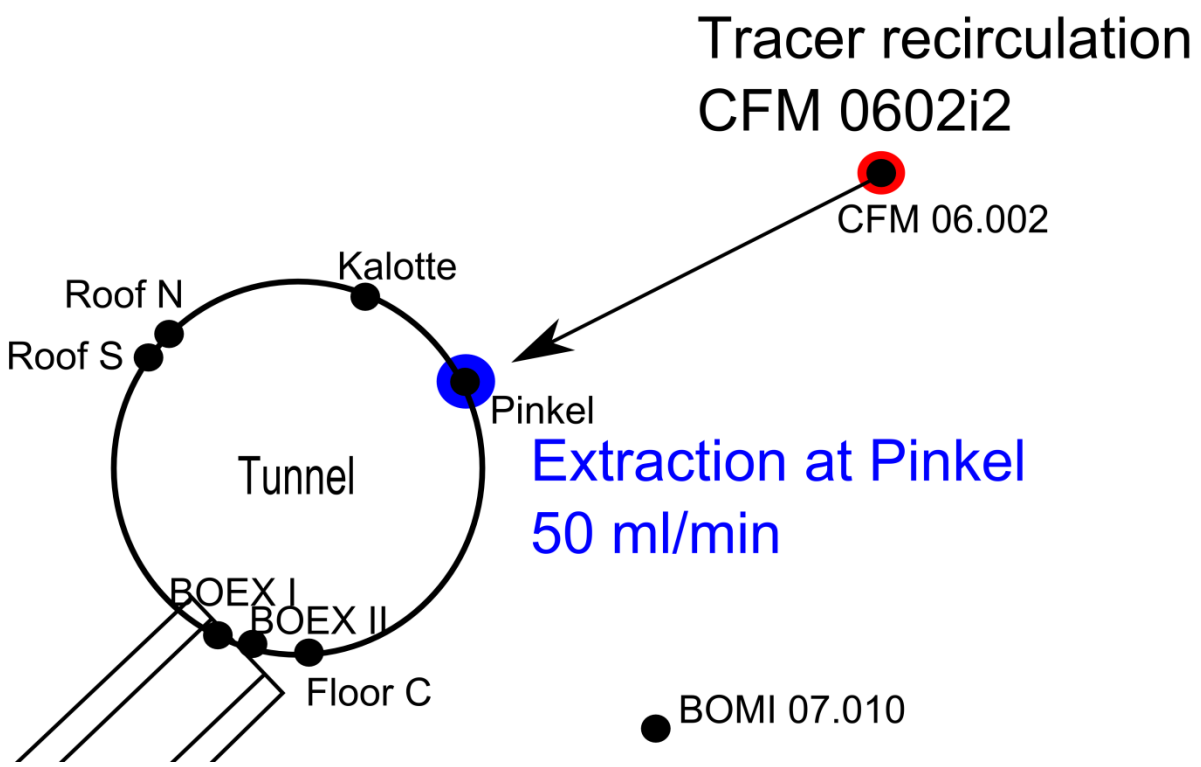

Figure 3.1: Layout of tracer test 09-01 and 10-01. The figure shows the position of the injection and extraction boreholes in the plane of the shear zone.

Table 3.1: Tracer test 09-01 and 10-01 parameters.

Parameters	**Test 09-01** Uranine	**Test 10-01** Uranine
Initial concentration [ppm]	50	5
Injected tracer volume [ml]	100	1000
Recirculation flow rate [ml/min]	~48	~48
Outflow rate Pinkel [ml/min]	~52-100	~48.4-46.8
Hydraulic gradient between CFM 06.02i2 and Pinkel [m/m]	0.0036	0.0012-0099
1st Peak at extraction site [min]	721	1676

The tracer test 10.01 with colloid/homologue include also conservative tracer such uranine and bromide. For illustration, the calculation results of the tracer test 10.01 (Homologue Test 1) are presented in Figure 3.2 to Figure 3.4. The comparison of the numerical results and measured breakthrough curves for uranine and bromide at the extraction hole is plotted in Figure 3.3.

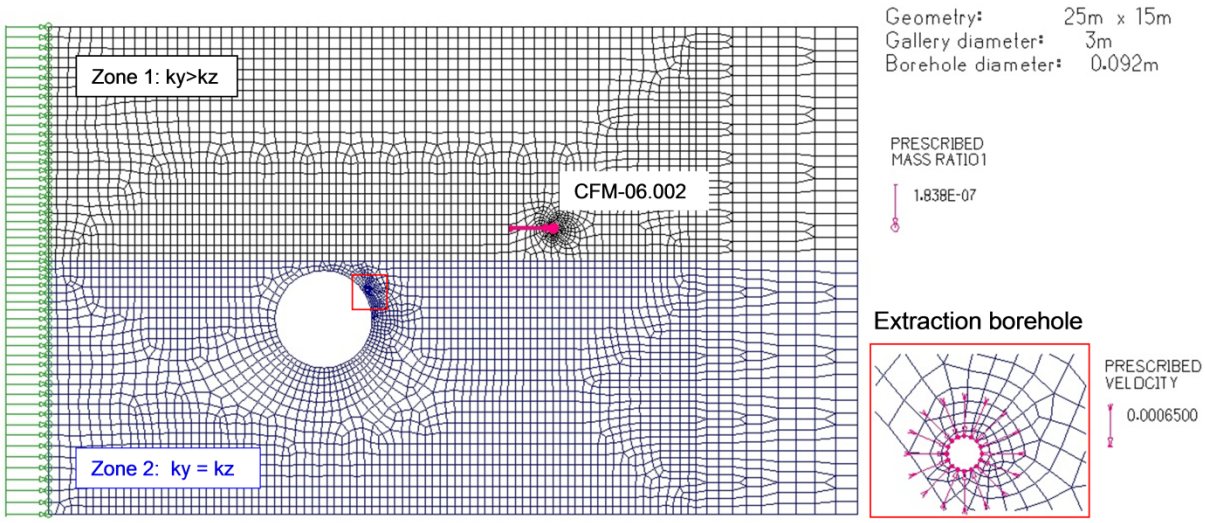

Figure 3.2: 2D-finite element model for the simulation of tracer tests. The model is composed of two zones with different hydraulic properties.

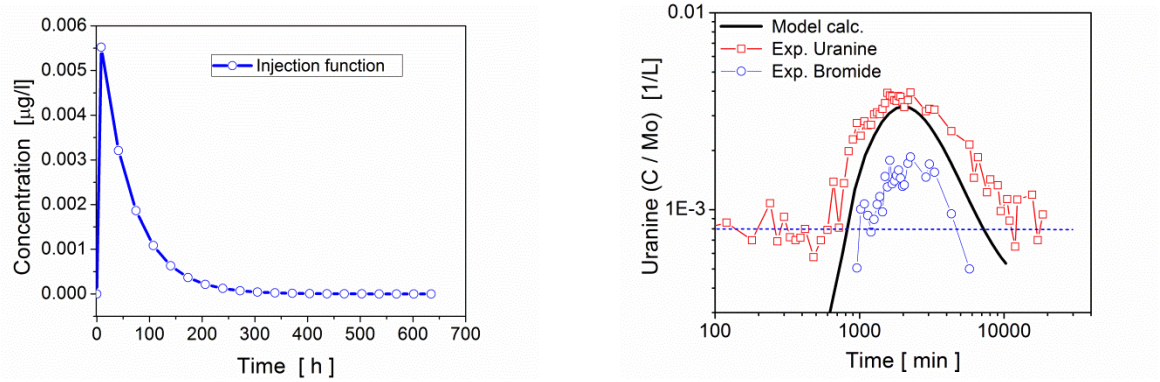

Figure 3.3: (Left) Measured input uranine function for tracer test 10-01. (Right) Calculation breakthrough curve and experiment measurements for uranine and bromide (logarithmic presentation).

The overall agreement of model results and experiment data is reasonable. However, the comparison of calculation results in the tailing part shows some differences. The long tailing seems to be induced by progressive release of the tracer late in the injection interval due to the fluid recirculation process. Table 3.2 shows the averaged hydraulic and transport parameters obtained from model calibration. Furthermore, these model parameters will be used to simulated the later tracer tests performed with Amino-G as a conservative tracer solute.

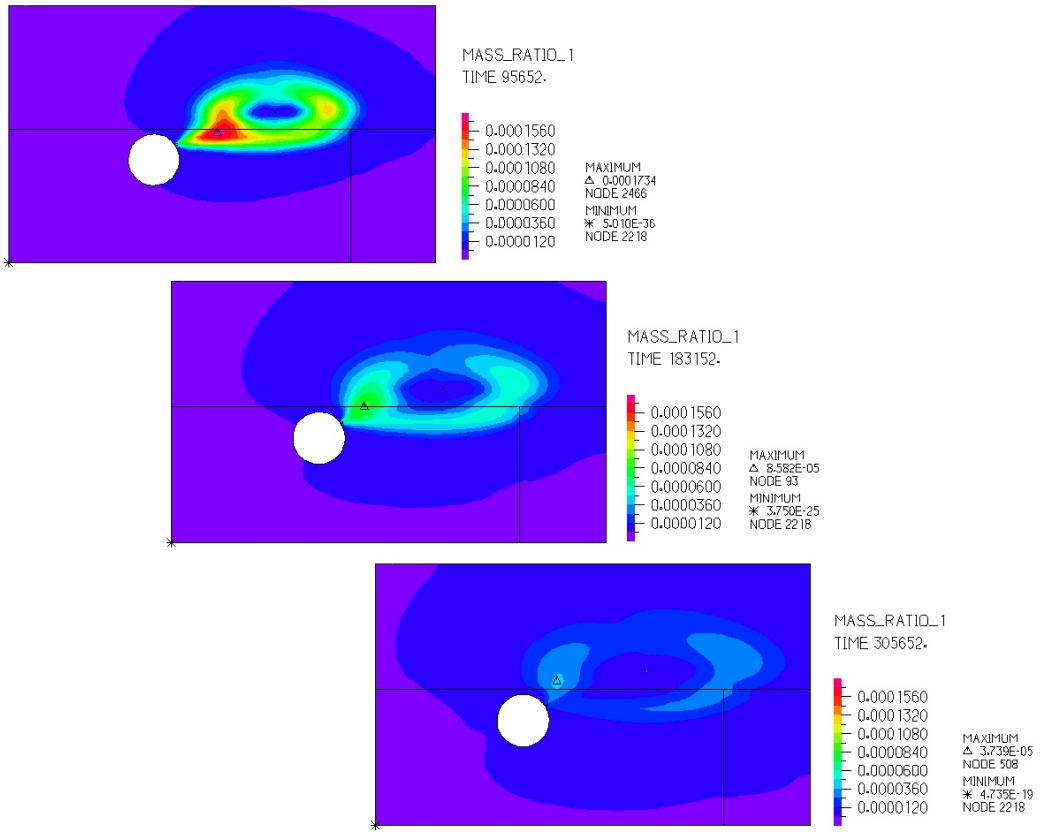

Figure 3.4: Distribution of the uranine concentration after different times (The time is given in seconds).

Table 3.2: Hydraulic and transport parameters of two different model zones.

Parameters	**TEST 09-01 & TEST 10-01**	
	Zone 1	Zone 2
Flow porosity	0.10	0.12
Horizontal permeability (m^2)	2e-09	2e-09
Vertical permeability (m^2)	1e-09	2e-09
Longitudinal dispersion (m)	0.001	0.001
Transversal dispersion (m)	0.0002	0.0002
Diffusion coefficient (m^2/s)	2e-11	2e-11

Simulation of the tracer tests 12-01 and 12-02

During last year the tracer test 12-01 was conducted to evaluate conservative tracer responses at the Pinkel surface packer when a small net injection rate was imposed in CFM 06.002i2 (because no tracer responses were observed at the extraction well in the 11-0x series tests. The tracer test 12-02 was conducted under the same injection and extraction

conditions as 12-01 but with the injection of a cocktail containing radionuclides and bentonite colloids. In Tab. 3 the extraction and injection flow rates, the residence times in the shear zone are presented.

Table 3.3: Tracer test 12-01 and 12-02 parameters.

Parameters	**Test 12-01** Amino-G	**Test 12-02** Amino-G (AGA)
Initial concentration [ppm]	50	1646
Initial injected mass [mg]		4.5-3.7
Injected tracer volume [ml]	100	100
Recirculation flow rate [ml/min]	0.395	0.49-0.36
Outflow rate Pinkel [ml/min]	25	25
1st Peak at extraction site [min]	721	1676

The local flow pathways around CFM 06.002i2 seem to be sliding influence due to the drilling of monitoring holes (CFM 11.001, 11.002 and 11.003) . The detailed studies of the flow field near the CFM 06.002i2 and monitoring borehole will be presented in the next chapter. Due to the poor recovery of uranine in earlier tests of the series 11-0x it was decide to use in the tests 12-01 and 12-2 also Amino-G as an conservative tracer.

For the numerical analysis the model presented in Figure 3.2 was extended to avoid the influence of assumed boundary conditions on calculated solute transport over long in situ resident time. The far field geometry behave about 30 x 40m.

Table 3.4: Hydraulic and transport parameters of two different model zones after the first calibration.

Properties	TEST 12-01 & TEST 12-02	
	Zone 1	Zone 2
Flow porosity	0.10 (0.08)	0.12
Horizontal permeability (m2)	2e-09	5e-09
Vertical permeability (m2)	2e-09	2e-09
Longitudinal dispersion (m)	0.001	0.001
Transversal dispersion (m)	0.0005	0.0002
Diffusion coefficient (m2/s)	2e-11	2e-11

A comparison of the numerical fits and experimental data is presented as breakthrough curves where the uranine concentration is plotted versus time (Figure 3.5 left and right). The measured tracer input functions for both experiment are also shown in the Figures. As can be seen, the simulation results match the experimental data fairly well. Nevertheless, the overall agreement of model and experiment is reasonable. The recovery of the amino-G was about 95 %.

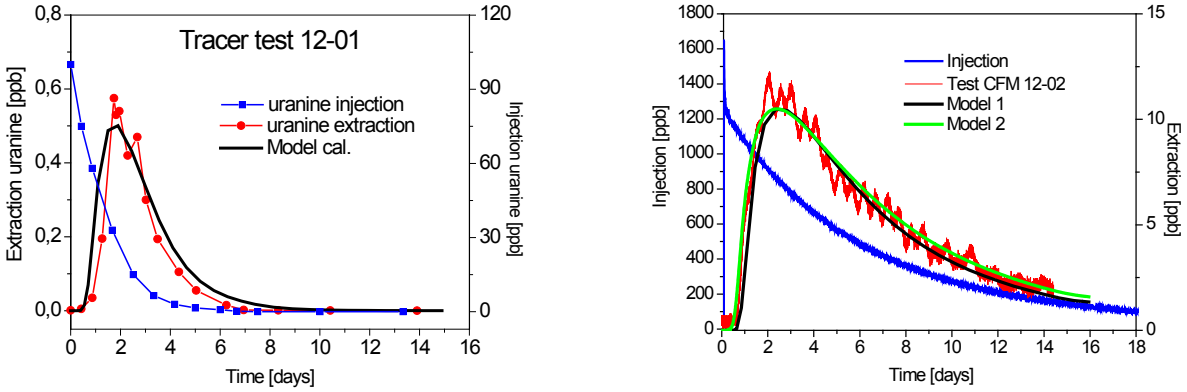

Figure 3.5: Comparison of measured and calculated breakthrough curves for uranine tests 12-01 in a dipole flow field. The injection concentration (blue curve) is also plotted. Comparison of measured and calculated breakthrough curves at the extraction well for test 12-02 with amino-G: (extraction at 25 ml/min and injection velocity ~0.4 ml/min).

Simulation of the flow field and solute transport in the near of CFM 06.002i2 and monitoring boreholes

In 2011, three observation/monitoring boreholes were drilled in the near vicinity (~40mm distance) of the injection borehole CFM 06.002. Figure 3.6 shows the layout of the monitoring boreholes in the plane of shear zone in vicinity of the existing CFM 06.002. In the test series CFM 11.001, 11.002 and 11.003 the monitoring boreholes were included in the flow pathway around the injection well CFM06.002. However, it seems that the drilling process of the monitoring boreholes has affected the hydraulic properties of the shear zone in the migration dipole.

In this numerical study, we will present the following case:

- In the central borehole CFM 06-002 (open) will be injected a tracer solute according an injection function with the injection flow rate of 10 ml/min.

- All the monitoring boreholes will stay open but from the borehole CFM 11- 003 will be extracted a small amount of groundwater (~ 0.1 ml/min)

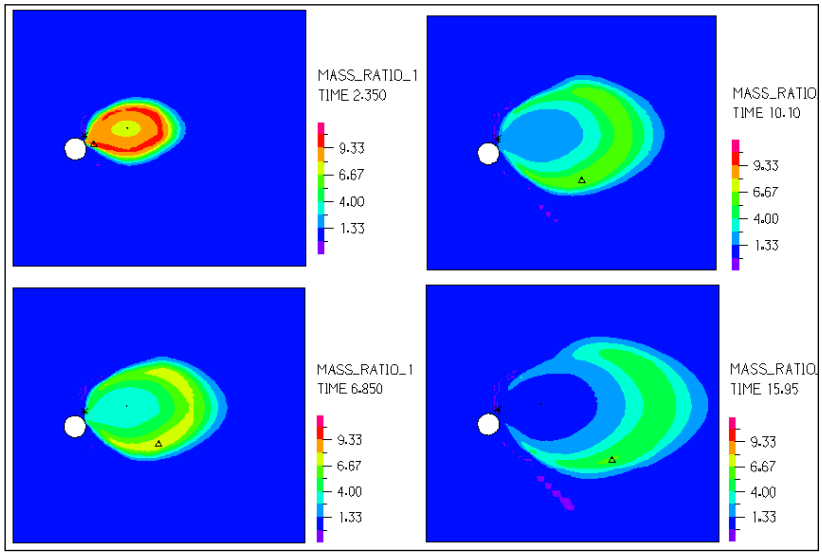

Figure 3.6: Test 12-02. Calculated distribution of the amino-G concentration (C/Mo) at different times (Tracer recovery ~ 90 %).

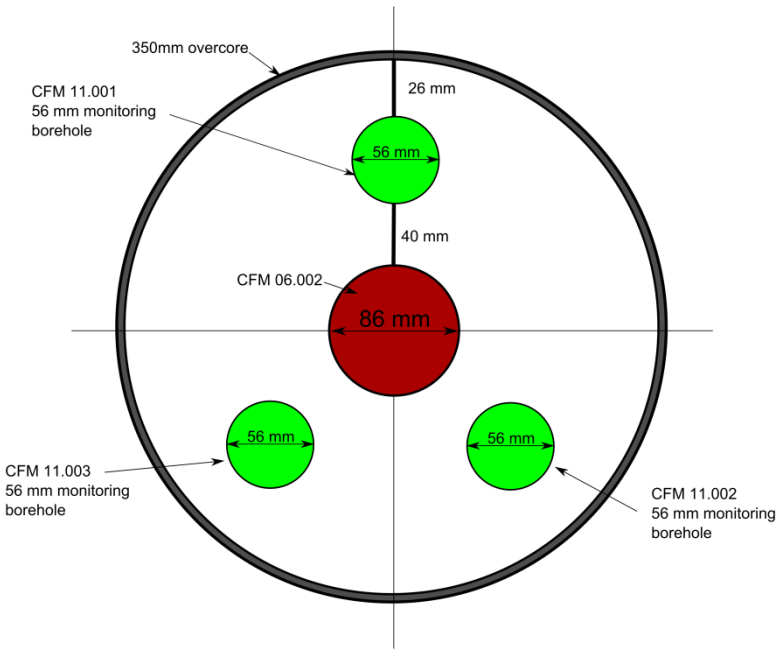

Figure 3.7: Layout of monitoring boreholes (CFM 11.001 to 11-03) around the injection borehole, CFM 06.002, in the migration shear zone.

In order to study the flow field and transport properties near the injection hole CFM 06.002 and the new monitoring boreholes CFM-11.001-003, computational fluid dynamics (CFDs) simulations with ADINA-F code were performed. The finite element model and boundary conditions are shown in Figure 3.7 and Figure 3.8. The 2D- model is composed of two do-

mains in the plane of the shear zone, namely the saturated porous material of the shear zone (zone 1) and the open holes filled with groundwater in which the hydraulic head is nearly constant (zone 2). The model extension covers a domain of 1m x 1m and at the outer side of the geometry a groundwater flow velocity of 10^{-5} m/s was assumed. The ability of the model to calculate the fluid flow in porous media and also in open boreholes allows to simulate different flow situations, expected near the main injection and monitoring holes. The model presented here was used to make generic studies and to calculate the flow field and the transport behavior around and into the monitoring boreholes over a short timescale.

Figure 3.9 shows the calculated fluid velocity field, the pressure field, and the distribution of the tracer at different times after injection of a hypothetical tracer in the CFM-06.002 borehole. The assumed injection function is also plotted in this figure. It can be observed that the influence of extraction of a small amount of fluid (~ 0.3 ml/min) from monitoring well CFM-11.003 is insignificant for the expected long-term migration through the planned large dipole experiment. The calculated breakthrough of tracer at the monitoring borehole CFM-11.003 is presented in

Figure 3.11. For instance, the curve has a qualitative character because the dilution in the open borehole was not correctly assumed.

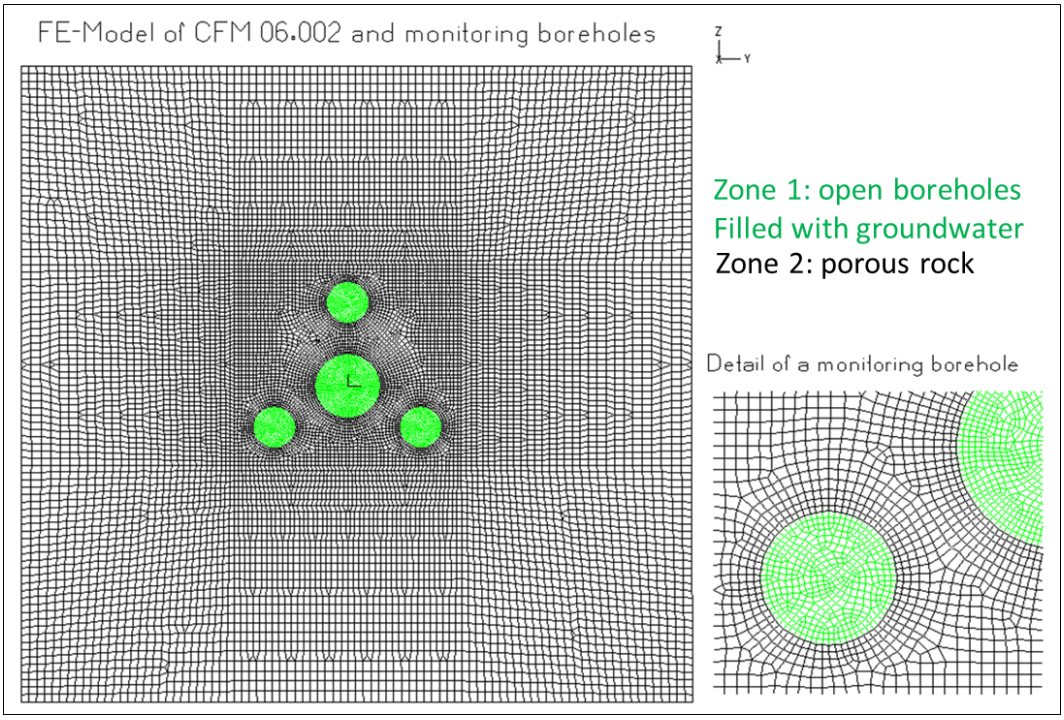

Figure 3.8: Finite element mesh used for simulation of flow field and solute transport (left: detail discretization of monitoring boreholes).

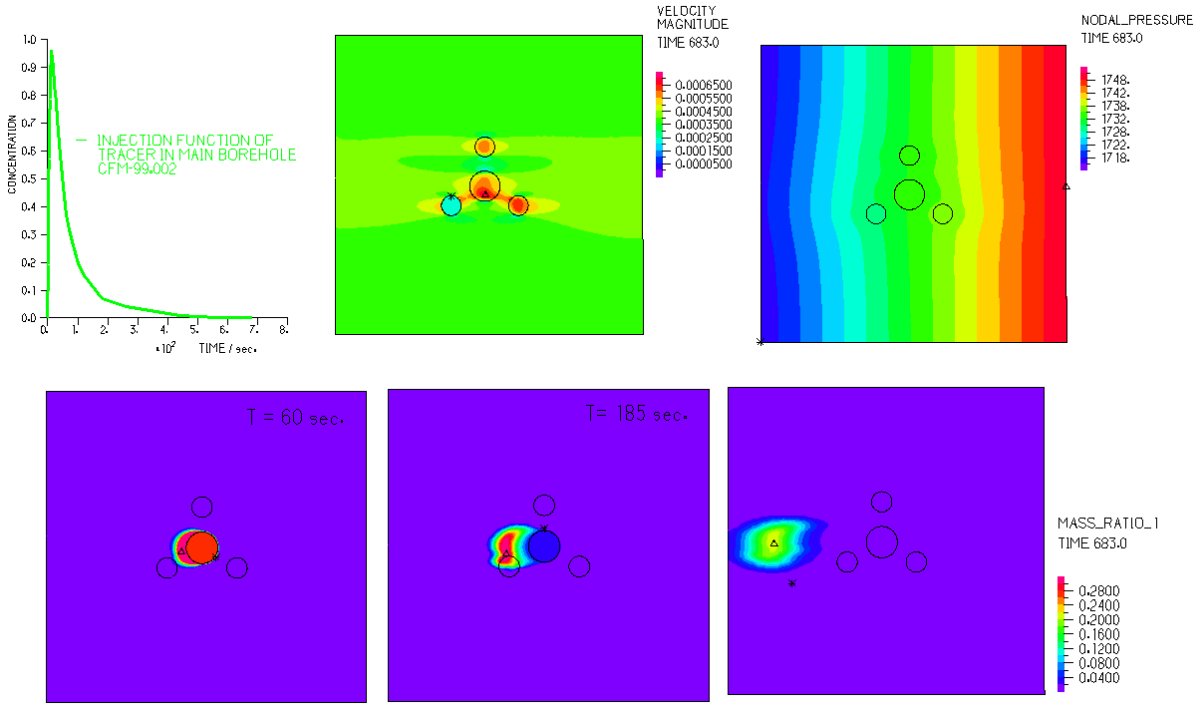

Figure 3.9: Calculation results for the study case: Injection of tracers in central borehole CFM06-0002 and stepwise extraction at 0.3 ml/min from monitoring holes CFM 11.003. Distribution of pore pressure and stream lines (upper plot) and the tracer distribution after different times.

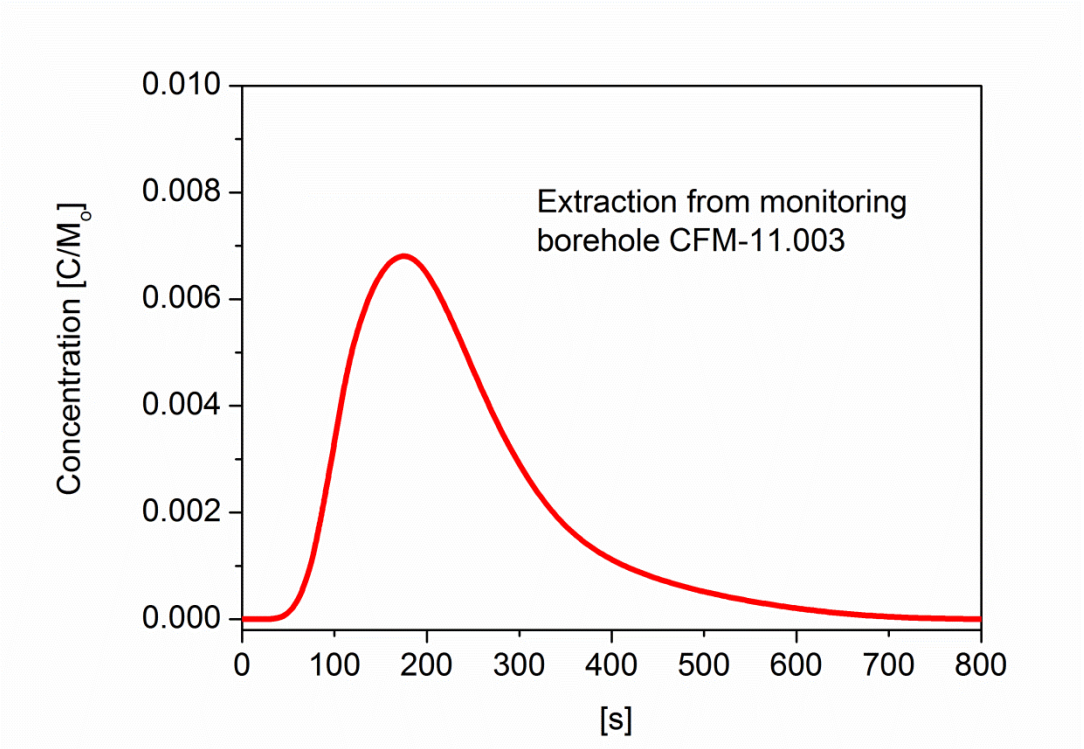

Figure 3.10: Calculated breakthrough curve of the tracer at the monitoring hole CFM-11.002.

Conclusions

The field data and modeling results provide a fairly consistent picture of the flow and transport characteristics in the shear zone at the location of the CFM experiments.

The 2D model considers uniform but anisotropic permeability and constant porosity in different zones. Therefore, the estimated flow and transport parameters must be considered as an approximation of the real structure which indicates heterogeneities in the distribution of hydraulic conductivity. The hydraulic and transport properties obtained from this calibration work on the new tracer tests show a preferential pathway for fluid migration. The application of relatively low velocity at the injection/extraction boreholes seems to induce a long residence time in the shear zone; the dispersive/diffusive processes become dominant.

Regarding the results of the simulation of monitoring boreholes, the sampling of 0.3 ml/min will not affect significantly the migration of injected solute into the large dipole.

In the next project step, further work is required to explore how the uncertainties on parameter estimation and the subsequent predictions at lower hydraulic gradients are affected by the choice of the present conceptual model. However, the tests with homologue radionuclides will be simulated using the transport parameters obtained by fitting the conservative tracer tests.

3.1.2 2D flow and colloid facilitated transport modeling including kinetically controlled sorption processes

Abstract

2D flow and transport calculations were performed to describe field dipole experiments in the shear zone at the Grimsel Test Site (see section 2.2.2) with FEBEX bentonite colloids and lanthanides (as homologues for tri- and tetravalent actinides). After calibration of the flow model using the uranine breakthrough curve of one dipole experiment, the model was successfully applied to other dipole experiments conducted at the same dipole at different flow velocities using the same hydraulic parameters. Firstly, the results show that the interaction of the colloids with the fracture filling material can be reasonably well described by one set of parameters considering a weak reversible and an irreversible attachment process. Secondly, the breakthrough curve of the colloid-bound lanthanides as well as their mass recovery is additionally controlled by the desorption kinetics from the colloids. One observation is a decrease of the desorption rate with travel time. The desorption rates obtained from the field experiment at longer residence time agree well with results from the reversibility batch experiments, described in section 2.1.1 and [74]. On the basis of the results from the homologue experiments a predictive simulation for the first radionuclide tracer experiment was done. The results agreed well with the experiment, for the calculation with low desorption rates observed for the homologue experiment with longest travel time.

Introduction

Experimental background for numerical modeling

The simulations rely on field data gathered in the CFM campaigns as well as on supporting laboratory results. A detailed description of the experimental basis is given in section 2.2 (field experiments) and 2.1 (lab experiments).

One group of experiments are dipole tests in the shear zone using FEBEX bentonite colloids (Ca-bentonite), injected together with radionuclides or homologues under defined flow conditions, which are similar to those expected in natural systems and are thus close to repository-relevant conditions. In a first step, the flow field and the transport of ideal tracers are modeled in order to understand the flow conditions in the Grimsel shear zone and the impact of the different dipoles on the flow field. In a second step, these transport models are applied to describe the interaction between radionuclides, colloids and sediment matrix, including kinetically-controlled sorption reactions, and to identify the relevant interaction processes during transport.

This report focuses on model simulations of the selected dipole experiments CFM RUN 08-01/02, CFM RUN 10-01, CFM RUN 10-03 and CFM RUN 12-02. A specific feature is the variation in outflow rates and therewith the variation of transport times over a range of

The specific objectives of this work can be summarized as follows:

- To formulate a suitable and fairly general model,
- To interpret field tests with model simulations to infer parameters, and
- To compare inferred parameters to results of laboratory experiments or independent estimates.

The simplest and most robust interpretation possible is used. Finally, the implications are interpreted by long term extrapolation.

The field tracer tests CFM RUN 08-01/02, CFM RUN 10-01, CFM RUN 10-03 and CFM RUN 12-02 have been performed in a dipole between the injection interval of borehole CFM 06.002 and the extraction point at the surface packer at the tunnel wall (Pinkel) as illustrated in

Figure 3.11. The distance between injection borehole and extraction point (Pinkel) is ca. 6.2 m. Details of the experiments are described in [204].

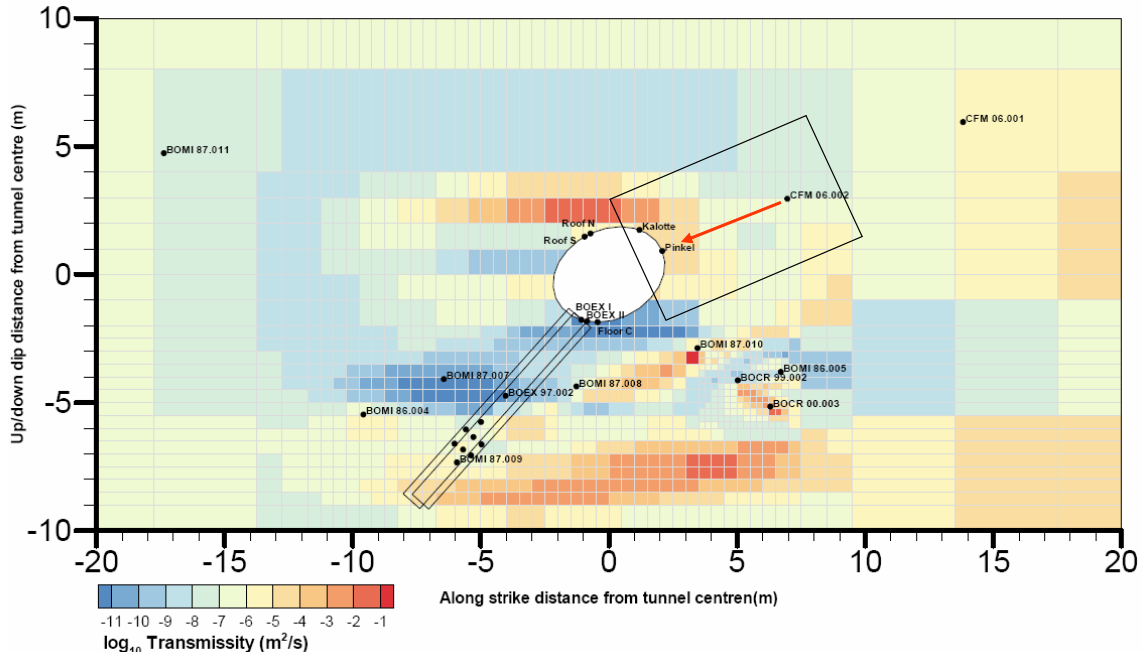

Figure 3.11: Transmissivity field and location of boreholes in the shear zone (after [205]). The dipole between borehole CFM 06.002 and the extraction point (Pinkel) for the CFM experiment is indicated by the red arrow.

While CFM RUN 08-01/02 and CFM RUN 12-02 were performed with a defined inflow, CFM RUN 10-01 and CFM RUN 10-03 were performed as point dilution tests. The transport velocity of the fluid and therewith the residence time of the tracers is mainly determined by the extraction flow rate at Pinkel, which is varied down to a range approaching the natural flow conditions within the shear zone. Relevant data for modeling including the injected amounts of the conservative tracer, bentonite colloids and homologue tracers are shown in

Table 3.5. Injection functions of all tracers have been monitored and provided for modeling (mass normalized concentration = observed concentration divided by injected mass, Figure 3.12). While for CFM RUN 08-02, only an inert tracer was used, the tests CFM RUN 08-01, CFM RUN 10-01, CFM RUN 10-03 and CFM RUN 12-02 employed homologue tracers and colloids. Uranine was used as a conservative tracer for CFM RUN 08-02, CFM RUN 10-01 and CFM RUN 10-03 (Figure 3.13) and Amino G Acid (AGA) for CFM RUN 12-02. For CFM RUN 10-03 no reliable uranine breakthrough curve was obtained. The FEBEX bentonite colloids and the homologues were equilibrated for a few days in Grimsel water before injection into the dipole. It was shown that the homologues are almost completely (between 95% and 100%) bound to the colloids in the injection solution. The breakthrough curves for the colloids and homologues in CFM RUN 10-01, CFM RUN 10-03 and CFM RUN 12-02 are shown in Figure 3.14, Figure 3.15 and Figure 3.16.

Table 3.5: Inflow/outflow conditions, injected amount of tracers m_0 and recovery of conservative tracers for the considered field tests [204]. n.c. denotes that these data are not considered for modeling.

	CFM RUN 08-01/08-02	**CFM RUN 10-01**	**CFM RUN 10-03**	**CFM RUN 12-02**
Inflow [ml min^{-1}]	10	-	-	0.33
Outflow [ml min^{-1}]	165	48	10	25
Injected amount m_0 [mg] of tracers considered for modeling				
Conservative tracer				4.5
FEBEX bentonite colloids[1]				330
^{152}Eu	15.4	5	9	^{243}Am: $4.87 \cdot 10^{-5}$
^{159}Tb	15	30	210	^{242}Pu: $1.37 \cdot 10^{-3}$
^{178}Hf	-	$11.96 \cdot 10^{-3}$	$45.48 \cdot 10^{-3}$	
^{232}Th	14.3	$10.10 \cdot 10^{-3}$	$45.44 \cdot 10^{-3}$	$2.09 \cdot 10^{-3}$
^{22}Na	23.4	$12.78 \cdot 10^{-3}$	$51.64 \cdot 10^{-3}$	$8.7 \cdot 10^{-6}$
^{133}Ba	19.8	$14.87 \cdot 10^{-3}$	$49.78 \cdot 10^{-3}$	$2.66 \cdot 10^{-4}$
^{137}Cs				$2.81 \cdot 10^{-4}$
^{237}Np				$4.99 \cdot 10^{-3}$
Recovery of the conservative tracer [%]	99	84	90[2]	80

[1] based on Al content measured by ICP-MS

[2] recovery of CFM RUN 10-02, which was performed under same flow conditions as CFM RUN 10-03

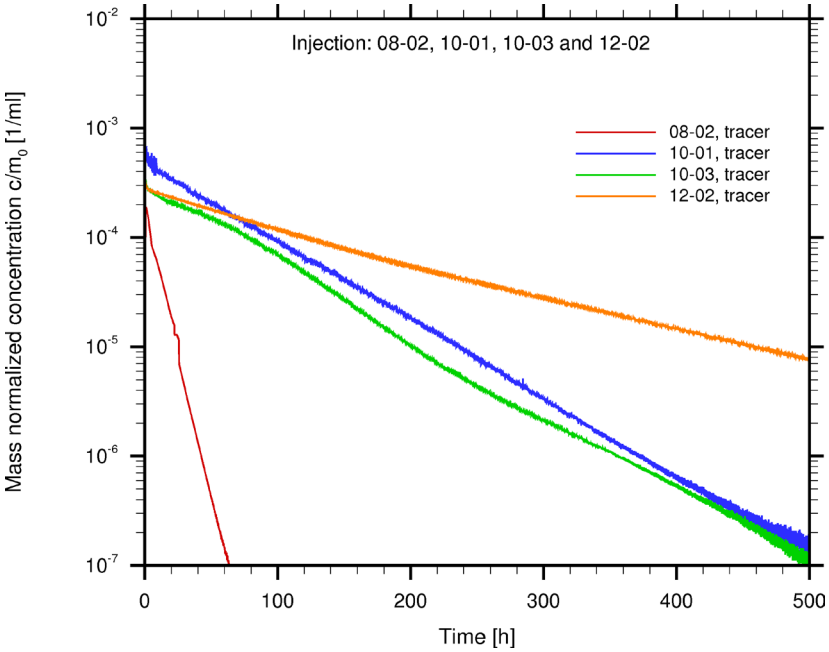

Figure 3.12: Mass normalized concentration injection functions (observed concentration divided by injected mass).

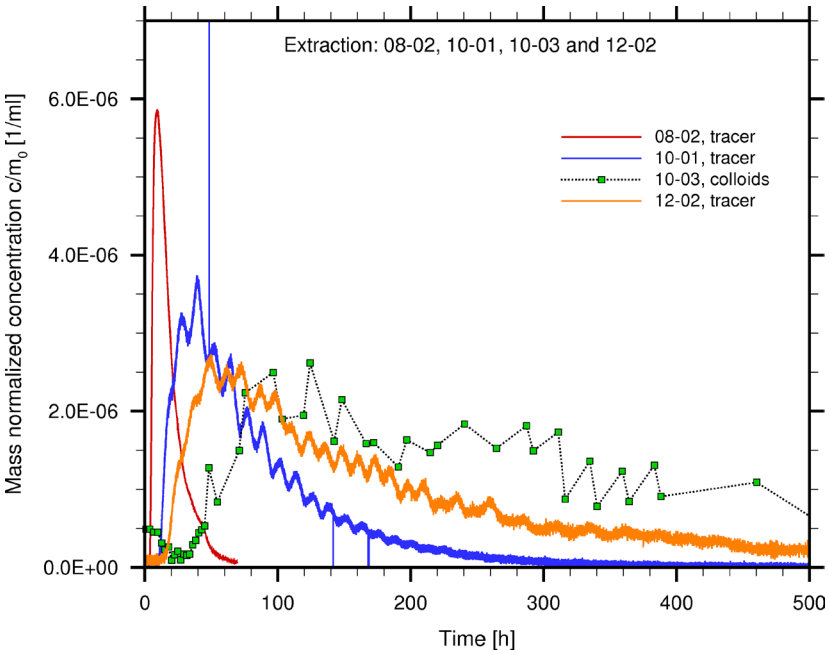

Figure 3.13: Mass normalized concentration breakthrough curves (observed concentration divided by injected mass).

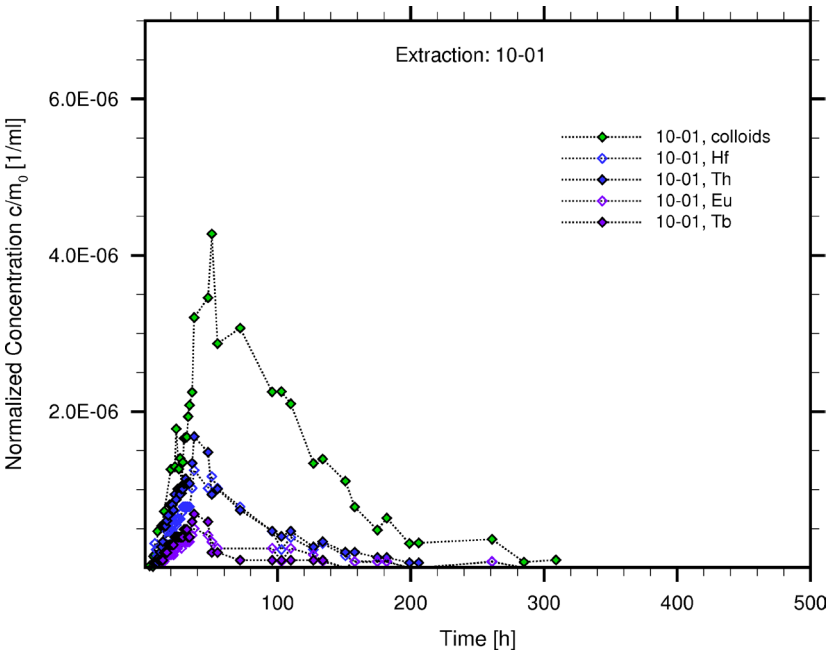

Figure 3.14: Mass normalized concentration breakthrough curves for colloids and homologues of CFM RUN10-01.

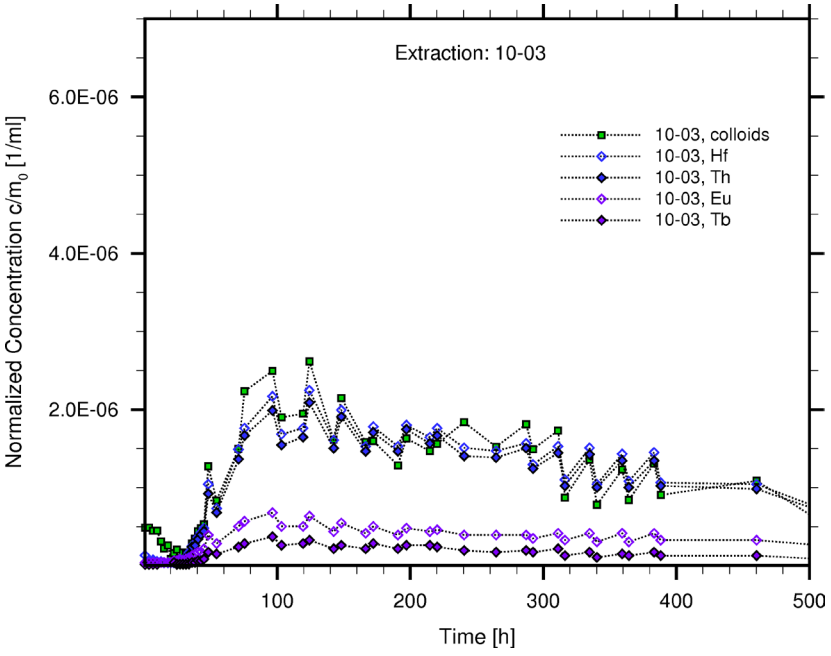

Figure 3.15: Mass normalized concentration breakthrough curves for colloids and homologues of CFM RUN10-03.

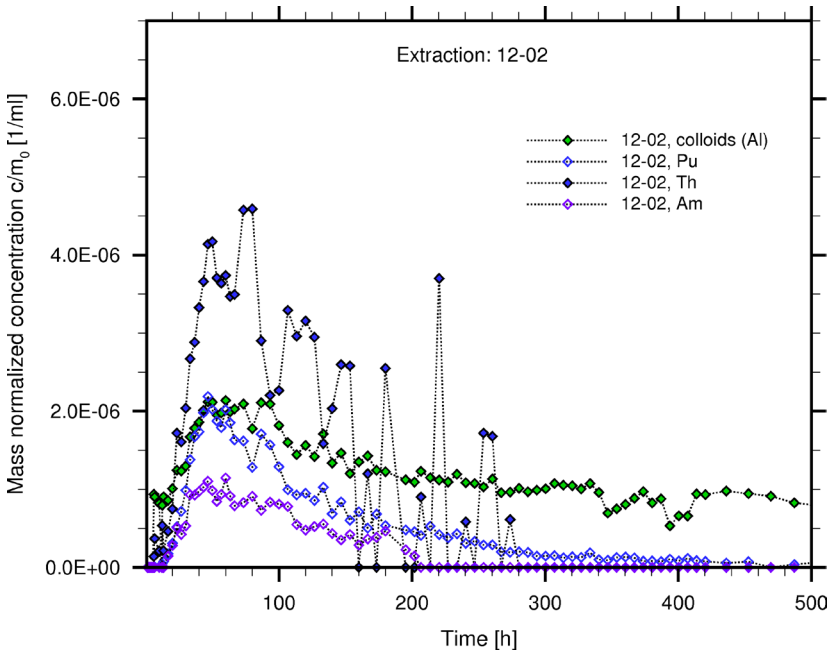

Figure 3.16: Mass normalized concentration breakthrough curves for colloids and homologues of CFM RUN12-02.

Conceptual framework

Flow

Transport calculations are based on the assumption of a steady-state flow field. The generalised Darcy law for two-dimensional groundwater flow [206] applies under consideration of the variable density and viscosity of the groundwater for density-driven flow [207, 208] (Equation 17):

$$v = -\frac{k}{\mu}(\nabla p - \rho g) \qquad \text{(Equation 17)}$$

where v is the Darcy velocity [L T^{-1}], k is the intrinsic permeability tensor [L^2], μ is the dynamic viscosity [M L^{-1} T^{-1}], p is the pressure [M L^{-1} T^{-2}], ρ is the bulk density of porous media [M L^{-3}], g is the gravitation vector [L T^{-2}] and where $\rho = \rho\,(c,T)$ and $\mu = \mu\,(c,T)$ with the concentration c of any substance in the groundwater and the temperature T of the groundwater. At the Grimsel Test Site the mineralisation of the groundwater can be regarded as constant and the temperature in the entire model domain is set to 20 °C, thus the density and viscosity are constant here. The groundwater flow is therefore described by the conservation equation for the total mass only (flow equation) [207] ((Equation 18):

$$\partial_t(\theta\rho) + \nabla \cdot (v\rho) = F \qquad \text{(Equation 18)}$$

Where θ is the porosity of porous media [L^3 L^{-3}] and F is the general expression of the sink-source (exchange) term.

Colloid transport and interactions

In order to describe the field experiments colloid filtration processes and kinetically controlled sorption and desorption processes are considered. Description of transport and interaction processes are based on previous works, see e.g. [55].

Transport

The medium is considered to be a three-dimensional, heterogeneous aquifer. The hydraulic conductivity K is a random space function. Groundwater flow is driven by a hydraulic gradient towards a receptor (supply well), where $v\ (v_1\ ;\ v_2\ ;\ v_3\ )$ [L T^{-1}] is the (spatially variable) fluid velocity at location $X\ (x; y; z)$, due to the spatial variability of the hydraulic conductivity.

Considering a tracer test conducted between injection point B and detection (pumping) point A, the flow takes place between B and A, from B to A along a mean trajectory defined by $X\ (t; x_B)$. Thus the transport of particles (colloids, tracer ions or molecules) can be considered as movement from B to A along trajectories; the mean of these is $X\ (t;\ x_B)$. Thus $X\ (t;\ x_B)$ quantifies the “flow path" between B and A.

The general form of the Eulerian mass balance equations in non-uniform, steady-state flow is ((Equation 19 and (Equation 20):

$$\frac{\partial}{\partial \mathrm{t}}(\theta \mathrm{C_c}) + \mathrm{div}(\mathrm{v_c C_c} - \theta \mathrm{D_c} \nabla \mathrm{C_c}) = -\mathrm{F} \qquad \text{(Equation 19)}$$

$$\frac{\partial}{\partial \mathrm{t}}(\rho_\mathrm{c} C_c^*) = \mathrm{F}^* \qquad \text{(Equation 20)}$$

where t is the time [T], v_c the Darcy velocity of the colloids [L T^{-1}], C_c [M L^{-3}] the concentration of the colloids in the aqueous phase, C_c^* [L^3 L^{-3}] the concentration of the colloids sorbed to the aquifer material, and ρ_c [M L^{-3}] the density of the colloids. The tensor D_c [L^3 T^{-3}] describes the diffusion and dispersion effects. $F,\ F^*$ are general expressions of the sink-source (exchange) term.

Colloid filtration

Concerning the interaction of colloids with the fracture filling material, the filtration (attachment) rate k_{cs} can be compared to results from deep bed filtration theory. The common approach of deep bed filtration, neglecting the detachment of filtered colloids leads to ((Equation 21):

$$k_{cs}\theta = \lambda_c v_c \qquad \text{(Equation 21)}$$

where the particle velocity is denoted as v_c and the efficiency of the filtration is described by the filter coefficient λ_c. Here it is assumed that the mechanism is independent of the amount of already filtrated colloids as it is for clean deep bed filtration. Important parameters are the porosity and pore size of the sediment, the diameter of the colloidal particles, and the viscosity. Here we refer to the model of *Tien and Payatakes* [209]. Under the conditions of the field experiment, particularly for an average colloid size in the range of 150 nm [53], the filtration efficiency η is dominated by diffusion and can be calculated according to *Yao et al.* [210] neglecting interception and sedimentation processes by ((Equation 22):

$$\eta_D = 0.9 \left(\frac{k_B T}{\mu d_p d_c v_c}\right)^{2/3} \qquad \text{(Equation 22)}$$

with the filtration efficiency for diffusion η_D, the Boltzmann constant k_B, the temperature T, the viscosity μ, the particle diameter d_p and the collector diameter d_c.

The filter coefficient is then defined as ((Equation 23):

$$\lambda_c = \frac{3}{2}\frac{1-\theta}{d_c}\eta\alpha \qquad \text{(Equation 23)}$$

The attachment factor α describes the colloid-matrix collision part which leads to binding.

Colloid facilitated solute transport / Modeling of sorption processes

For interpreting the CFM tests, four mobile and two immobile components are considered (which can be subject to change for other models depending on the nature and scale of the problem).

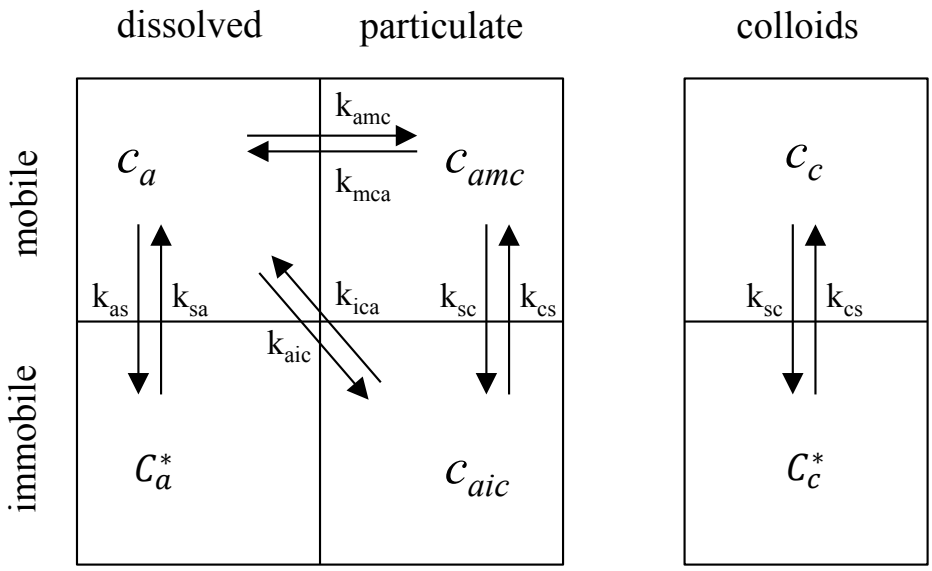

Figure 3.17: General concept of considered phases and interactions between them.

The transport equations given below have essentially been given by *Ibaraki and Sudicky* [211] and *Knabner et al.* [212]. The continuity equations for the contaminants dissolved in the aqueous phase or sorbed to the aquifer material are obtained to be (Equation 24 and (Equation 25):

$$\frac{\partial}{\partial t}(\theta C_a) + div(v_a C_a - \theta D_a \nabla C_a) = -F^a_{as,sa} - F^a_{amc,mca} - F^a_{aic,ica} \quad \text{(Equation 24)}$$

$$\frac{\partial}{\partial t}(\rho_b C^*_a) = F^a_{as,sa} \quad \text{(Equation 25)}$$

The mass balance equation for the contaminants sorbed to mobile and immobile colloids is governed by ((Equation 26 and (Equation 27):

$$\frac{\partial}{\partial t}(\theta C_{amc}) + div(v_c C_{amc} - \theta D_c \nabla C_{mca}) = -F^a_{cs,sc} - F^a_{amc,mca} \quad \text{(Equation 26)}$$

$$\frac{\partial}{\partial t}(\rho_c C^*_c C_{aic}) = F^a_{cs,sc} + F^a_{aic,ica} \quad \text{(Equation 27)}$$

where

C_c mobile colloid concentration [M L^{-3}]

C_a mobile solute concentration [M L^{-3}]

C_{amc} solute concentration attached to mobile colloids [M(solute) M(colloids)$^{-1}$]

C_{aic} solute concentration attached to immobile colloids [M(solute) M(colloids)$^{-1}$]

C_c^* immobile colloid concentration [M(colloids) M(solid)$^{-1}$]

C_a^* immobile solute concentration [M(solute) M(solid)$^{-1}$]

k_{cs} first-order transfer rate of colloids from mobile to immobile phase [T^{-1}]

k_{sc} first-order transfer rate of colloids from immobile to mobile phase [T^{-1}]

k_{as} first-order transfer rate of solute from mobile to immobile phase [T^{-1}]

k_{sa} first-order transfer rate of solute from immobile to mobile phase [T^{-1}]

k_{amc} first-order transfer rate of solute from mobile aqueous phase to mobile colloids [T^{-1}]

k_{mca} first-order transfer rate of solute from mobile colloids to mobile aqueous phase [T^{-1}]

k_{aic} first-order transfer rate of solute from mobile aqueous phase to immobile colloids [T^{-1}]

k_{ica} first-order transfer rate of solute from immobile to mobile aqueous phase [T^{-1}]

$F_{as,sa}^a$ rate loss of solute from mobile to immobile phase [M L^{-3} T^{-1}]

$F_{cs,sc}^a$ rate loss of colloids from mobile to immobile phase [M L^{-3} T^{-1}]

$F_{amc,mca}^a$ rate loss of solute from mobile aqueous phase to mobile colloids [M L^{-3} T^{-1}]

$F_{aic,ica}^a$ rate loss of solute from mobile aqueous phase to immobile colloids [M L^{-3} T^{-1}]

D_a tensor for diffusion and dispersion effects of the solutes [L T^{-1}]

D_c tensor for diffusion and dispersion effects of the colloids [L T^{-1}]

ρ_b bulk density of porous media [M L^{-3}]

ρ_c colloid density [M L^{-3}]

θ porosity of porous media [-]

v_a Darcy velocity of the solutes [L T^{-1}]

v_c Darcy velocity of the colloids [L T^{-1}].

In our model all rates are assumed to be constant.

The mass exchange between the phases shown in Figure 3.17 is governed by the following source terms F((Equation 28, (Equation 29 and (Equation 30):

$$F^a_{as/sa} = k_{as/sa}\rho\left(f_{as/sa}(C_a)C_a - C^*_a\right) \quad \text{(Equation 28)}$$

$$F^a_{amc/mca} = k_{amc/mca}\theta(f_{amc/mca}(C_a)C_a - C_{amc}) \quad \text{(Equation 29)}$$

$$F^a_{aic/ica} = k_{aic/ica}(\rho_c C^*_c f_{aic/ica}(C_a)C_a - C_{aic}) \quad \text{(Equation 30)}$$

with effective matrix porosity θ, matrix bulk density ρ, colloid density ρ_c, and sorption isotherms f_i. The sorption isotherms f_i can be linear (K_d) or non-linear (Langmuir or Freundlich) type. For simulation of the homologue experiments in CFM, the linear K_d-concept is chosen for all pathways, since the tracer concentrations are low enough to be far below saturation of sorption sites and no inhomogeneities and competition for sorbing sites on the rock matrix and colloid surfaces are considered.

The interaction of colloids with the sediment can be described in r^3t by a first order kinetic according to ((Equation 31):

$$F^c_{sc/cs} = k_{cs}\theta C_c - k_{sc}\rho_c C^*_c \quad \text{(Equation 31)}$$

with the attachment and detachment rates k_{cs} and k_{sc}. An irreversible attachment / filtration of colloids can be realized by setting a detachment rate of zero. Consistent with this formulation the change of the contaminant concentration caused by colloid sediment interactions is given as follows ((Equation 32):

$$F^a_{sc/cs} = k_{cs}\theta C_{amc} - k_{sc}C_{aic} \quad \text{(Equation 32)}$$

Initial and boundary conditions

The initial condition is assumed to be zero for all concentrations.

If multiple tracers are injected simultaneously, then the following quantities should be equivalent for all tracers: $\bar{\tau},\ \zeta,\ Q_A, Q_B, V, D_\tau$ (note: Colloids and solute are assumed to be subject to the same macro-dispersion). All rates and the partitioning coefficient are solute dependent.

Mass of solute M_a [M] is dissolved in a volume of water V [L^3] and mixed with a mass of colloids M_c. The mixture is equilibrated whereby the solute partitions between the aqueous solution and colloids such that the fraction f_a [-] is in the aqueous solution and $1 - f_a$ is attached to colloids. The mixture is then injected into the shear zone at point B and carried towards the detection point A by a flow rate Q_B [$L^3\ T^{-1}$]. The extraction flow rate at point A is Q_A [$L^3\ T^{-1}$].

The boundary conditions at x_B (i.e. $T = 0$) and x_A (i.e. $T = \bar{\tau}$ where $\bar{\tau}$ is the mean water residence time between B and A) are written as follows:

$$C_c(0,t) - D_\tau \frac{\partial C_c(0,t)}{\partial T} = \frac{M_c}{\epsilon Q_A} e^{-t/\epsilon} \qquad \text{(Equation 33)}$$

$$C_a(0,t) - D_\tau \frac{\partial C_a(0,t)}{\partial T} = f_a \frac{M_a}{\epsilon Q_A} e^{-t/\epsilon} \qquad \text{(Equation 34)}$$

$$C_c(0,t) C_{amc}(t,0) - D_\tau \frac{\partial C_c(0,t) C_{amc}(0,t)}{\partial T} = (1 - f_a) \frac{M_a}{\epsilon Q_A} e^{-t/\epsilon} \qquad \text{(Equation 35)}$$

$$\frac{\partial C_c(\bar{\tau},t)}{\partial T} = \frac{\partial C_a(\bar{\tau},t)}{\partial T} = \frac{\partial C_c(\bar{\tau},t)}{\partial T} = 0 \qquad \text{(Equation 36)}$$

Where

$$\epsilon \equiv \frac{V}{Q_B} \qquad \text{(Equation 37)}$$

is the injection turnover time [T].

Simulations

One of the goals of this work is to shed light on the multitude of different interaction processes between radionuclides, colloids and the sediment matrix, especially on the consequences of kinetically controlled adsorption and desorption. In the previous project Kollorado-1 [53] only one field test with colloids and homologues performed within CFM was available. In the current project phase several field test performed under different flow conditions enabled us to better identify the role of the different processes.

For the computer simulations, we use a 2D-transport code. The colloid-bound radionuclide transport is described using the code r^3t, the latter based on flow simulations using the code d^3f [213]. Visualization was realized on the basis of the software package GRAPE (GRAphics Programming Environment) developed by the Universities of Bonn and Freiburg [214]. Colloid transport and kinetically controlled interaction processes between contaminants and colloids have been implemented and tested [53].

One of the main characteristic of d^3f is the possibility to calculate the groundwater flow in large model domains over long periods in time. Density-driven flow, resulting from different salt concentrations in the groundwater, is not taken into account in this study, but can be simulated with d^3f. Two- or three-dimensional models of water saturated, porous, heterogeneous, anisotropic and incompressible media can be set up in form of transient or steady-state flow models. The temperature can be defined as a temporally and spatially variable field, and heat transport can be considered. Transport calculations with r^3t are based on steady-state or transient flow fields calculated by d^3f. The most important feature of r^3t is the possibility to simulate pollutant transport in very large model domains for long periods of time. Transport mechanisms, such as advection, dispersion, diffusion and reaction are regarded according to [215] and [216]. In addition to radioactive decay, relevant interaction processes, such as sorption, precipitation, and diffusion into immobile pore waters can be regarded [213]. All numerical algorithms applied in these codes are based on finite volume methods with robust solvers in form of multigrid algorithms.

The presented model is used to simulate flow, transport and interaction processes. The modeling strategy comprised four steps:

- Calibrate the hydraulic parameters using the breakthrough curves of the conservative tracers
- Characterise the interactions between colloids and fracture filling material by fitting the colloid breakthrough curves
- Identify and describe the interaction process between homologues and colloids by fitting the homologue curves
- Use the calibrated fit parameters to make predictions for the radioactive tracer test in the same dipole at different flow conditions.

The results are then compared to results from laboratory geochemical data, particularly equilibrium sorption experiments in ternary systems as measured by KIT-INE [74] and the filtration theory.

Model setup

The shear zone of the CFM experiment consists of a network of open channels embedded into fracture infill material and enclosed by quasi-parallel granite walls. The modeling approach simplifies the complexity of the fracture network by treating the shear zone as a porous medium with effective flow properties. The typical number of fractures in the shear zone and representative aperture widths are given in [205]. From these values, an average model shear zone thickness of about 5 mm is derived, which is necessary to reduce the model and boundary conditions to two dimensions.

The flow in the shear zone is determined by the transmissivity field, which is mainly dominated by the external boundary conditions (inflow/outflow) of the dipole. The model size is chosen to be large enough to reduce wall effects [217] (section 6.1). A scheme of the conceptual model, with boundary conditions for both flow and transport simulations employed for the tracer tests is shown in .

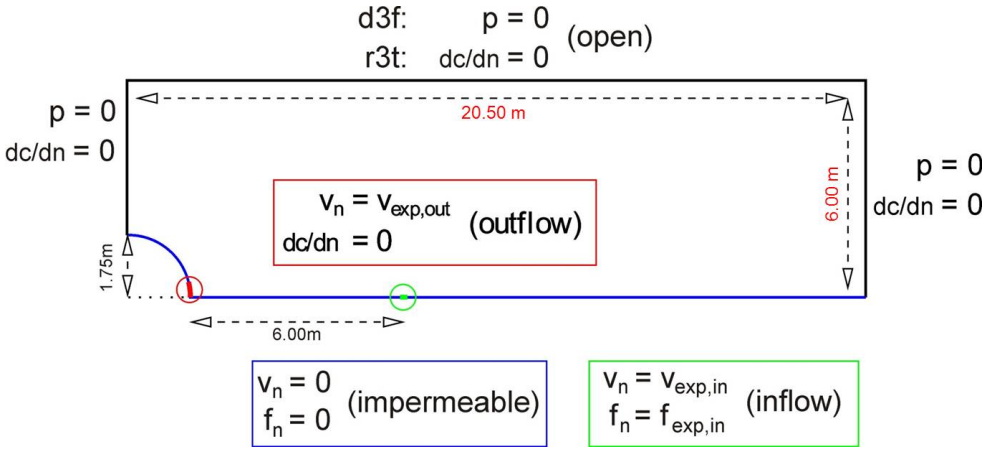

Figure 3.18: Geometry and hydrogeological/transport-related boundary conditions of the 2D computer model. Green: Inflow; Red: Outflow; Blue: Sealed tunnel wall and symmetry axis; Black: Permeable virtual boundaries within the shear zone. Notation: c = concentration; p = pressure; v = fluid velocity; f = pollutant mass flux; n is used either as a subscript to denote the normal component or in fractions in which n symbolizes the normal derivative of the respective variable.

For all interactions of the solutes with fracture filling material and colloids linear isotherms of K_d type are used. For the interactions of colloids with fracture filling material irreversible filtration processes (k_{sc} = 0) as well as kinetically controlled reversible interactions are applied. An overview of the employed model and the calibrated hydraulic parameters is given in Figure 3.18. The conceptual and mathematical model for transport of colloids and pollutants as well as for the interaction processes is described in detail in [55].

Table 3.6: Overview of the model assumptions and calibrated hydraulic parameters as applied by the three different modeler groups.

Parameter	Value
Dimensionality	2D
Model thickness [m]	$5 \cdot 10^{-3}$
Dipole distance [m]	6.2
Porosity [-]	0.115
Dispersion length [m]	
- Longitudinal	0.3
- Transversal	0.1
Diffusion coefficient [$m^2\ s^{-1}$]	$2.0 \cdot 10^{-11}$
Permeability [m^2]	$5.5 \cdot 10^{-11}$
Rock density [kg m^{-3}]	2670
Temperature [K]	293.15

Flow simulations

The test runs CFM RUN 10-01 and CFM RUN 10-03 were performed as point dilution experiments. For the model simulations, a certain very small inflow of fluid was defined due to numerical reasons. The inflow velocity for CFM RUN 10-01 was set to 0.56 ml min^{-1}, while it was set to 1.27 ml min^{-1} for CFM RUN 10-03.

Generally, for all four test runs, the flow is directed from the injection location CFM 06.002 to the extraction location Pinkel. Lowest flow velocities are observed for the CFM RUN 10-03, where the outflow rate is 10 ml min-1 only, while the highest flow velocities are observed for CFM RUN 08-02, where an outflow rate of 165 ml min-1 was applied, cf.

Table 3.5. The inflow rate is very low and ranges from 10 ml min^{-1} to 0.33 ml min^{-1}, thus the variation of the inflow rate is of less importance than the outflow rate. The flow fields for the different dipole tests are shown in Figure 3.19. They confirm that the flow is dominated by the extraction at Pinkel. From all open model boundaries, the flow is directed into the model domain towards the extraction location. From the inflow location at CFM 06.002 the water flows radially and partially reverses the prevailing flow direction in the vicinity of the inflow. This effect is restricted to the direct vicinity of the injection location. Generally, it was assumed that the flow is determined by the dipole and the natural flow in the system is of negligible impact.

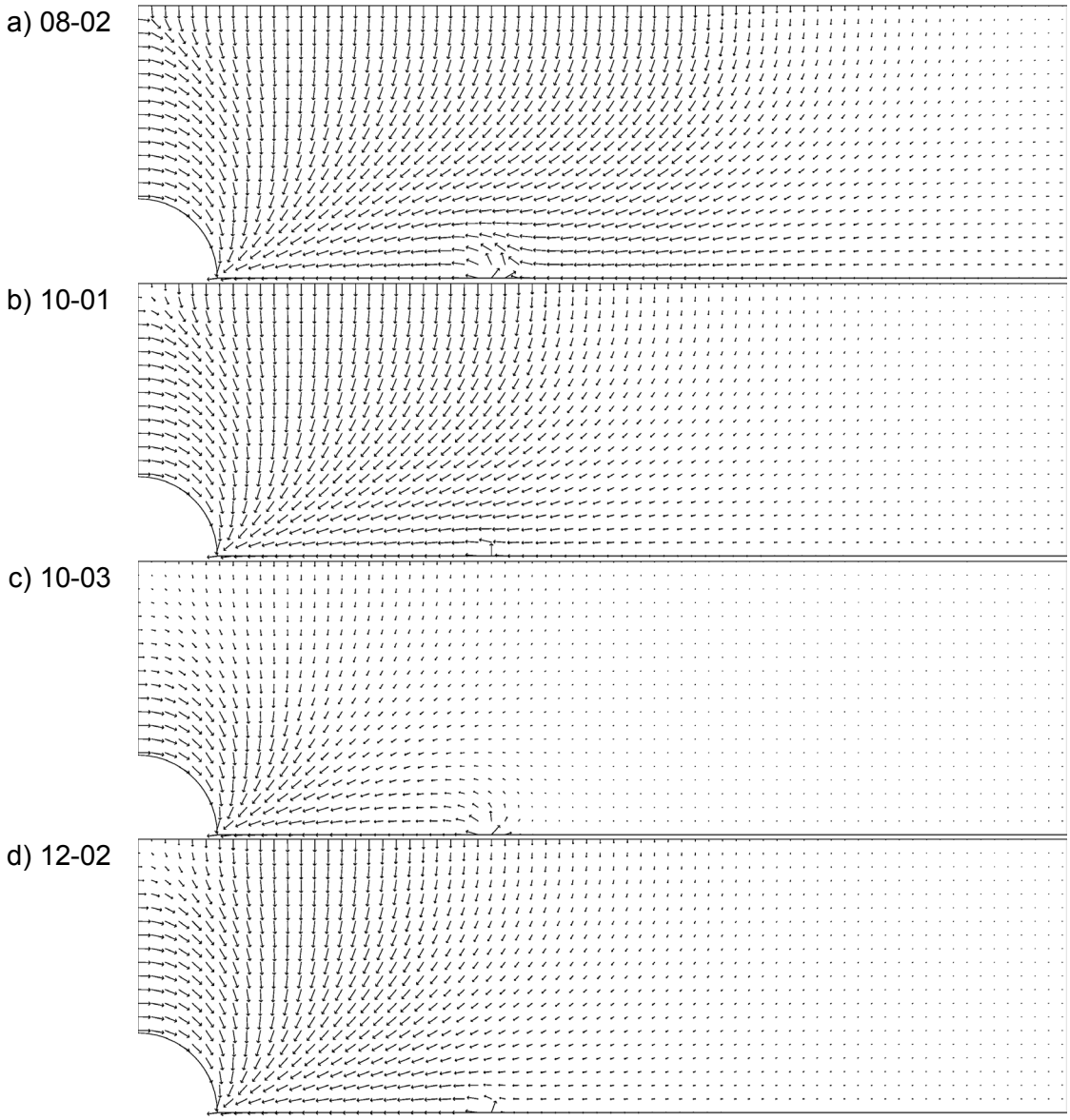

Figure 3.19: Velocity vectors of the steady-state flow fields for the considered tracer test runs: a) CFM RUN 08-02 (outflow rate 165 ml min^{-1}), b) CFM RUN 10-01, c) CFM RUN 10-03, and CFM RUN 12-02.

Transport simulations

In the first step, the non-sorbing solute tracer breakthrough curve of uranine was fitted for CFM RUN 08-02 and CFM RUN 10-01 by varying the dispersivity and porosity. The mass normalized breakthrough curves are shown in Figure 3.20. Based on these results, the hydraulic parameters of the shear-zone were determined

Then flow and transport calculations were performed for CFM RUN 10-03 and CFM RUN 12-02 using the same hydraulic parameters but different inflow/outflow boundary conditions and injection functions as given by the respective experiment. Simulated breakthrough curves of the non-sorbing solute tracers show a reasonably good agreement, i.e all investi-

gated dipole tests covering a transport time between 8 and 200 minutes (with respect to the peak maximum), can be described with the same hydraulic parameters. It should be noted that tracer recoveries in the simulations amounted to 100 % and thus were scaled to the recoveries achieved in the field experiments for CFM RUN 10-01 (84 %), CFM RUN 10-03 (90 %) and CFM RUN 12-02 (80 %, Table 3.5), to account for the mass losses during the experimental tests.

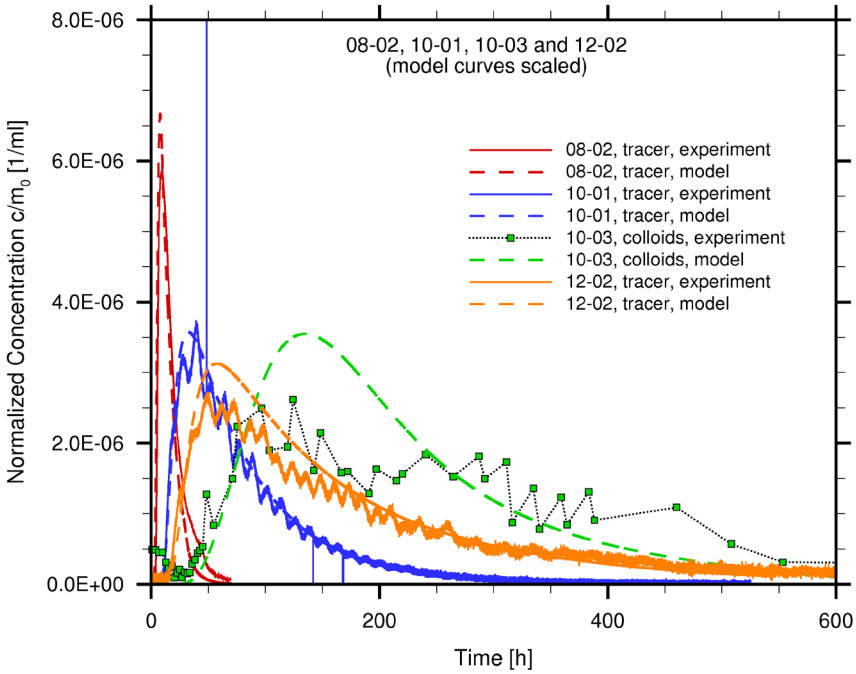

Figure 3.20: Conservative tracer breakthrough curves for the dipole experiments CFM RUN 08-02, CFM RUN 10-01, CFM RUN 10-03 and CFM RUN 12-02 (continuous line), and simulated breakthrough curves (dashed line) applying the best-fit hydraulic parameters given in Table 3.6.

For CFM RUN 10-03 a reliable breakthrough curve of the conservative tracer was not available due to problems with the recovery of the uranine tracer. Only for illustration, the curve for the colloids is shown in Figure 3.20, which is also simulated with the same flow parameters, but with additional interaction rates for the colloids. The curve was scaled to the recovery of the uranine tracer of CFM RUN 10-02, which was performed under the same conditions in the same dipole. The model parameters for flow and transport of the conservative tracer are listed in Table 3.6. The porosity of 0.115 is in the lower range of porosities observed for the fracture filling material from the shear zone but still in agreement with values between 10 and 40% given in [205].

In the second step the migration of the colloids and their interaction with the fracture filling material as well as the migration of the homologues and their interactions with colloids and fracture filling material are simulated for the tests CFM RUN 10-01. The results are shown in Figure 3.21 and Figure 3.22. A slight shift of the experimental colloid breakthrough curve indicates a weak retardation of the colloids. A further characteristic is a weaker increase of the breakthrough curve compared to uranine. Both effects can be described by a kinetically controlled interaction of the colloids with the fracture filling material with a colloid attachment

rate k_{cs} = 0.054 h^{-1} and a detachment rate k_{sc} = 0.108 h^{-1}. This ratio corresponds to a retardation factor of about 1.5 for the colloids. However, under the conditions considered here, the mutual reaction of colloids and fracture filling material is not in equilibrium. Further, a filtration rate of 0.01 h^{-1} was applied to account for an additional irreversible filtration.

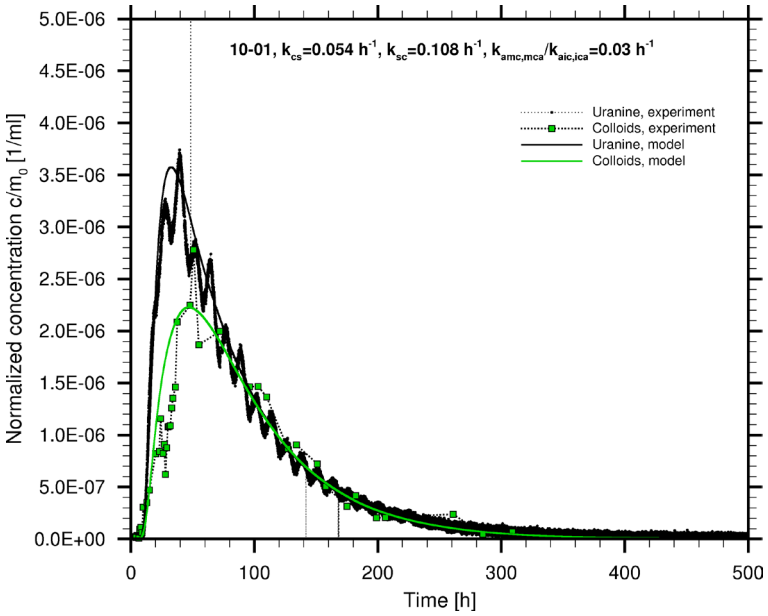

Figure 3.21: Experimental and simulated breakthrough curves for CFM RUN 10-01 for the uranine tracer and the colloids, linear scale.

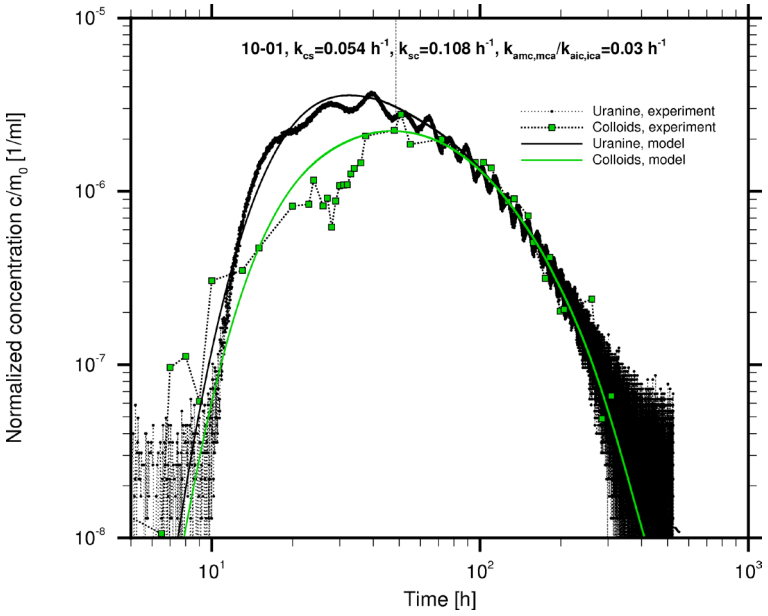

Figure 3.22: Experimental and simulated breakthrough curves for CFM RUN 10-01 for the uranine tracer and the colloids, logarithmic scale.

In the third step the homologue transport is simulated. Batch sorption experiments suggest that the tri- and tetravalent cations are strongly sorbed onto the fracture filling material, i.e.

the non-colloid-bound fraction will not migrate through the dipole over the time period the experiment is conducted. Only the colloid-bound fraction is expected to travel at a similar velocity as the fluid.

Therefore, the field experiment results are explained by the following processes as described in section 2.2. The homologues are equilibrated with the colloid-bearing solution in advance and are quantitatively bound to the colloids, when injected into the dipole. During the transport through the fracture, the homologues desorb from the colloids and subsequently adsorb to the fracture filling material. The velocity of these processes is determined by the detachment rate k_{mca} of the homologues from the colloids, since the adsorption reaction of the homologues to the fracture filling material is assumed to be fast. With an increasing desorption rate $k_{mca,}$ the peak maximum and the recovery of the homologue breakthrough curves decrease. From batch experiments it is indicated that distribution coefficients of trivalent and tetravalent elements on the fracture material are so high that the free cations are not expected to reach the outflow within the time frame of the field test.

The experimental breakthrough curves show a difference between the trivalent and the tetravalent homologues. The peak maximum as well as the recovery is higher for tetravalent thorium and hafnium than for trivalent europium and terbium. Consequently, higher desorption rates are expected for the trivalent homologues. For CFM RUN 10-01 in our model the breakthrough curves are quite well described with a detachment rate of $k_{amc/mca}$ = 0.03 h^{-1} for the tetravalent and $k_{amc/mca}$ = 0.075 h^{-1} for the trivalent homologues, see Figure 3.23 to Figure 3.26.

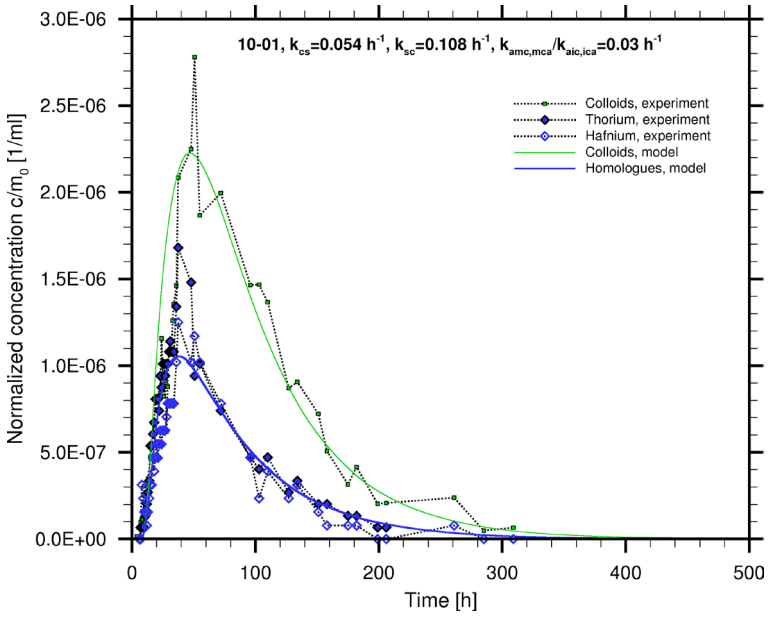

Figure 3.23: Simulated and experimental breakthrough curves for the tetravalent homologues Hafnium and Thorium for CFM RUN 10-01, linear scale. Best estimate parameters for $k_{amc,mca}/k_{aic,ica}$ are shown.

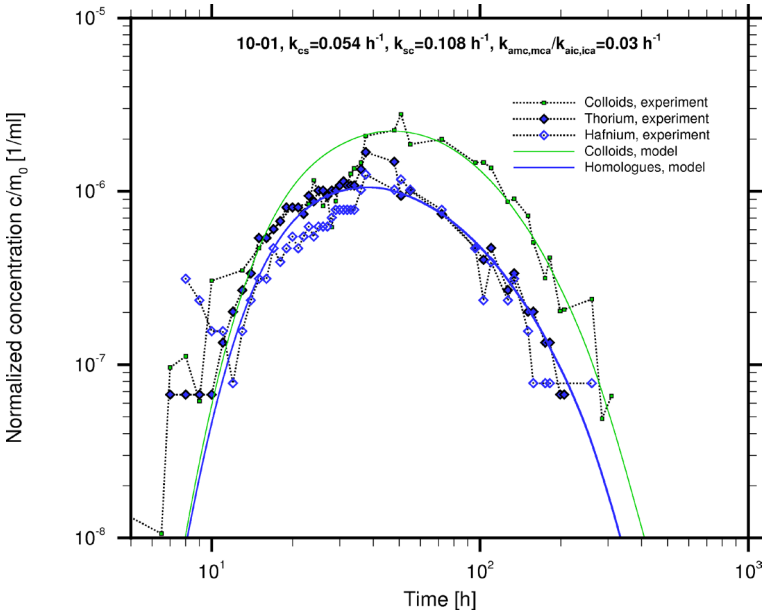

Figure 3.24: Simulated and experimental breakthrough curves for the tetravalent homologues Hafnium and Thorium for CFM RUN 10-01, logarithmic scale. Best estimate parameters for $k_{amc,mca}/k_{aic,ica}$ are shown.

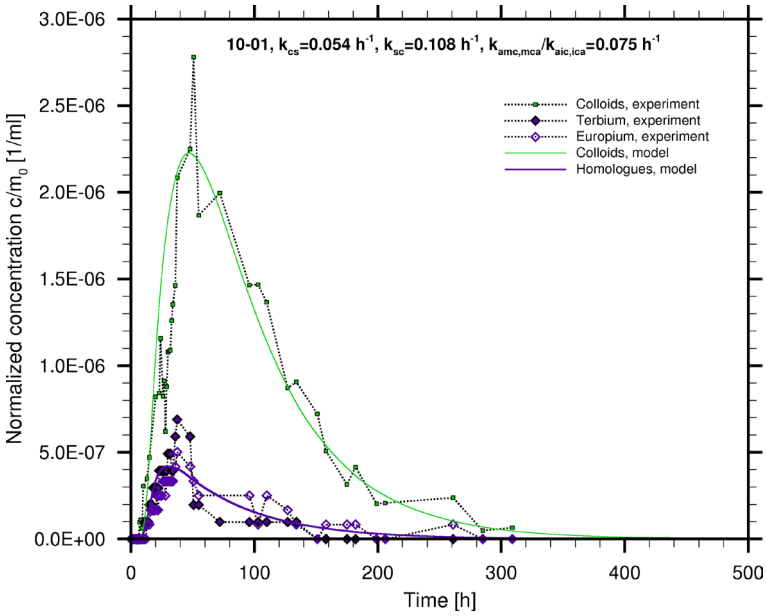

Figure 3.25: Simulated and experimental breakthrough curves for the trivalent homologues Terbium and Europium for CFM RUN 10-01, linear scale. Best estimate parameters for $k_{amc,mca}/k_{aic,ica}$ are shown.

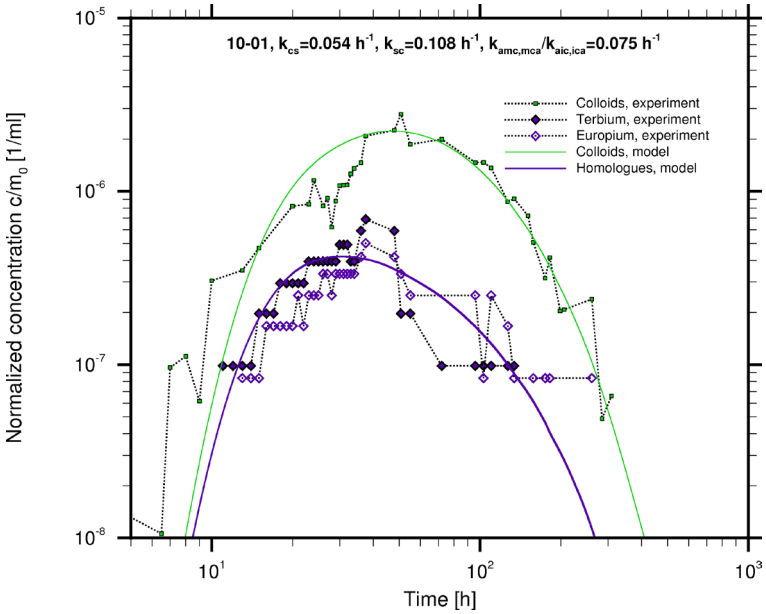

Figure 3.26: Simulated and experimental breakthrough curves for the trivalent homologues Terbium and Europium for CFM RUN 10-01, linear scale. Best estimate parameters for $k_{amc,mca}/k_{aic,ica}$ are shown.

In addition to comparing the shape of the curves, the mass recoveries of experiment and simulation can be analyzed (Table 3.7). In general, the recoveries of colloids and homologues in CFM RUN 10-01 are also quite well reproduced by the model calculations.

In the same way the colloid and homologue transport for CFM RUN 10-03 is simulated (Figure 3.27 and Figure 3.28). Due to a lower extraction rate at Pinkel, the travel time is increased compared to CFM RUN 10-01. One important question is whether the breakthrough curves and recoveries can be described with the same interaction rates. For the colloids the interaction parameters as applied for CFM RUN 10-01 give a reasonable result with respect to the peak of the breakthrough curve. However, the tailing at travel times of > 400 h is slightly underestimated. Nevertheless, the recovery of 41 % as observed in the experiment is again well reproduced by the calculation with a value of 45.1 % (Table 3.7). Therefore, it seems reasonable to describe the interaction between colloids and fracture filling material with the same parameters in both dipole tests.

For the homologues it was clear that significantly lower desorption rates have to be assumed in CFM RUN 10-03 than those for CFM RUN 10-01. The recoveries of the trivalent homologues are similar for both tests. The recoveries of the tetravalent homologues were even slightly higher in CFM RUN 10-03 than in CFM RUN 10-01. This is unexpected, since a longer travel time should increase the amount of desorbed homologues and therewith lead to a reduced recovery. Therefore, for CFM RUN 10-03 lower desorption rates of 0.02 h^{-1} and 0.0025 h^{-1} have been applied to describe the breakthrough curves of the tri- and tetravalent homologues, respectively. With these rates, the peaks of the curves are well reproduced but again the tailing and also the recoveries are to some extent underestimated.

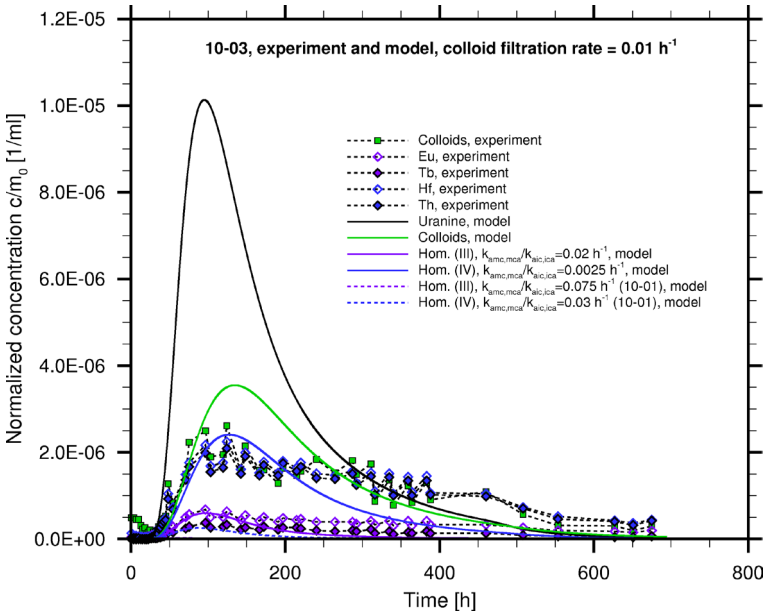

Figure 3.27: Simulated and experimental breakthrough curves for the colloids as well as for the trivalent and tetravalent homologues Europium, Terbium, Hafnium and Thorium for CFM RUN 10-03, linear scale. Best estimate parameters for $k_{amc,mca}/k_{aic,ica}$ are shown.

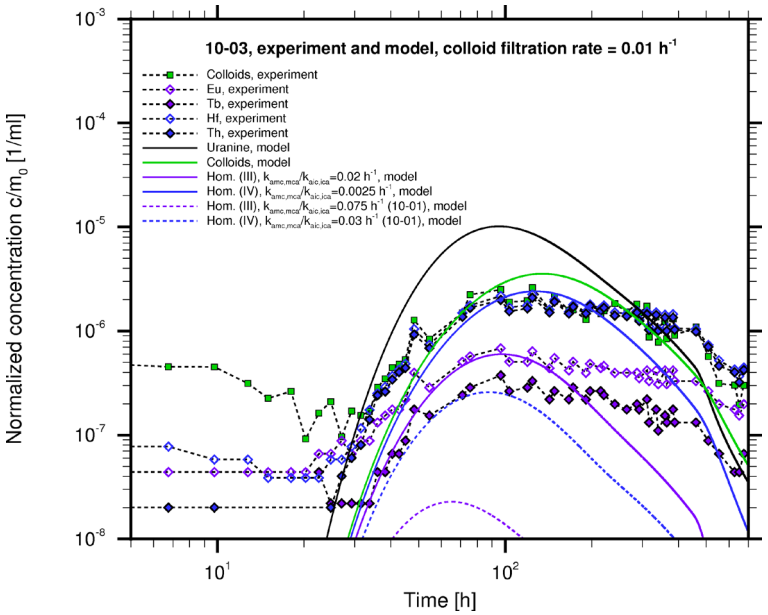

Figure 3.28: Simulated and experimental breakthrough curves for the colloids as well as for the trivalent and tetravalent homologues Europium, Terbium, Hafnium and Thorium for CFM RUN 10-03, logarithmic scale. Best estimate parameters for $k_{amc,mca}/k_{aic,ica}$ are shown.

Blind predictive modeling

In the fourth step blind predictive modeling was conducted for the radionuclide transport for CFM RUN 12-02. Besides an inert tracer (Amino G Acid), colloids and radionuclides accord-

ing to [218] were injected into the dipole. In our model simulations, we predicted the breakthrough of tri- and tetravalent radionuclides at the extraction location Pinkel. Different datasets of interaction parameters were employed for these simulations.

The interaction of colloids with the fracture filling material is described with the same parameters as used in CFM RUN 10-01 and 10-03. Concerning the interaction of the radionuclides with the colloids three datasets are used for illustration purposes:

- Dataset 1 (DS1), derived from CFM RUN 08-02 and CFM RUN 10-01:
  $k_{amc,mca}/k_{aic,ica}$ (Homologues (III)) = 0.075 h^{-1}
  $k_{amc,mca}/k_{aic,ica}$ (Homologues (IV)) = 0.03 h^{-1}
- Dataset 2 (DS2), derived from CFM RUN 10-03:
  $k_{amc,mca}/k_{aic,ica}$ (Homologues (III)) = 0.02 h^{-1}
  $k_{amc,mca}/k_{aic,ica}$ (Homologues (IV)) = 0.0025 h^{-1}
- Dataset 3 (DS3), :
  $k_{amc,mca}/k_{aic,ica}$ (Homologues (III)) = 0.05 h^{-1}
  $k_{amc,mca}/k_{aic,ica}$ (Homologues (IV)) = 0.014 h^{-1}

Dataset 1 corresponds to the simulation of CFM RUN 10-01 and dataset 2 to the simulation of CFM RUN 10-03, where the rates are significantly reduced. The explanation for the effect of decreased desorption rates with transport time is not identified so far. However, since the transport time of CFM RUN 12-02 (outflow 25 ml/min) is higher than in CFM RUN 10-01 (outflow 48 ml/min) and lower than in CFM RUN 10-03 (outflow 10 ml/min) a third dataset, interpolating between DS1 and DS 3 is used and proposed.

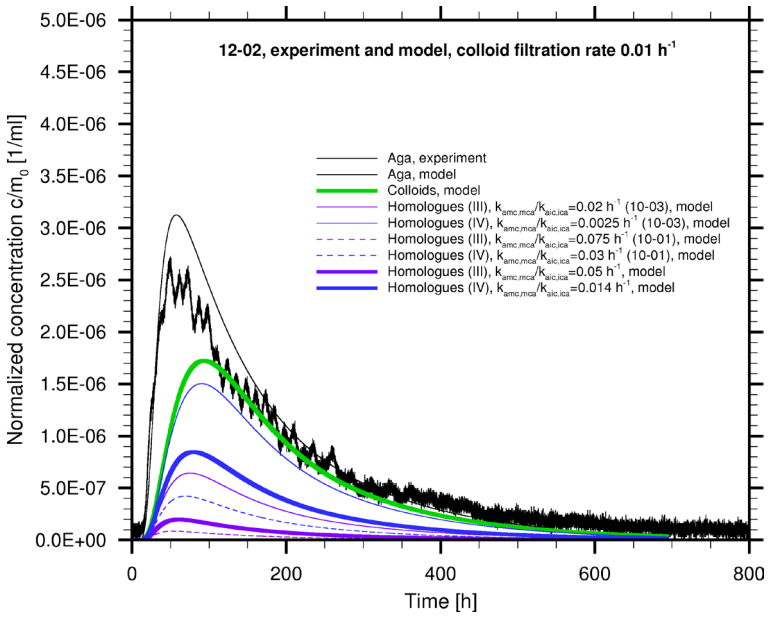

Figure 3.29: Simulated and experimental breakthrough curves for the colloids and simulated breakthrough curves for the trivalent and tetravalent homologues for CFM RUN 12-02. Best estimate parameters of $k_{3,4}$ are given.

The breakthrough curves for the tracer (both for the experiment and the model) and predicted breakthrough curves for colloids and homologues using the three different datasets DS1 to DS3 are shown in Figure 3.29. As discussed above, we have evidence for a decrease of the desorption rate with increasing travel time. As most probable prediction the dataset 3 is assumed, which are depicted as bold line of the breakthrough curves in Figure 3.29 and Figure 3.30.

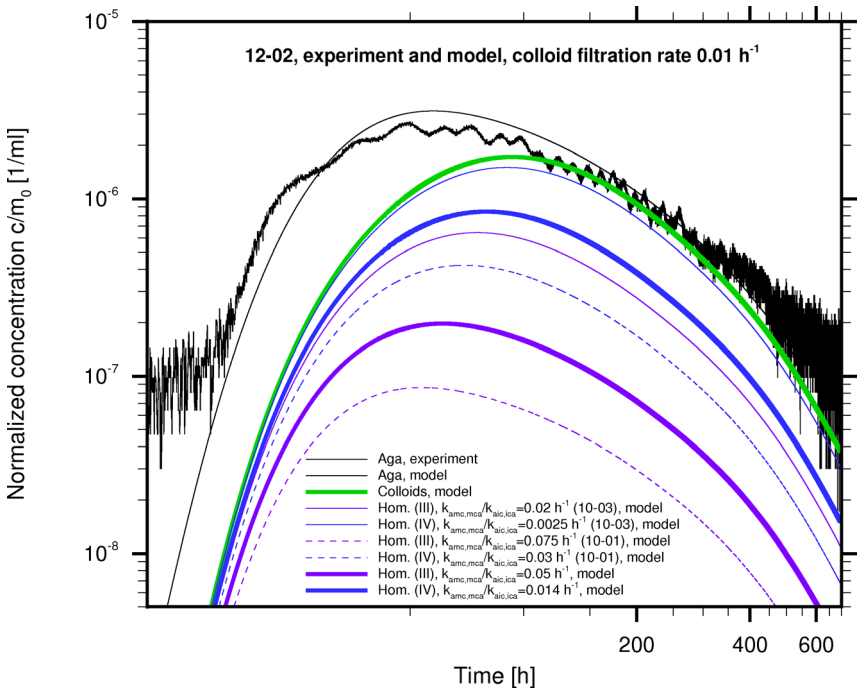

Figure 3.30: Simulated and experimental breakthrough curves for the colloids and simulated breakthrough curves for the trivalent and tetravalent homo-logues for CFM RUN 12-02. Best estimate parameters of $k_{3,4}$ are given.

Further evaluation of run 12-02

After finalization of the predictive modeling the breakthrough curves for colloids and radionuclides became available. In Figure 3.31 the experimental curves for the trivalent radionuclide Am-243 and the tetravalent radionuclide Pu-242 are shown together with the predictive simulation results. The first observation is that the breakthrough curves are higher than the ones predicted with DS3. It is obvious that the curves calculated with dataset 2 much better fit the experimental data indicating a similar low desorption rate for radionuclides/homologues from the colloids as derived from CFM RUN 10-03. Therefore, the curves based on DS2 are shown as bold lines in Figure 3.31.

The second observation is an earlier arrival of the radionuclides compared to the model prediction. This might have different reasons. One reason (also indicated by the experimental breakthrough curve of the colloids, not shown) is that the reversible interaction of colloids with the fracture filling material is not that pronounced as in CFM RUN 10-01 and CFM RUN 10-03. A simulation assuming no reversible interaction of colloids with the fracture filling material is shown in Figure 3.32. The shape of the simulated breakthrough curve already fits the breakthrough curves for Am-243 and Pu-242 quite well. As discussed before

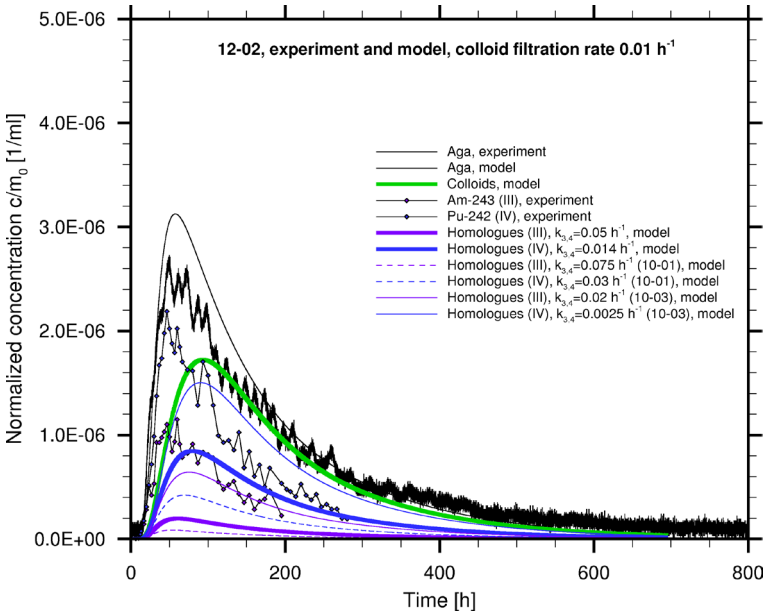

Figure 3.31: Simulated and experimental breakthrough curves for the colloids as well as for the trivalent and tetravalent homologues for CFM RUN 12-02. Best estimate parameters from blind predictive modeling of $k_{3,4}$ are given.

the same hydraulic parameters have been applied to all four considered CFM RUNs. A slight modification of the flow field with slightly decreased porosity, which might even better fit the curve of the non-sorbing tracer, would match the breakthrough curves curves of model and radionuclides even better. However, a further detailed investigation of all runs using the existing results will be done within the follow-on project Kollorado-e.

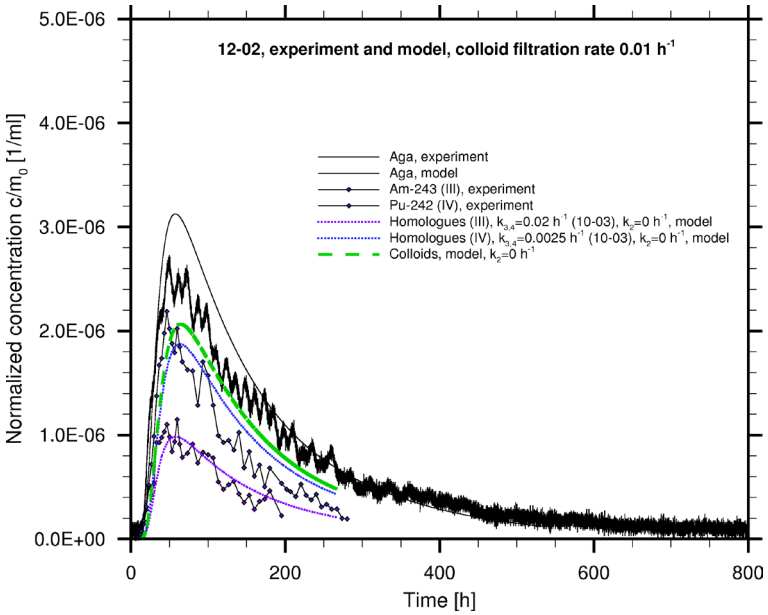

Figure 3.32: Simulated and experimental breakthrough curves for the colloids as well as for the trivalent and tetravalent homologues for CFM RUN 12-02. Best estimate parameters of $k_{3,4}$ are given.

Recoveries

Table 3.7summarizes the experimental and simulated mass recoveries of the tracer, the colloids and the homologues for all considered test runs. The experimentally observed decrease in recoveries for the colloids with increasing travel time is well matched by the calculations. As discussed before only one dataset is used to describe filtration rates and reversible interactions. In general, the recoveries for the homologues and radionuclides are also fairly well reproduced in all runs with exception of the tetravalent homologues in CFM RUN 10-03. However, the observations of an increased recovery of Th and Hf in the experiment with longer travel time, CFM RUN 10-03, compared to CFM RUN 10-01 is still surprising and need to be confirmed in further field tests, which are already planned. The experimental recoveries CFM RUN 12-02, particularly for Am-243, are best reproduced with DS2, which was already visible by the shape of the breakthrough curves as discussed above.

Table 3.7: Mass recoveries [%] for CFM RUNs 10-01, 10-03 and 12-02 and for the model simulations, light blue fields indicate the experiments, for which blind predictive modeling was performed. For details about the used datasets (DS) see text.

<table>
<tr><th rowspan="2"></th><th colspan="2">08-01 / 02</th><th colspan="2">10-01</th><th colspan="3">10-03</th><th colspan="4">12-02</th></tr>
<tr><th>Exp.</th><th>DS1</th><th>Exp.</th><th>DS1</th><th>Exp.</th><th>DS1</th><th>DS2</th><th>Exp.</th><th>DS1</th><th>DS2</th><th>DS3</th></tr>
<tr><td>Tracer</td><td colspan="2">99</td><td colspan="2">84</td><td colspan="3">90</td><td colspan="4">80</td></tr>
<tr><td rowspan="3">Colloid</td><td rowspan="3">99</td><td rowspan="3">84</td><td>64</td><td rowspan="3">67</td><td rowspan="3">41</td><td rowspan="3" colspan="2">45</td><td>66[a]</td><td rowspan="3" colspan="3">54</td></tr>
<tr><td>53</td><td>34-37[b]</td></tr>
<tr><td>47</td><td>33-38[b]</td></tr>
<tr><td>Th</td><td>93</td><td rowspan="2">70</td><td>32</td><td rowspan="2">28</td><td>43</td><td rowspan="2">2</td><td rowspan="2">28</td><td rowspan="2">Pu ~32</td><td rowspan="2">11</td><td rowspan="2">46</td><td rowspan="2">24</td></tr>
<tr><td>Hf</td><td>78</td><td>30</td><td>46</td></tr>
<tr><td>Tb</td><td>56</td><td rowspan="2">54</td><td>7</td><td rowspan="2">10</td><td>6</td><td rowspan="2">0.1</td><td rowspan="2">5</td><td rowspan="2">Am ~16</td><td rowspan="2">2</td><td rowspan="2">18</td><td rowspan="2">5</td></tr>
<tr><td>Eu</td><td>n.a.</td><td>14</td><td>14</td></tr>
</table>

[a] Recovery measured by LIBD, [b] recovery range derived from Al brakthrough, [c] recovery range derived from Ni brakthrough (bentonite colloids have been spiked with Ni, see section 2.2).

The modeling results are based on several assumptions and the experimental results are covered by uncertainties. For example the recoveries of the colloids analyzed by LIBD significantly differ from the recoveries detected by Al and Ni signals. The desorption rates for the homologues / radionuclides derived from the breakthrough curves also depend on the assumptions on the colloid – fracture filling material interactions. The uncertainties and their impact on modeling results will be tackled in the follow-on project.

Comparison with results from laboratory experiments and filtration theory

Sorption data for the homologues and particularly the desorption rates from the colloids have been determined by independent batch experiments for the ternary system homologue – colloid – fracture filling material [74]. In these experiments, the pollutants are equilibrated with colloids in solution for a few days before adding the fracture filling materials. After addition of the fracture filling material, part of the pollutants desorb from the colloids and sorb on

the fracture filling material. Assuming that the time dependence of the K_d-value is determined by the desorption rate, that the process is in equilibrium after 7500 h (the endpoint of the experiment) and neglecting an interaction of colloids with the fracture filling material Huber et al. derived detachment rates from the colloids of 0.0037 h^{-1} for the trivalent americium and 0.0014 h^{-1} for the tetravalent elements plutonium and thorium [74]. A batch modeling attempt using the same sorption coefficients and attachment rates as applied for the field experiment for Am and Pu yielded similar detachment rates k_3/k_4 of 0.0035 h^{-1} and 0.0022 h^{-1} for Am and Pu, respectively. The resulting curves compared to the experimental data are shown in Figure 3.33.

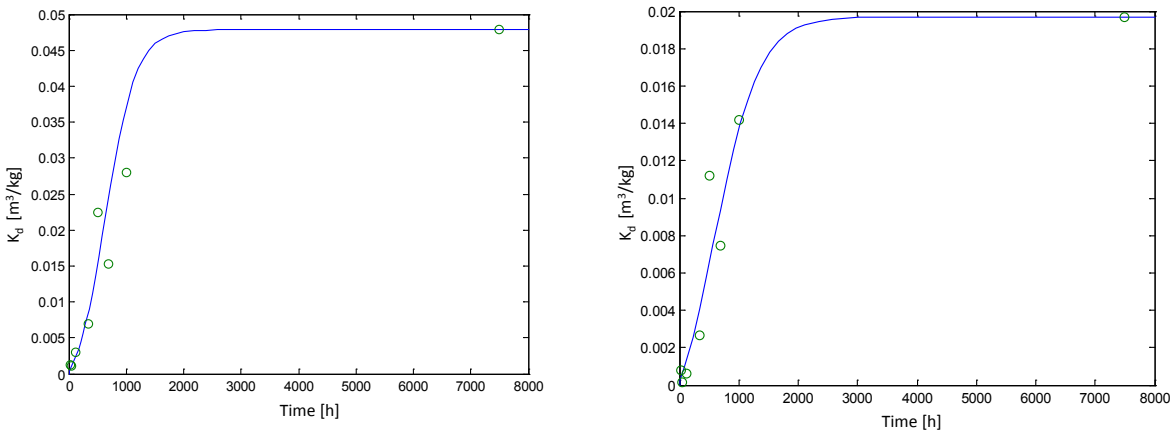

Figure 3.33: K_d-values for experiment (dots, [74]) and simulation (line) as a function of time in the ternary batch system bentonite colloids, fracture infill and pollutant Am (left, model data: K_{d1} = 2 m^3/kg, K_{d3} = 1600 m^3/kg, k_1= 1 h^{-1} and k_3 = 0.0035 h^{-1}) and Pu (right, model data: K_{d1} = 0.825 m^3/kg, K_{d3} = 1600 m^3/kg, k_1= 1 h^{-1} and k_3 = 0.0022 h^{-1}).

The results show that the desorption rates, which determine the homologue breakthrough curves and recoveries derived in our model simulations for CFM RUN 10-03, are in a similar range as those derived from independent batch experiments. For CFM RUN 10-01 performed at a higher extraction rate and therewith lower residence time, higher desorption rates are observed. Such decrease in reaction rates is observed in other natural systems and was also found for the transport of lanthanides bound to humics, e.g. [55]. However, the reason for this difference in desorption rates in the experiments discussed here is not yet clear. One explanation might be that the colloid concentration in CFM RUN 10-03 is significantly higher, whereas the concentration of homologues is the same. Therefore, a decreased desorption rate of homologues at lower coverage of the bentonite colloids could explain this behavior. But, so far, there is no experimental evidence for this.

The interaction of colloids with fracture filling material can be described in a simple way by the filtration theory. Using (Equation 21, (Equation 22 and (Equation 23 filtration rates can be calculated. The data to be used are discussed in the following. The attachment factor α describes the colloid-matrix collision part which leads to binding. The attachment process of colloidal bentonite particles on granite infill material under Grimsel groundwater conditions

has been investigated in experiments by [49]. From these investigations an attachment factor of $2 \cdot 10^{-4}$ was determined. All other parameters, which are adapted to the conditions of the CFM experiments, are listed in Table 3.8. The viscosity and fluid density are given for the low mineralized Grimsel groundwater. For the bentonite colloids, the rock density of bentonite is applied. A collector diameter of 10^{-4} m is selected as an average grain size of the fracture infill material. For the particle velocities in the range of 10^{-4} to 10^{-5} ms^{-1} filtration rates K_2 = 0.11 to 0.05 h^{-1} are calculated, which are higher than the irreversible rate of 0.01 h^{-1}, derived from the CFM-RUNs. However, taking into account that we have assumed an additional reversible attachment process, with a rate of 0.054 h^{-1}, the observed interaction rates fit into the range obtained by deep bed filtration theory. A further discussion also connected to the uncertainties of recovery data is needed and will be performed in a follow-on project.

Table 3.8: Parameters used for the deep bed filtration approach.

Parameter	unit	Value
dynamic viscosity μ	Ns m^{-2}	$1 \cdot 10^{-3}$
fluid density ρ	Kg m^{-3}	1000
colloid density ρ_P	Kg m^{-3}	2670
collector diameter d_C	m	$1 \cdot 10^{-4}$
gravitation constant g	m s^{-2}	9.81
temperature T	K	288.15
Boltzmann constant k_B	J/K	$1.38 \cdot 10^{-23}$
porosity Θ		0.15
attachment factor α		$2 \cdot 10^{-4}$

Conclusions and performance assessment aspects

The successful performance of CFM RUNs 08-01, 10-01, 10-03 and 12-02 within the CFM project covers a wide range of transport times. The flow conditions are approximating the natural conditions in fractured rock systems. This and the fact that all test have been performed within the same dipole enabled us to study the impact of kinetically controlled processes like colloid filtration and homologue/radionuclide desorption, which was not possible under the conditions of the CRR experiment. Although the shear zone is considered as a porous medium with respect to flow and transport the simulation results are very promising.

As discussed before the shape of the colloid breakthrough curves can fairly well be described with one dataset for the filtration process for all four CFM RUNs. The first important statement for performance assessment is that filtration (on the time scale of the experiment) is of relevance under the conditions in this CFM dipole and the respective transport times. The calculated recoveries compared to the experimentally observed ones are shown in Fig-

ure 3.34 as a function of transport time (note that as transport time the time of the peak maximum is used). The graph shows that the calculated recoveries quite well follow the experimentally observed recoveries.

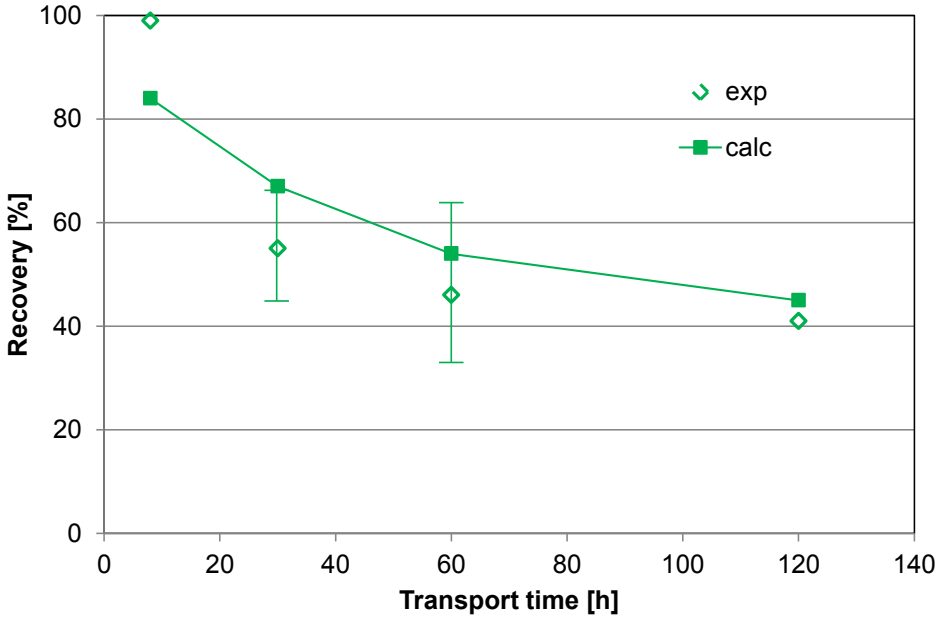

Figure 3.34: Colloid recoveries observed in the field experiment and derived from model calculations as function of transport time. The error bars indicate the recovery range of the colloids as determined by different analytical methods.

Some of the field tests also indicate a low reversible interaction, which is however not observed in CFM RUN 12-02. From the viewpoint of performance assessment the filtration process is of high relevance, since an immobilization of the colloids has the potential to significantly reduce the consequences of colloid facilitated radionuclide transport with respect to radiation exposures. In order to quantify the filtration processes it needs to be known, whether the process is irreversible on the considered time scale. Its impact also depends on the desorption rate of the radionuclides from the colloids. A low reversible interaction with retardation factors in the order of 1.5 are judged to be of low relevance for PA, since it would only slightly retard the transport of colloid-bound radionuclides.

The second process of high relevance is the desorption of the radionuclides from the colloids. The impact of the desorption process of course depends on the properties and behavior of the colloids. Two limiting cases can be distinguished: (i) The colloids are irreversibly filtrated. In this case a slow desorption rate would be positive for long-term safety, since the radionuclides are bound to immobile colloids. (ii) The colloids are transported along the flow path without retardation: In this case a fast desorption rate would be positive for long-term safety, since the transport of the free radionuclides is much slower than the colloid-bound transport.

From the CFM field experiments desorption rates can be derived. The results show that on the timescale of the experiments desorption clearly plays a role. The recoveries of the homo-

logues/radionuclides, particularly the trivalent ones, are lower than those of the colloids. In Figure 3.35 the recoveries for the tetravalent and the trivalent homologues/radionuclides obtained from field experiments and calculations for the four CFM RUNs are shown. Firstly, the recoveries for trivalent homologues/radionuclides are generally lower than for tetravalent, i.e. the desorption rates for the trivalent are higher than for the tetravalent. This is true for all transport times.

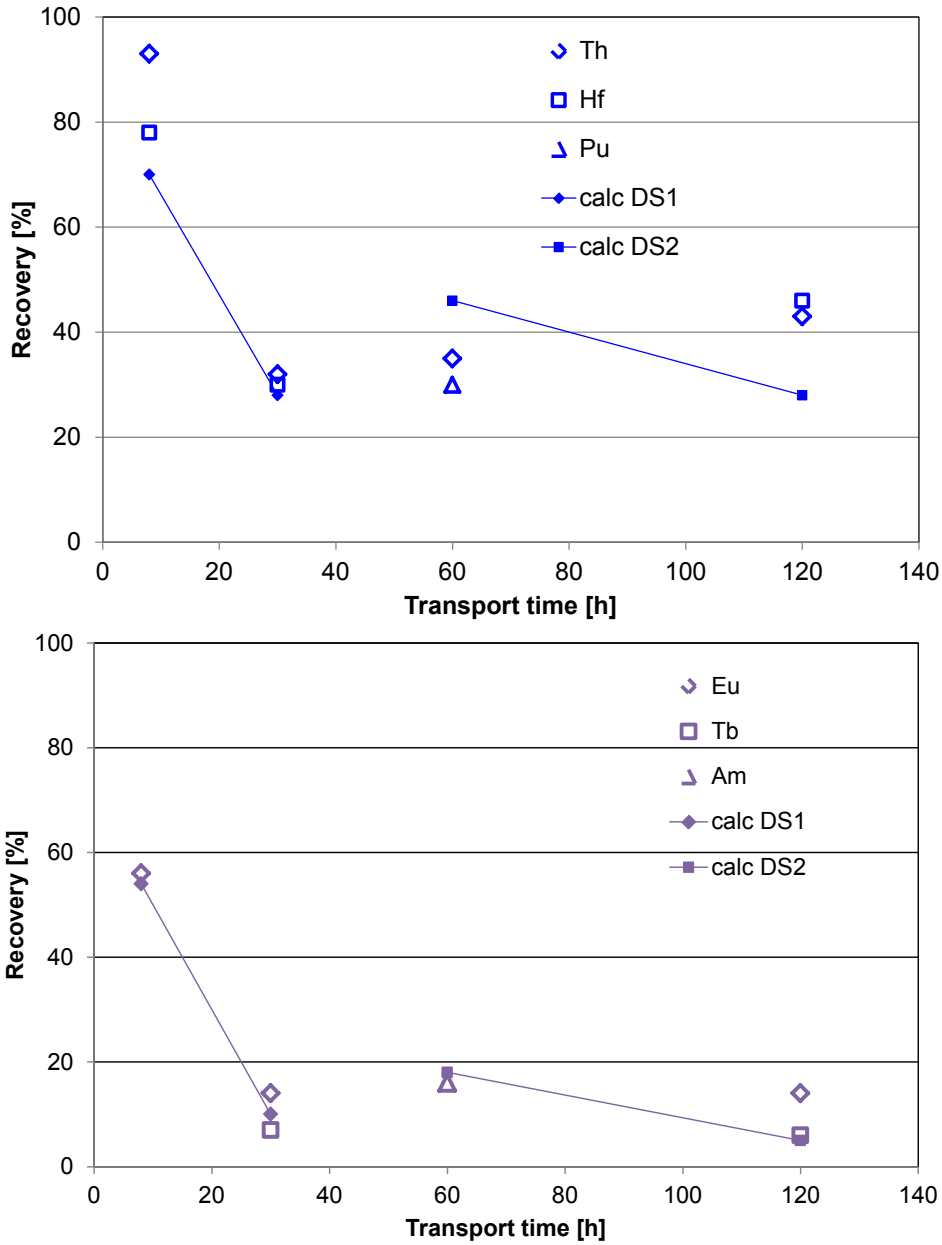

Figure 3.35: Recoveries for tetravalent (top) and trivalent homologues/radionuclides (bottom) observed in the field experiment and determined from model calculations with respective datasets.

Further, the experimental data indicate a clear decrease of the recovery with increasing transport time at transport times < 30 h. The values derived for transport times > 30 y are in

the same order of magnitude, for trivalent as well as for tetravalent homologues/radionuclides. Assuming a decreasing recovery of the colloids with transport time as indicated by Figure 3.34 this can only be explained by a decrease in the desorption rate. This is the most interesting observation with respect to performance assessment that the desorption rate for short transport times (< 30 h peak maximum) are significantly higher than for longer transport times (≥ 60 h peak maximum), which is considered in the simulations by the application of two datasets.

As described in section 0 the low desorption rates are in the same range as those derived from batch reversibility experiments. However, application of the lowest desorption rates derived from the field tests so far, still shows a low impact on a simplified test case performed in [53]. If no colloid filtration is assumed the lowest desorption rate of 0.001 h^{-1} (corresponding to 8.5 y^{-1}) still shows a very similar curve as the one assuming equilibrium sorption, see Figure 3.36 (compare reference curve and curve with desorption rate 5.5 y). For more detailed information please see [53].

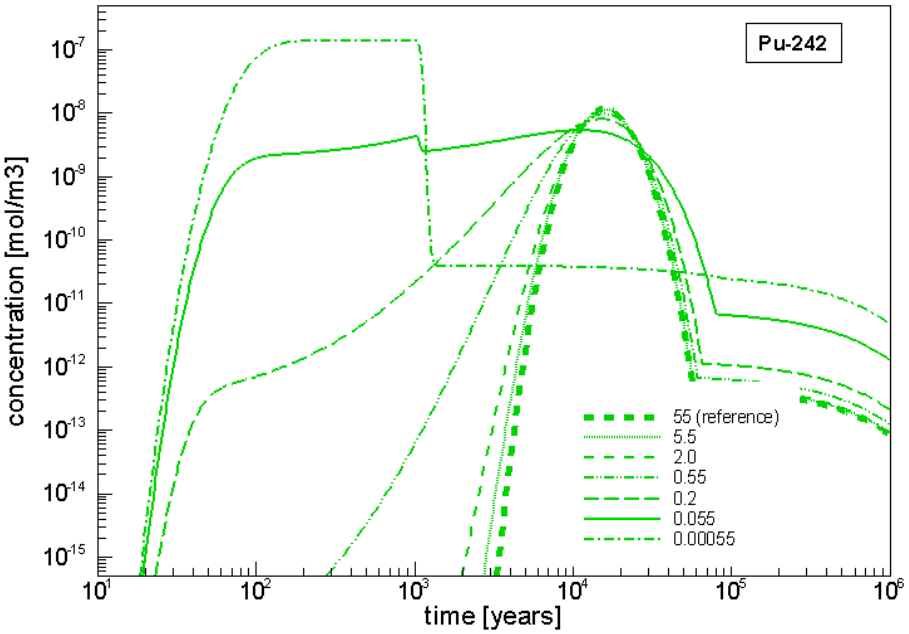

Figure 3.36: Breakthrough curves of Pu-242 for the different test cases applying different desorption rates without colloid filtration described in [53].

Within the follow-on project a test case based on the Finnish safety case [219] will be investigated. This test case will address

- more realistic assumptions for container failure concerning the number of containers and point in time,
- inflow of colloidbound radionuclides, i.e. radionuclide diffusion vs. colloid formation and point in time,
- the flow characteristics in the granite and

- the consideration of glacial cycles.

The calculations will be performed with the transport code GEOTREND-FC, which is currently being developed at GRS. A schematic view of the processes considered is shown in Figure 3.37. This model represents a double porosity approach for fractured media including the process of matrix diffusion.

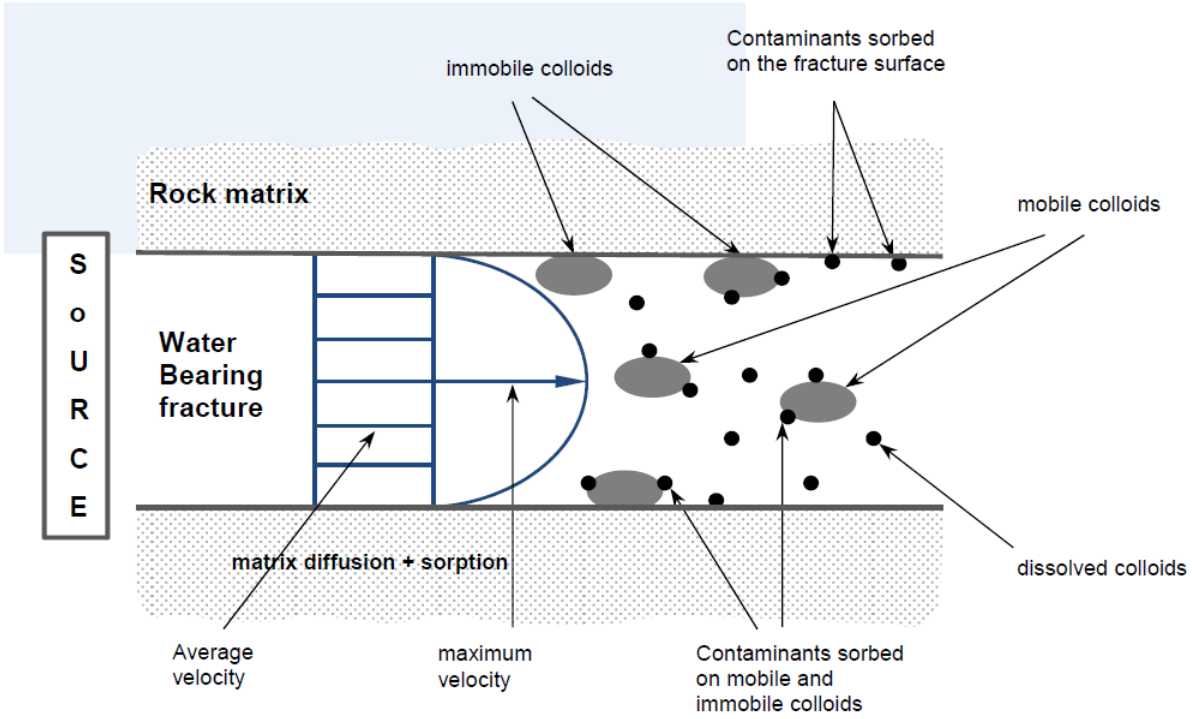

Figure 3.37: Transport code GeoTREND-FC to be applied for PA calculations.

Important questions for the next CFM phase are, whether the results observed at the dipole can be transfer to other dipoles. A new field test will be performed in June 2013. Predictive calculations based on the datasets received from these investigations are currently carried out. A deeper understanding is necessary to clarify the reason for the decrease in desorption rates with increasing transport time.

3.2 Natural micro-scale heterogeneity induced solute and nanoparticle retardation

Abstract

We studied tracer (tritiated water (HTO); Tritium replaces one of the stable hydrogen atoms in the H_2O molecule) and nanoparticle (quantum dots (QD)) transport by means of column migration experiments and comparison to 3D CFD modeling. Concerning the modeling approach, a natural single fracture was scanned using micro computed tomography (µCT) serving as direct input for the model generation. The 3D simulation does not incorporate any chemical processes besides the molecular diffusion coefficient solely reflecting the impact of fracture heterogeneity on mass (solute and nanoparticles) transport. Complex fluid velocity distributions (flow channeling and flow path heterogeneity) evolve as direct function of fracture geometry. Both experimental and simulated solute and colloidal breakthrough curves show heavy tailing (non-Fickian transport behavior), respectively. Regarding the type of quantum dots and geochemical conditions prevailing (Grimsel groundwater chemistry, QD and diorite surface charge, respectively and porosity of the Äspö diorite drill core) experimental breakthrough of the quantum dots always arrives faster than the solute tracer in line with the modeling results. Besides retardation processes like sorption, filtration, straining or matrix diffusion, the results show that natural 3D fracture heterogeneity represents an important additional retardation mechanism for solutes and colloidal phases. This is clearly verified by the numerical simulations, where the 3D real natural fracture geometry and the resulting complex flow velocity distribution is the only possible process causing solute/nanoparticle retardation. Differences between the experimental results and the simulations are discussed with respect to uncertainties in the µCT measurements and experimental and simulation boundary conditions, respectively.

Materials and Methods

X-ray computed tomography. The drill core used in this study was obtained from the Äspö hard rock laboratory (HRL, Sweden) from the drill hole KOV 01 774.7-775.2. For a thorough mineralogical and chemical analysis of the Äspö diorite the reader is referenced to the literature [220]. Prior to characterization by µCT, the core was sealed on the outside by placing it in a custom made Plexiglas column and equipped with devices and tubing for the migration experiments (Figure 3.38). To gain information about fracture geometry, aperture and porosity distribution the drill core was scanned using a µCT [221]. This method serves as a non-destructive tool to obtain information of internal structures and spatial characteristics of the specimen down to the micro-meter and even nano-meter scale. For further generic information about technical details of the method, see Duliu et al. (1999). The µCT instrument used in this study is an own development of the Federal Institute for Material Research and

Testing (BAM) in Berlin. A unique 320 kV X-ray micro-focus source was used with a flat panel 1024^2 with 400x400 µm². A scanning energy of 220 kV with 0.14 mA was used, with prefiltering of source 0.5 mm Cu and 0.75 mm Sn. In total 900 projections of 360° were measured in 3 vertical parts. The resulting voxel resolution after projection reconstruction is 80 µm per voxel. The complete dataset has a dimension of 681x681x1691. A beam-hardening correction was done by an own development based on hypersurface fittings of beam hardening body. After corrections, a simple threshold segmentation was possible.

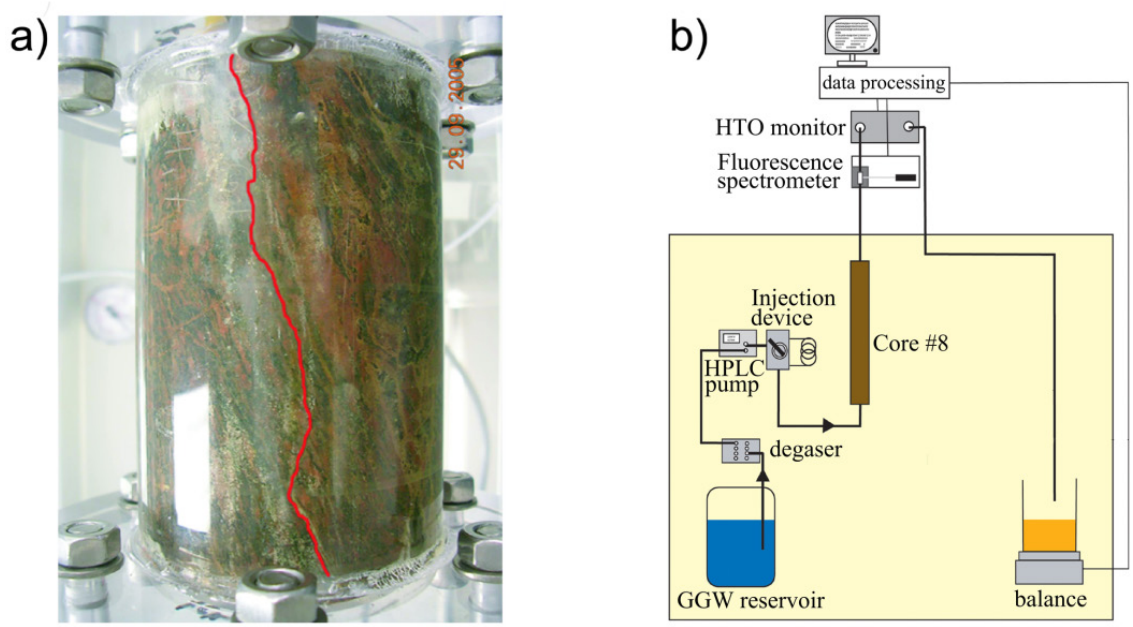

Figure 3.38: a) Drill core as installed in the laboratory. In red, the fracture suture is marked. b) A schematically sketch of the set-up as installed in the laboratory for use in the migration experiments.

Quantum dots characterization by Flow-Field-Flow Fractionation (AsFlFFF). Engineered nanoparticles, namely quantum dots were applied to test their mobility in the drill core. This material consists of a CdSe/ZnS core with PEG lipid surface coating coupled to comb hair type carboxyl terminal groups, which were delivered as stable suspension in de-ionized water (Evident Technologies). The Asymmetrical Flow-Field-Flow Fractionation (AsFlFFF) coupled to an ICP-Mass spectrometer is used to characterize these particles (Figure 3.39). This technique has been previously used to characterize clay and humic colloids [59, 68] and to study their interaction with actinides or lanthanides as their chemical homologues [41, 62, 95]. We, as well as other groups, have already used this technique successfully to the characterization of quantum dots [68, 222, 223].

The general principle of the flow field−flow fractionation method can be found in [104] and [65]. The experimental equipment used in this study (HRFFF 10.000 A4F, Postnova analytics, Landsberg, Germany) was described in details previously by Bouby et al. (2008, 2011). The nanoparticle suspension is injected in a thin ribbon−like channel. The sample components (colloids/nanoparticles) are eluted by a carrier solution (ultra−pure water adjusted to

pH = 9.3 by addition of 1 M NaOH ultra pure) having a laminar parabolic flow profile under the action of a secondary perpendicularly applied flow field (the cross−flow). This drives the components to the accumulation wall which is covered by an ultra−filtration membrane made of regenerated cellulose (5 kDa). This membrane retains the sample components that are larger than the membrane nominal molecular weight cut−off within the channel. The diffusion of the components back in the channel counterbalances the cross−flow. Smaller particles with higher diffusion rates reach faster flow streamlines and are eluted prior to the larger particles (in the so− called “normal” elution mode). After fractionation, the effluent is mixed with 6 % HNO3 containing Rh as internal standard and is injected in the ICP−MS for quantitative analysis. The size calibration is achieved with carboxylated polystyrene reference particles (Magsphere, USA). Details on the procedure can be found in Bouby et al. (2008). This hyphenated system allows the determination of the colloidal size distribution and its elemental content.

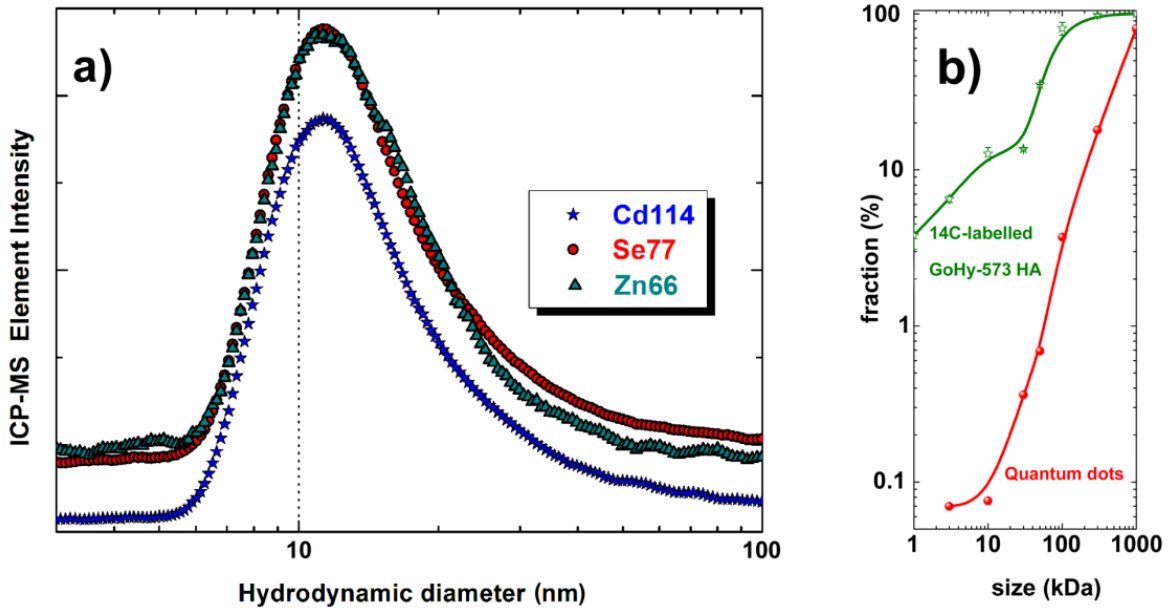

Figure 3.39: a) ICP-MS fractograms obtained after injection of 100 µL of a QD solution diluted at 1 mg/L in the AsFlFFF eluent (ultrapure water + NaOH; pH 9.3). The system is calibrated prior to the QD size measurements by injection of a mixture of polystyrene sulfonate standard (PSS) salt and carboxylated polystyrene nanoparticles. (b) Size distribution analysis via ultrafiltration (UF) of the QD in comparison to 14C-labelled Gorleben humic acid (GoHy-573HA) [224].

In the present study the quantum dots suspension at 1 mg/L was injected (100 µL) into the AsFlFFF system. The AsFlFFF eluent is at pH 9.3 and consequently quite close to the pH of the Grimsel groundwater (pH ~9.7) used for the drill core migration experiments. At that pH, the PEG are supposed to be deprotonated and the overall charge of the QDs is negative [225].

Core migration experiments. In the laboratory core migration experiments a set-up comparable to [41] was used (Figure 3.38). The inflow from the tubing was directly connected to the

fracture inlet without the use of a flow disperser, e.g. porous filter plate. This configuration was necessary since migration experiments using strong sorbing radionuclides on the same drill core have been carried out in parallel. By means of a HPLC pump (Knauer Smartline 1000) the desired flow rates were established. The flow rate was measured independently using a balance collecting the eluted fluid volume. The core was equilibrated by pumping

Table 3.9: Chemical composition of the original Grimsel groundwater (GGW) used in the migration experiments.

	Grimsel GW
pH	9.67
Ionic strength	1.2 mM
$[Mg^{2+}]$	12.6 µg/L
$[Ca^{2+}]$	5.3 mg/L
$[Fe^{2+, 3+}]$	< D.L.
$[Mn^{2+}]$	< D.L.
$[Sr^{2+}]$	182 µg/L
$[Cs^{+}]$	0.79 µg/L
$[La^{3+}]$	< D.L.
[U]	n.d.
$[Al^{3+}]$	42.9 µg/L
$[Na^{+}]$	14.7 mg/L
$[Cl^{-}]$	6.7 mg/L
[Si]	5.6 mg/L
$[SO_4^{2-}]$	5.8 mg/L
$[F^{-}]$	6.3 mg/L
$[Br^{-}]$	n.d.
$[NO_3^{2-}]$	< D.L.
$[HCO_3^{-}]$	3.0 mg/L

with natural Grimsel groundwater over a period of several weeks prior to the experiments. A tracer cocktail was prepared using natural Grimsel groundwater (ionic strength 1.2 mM; pH 9.67) as background electrolyte (Table 3.9). The total activity of HTO in the cocktail was 400 kBq and a QD concentration of 12.5 mg/L has been adjusted. HTO and QD concentrations were measured online using a HTO monitor (Raytest, MIRA-/GINASTAR) and a Luminescence spectrometer (AMINCO-Bowman Series 2), respectively. Errors in the online measurements of HTO and QD are estimated to be approximately 5 – 10 %, respectively. Injection of the tracer cocktail was applied using an injection valve (Upchurch Scientific) with a volume of 100 µL. After tracer injection the valve was switched back to natural Grimsel groundwater until the end of the experiments. Two different volume fluxes have been used in the experiments: 66.8 and 14.2 µL/min, respectively (see Table 3.10 for additional details). The question of artificially induced dispersion due to the tubing in the experimental setup was addressed by a tracer experiment using the exact setup as in the migration studies but without the drill core. It was found that only a negligible tailing (dispersion) occurred in the breakthrough curve.

CFD modeling

Governing equations of flow and transport. The governing equations describing fluid flow through arbitrary geometries are the Navier-Stokes equations. For a steady state laminar flow of a single phase, incompressible Newtonian fluid with constant viscosity it can expressed in vector form ((Equation 38 and (Equation 39) as [226]:

$$\nabla \cdot \boldsymbol{v} = 0 \qquad \text{(Equation 38)}$$

$$\nabla \cdot (\rho\, \boldsymbol{v}\, \boldsymbol{v}) = -\nabla p + \nabla \cdot (\tau) \qquad \text{(Equation 39)}$$

where ρ is the fluid density (kg/m^3), p is the static pressure (Pa), $\boldsymbol{v}$ = (v_x, v_y, v_z) is the velocity vector (m/s) and τ is the stress tensor (Pa). The assumption of an incompressible fluid holds for most of the fluids in the subsurface environment [227]. Surface walls are treated as "no-slip" boundary conditions constraining all velocity components to zero at the model walls. The inlet is defined as pressure inlet and pressure outlet boundary condition (prescribed gauge pressure = 0 Pa) is assigned at the outlet. In fluid mechanics, typically the Reynolds number (Re) is applied to characterize the type of flow. The Reynolds number provides a ratio of the inertia to the vicious forces or, in other words, the ratio of the velocity of convection to the diffusive velocity [228]. The Reynolds number for fluid flow in a fracture can be expressed as ((Equation 40) [229]:

$$Re = \frac{u \cdot a_m}{\eta} \qquad \text{(Equation 40)}$$

where *u* is a characteristic velocity (here, the volume averaged velocity magnitude; Table 3.10) (m/s), a_m is a characteristic length (here, the arithmetic average of fracture aperture) (m) and η is the kinematic viscosity (m^2/s).

Mass transport is modeled by the advection-diffusion equation ((Equation 41) [230]:

$$\frac{\partial}{\partial t}(\rho Y_i) + \nabla \cdot (\rho \boldsymbol{v} Y_i) = -\nabla \cdot \boldsymbol{J}_i \qquad \text{(Equation 41)}$$

where Y_i is the mass fraction of ith species (-), t is the time (s) and $\boldsymbol{J}_i$ is the diffusive flux of species i (1/m^2·s).

The influence of both hydrodynamic dispersion and diffusion on the transport behavior is generally expressed by the Peclet number (Pe) ((Equation 42) [231]:

$$Pe = \frac{u \cdot b}{D_m} \qquad \text{(Equation 42)}$$

where b is the mean aperture (m) and D_m is the molecular diffusion coefficient (m^2/s). It describes the ratio between advection and molecular diffusion. For high Pe numbers (Pe > ~ 50) advection dominates whereas low Peclet numbers (Pe < ~1) indicate dominance of molecular diffusion.

Table 3.10: Conditions and results from migration experiments and CFD simulations.

	Run #1	**Run #2**
Flux [µl/min]	66.8	14.2
Re [-]	0.026	0.0058
Pe HTO[-]	10	2
Pe QD [-]	607	135
max. velocity magnitude [m/s]	1.3×10^{-3}	2.9×10^{-4}
volume averaged velocity magn. [m/s]	5.67×10^{-5}	1.26×10^{-5}
R_p (Peak max. exp. HTO) [min]	51	129
R_p (Peak max. exp. QD) [min]	48	128
R_p (Peak max. model. HTO) [min]	50	161
R_p (Peak max. model. QD) [min]	49	159
R_f exp. [-]	0.94	0.99
R_f model [-]	0.98	0.99
Recovery QD	88%	68%

R_p = peak elution time; R_f = retardation factor ($R_f = R_p$[QD]/ R_p[HTO])

3D model generation. The 3D model applied in this study is generated using the drill core µCT measurements data. The µCT scan resulted in 1691 stacked 2D slices transformed into a 3D model representation of the drill core. Care was taken to accurately capture the fracture geometry. The resulting pixel length was 80 µm horizontally and vertically, respectively. Main µCT artifact reduction is preprocessing/correction of beam hardening effects by hypersurface fitting. A separate publication for this method is in preparation. After this correction and applying noise reduction filters (3D median filter), a simple, but exactly threshold segmentation was possible, checked by eye and several numerical methods (e.g. moving threshold window). For these steps the software MATLAB© (Mathworks, USA) and Amira/Avizo© (Visualization Science Group, USA) have been applied. Subsequently, 3D triangulated surfaces of the fracture (in STL format) were produced out of the full resolution segmented µCT data by means of the software Mimics© (Materialise, Belgium). This 3D STL data was afterwards imported in the software ICEM CFD© (ANYSY, 2009) for further processing. First, remeshing of the surfaces has been conducted constrained to user defined surface element size and quality resulting in a 3D surface mesh with ~ 1.1 million elements. Additionally, this

meshing approach required the adjustment of the element size otherwise an accurate representation of complex geometrical features of the fracture would not have been feasible. The resulting element sizes for the surface mesh ranged between 0.012 mm up to 0.39 mm. The surface elements have been smoothed to obtain the best possible distribution in the element aspect ratios which describes the length ratio of the triangles sides. Ideally, a perfect element possesses an aspect ratio of 1 when all 3 sides are equal in length. The final surface mesh contains over 85 % of elements having an aspect ratio > 0.8. Furthermore, the skewness of the elements has been inspected giving the ratio between the area of the element and the area of an ideal (equilateral) element (max = 1). The final mesh resulted in a mean skewness of 0.97. As a measure for the quality of the deviation of the mesh from the actual geometry the parameter “surface dev” was determined. The overall majority of surface deviation (> 95%) is in the range between 0 mm and 0.004 mm. These quality criterions were applied to guarantee a suitable and accurate surface grid upon the generation of a high quality volume mesh is feasible. Regarding the volume mesh generation, four boundary layers on every fracture surface using prismatic elements have been generated to better resolve near-wall flow and transport dynamics. With this type of mesh elements it was furthermore assured that even in areas where the aperture is very small sufficient elements are present to resolve the flow and mass transport dynamics. The remaining fracture interior was filled with tetrahedral elements. The final mesh of the fracture consists of ~ 10.5 million elements (3156334 nodes) in total with ~5.3 million tetrahedral elements and ~4.02 million prismatic elements.

CFD solver setup. Flow and mass transport simulations were modeled using the finite volume CFD software FLUENT© [230]. The flow was calculated using the steady state, double precision, implicit, pressure based solver. The SIMPLE (Semi-Implicit Method for Pressure-Linked Equations; [232]) algorithm was chosen as the solution method for Pressure-Velocity coupling. Pressure and momentum were solved applying a 2nd order and 3rd order MUSCL scheme, respectively. A convergence criterion of 10^{-6} was used for the continuity equation as absolute solution residual. Mass was introduced as a classical step input boundary condition. Initial concentration is defined as zero in the whole computational domain ((Equation 43):

$$C = 0[-\infty \leq x \leq +\infty; 0 \leq y \leq +\infty; 0 \leq z \leq +\infty; t = 0] \quad \text{(Equation 43)}$$

At the inlet ((Equation 44):

$$C = 1 \; for \; t > 0 \quad \text{(Equation 44)}$$

A molecular diffusion coefficient for HTO of 2.5e-9 m^2/s was applied [233]. The molecular diffusion coefficient of 4.2e-11 m^2/s for the QD was calculated based on their hydrodynamic diameter (12 nm) using the Stokes-Einstein equation [234] ((Equation 45):

$$D_m = \frac{k \cdot T}{3 \cdot \pi \cdot \eta \cdot d_p} \qquad \text{(Equation 45)}$$

where k is the Boltzmann´s constant (J/K), d_p is the particle diameter (m) and T is the absolute temperature (K). By derivation of the BTCs calculated with step input functions residence time distributions are obtained. Calculations were carried out on the Karlsruhe Institute of Technology (KIT) high performance cluster HP XC3000.

Results & Discussion

Core analysis by x-ray computed tomography. The spatial dimensions of the core are 0.1352 m in length and 0.05048 m in diameter. With the µCT setup a voxel resolution of 80 µm was achieved. By utilization of the complete µCT dataset a total porosity of 0.68 % and an aperture distribution of the fracture could be derived. As expected for a natural fracture, it possesses a complex 3D spatial geometry and fracture surface morphology (Figure 3.40). Zones where two fracture planes intersect each other (asperities) are visible heterogeneously distributed throughout the fracture. Especially in the upper third of the fracture a big asperity is visible in an area where the fracture is folded ~ 90° perpendicular to the z direction Figure 3.40a). One side of the core shows a relatively sharp border, while the other side has a very irregular boundary. The fracture exhibits a wedge-shaped geometry resulting in higher apertures at the more open regular left boundary and smaller apertures in the vicinity of the irregular boundary on the right side of the fracture. A possible presence of porous media (porous fracture filling material and microcracks lower than 80 µm) at the right fracture boundary is impossible to resolve on the basis of these µCT data, but cannot be excluded. This circumstance would directly impact the total volume of the fracture and thus the flow and mass transport dynamics. Additionally, the fracture walls could possess a porosity facilitating solute matrix diffusion. Since no unambiguous decision can be drawn, it was decided to treat the complete fracture as void space without the presence of porous media and the fracture walls were considered as impermeable for both flow and mass transport. The determination of the fracture aperture distribution was done by means of the software 3matic© (Materialise, Belgium) applying the final 3D surface mesh. First, the software automatically calculates a plane parallel the two fracture surfaces (midplane). This midplane is located in the middle of the two fracture surfaces, that is, this plane has the same distance to each fracture surface. Subsequently, the software is then able to measure the distance between the midplane and the surrounding fracture surfaces giving the fracture aperture. An overview of the aperture distribution is depicted in Figure 3.40. A mean aperture of 0.45 mm and a maximum aperture of 1.5308 mm can be derived. Approximately 56 % of the aperture values are in the range between 0.42 mm and 0.56 mm, 14% are in the range between 0.56 mm and the maximum aperture of 1.5308 mm and 28 % are distributed in the range between 0.42 mm to 0 mm

(Figure 3.41). One has to keep in mind, that all apertures smaller than the µCT resolution of 80 µm are treated as zero aperture, though smaller apertures than 80 µm may prevail in the fracture.

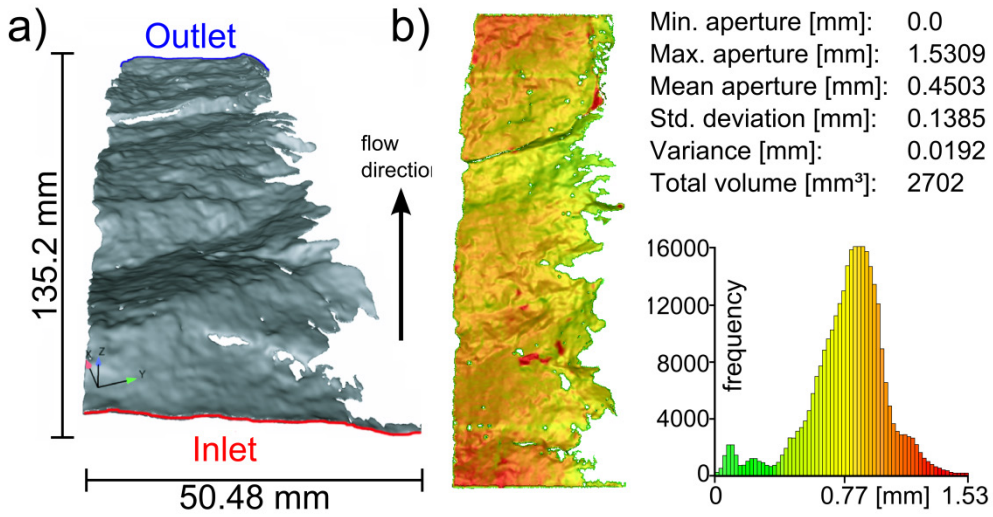

Figure 3.40: a) Rendered view of the fracture on basis of the µCT data set showing the complex fracture geometry and morphology together with the spatial dimensions. b) Colored fracture aperture distribution in conjunction with an aperture histogram and several statistical parameters of the fracture.

AsFlFFF-ICP-MS results. The AsFIFFF-ICP-MS fractograms obtained for the different components constituting the core/shell of the quantum dots, namely Zn, Se, Cd are used to determine the QD's hydrodynamic diameter. These fractograms superimpose as expected very well (Figure 3.39a). According to the calibration with polystyrene sulfonate standard (PSS) salt and carboxylated polystyrene nanoparticles, the hydrodynamic diameter of the QDs is 11.4 ± 0.5 nm with a FWHM (Full width at half maximum) of 12 nm. This is deduced from the peak maxima position of the Cd, Se and Zn- ICP-MS fractograms which are, as said, the fingerprints of the QDs .The hydrodynamic diameter value obtained from AsFIFFF measurements is the one considered hereafter.

Flow modeling. Figure 3.41a shows a volume rendering plot of the simulated normalized velocity magnitude for the fracture. Generally speaking, the simulated 3D flow field reflects the spatial complexity of the fracture geometry. The resulting flow field is a combination of four spatial fracture characteristics: (a) the wedge-shaped nature of the fracture, (b) the aperture variability, (c) the asperities and (d) the irregular right fracture boundary. One characteristic feature of fracture flow is channeling due to either aperture variability [235] or the influence of the asperities [236, 237] which is obvious, e.g. in the upper third model domain where the fracture is closed to a high extent. Here, flow velocities strongly increase to its maximum value as a result of the narrowing of the flow cross sectional area. High flow velocities (red colors in Figure 3.41) always occur in the vicinity of asperities indicating their paramount impact on the flow field. Moreover, the high velocity zone in the upper third of the fracture also develops as a consequence of a narrow section of the fracture planes leading to increased flow

velocities. The very irregular right fracture boundary is characterized by low velocities (blue colors in Figure 3.41) in contrast to the middle and left part of the fracture where the apertures are larger and thus higher flow velocities can be observed (green and yellow colors in Figure 3.41). To enhance the visualization of the flow dynamics, snapshots of virtual particle traces are presented in Figure 3.41b for three different travel times. These virtual particles are purely transported by advection following the streamlines and do not exhibit any molecular diffusion. Uniformly introduced at the inlet surface the particles spread out heterogeneously due to flow velocity variability and are constraint by the flow path heterogeneity on their way through the fracture. Particles starting near the right irregular boundary where low flow velocities prevail are delayed compared to particles traveling in the middle and left part of the fracture. These low speed particles creep along the right fracture boundary and reach the outlet at much later times than the overall particle ensemble. Flow velocity distributions are shown in Figure 3.41c as a log-log histogram for both Re numbers applied. Additionally inserted in Figure 3.41c, the velocity distribution for a 3D parallel plate model (3DPPM) using the mean fracture aperture is shown. While the 3DPPM exhibits a homogeneously distribution due to geometry uniformity, the distribution of the real fracture directly reflects the complex fracture geometry. The normalized frequency maximum represents the highest flow velocities in case of the 3DPPM. This is in distinct contrast to the histogram of the real 3D fracture where most of the flow velocities are low flow velocities and only a very small fraction represents high flow velocities. By comparison of both Re numbers applied for the real fracture (Figure 3.41c), it is obvious that only very little variations occur except for the highest flow velocities which shows some deviations. That is, the flow field linearly correlates to the applied pressure gradient (Darcy-type).

Core migration experiments

Figure 3.42 depicts the experimental breakthrough curves for both runs in conjunction with the 3D mass transport simulations results. Table 3.10 lists further details about experimental and model parameters and results. For simplification, in the following Run#1 represents the high flux experiment (Re = 0.026) and Run#2 denotes the low flux experiments (Re = 0.0058), respectively.

Run#1. In general, both the experimental HTO and QD BTC show a pronounced tailing (Figure 3.42a,b). The shapes of both BTCs differ from each other such that QD show a Δt between first arrival and peak maximum of 470 s compared to a Δt of 600 s for HTO indicating a sharper leading edge for the QD. The tailing of the HTO BTC can be approximated fairly well by fitting to a power law of t-3/2. This type of power law is often referred to as matrix diffusion and has been observed both in field and laboratory studies [238]. Considering the Pe numbers prevailing (Table 3.10), the occurrence of matrix diffusion seems reasonably to some extent. In contrast to the HTO BTC, the QD residence time distribution is much more

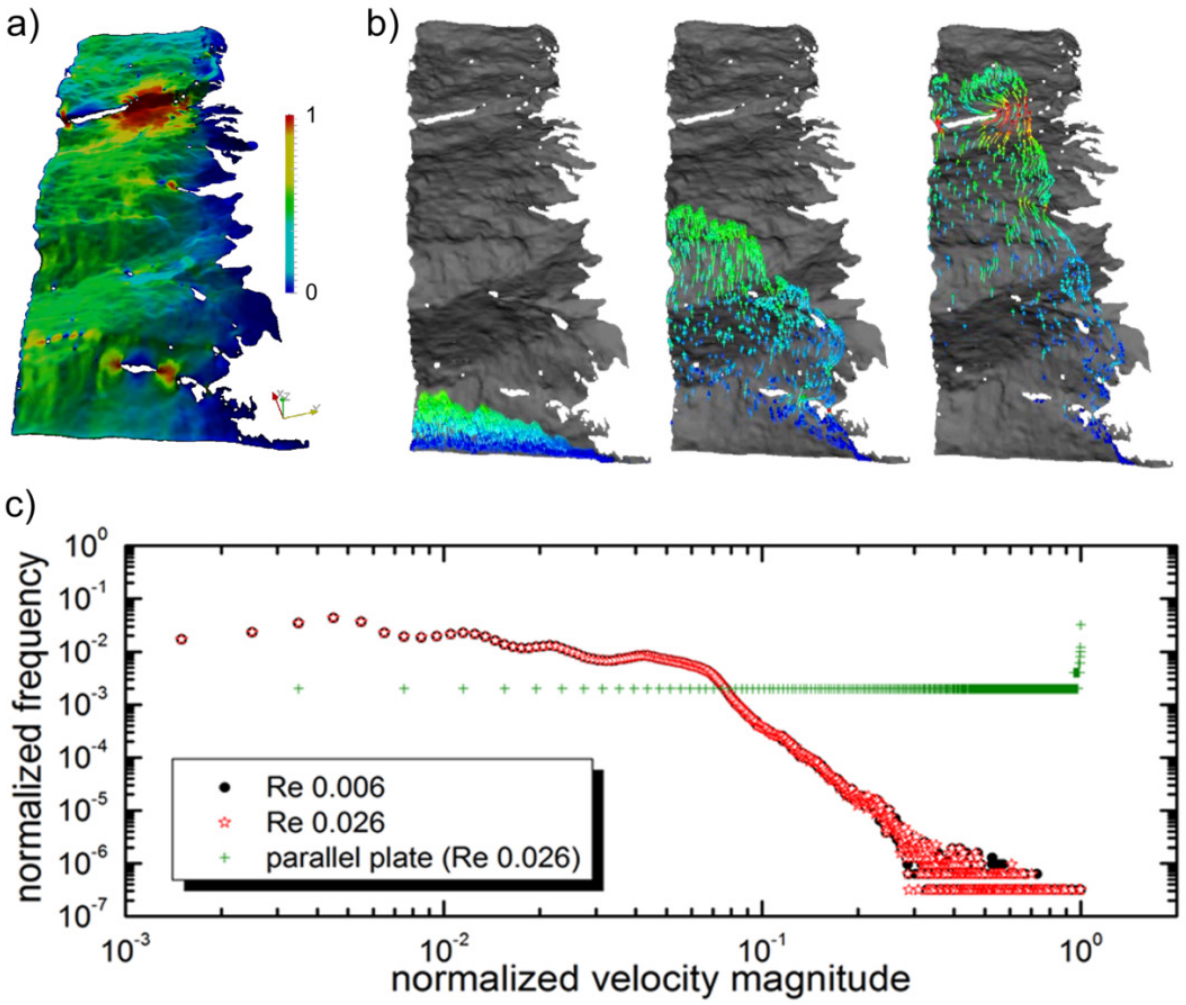

Figure 3.41: a) Normalized volume rendering plot of the flow field as calculated on basis of the µCT data. b) Particle traces snapshots showing the heterogeneous particle spreading due to flow velocity variability. c) Normalized histogram of the flow velocities for both Re numbers. Number of bins are 1000. Frequency is normalized to total number of frequencies; velocity magnitude is normalized by the maximum velocity magnitude.

broadened but also characterized by a pronounced tailing. As expected for colloidal transport, the QD peak maximum arrives faster than the HTO peak maximum yielding retardation factors < 1 which is a frequent observation in both field and laboratory experiments [23, 41, 239-242].

As a measure of the retardation we introduce the retardation factor Rf which is defined as ((Equation 46):

$$R_f = \frac{R_p[QD]}{R_p[HTO]} \qquad \text{(Equation 46)}$$

where $R_p[QD]$ is the peak elution time of the Quantum Dots and $R_p[HTO]$ is the peak elution time of HTO.

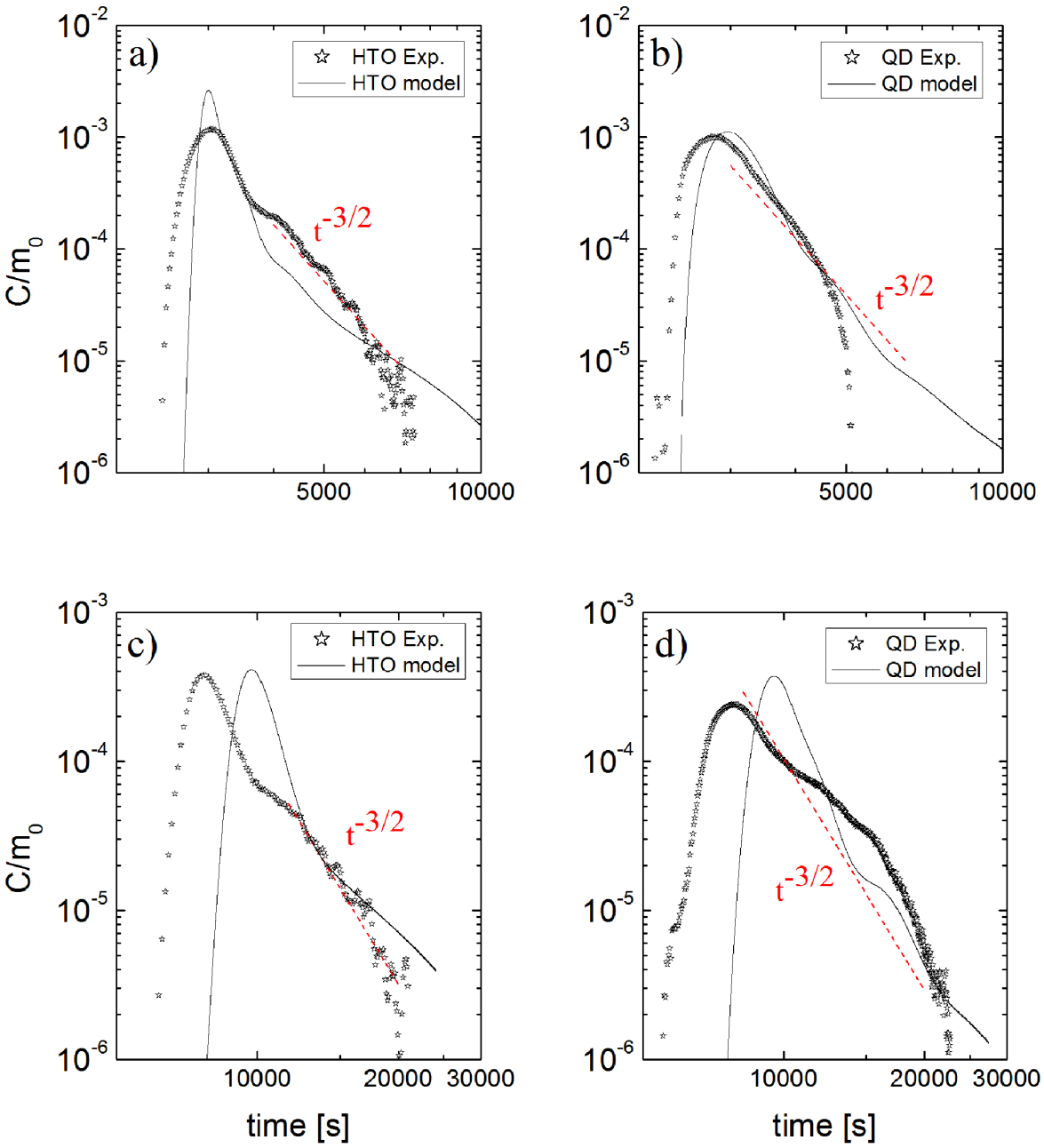

Figure 3.42: Experimentally derived BTCs (open stars) in comparison to simulated BTCs (black lines). a) HTO BTCs for Run#1 b) QD BTCs for Run#1 c) HTO BTCs for Run#2 and d) QD BTCS for Run#2. Red lines in a) and b) represents the empirical power law for matrix diffusion ($t^{-3/2}$), respectively.

The calculated experimental retardation factor (R_f) for the QD peak is 0.94 based on the positions of the peak maximum time of HTO and QD (Table 3.10). This finding can be explained by the different chemical properties and physical transport behavior of the colloids compared to solutes. In addition to a lower molecular diffusion coefficient for colloids, it was shown that finite sized nanoparticles are preferentially transported in the higher flow veloci-

ties portions of a parabolic velocity profile and do not map the low flow velocity areas [243]. Depending on the nature of the nanoparticles, their surface properties (e.g. hydrophilic or hydrophobic, negative or positive surface charge) may differ significantly from the chemical characteristics of solutes, altering their migration behavior. Under the geochemical conditions prevailing in the experiments both the QD and the mineral surfaces of the diorite drill core are characterized by negatively charged surfaces [244, 245]. [225] applied CdTe/CdS QD with PEG surface coating in column studies at pH 7.8 and determined a zeta-potential of the QD of -30 to -45 mV depending on the ionic strength. Regarding the surface charge of the diorite, we conducted streaming potential measurements on the Äspö diorite yielding zeta-potentials of ~ -55 mV at a pH of ~9.7. This assumption is further corroborated by [246] stating that in most natural aquatic environments negatively charged mineral surfaces predominate. Therefore, processes like anion exclusion due to repulsive electrostatic interactions should dominate and physiochemical filtration/adsorption appears unlikely under the chemical conditions of the Grimsel groundwater (high pH of ~9.6 and low ionic strength), respectively. A possible straining of the QDs cannot neglected completely and may contribute to the lower recoveries observed compared to HTO recoveries. The QD BTC tailing cannot be described by the empirical matrix diffusion power law. This observation can be expected since the diffusion coefficient of the QD is almost two orders of magnitude lower than it is the case for HTO which is further reflected in the Pe number of 607 for the QD and only 10 for HTO, respectively. This indicates that the QD are more strongly influenced by advection whereas HTO exhibits a much higher impact of molecular diffusion facilitating matrix diffusion. Matrix diffusion coefficients for colloids range between $7e^{-18}$ m^2/s for 2 nm to $1.5e^{-18}$ m^2/s for 100 nm colloids, respectively [44]. Based on the assumption of a diffusion perpendicular to the main flow direction, the diffusion length x can be estimated with the following equation ((Equation 47):

$$x = \sqrt{2D\tau} \qquad \text{(Equation 47)}$$

where D is the molecular diffusion coefficient [m^2/s], τ is the tracer/colloid residence time [s]. Using the experimental residence times of 3412 s for e.g. the HTO experiments of Run #1 and 10186 s e.g. for the QD experiments of Run #2 and matrix diffusion coefficients of $2.5e^{-10}$ m^2/s (HTO) and $7e^{-18}$ m^2/s (QD) a diffusion length of ~ $1e^{-3}$ m and ~ $3.8e^{-7}$ m can be derived. Therefore, considering the mean fracture aperture of 0.45 mm a matrix diffusion process in case of the QD can be neglected, whereas HTO may be influenced by matrix diffusion under these conditions. Moreover, the QD are likely to be effectively hindered to diffuse into a possible porous fracture wall matrix due to other processes like e.g. size exclusion effects [247].

Run#2. The HTO BTC is again characterized by a sharper increase in concentration and peak maximum compared to the QD BTC. The QD BTC shows a Δt between first arrival and peak maximum of 1740 s compared to a Δt of 1370 s for HTO indicating this time a sharper leading edge for the HTO compared to the QD BTC. The tailing of the HTO can be approximated by the empirical matrix diffusion power law in line with the BTC from Run#1. The Pe number for HTO in Run#2 is 2 indicating an even stronger impact of molecular diffusion on

the transport behavior. Consequently, the prevailing flow and transport conditions even more facilitate a diffusion of the HTO into a possible core matrix. Recoveries of HTO are within analytical uncertainty quantitative both for Run#1 and Run#2 and decrease for the QD with decreasing flow velocities from 88% in Run#1 to 68% in Run#2, respectively. This leads to the conclusion of a more pronounced interaction of the QD with the fracture surfaces with decreasing flow velocity in terms of straining processes and/or, though to a much lesser extent as stated above, to some extent of filtration/adsorption due to possible charge heterogeneities of the mineral surfaces explaining the observed difference in the rising edge of the BTCs. Similar to Run#1, the QD BTC shows an earlier first arrival time than the HTO peak, but the position of the peak maximum between the QD and HTO BTCs are almost identical (Rf QD = 0.99) showing that the mean residence times approach each other with decreasing flow velocity.

Transport modeling (Run#1 & Run#2). Based on the classical filtration theory [248-250] and taking into account the QD hydrodynamic diameter of 12 nm the single collector efficiency is solely controlled by diffusion. Therefore, in this study we simplified the colloidal transport modeling by variation of the diffusion coefficient. The general applicability of this approach to colloid transport is therefore only valid for similar colloid sizes and colloid charge.

Regarding the first arrival of the modeled BTCs, the QD BTCs for both flow velocities show an earlier arrival times compared to the HTO BTCs in line with the experimental findings. Furthermore, the position of the QD peak maximum is also shifted to earlier times compared to the HTO BTC. Again, this observation fits to the experimental findings. The overall modeled BTC positions are shifted to later times for the lower flow velocity (Run#2) compared to the experimental BTCs, whereas for Run#1 the positions are comparable covering a range of~ 0.6 – 3.1 % and 3.1 – 7.8 % for HTO and QD, respectively depending on the analysis of goodness of fit shown below.

Though, the Rf value of 0.98 for the simulated QD peak is slightly higher than the experimental QD Rf (0.94) in Run#1, whereas the QD Rf value of 0.99 is equal to the experimental QD Rf value (0.99). Concerning HTO, the modeled BTC (Run#1) describes the peak maximum position quite good though over-predicts the maximum normalized concentration. The modeled HTO BTC of Run#2 can reproduce the experimental maximum concentration very well and also the overall peak shape of the BTC fits satisfactorily to the experimental BTC though shifted to much later times.

In contrast, the simulated QD BTC of Run#1 describes the normalized concentration of the experimental BTC very good, but is shifted to later times as mentioned above. The modeled QD BTC of Run#2 shows in addition to the time shift also a higher peak maximum and the agreement to the experimental BTC in terms of predicted maximum concentrations and overall peak shape is rather poor. Here, the model exhibits a much sharper peak shape than the experimental QD BTC. The deviation in Run#2 can be explained with the observed decrease in QD recovery (Table 3.10), which would dampen the peak maximum and influence through retardation the shape of the BTC tailing.

As a measure of goodness of fit of the BTC, we used the different temporal moments both for the modeled and experimental BTC. It has to be clearly stated, that forward simulations were conducted in this study and therefore the term fit is somewhat misleading, since no fitting at all was tried by the simulations. The different temporal moments are given as ((Equation 48, (Equation 49 and (Equation 50) [251]:

$$m_0 = \int_0^\infty c\,dt \qquad \text{(Equation 48)}$$

$$m_1 = \int_0^\infty \frac{c \cdot t}{m_0} dt \qquad \text{(Equation 49)}$$

$$m_2 = \int_0^\infty \frac{c \cdot t^2}{m_0} - \langle m_1 \rangle^2 dt \qquad \text{(Equation 50)}$$

in which m_i is the i^{th} temporal moment of the breakthrough curve, c is the concentration at the outlet and t is the time. The mean arrival time is given by the first temporal moment m_1 divided by the zero-order moment m_0. It is positioned at the center of mass of the BTC and in consequence this position is more shifted for pronounced tailings. Since the simulated BTC delivers longer tailings than the experimental BTC, it was decided to compare both the full simulated BTC (called “model full” in Table 3.11) and a truncated version of the simulated BTC to the last experimental data point obtained (called “model cut” in Table 3.11). Table 3.11 lists the results of the three moments for all BTCs.

Concerning Run#1, the first moment (m_1) of HTO (“model full”) and the experimental HTO BTC are nearly perfect with a deviation of only 0.61 %, whereas the second moment (m_2) of both BTCs are not in a good agreement with a deviation of 61.1 % due to the sensitivity of the second moment to the much longer tailing in the model(full) BTC. Thus, this deviation becomes significantly smaller (26.9 %) when the HTO (“model cut”) is compared to the experimental HTO BTC. But, in this case, the first moment (m1) deviates slightly more (3.1 %), but still is in fairly good agreement. Similar results are obtained for the QD BTCs of Run#1. A deviation of 7.8% for m_1 is obtained when comparing the QD (“model full”) with the QD experimental BTC. The second moment (m_2) is again quite high with a deviation of 70.1 % and again shows a much higher agreement between the BTCs when the QD (“model cut”) is compared to the experimental QD BTC (deviation of 17.1 %). Here, also the deviation of the first moment (m_1) reduces to 3.8 %. Regarding Run#2, the second moment (m_2) of the HTO (“model full”) compared to the experimental HTO BTC shows the smallest deviation of only 6.2%. The shape of both BTCs is very similar except that the BTCs are shifted in time to each other. This shift is expressed in a deviation of 15.3 % of m_1. This difference is slightly reduced to 13.9 % when comparing the HTO (“model cut”) with the experimental HTO BTC

but in this case the second moment deviates much more (30.6%) again due to differences in the tailing and the corresponding sensitivity of the parameter m_2. A better congruency for

Table 3.11: Results of the temporal moment's calculations for the experimental and simulation breakthrough curves.

		m_0	m_1	m_2		m_0	m_1	m_2
Run#1	HTO Model (full)	0.99	3433	1355398	HTO Model (cut)	0.98	3308	415235
	HTO Exp.	1.00	3412	527342	HTO Exp.	1.00	3412	527342
	Deviation (%)	0.1	0.61	61.1	Deviation (%)	2.1	3.1	26.9
	QD Model (full)	0.99	3356	884804	QD Model (cut)	0.96	3217	226018
	QD Exp.	1.00	3095	264539	QD Exp.	1.00	3095	264539
	Deviation (%)	0.3	7.8	70.1	Deviation (%)	4.0	3.8	17.1
Run#2	HTO Model (full)	0.97	10928	6790202	HTO Model (cut)	0.95	10757	4874178
	HTO Exp.	0.94	9251	6367815	HTO Exp.	0.94	9251	6367815
	Deviation (%)	2.9	15.3	6.2	Deviation (%)	1.6	13.9	30.6
	QD Model (full)	0.98	10807	6564891	QD Model (cut)	0.97	10688	4927821
	QD Exp.	1.00	10186	9722107	QD Exp.	1.00	10186	9722107
	Deviation (%)	1.9	5.7	48.1	Deviation (%)	2.9	4.7	97.3

parameter m_1 is obtained regarding the QD ("model full") and QD ("model cut") in comparison to the experimental QD BTC (5.7 % and 4.7 %, respectively). In contrast the parameter m_2 shows a deviation of 48.1 % and even 97.3 % for the QD ("model full") and QD ("model cut"), respectively.

Overall, as in the case for the experimental BTCs, the simulated residence time distributions show pronounced tailings. Since the model does not include matrix diffusion the tailing cannot be fitted to a power law of $t^{-3/2}$. Generally speaking, the observed heavy tailings in the simulated breakthrough curves can be clearly attributed solely to dispersion due to the fracture geometry and confirms the proposal made by [252] that tailing of the colloids is mainly caused by the structure of the flow field and that for colloid/nanoparticle transport, matrix diffusion is of minor importance [252].

Uncertainties in µCT analysis and boundary conditions. As stated above a voxel resolution of 80 µm has been achieved in the µCT analysis. In consequence, spatial features (apertures and microcracks) smaller than this threshold resolution remain unresolved and therefore ex-

cluded in the model. Moreover, the right fracture boundary may represent a porous media (porous fracture filling) type material but is treated as open space in the model resulting in a higher void volume compared to the drill core. If this would be the case, applying the same pressure gradient in both experiments and simulations would cause higher flow velocities in the experiment due to the smaller total volume resulting in a faster arrival of the experimental BTCs. For this, more systematic simulations with varying boundary conditions and changing spatial features (erosion and dilatation of fracture surface, means adding/subtracting volume) are necessary to understand the impact of available volume in the computing domain. Furthermore, a possible matrix porosity in the vicinity of the fracture walls are not visible in the CT data and thus not taken into account in the modeling exercise. For testing this, a coupling of the transport simulations with a dual porosity approach would be useful. The experimental BTCs for HTO may indicate matrix diffusion since the tailings can be approximated with the empirical power law of $t^{-3/2}$. Assuming matrix diffusion present in the experiments would lead to a broadening of the HTO BTC compared to the calculated HTO BTC due to the lack of fracture wall porosity in the model. This deviation between the model and the experiment could explain the smaller normalized maximum concentrations in the experimental data.

Much effort has been spent to generate the best possible computational grid in terms of mesh resolution and computational resources and times, respectively. Mesh resolution studies using 1.5, 3, 5.5, 7.5, 9, 10.5 and 14 million elements revealed that the mesh resolution of 10.5 Mio elements applied is sufficiently detailed to capture the flow and mass transport dynamics providing a so called grid independent solution. That is, the solution of arbitrarily chosen parameters (e.g. flow velocity or pressure) at selected points of interest within the model did not further change (or only to a very marginal extent according to user defined criterions) for a refined mesh. Numerical diffusion/dispersion was minimized using appropriate small time steps (0.1 s) fulfilling the Courant and Neumann criterion, respectively.

Concerning boundary conditions it cannot be excluded that conditions set in the flow and transport simulation do not match exactly the conditions prevailing in the experiments. The application of a pressure inlet boundary condition correctly takes into account the influence of inlet surface geometry on fluid flow resulting in a heterogeneous velocity distribution along the inlet surface. On the other hand, a perfect uniformly introduced tracer in the simulations may not represent the real experimental conditions prevailing. It is likely that the tracer is introduced more concentrated in terms of surface area in the experiments (point source type). This circumstance should result in a narrower BTC since the tracer would not map all the fracture volume. In contrast, the experimental BTCs are always broadened compared to the simulated BTCs. Here, the occurrence of matrix diffusion could be the responsible process for HTO leading to the broadening of the experimental BTCs.

Conclusions

Overall, our study clearly shows the mobility of the ENP's (hydrophilic QDs) in a natural single fracture under natural Grimsel groundwater conditions. Concerning the core migration experiments, a decrease in QD recovery is observed with lower flow velocity (1.5 m/d) indicating possible fracture surface interaction effects (straining, adsorption/filtration). Simulated HTO and QD breakthrough curves exhibit heavy tailing reflecting unequivocally the influence of fracture heterogeneity on flow velocity distributions and on mass transport. Especially the 3D numerical modeling unequivocally verifies the impact of real natural fracture geometry and the resulting complex flow field as an additionally retardation mechanism for solutes/nanoparticles since no matrix diffusion, sorption, straining or filtration has been incorporated in the model. Nonetheless, in case of the QD migration experiments straining processes and, most likely to a much lesser extent, adsorption/filtration at the fracture surfaces due to surface charge heterogeneities may also contribute to the observed long tailing effects and the decreasing recovery for decreasing flow velocity. Strictly speaking, the experimental QD results presented are valid for the type of QD, diorite drill core and the Grimsel groundwater chemistry applied in this study. The results for HTO are more generally valid since processes like sorption, filtration or straining are irrelevant and also no dependency of HTO migration behavior is expected for varying groundwater chemistry. Thus, the differences observed in the experimental HTO BTCs should be solely attributed to hydrodynamics due to fracture geometry and matrix diffusion.

Despite the higher computational and technical effort in creating a 3D model on basis of µCT data of a real natural single fracture, the results provide a step forward towards a more fundamental understanding of the processes governing fluid flow and mass transport in real single fractures. Furthermore, this approach facilitates the interpretation and analysis of migration experiments which most often represent black box type experiments.

4 Conclusions and Outlook

The results of this project contribute in different ways to the safety case for a radioactive waste repository. Firstly, it accounts for the assessment basis, since the knowledge and understanding of processes, particularly on colloid/nanoparticle generation and colloid/ nanoparticle stability has significantly increased. Secondly, the work in Kollorado-2 strongly contributes to a further improvement of the in-situ experiments, which are important for upscaling as well as demonstration issues required in a safety case. Thirdly, the results from the experimental program are abstracted to performance assessment and transport codes are applied to simulate the colloid-facilitated transport under near natural hydraulic conditions. The results of all three aspects are summarized in the following sections.

4.1 Understanding of colloidal/nanoparticle processes

A number of different aspects concerning the colloid/nanoparticle formation and fate have been tackled within the KOLLORADO-1 project and the investigation has now been continued within its follow-on project KOLLORADO-2.

Radionuclide speciation and interaction with bentonite/montmorillonite. Experiments carried out with fracture filling materials from Äspö and Grimsel under Grimsel groundwater conditions (glacial melt water reference) demonstrate different interaction behavior of long-lived radionuclides with colloids and mineral surfaces. Within Kollorado-2 batch experiments on RN sorption reversibility kinetics with Zn– and Ni-labeled montmorillonite colloids in the presence of granite fracture filling material and Grimsel groundwater have been conducted identical to previous experiments using natural FEBEX bentonite colloids ([74]). The new experiments generally confirmed the previous results and show comparable behavior of the synthetic montmorillonite colloids. The tri-and tetravalent radionuclides ^{232}Th(VI), ^{242}Pu(IV) and ^{243}Am(III) are almost quantitatively associated with clay colloids and show sorption reversibility. The reversibility kinetics are slower in case of the synthetic Zn- and Ni-montmorillonite colloids compared to the FEBEX colloids. The difference in surface area ratio (colloid/FFM) due to the higher specific surface area (~ a factor of 2) for the synthetic Zn-/Ni-clay colloids is hypothesized as explanation. As observed in earlier studies ^{99}Tc(VII), ^{233}U(VI) and ^{237}Np(V) are not initially associated to the synthetic Zn- and Ni-montmorillonite colloids. However, regarding these RN, within the duration of the experiments a distinct drop in redox potential is observed. In consequence, the redox sensitive elements ^{99}Tc(VII), ^{233}U(VI) and ^{237}Np(V) are prone to reduction processes in this study. The similar behavior of ^{99}Tc(VII) and ^{237}Np(V) indicates for both a reduction to the tetravalent state. For Tc this leads either to sorption to the fracture filling material or precipitation of a sparingly soluble Tc(IV) phase associated with the FFM surface, but not the clay colloids. However, for ^{237}Np(IV) an interaction with the clay colloids or the formation of eigencolloids stable in solution has to be postulated based on the removability via ultracentrifugation. For U(VI) a slow decrease in concentration

over the whole experimental duration may be either due to a slow $^{233}U(VI)$ sorption and/or reduction to $^{233}U(IV)$.

Colloid generation at the compacted bentonite fracture interface. A pH and ionic strength dependent extent of colloid generation from a compacted bentonite source was observed very much driven by the respective CCC. For conditions below the CCC, colloid generation is confirmed, whereas in experiments with an ionic strength lying above the CCC, colloid generation within the observation period is negligible. The experiments substantiate the important influence of the CCC for the potential release of clay colloids from bentonite.

Furthermore, mock-up tests to optimize the final design of the CFM long-term in situ study and show the general feasibility are performed. The results will be used to optimize the analytical long-term monitoring program for the field experiments. Both, mechanical erosion due to the swelling into the artificial 1 mm fracture as well as chemical erosion evidenced by chemical long-term changes in contact water composition (chloride, sulfate) have been observed. The swelling pressure is sufficient to break the glass ampules filled with labeled synthetic Ni-montmorillonite, Na fluorescein and the sorbed tri- and tetravalent elements. Eroded bentonite concentrations determined under the adjusted flow velocity for the CFM experiment of 1.8 - $2.3 \cdot 10^{-5}$ m/s reach 6 – 15 mg/L with a bimodal size distribution of < 45 nm colloids and colloids in the size range of 150-500 nm, respectively. Concerning the labeling with glass ampules the contact area and released proportion of total colloid mass has to be taken into account concerning the detection limits of the analytics. Radioisotopes and pre-concentration methods (exchange resins in collaboration with Helsinki University) are currently tested in the ongoing laboratory program for the CFM long-term in situ study.

The implementation of this data in currently available erosion models is an ongoing field of research activity within CFM and the EU project CP BELBaR.

Colloid – Mineral surface interactions. The results of the KOLLORADO-1 project showed that the interaction of colloids with mineral surfaces is mainly controlled by electrostatic interactions. Strongest attractive forces are observed close to or below the individual point of zero charge (pH_{pzc}) of the minerals. According to the results, colloid adsorption (adhesion forces) in alkaline regime (e.g., Grimsel groundwater conditions) is weak. Investigation using latex microspheres revealed only attractive forces for the mineral phase apatite, which occurs as accessory mineral in the Grimsel Granodiorite. Separate measurements show that Ca(II) concentrations as low as 10^{-4} M as present in Grimsel groundwater reduce colloid-mineral surface repulsive forces by a factor of about three and adhesion forces become detectable even at high pH. Therefore, the probability of colloid attachment to mineral surfaces increases also in low mineralized groundwater at high pH. Experimental observations of weak colloid retention in such systems can be qualitatively also explained by such kinetically controlled processes. A further microscopic investigation in Kollorado-2 project emphasized the importance of surface heterogeneity and its role to retain colloidal particles onto surfaces under unfavorable conditions (surfaces with same charge) using vertical scanning interferometry (VSI) and atomic force microscopy (AFM) techniques. The results presented suggest that a mixture of several mechanisms, such as local DLVO potential variation as well as local

fluid dynamics are involved in the complex behavior of colloid retention increase at the rough rock surface under unfavorable conditions.

Colloid mobility. Based on the results of the laboratory migration studies Febex bentonite colloid mobility is relatively high and only small colloid fractions are found to be retained in the fracture under the Grimsel groundwater conditions. As mentioned above this finding is in qualitative agreement with colloid-mineral interaction studies. Compared to the colloid recovery the initially colloid associated metal recovery is significantly lower and decreases with increasing residence time clearly indicating the relevance of kinetically controlled desorption processes under these conditions. This confirms earlier findings obtained by other authors [23, 41, 76] at considerably shorter migration times. Tetravalent actinide ions such as Th(IV) show slower dissociation rates as compared to those of the trivalent metal ions Eu(III) and Tb(III). The time dependent decrease of metal ion recovery observed in column experiments is again in qualitative agreement with the outcome of batch sorption tests. Both studies confirm the importance of considering radionuclide desorption kinetics for the assessment of colloid mediated radionuclide transport for nuclear waste disposal (see discussion below). Without this consideration, results of short-term laboratory experiments cannot be applied to make long-term predictions.

4.2 Improvement and optimization of in-situ experiments

During this project phase significant progress concerning the colloid migration under near natural hydraulic conditions at the Grimsel Test Site was achieved. The control of the hydraulic system has allowed further decreasing the gradients and consequently increasing the travel times in the dipole experiments. The established flow velocity and gradient in the MI shear zone is more relevant to post-closure situation with 1% gradient and ~10^{-5} m/s flow velocity. Even under these conditions high recovery of ideal tracers are established.

In order to reduce the analytical uncertainties in determining bentonite colloid concentration, particularly under the conditions of the in-situ experiments, synthetic Zn- and Ni-labeled montmorillonite colloids have been developed. As shown in reversibility experiments these colloids display a very similar behavior to the FEBEX bentonite colloids. The use of the Zn and Ni ICP-MS signal significantly reduces the uncertainties coupled with the determination of the colloids concentration in solution especially in presence of other natural colloids, thus providing confidence in the field as well as in the reversibility results obtained.

The improved conditions particularly allowed to study in more detail filtration/sorption processes of colloids on fracture fill material, and desorption processes of radionuclides/homologues from the colloids during transport in the shear zone. The experiments showed that radionuclide/homologue colloid associated transport over increasing residence time is detectable in the shearzone, which is a proof of concept for the planned long-term in situ test monitoring bentonite erosion.

- Radionuclide/Homologue recovery is lower and in turn the sorption reversibility faster for trivalent actinides compared to tetravalent actinides.

- Overall, the bentonite colloid sorption reversibility kinetics are faster in the in-situ dipole experiments than observed in batch type studies.

- Redox reactions are faster compared to lab batch-type studies, which is a clear result from the more reducing redox conditions established in-situ.

These experiments on the demonstration of colloid mobility under defined hydraulic conditions are of paramount importance to be used for spatial and temporal scaling of laboratory results to more natural conditions.

With respect to the CFM project they are crucial to judge later on the potential bentonite erosion and colloid formation in the long-term in situ test, which is planned to be started in 2014. The megapacker sealing system works well and is ready for this experiment. Concerning the colloid/radionuclide source of the long-term in-situ experiment mock-up tests have been performed to optimize the final design of the CFM long-term in situ study and show the general feasibility (see above).

4.3 Impact on long-term safety assessment

Data and process understanding gathered within the present project allows a much better appraisal of the impact of colloid-facilitated radionuclide transport on the long-term safety assessment of a geological repository. In the presence of colloids/nanoparticles radionuclide transport might be increased or decreased, depending on the interaction between radionuclides, colloids and the sediment matrix. It is particularly important to know, firstly, the kinetics of radionuclide interaction with colloids and notably the dissociation rates, i.e. to what extent do initially colloid-bound radionuclides desorb from the colloids during their migration through the geological formation and, secondly, how strong the interaction of colloids with the sediment matrix is and what is the time dependence of processes involved.

Earlier approaches to the description of the colloid-mediated migration of pollutants and radionuclides by coupled reactive transport codes assuming instantaneous establishment of chemical equilibrium usually failed to reproduce experimental data. As a consequence ‘irreversible’ sorption processes were often invoked to explain this discrepancy. The ‘irreversibility’ hypothesis, however, implies that otherwise strongly retarded polyvalent actinide ions can migrate via colloidal transport without any retention. Therefore, in our transport calculations most emphasis was placed on the investigation of kinetic effects supported by experimental data and their impact on the arrival time and recovery of radionuclides and colloids.

Transport calculations have been performed with respect to tri- and tetravalent lanthanides/actinides, which show strong association to the bentonite (montmorillonite) colloids. Several dipole tests performed in one dipole covered a wide range of transport times. The flow conditions are approximating the natural conditions in fractured rock systems. This and the fact that all test have been performed within the same dipole enabled us to study the impact of kinetically controlled processes like colloid filtration and homologue/radionuclide desorption, which was not possible under the conditions of the CRR experiment. Although the

shear zone was considered as a porous medium with respect to flow and transport the simulation results are very promising.

The first important statement for performance assessment is that filtration (on the time scale of the experiment) is of relevance under the conditions in this CFM dipole and the respective transport times. The calculated recoveries quite well follow the experimentally observed recoveries. Some but not all of the field tests also indicate a low reversible interaction. From the viewpoint of performance assessment a filtration process is of high relevance, since an immobilization of the colloids has the potential to significantly reduce the consequences of colloid facilitated radionuclide transport with respect to radiation exposures. In order to quantify the filtration processes it needs to be known, whether the process is irreversible on the considered time scale. Its impact also depends on the desorption rate of the radionuclides from the colloids. A low reversible interaction with retardation factors in the order of 1.5 are judged to be of low relevance for PA, since it would only slightly retard the transport of colloid-bound radionuclides.

The second process of high relevance is the desorption of the radionuclides from the colloids. The impact of the desorption process of course depends on the properties and behavior of the colloids. Two limiting cases can be distinguished: (i) The colloids are irreversibly filtrated. In this case a slow desorption rate would be positive for long-term safety, since the radionuclides are bound to immobile colloids. (ii) The colloids are transported along the flow path without retardation: In this case a fast desorption rate would be positive for long-term safety, since the transport of the free radionuclides is much slower than the colloid-bound transport.

From the simulation of the CFM field experiments desorption rates can be derived. The results show that on the timescale of the experiments desorption clearly plays a role. Firstly, the recoveries for trivalent homologues/radionuclides are generally lower than for tetravalent, i.e. the desorption rates for the trivalent are higher than for the tetravalent. This is true for all transport times. Further, the experimental data indicate a clear decrease of the recovery with increasing transport time at transport times, which is another important observation with respect to performance assessment and more discussed below.

Within Kollorado-2 project further qualification of transport models was achieved. Predictive calculations for colloid-bound radionuclide transport in dipole experiments under near natural hydraulic conditions have been successfully performed. This became possible because of the improvements in the field studies and the establishment of stable flow conditions in the shear zone as described above. Further, 3D CFD simulations (on the basis of real 3D geometry obtained by µCT) of the transport of tritiated water and nanoparticles – so called quantum dots – in drill-core column experiments were performed. The experimental results show that natural 3D fracture heterogeneity represents an important additional retardation mechanism for solutes and colloidal phases besides retardation processes like sorption, filtration, straining or matrix diffusion. This is clearly verified by the numerical simulations, where the 3D real natural fracture geometry and the resulting complex flow velocity distribution is the only possible process causing solute/nanoparticle retardation. The results provide a step

forward towards a more fundamental understanding of the processes governing fluid flow and mass transport in real single fractures.

Furthermore, a PA model considering colloid facilitated radionuclide transport with kinetically controlled processes for fractured (not porous) media to estimate consequences for long-term safety assessment is now available. First applications regarding the Finnish safety case are just started.

Such results will then be compared to the PA calculations performed in Kollorado-1 project. The conclusions from these calculations are still valid. They showed that colloid impact on actinide transport under given conditions (clay colloid concentration: 20 mg/L, Grimsel groundwater conditions with low ionic strength and high pH, migration through a stream tube with low dispersion) is very limited and can be described by an equilibrium approach. This conclusion holds for the assumption that colloids are stable and not filtered. Unretarded colloid-mediated transport only becomes relevant for very slow actinide desorption rates, which have hitherto not been observed in experiments. The only conceivable geochemical process leading to such low rates for actinide dissociation from colloids would be incorporation into colloid structures, e.g. in the course of secondary colloid phase formation processes as observed in the mixing zone at the bentonite/groundwater interface. Concentrations of those neo-formed colloids, however, has been found to be very low.

However, when applying the new code for fractured media now more realistic conditions will be assumed. These include (i) assumptions for container failure concerning the number of containers and point in time, (ii) the source term of colloid-bound radionuclides, i. e. a better estimate of radionuclide/colloid inflow based on the knowledge on colloid formation, (iii) the flow characteristics in the granite and (iv) the consideration of glacial cycles.

The conclusions formulated here are derived for fractured, granitic rock. For repositories in such host rocks a bentonite buffer is currently the preferred component in the engineered barrier system (EBS) in many countries. The release of bentonite colloids/nanoparticles from the outer rim of a bentonite buffer (gel layer) into water conducting fractures is an important process notably for scenarios considering glacial melt water intrusion that has to be addressed in the safety case.

With respect to other host rocks the following general conclusions can be drawn from the outcome of the present study. In several countries the EBS concept for repositories in clay or claystone is similar with regard to the buffer material, usually bentonite or other swelling clays, considered as preferred buffer around the waste containers. However, the characteristics of different host-rock types severely influences colloid mobility. Usually, the pore sizes in claystone are very low (in the range of several nm), resulting in a mechanical filtration of colloids. Under these conditions the impact of clay colloids on radionuclide transport through the host rock is low. Colloid facilitated transport is only becoming relevant, if water conducting fractures or fissures appear in the claystone and stay open for considerable periods. Even then, clay colloids are only mobile if they remain stable in the groundwater. Clay formations in Northern Germany are characterized by rather saline porewaters. Based on the data set

generated within this project, criteria can be established related to clay colloid stability in specific groundwater types. Critical coagulation concentrations lie thus at ≤0.4 mol/L NaCl and 1 mmol/L $CaCl_2$. As concentrations in saline porewaters exceed those values, bentonite colloids are not stable in such water. The effect of relatively high salinity on radionuclide-colloid-rock interactions has been demonstrated for granitic groundwater from the Äspö site, The Swedish underground rock laboratory operated by SKB. Under those conditions clay colloids lead to an even stronger retention of actinides due to sorption to agglomerating colloids. For the scenario of low mineralized glacial melt water intrusion, where colloids are presumably stable, the results obtained for radionuclide – colloid interaction reactions obtained in our studies in the Grimsel system should be transferable to some extent. Interaction parameters have however to be adapted to the specific geochemical conditions of a given site.

Bentonite is not the preferred material for buffer, backfill or sealing in a repository located in rock salt. Colloids may be generated from different sources such as e.g. secondary phase formation upon container or waste form corrosion. However, due to the very high ionic strength of the (in case of an unexpected repository evolution scenario) intruding saturated brines colloids are not expected to be stable. Of higher concern for a repository in rock salt are organic colloids in the overburden of the host rock. At Gorleben site humic colloids occur in quite high concentrations of up to 200 mg C/L [253-256]. These colloids might act as radionuclide carrier in the far field of the repository [95, 257-260].

5 References

1. Smith, P.A., et al., *CFM Phase I Modeling Report NAB 08-31*, 2008, Nagra: Wettingen (Switzerland).
2. SKB, *Long-term safety for KBS-3 repositories at Forsmark and Laxemar - a first evaluation; Main report of the SR-Can project. SKB Technical report TR-06-09*, 2006, Svensk Kärnbränslehantering AB: Stockholm, Sweden. p. 620.
3. SKB, *Buffer and backfill process report for the safety assessment SR-Can*, 2006, Svensk Kärnbränslehantering AB: Stockholm, Sweden. p. 620.
4. Alonso, U., et al., *Role of inorganic colloids generated in a high-level deep geological repository in the migration of radionuclides: open questions.* Journal of Iberian Geology, 2006. **32**(1): p. 79.
5. Yoshida, H. and M. Takeuchi, Metcalfe, R., *Long-term stability of flow-path structure in crystalline rocks distributed in an orogenic belt, Japan.* Engineering Geology, 2005. **78**: p. 275.
6. Nagra, *Project Opalinus Clay - Safety Report - Demonstration of disposal feasibility for spent fuel, vitrified high-level waste and long-lived intermediate level waste (Entsorgungsnachweis)*, 2003, Nagra: Wettingen (Switzerland). p. 360.
7. SKB, *Interim process report for the safety assessment SR-Can*, 2004, Svensk Kärnbränslehantering AB.
8. Pusch, R., *Stability of bentonite gels in crystalline rock - physical aspects, SKBF/KBS report TR 83-04*, 1983, University of Luleå: SKB was formerly: SKBF/KBS; SKBF - Svensk Kärnbränsleförsörjning AB.
9. Push, R., *Stability of bentonite gels in crystalline rock - Physical aspects*, 1983, SKB: Stockholm.
10. SKB, *Long-Term Safety for the Final Repository for Spent Nuclear Fuel at Forsmark. Main Report of the SR-Site Project.*, 2011, Svensk Kärnbränslehantering AB.
11. Liu, J. and I. Neretnieks, *Physical and chemical stability of the bentonite buffer*, 2006, Svensk Kärnbränslehantering AB.
12. Gallé, C., *Gas breakthrough pressure in compacted Fo-Ca clay and interfacial gas overpressure in waste disposal context.* Applied Clay Science, 2000. **17**(85-97).
13. Robinson, P. and A. Bath, *Workshop on copper corrosion and buffer erosion. Stockholm 15-17. September 2010. SSM Research Report: 2011:8*, 2011.
14. Apted, M.J., et al., *Buffer erosion: An overview of concepts and potential safety consequences. SSM Research Report: 2010:31*, 2010.
15. Moreno, L., I. Neretnieks, and L. Liu, *Modelling of erosion of bentonite gel by gel/sol flow*, 2010, SKB Technical Report 10-64, Svensk Kärnbränslehantering AG, Stockholm, Sweden: . p. 43.
16. Schäfer, T., et al., *Nanoparticles and their influence on radionuclide mobility in deep geological formations.* Applied Geochemistry, 2012. **27**(2): p. 390-403.
17. Birgersson, M., et al., *Bentonite erosion (Final report), SKB Technical Report TR-09-34*, 2009, Clay Technology, AB.
18. Jansson, M., *Bentonite erosion (Laboratory studies) SKB Technical Report TR-09-33*, 2009.
19. Missana, T., T. Alonso, and M.J.S. Turrero, *Generation and stability of bentonite colloids at the bentonite/granite interface of a deep geological radioactive waste repository.* Journal of Contaminant Hydrology, 2003. **61**(1-4): p. 17-31.
20. Baik, M.H., W.J. Cho, and P.S. Hahn, *Erosion of bentonite particles at the in-terface of a compacted bentonite and a fractured granite.* Engineering Geology, 2007. **91**(2-4): p. 229-239.
21. Alonso, U., T. Missana, and M. García-Gutiérrez, *Experimental approach to study the bentonite colloid generation source term in different geochemical conditions*, in *2nd Annual Workshop Proceedings of the Integrated Project "Fundamental Processes of Radionuclide Migration" - 6th EC FP IP FUNMIG*, G. Buckau, et al., Editors. 2007, SKB: Stockholm. p. 329-335.
22. Kunze, P., et al., *The influence of colloid formation in a granite groundwater bentonite pore water mixing zone on radionuclide speciation.* Journal of Contaminant Hydrology, 2008. **102**: p. 263-272.
23. Geckeis, H., et al., *Results of the Colloid and Radionuclide Retention experiment (CRR) at the Grimsel Test Site (GTS), Switzerland -Impact of reaction kinetics and speciation on radionuclide migration-.* Radiochimica Acta, 2004. **92**(9-11): p. 765-774.

24. Möri, A., et al., *The colloid and radionuclide retardation experiment at the Grimsel Test Site: influence of bentonite colloids on radionuclide migration in a fractured rock.* Colloids and Surfaces a-Physicochemical and Engineering Aspects, 2003. **217**(1-3): p. 33-47.
25. Kretzschmar, R. and T. Schäfer, *Metal retention and transport on colloidal particles in the environment.* Elements, 2005. **1**(4): p. 205-210.
26. Zänker, H., W. Richter, and G. Hüttig, *Scavenging and immobilization of trace contaminants by colloids in the waters of abandoned ore mines.* Colloids and Surfaces a-Physicochemical and Engineering Aspects, 2003. **217**(1-3): p. 21-31.
27. Zänker, H., et al., *The colloid chemistry of acid rock drainage solution from an abandoned Zn-Pb-Ag mine.* Applied Geochemistry, 2002. **17**(5): p. 633-648.
28. Wan, J., et al., *Colloid formation at waste plume fronts.* Environmental Science & Technology, 2004. **38**: p. 6066-6073.
29. Kim, M.A., et al., *Interaction of actinides(III) with aluminosilicate colloids in "statu nascendi" Part III. Colloid formation from monosilanol and polysilanol.* Colloids and Surfaces a-Physicochemical and Engineering Aspects, 2005. **254**(1-3): p. 137-145.
30. Buddemeier, R.W. and J.R. Hunt, *Transport of colloidal contaminants in groundwater: radionuclid migration at the Nevada test site.* Appl. Geochem., 1988. **3**: p. 535-548.
31. Kersting, A.B., et al., *Migration of plutonium in ground water at the Nevada Test Site.* Nature, 1999. **397**: p. 56-59.
32. Vilks, P., H.G. Miller, and D.C. Doern, *Natural Colloids and Suspended Particles in the Whiteshell Research Area, Manitoba, Canada, and Their Potential Effect on Radiocolloid Formation.* Applied Geochemistry, 1991. **6**(5): p. 565-574.
33. Novich, B.E. and T.A. Ring, *Colloid stability of clays using photon correlation spectroscopy.* Clays and Clay Minerals, 1984. **32**(5): p. 400-406.
34. Missana, T. and A. Adell, *On the applicability of DLVO theory to the prediction of clay colloids stability.* J. Colloid Interface Sci., 2000. **230**: p. 150-156.
35. Kretzschmar, R., H. Holthoff, and H. Sticher, *Influence of pH and humic acid on coagulation kinetics of kaolinite: a dynamic light scattering study.* J. Colloid and Interface Science, 1998. **202**: p. 95-103.
36. Jasmund, K. and G. Lagaly, eds. *Tonminerale und Tone: Struktur, Eigenschaften, Anwendungen und Einsatz in Industrie und Umwelt*. 1993, Steinkopf: Darmstadt. 490.
37. Meunier, A., *Clays*2005, Berlin, Heidelberg: Springer. 472.
38. Derjaguin, B.V. and L. Landau, *Theory of the stability of strongly charged lyophobicsols and the adhesion of strongly charged particles in solutions of electrolytes.* Acta Physicochim. URSS, 1941. **14**.
39. Verwey, E.J.W. and J.T.G. Overbeek, *Theory of the stability of lyophobic colloids*1948, Amsterdam: Elsevier.
40. Mahmood, A., et al., *A micromechanics approach for attachment and detachment of asymmetric colloidal particles.* Colloids and Surfaces A: Physicochemical and Engeneering Aspects, 2001. **177**: p. 99-110.
41. Schäfer, T., et al., *U, Th, Eu and colloid mobility in a granite fracture under near-natural flow conditions.* Radiochimica Acta, 2004. **92**: p. 731-737.
42. Missana, T., et al., *Role of bentonite colloids on europium and plutonium migration in a granite fracture.* Applied Geochemistry, 2008. **23**(6): p. 1484-1497.
43. Bowen, W.R. and T.A. Doneva, *Atomic force microscopy studies of membranes: Effect of surface roughness on double-layer interactions and particle adhesion.* Journal of Colloid and Interface Science, 2000. **229**(2): p. 544-549.
44. Alonso, U., et al., *Colloid diffusion in crystalline rock: An experimental methodology to measure diffusion coefficients and evaluate colloid size dependence.* Earth and Planetary Science Letters, 2007. **259**(3-4): p. 372-383.
45. Patelli, A., et al., *Validation of the RBS analysis for colloid migration through a rough granite surface.* Nuclear Instruments & Methods in Physics Research Section B-Beam Interactions with Materials and Atoms, 2006. **249**: p. 575-578.
46. Stumpf, S., et al., *Immobilization of trivalent actinides by sorption onto quartz and incorporation into siliceous bulk: Investigations by TRLFS.* Journal of Colloid and Interface Science, 2008. **318**(1): p. 5-14.
47. Vakarelski, I.U., K. Ishimura, and K. Higashitani, *Adhesion between silica particle and mica surfaces in water and electrolyte solutions.* Journal of Colloid and Interface Science, 2000. **227**(1): p. 111-118.

48. Johnson, P.R., N. Sun, and M. Elimelech, *Colloid transport in geochemically heterogeneous porous media: Modeling and measurements.* Environmental Science & Technology, 1996. **30**(11): p. 3284-3293.
49. Degueldre, C., et al., *Colloid properties in granitic groundwater systems .2. Stability and transport study.* Applied Geochemistry, 1996. **11**(5): p. 697-&.
50. Alonso, U., et al., *μPIXE study on colloid heterogeneous retention due to colloid/rock electrostatic interactions*, in *Laboratori Nazionali die Legnaro Annual Report 2004*2004. p. 68.
51. Velegol, D. and P.K. Thwar, *Analytical model for the effect of surface charge nonuniformity on colloidal interactions.* Langmuir, 2001. **17**(24): p. 7687-7693.
52. Taboada-Serrano, P., et al., *Surface charge heterogeneities measured by atomic force microscopy.* Environmental Science & Technology, 2005. **39**(17): p. 6352-6360.
53. Schäfer, T., *Colloid/ Nanoparticle formation and mobility in the context of deep geological nuclear waste disposal (Project KOLLORADO-1; Final report)*2010, Karlsruhe: Forschungszentrum Karlsruhe in der Helmholtz-Gemeinschaft FZKA.
54. Lührmann, L., *Modellierung des kolloidgetragenen Schadstofftransports mit dem Rechenprogramm TRAPIC*, 1999, Gesellschaft für Anlagen- und Raktorsicherheit (GRS) mbH: Braunschweig.
55. Lührmann, L., U. Noseck, and C. Tix, *Model of contaminant transport in porous media in the presence of colloids applied to actinide migration in column experiments. .* Water Resources Research, 1998. **34**(3): p. 421-426.
56. Adina, *ADINA (Automatic Dynamic Incremental Nonlinear Analysis)*, A.R.D. Inc., Editor 2007: Watertown, MA, USA.
57. Reinholdt, M., et al., *Hydrothermal Synthesis and Characterization of Ni-Al Montmorillonite-Like Phyllosilicates.* Nanomaterials, 2013. **3**(1): p. 48-69.
58. Reinholdt, M., et al., *Fluorine route synthesis of montmorillonites containing Mg or Zn and characterization by XRD, thermal analysis, MAS NMR, and EXAFS spectroscopy.* European Journal of Inorganic Chemistry, 2001(11): p. 2831-2841.
59. Plaschke, M., et al., *Size characterization of bentonite colloids by different methods.* Analytical Chemistry, 2001. **73**(17): p. 4338-4347.
60. van Olphen, H., *Clay Colloid Chemistry - For Clay Technologists, Geologists and Soil Scientists*. second ed1977: John Wiley & Sons. 318.
61. Pettersson, T., E. Thormann, and P. Claesson, *AFM study of montmorillonite*, 2010, SKB: Sweden.
62. Bouby, M., et al., *Interaction of bentonite colloids with Cs, Eu, Th and U in presence of humic acid: A flow field-flow fractionation study.* Geochimica et Cosmochimica Acta, 2011. **75**(13): p. 3866-3880.
63. Bouby, M., et al., *Laser-induced breakdown detection combined with asymmetrical flow field-flow fractionation: application to iron oxi/hydroxide colloid characterization.* Journal of Chromatography A, 2004. **1040**(1): p. 97-104.
64. Bouby, M., et al. *Laboratory study on colloid stability and radionuclide-colloid interaction under Äspö groundwater conditions*. in *3rd Annual workshop Proceedings of IP FUNMIG, NDA report*. 2008. Edinburgh (Scotland): Nuclear Decommissioning Authority (NDA).
65. Schimpf, M., K. Caldwell, and J.C. Gilding, *Field-Flow Fractionation Handbook*. Wiley-Interscience2000: John Wiley & Sons, New York.
66. Thang, N.M., et al., *Application of the flow field flow fractionation (FFFF) to the characterization of aquatic humic colloids: evaluation and optimization of the method.* Colloids and Surfaces a-Physicochemical and Engineering Aspects, 2001. **181**(1-3): p. 289-301.
67. Wijnhoven, J., et al., *HOLLOW-FIBER FLOW FIELD-FLOW FRACTIONATION OF POLYSTYRENE SULFONATES.* Journal of Chromatography A, 1995. **699**(1-2): p. 119-129.
68. Bouby, M., H. Geckeis, and F.W. Geyer, *Application of asymmetric flow field-flow fractionation (AsFlFFF) coupled to inductively coupled plasma mass spectrometry (ICPMS) to the quantitative characterization of natural colloids and synthetic nanoparticles.* Analytical and Bioanalytical Chemistry, 2008. **392**(7-8): p. 1447-1457.
69. Walther, C., et al., *Laser induced breakdown detection for the assessment of colloid mediated radionuclide migration.* Nuclear Instruments & Methods in Physics Research Section B-Beam Interactions with Materials and Atoms, 2002. **195**(3-4): p. 374-388.
70. Walther, C., et al., *Probing particle size distributions in natural surface waters from 15 nm to 2 mu m by a combination of LIBD and single-particle counting.* Journal of Colloid and Interface Science, 2006. **301**(2): p. 532-537.

71. Kralik, M., et al., *Recurrent fault activity in the Grimsel Test Site (GTS, Switzerland): revealed by Rb-Sr, K-Ar and tritium isotope techniques.* Journal of the Geological Society, 1992. **149**(2): p. 293-301.
72. Bossart, P. and M. Mazurek, *Grimsel Test Site: Structural geology and water flow-paths in the migration in the shear zone*, 1992, NAGRA: Wettingen, Switzerland.
73. Meyer, J., M. Mazurek, and W.R. Alexander, *Petrographic and mineralogical characterization of fault zones AU 96 and AU 126*, M.H. Bradbury, Editor 1989, NAGRA: Baden, Switzerland.
74. Huber, F., et al., *Sorption reversibility kinetics in the ternary system radionuclide-bentonite colloids/nanoparticles-granite fracture filling material.* Applied Geochemistry, 2011. **26**(12): p. 2226-2237.
75. Grenthe, I., et al., *Redox potentials and redox reactions in deep groundwater systems.* Chemical Geology, 1992. **98**(1-2): p. 131-150.
76. Möri, A., et al., *The colloid and radionuclide retardation experiment at the Grimsel Test Site: influence of bentonite colloids on radionuclide migration in a fractured rock.* Colloids and Surfaces A: Physicochemical and Engineering Aspects, 2003. **217**(1–3): p. 33-47.
77. Bondietti, E.A. and C.W. Francis, *Geologic Migration Potentials of Technetium-99 and Neptunium-237.* Science, 1979. **203**(4387): p. 1337-1340.
78. Kim, J.I., *Actinide Colloids in Natural Aquifer Systems.* Mrs Bulletin, 1994. **19**(12): p. 47-53.
79. Neck, V. and J.I. Kim, *Solubility and hydrolysis of tetravalent actinides.* Radiochimica Acta, 2001. **89**(1): p. 1-16.
80. Fanghanel, T. and V. Neck, *Aquatic chemistry and solubility phenomena of actinide oxides/hydroxides.* Pure and Applied Chemistry, 2002. **74**(10): p. 1895-1907.
81. Degueldre, C., et al., *Colloid properties in granitic groundwater systems .1. Sampling and characterisation.* Applied Geochemistry, 1996. **11**(5): p. 677-&.
82. Pettersson, C., J. Ephraim, and B. Allard, *On the composition and properties of humic substances isolated from deep groundwater and surface waters.* Org. Geochem. **21**: p. 443-451.
83. Ticknor, K.V., P. Vilks, and T.T. Vandergraaf, *The effect of fulvic acid on the sorption of actinides and fission products on granite and selected minerals.* Applied Geochemistry, 1996. **11**(4): p. 555-565.
84. Karlsson, F., et al., *Natural organic substances in granitic groundwater and their implications for nuclear waste disposal.*, in *Proceedings of an NEA Workshop on Binding Models concerning Natural Organic Substances*, NEA, Editor 1994: Bad Zurach, Switzerland. p. 45-54.
85. Missana, T., U. Alonso, and M.J. Turrero, *Generation and stability of bentonite colloids at the bentonite/granite interface of a deep geological radioactive waste repository.* Journal of Contaminant Hydrology, 2003. **61**(1-4): p. 17-31.
86. Buddemeier, R.W. and J.R. Hunt, *Transport of colloidal contaminants in groundwater: radionuclide migration at the Nevada Test site.* Applied Geochemistry, 1988. **3**: p. 535-548.
87. Kersting, A.B., et al., *Migration of plutonium in ground water at the Nevada Test Site.* Nature, 1999. **397**(6714): p. 56-59.
88. Honeyman, B.D., *Geochemistry - Colloidal culprits in contamination.* Nature, 1999. **397**(6714): p. 23-24.
89. Lieser, K.H., et al., *Colloids in Groundwater and Their Influence on Migration of Trace-Elements and Radionuclides.* Radiochimica Acta, 1990. **49**(2): p. 83-100.
90. Choppin, G.R., *The Role of Natural Organics in Radionuclide Migration in Natural Aquifer Systems.* Radiochimica Acta, 1992. **58-9**: p. 113-120.
91. Artinger, R., et al., *Effects of humic substances on the Am-241 migration in a sandy aquifer: column experiments with Gorleben groundwater/sediment systems.* Journal of Contaminant Hydrology, 1998. **35**(1-3): p. 261-275.
92. Schäfer, T., et al., *Colloid-borne Americium migration in Gorleben groundwater: Significance of iron secondary phase transformation.* Environmental Science & Technology, 2003. **37**(8): p. 1528-1534.
93. Geckeis, H., et al., *Results of the colloid and radionuclide retention experiment (CRR) at the Grimsel Test Site (GTS), Switzerland - impact of reaction kinetics and speciation on radionuclide migration.* Radiochimica Acta, 2004. **92**(9-11): p. 765-774.
94. Smith, P.A. and C. Degueldre, *Colloid-facilitated transport of radionuclides through fractured media.* Journal of Contaminant Hydrology, 1993. **13**(1-4): p. 143-166.
95. Geckeis, H., et al., *Humic colloid-borne natural polyvalent metal ions: Dissociation experiment.* Environmental Science & Technology, 2002. **36**(13): p. 2946-2952.

96. Schafer, T., et al., *U, Th, Eu and colloid mobility in a granite fracture under near-natural flow conditions.* Radiochimica Acta, 2004. **92**(9-11): p. 731-737.
97. Bossart, P. and M. Mazurek, *Grimsel Test Site: Structural geology and water flow paths in the migration shear zone.* , in *NAGRA Technical Report*1991, Nagra, Wettingen, Switzerland.
98. Duro, L., et al., *Prediction of the solubility and speciation of RN in FEBEX and Grimsel Waters. Colloid and Radionuclide Retardation project.* , N.T.R. 99-218, Editor 2000, Nagra, Wettingen, Switzerland.
99. Enresa, *FEBEX bentonite: Origin, properties and fabrications of blocks*, E.T.P. 05/98, Editor 1998, ENRESA, Madrid. .
100. Mori, A., et al., *The colloid and radionuclide retardation experiment at the Grimsel Test Site: influence of bentonite colloids on radionuclide migration in a fractured rock.* Colloids and Surfaces a-Physicochemical and Engineering Aspects, 2003. **217**(1-3): p. 33-47.
101. Möri, A., et al., *The CRR final project report series: 1. Description of the Field Phase-Methodologies and Raw Data*, in *NAGRA Technical Report 03-01*, NAGRA, Editor 2004: Wettingen, Switzerland.
102. Amorim, C.L.G., et al., *Effect of clay-water interactions on clay swelling by X-ray diffraction.* Nuclear Instruments & Methods in Physics Research Section a-Accelerators Spectrometers Detectors and Associated Equipment, 2007. **580**(1): p. 768-770.
103. Wolf, M., G. Buckau, and S. Geyer, *Isolation and characterisation of new batches of GoHy-573 humic and fulvic acids, in G. Buckau (Ed.), Humic substances in performance assessment of nuclear waste disposal: Actinide and iodine migration in the far-field.* , in *Humic substances in performance assessment of nuclear waste disposal: Actinide and iodine migration in the far-field. FZKA report 6969, p111-124. 2004.*
104. Giddings, J.C., F.J.F. Yang, and M.N. Myers, *FLOW FIELD-FLOW FRACTIONATION - VERSATILE NEW SEPARATION METHOD.* Science, 1976. **193**(4259): p. 1244-1245.
105. Wahlund, K.G. and J.C. Giddings, *Properties of an Asymmetrical Flow Field-Flow Fractionation Channel Having One Permeable Wall.* Analytical Chemistry, 1987. **59**(9): p. 1332-1339.
106. Schimpf, M., K. Caldwell, and G. J.C., *Field-Flow Fractionation Handbook*, ed. M. Schimpf, Caldwell, K. and Gidding J.C. 2000, New York: Wiley-Interscience, John Wiley & Sons Inc. New York.
107. Luo, J., et al., *Size characterization of green fluorescent protein inclusion bodies in E. coli using asymmetrical flow field-flow fractionation-multi-angle light scattering.* Journal of Chromatography A, 2006. **1120**(1-2): p. 158-164.
108. Millipore. 2000; Available from: www.millipore.com/techpublications/tech1/pf1172en00.
109. Hauser, W., et al., *A mobile laser-induced breakdown detection system and its application for the in situ-monitoring of colloid migration.* Colloids and Surfaces a-Physicochemical and Engineering Aspects, 2002. **203**(1-3): p. 37-45.
110. Seher, H., et al., *Febex bentonite colloid stability in ground water*, in *SKB Technical report*2007, SKB p. 397-402.
111. Holthoff, H., et al., *Coagulation rate measurements of colloidal particles by simultaneous static and dynamic light scattering.* Langmuir, 1996. **12**(23): p. 5541-5549.
112. Bradbury, M.H. and B. Baeyens, *Modelling the sorption of Mn(II), Co(II), Ni(II), Zn(II), Cd(II), Eu(III), Am(III), Sn(IV), Th(IV), Np(V) and U(VI) on montmorillonite: Linear free energy relationships and estimates of surface binding constants for some selected heavy metals and actinides.* Geochimica Et Cosmochimica Acta, 2005. **69**(4): p. 875-892.
113. Guillaumont, R., et al., *Update on the chemical thermodynamics of uranium, neptunium, plutonium, americium and technetium*. Chemical Thermodynamics ed. R.F. Guillaumont, T.; Fuger, J.; Grenthe, I.; Neck, V.; Palmer, D. A. and Rand, M. H. . Vol. 5. 2003: ELSEVIER B.V., Amsterdam, The Netherlands.
114. Rand, R., et al., *Chemical thermodynamics of thorium*. Chemical Thermodynamics, ed. R.F. Rand, J.; Neck, V.; Grenthe, I.; Rai, D. . Vol. 11. 2009: OECD publishing.
115. Missana, T. and A. Adell, *On the applicability of DLVO theory to the prediction of clay colloids stability.* Journal of Colloid and Interface Science, 2000. **230**(1): p. 150-156.
116. Milne, C.J., et al., *Generic NICA-Donnan model parameters for metal-ion binding by humic substances.* Environmental Science & Technology, 2003. **37**(5): p. 958-971.
117. Keijzer, M.G. and W.H. van Riemsdijk, *A Computer Program for the Equilibrium Calculation of Speciation and Transport in Soil-Water Systems (ECOSAT 4.7)*, 2002: Wageningen University.
118. Baes, C.F. and R.E. Mesmer, *The hydrolysis of cations*1976: Wiley-Interscience Publication, John Wiley and sons, New York, London, Sydney, Toronto.

119. Bradbury, M.H. and B. Baeyens, *Discussion on: "A mechanistic description of Ni and Zn sorption on Na-montmorillonite. Part I: Titration and sorption measurements. Part II: Modelling" by Bart Baeyens and Michael H. Bradbury - Reply to some comments.* Journal of Contaminant Hydrology, 1997. **28**(1-2): p. 11-16.
120. Tournassat, C., et al., *Nanomorphology of montmorillonite particles: Estimation of the clay edge sorption site density by low-pressure gas adsorption and AFM observations.* American Mineralogist, 2003. **88**(11-12): p. 1989-1995.
121. Righetto, L., et al., *Competitive Actinide Interactions in Colloidal Humic-Acid Mineral Oxide Systems.* Environmental Science & Technology, 1991. **25**(11): p. 1913-1919.
122. Fairhurst, A.J. and P. Warwick, *The influence of humic acid on europium-mineral interactions.* Colloids and Surfaces a-Physicochemical and Engineering Aspects, 1998. **145**(1-3): p. 229-234.
123. Reiller, P., et al., *Retention behaviour of humic substances onto mineral surfaces and consequences upon thorium (IV) mobility: case of iron oxides.* Applied Geochemistry, 2002. **17**(12): p. 1551-1562.
124. Reiller, P., et al., *On the study of Th(IV)-humic acid interactions by competition sorption studies with silica and determination of global interaction constants.* Radiochimica Acta, 2003. **91**(9): p. 513-524.
125. Reiller, P., F. Casanova, and V. Moulin, *Influence of addition order and contact time on thorium(IV) retention by hematite in the presence of humic acids.* Environmental Science & Technology, 2005. **39**(6): p. 1641-1648.
126. Murphy, R.J., J.J. Lenhart, and B.D. Honeyman, *The sorption of thorium (IV) and uranium (VI) to hematite in the presence of natural organic matter.* Colloids and Surfaces a-Physicochemical and Engineering Aspects, 1999. **157**(1-3): p. 47-62.
127. Read, D., D. Ross, and R.J. Sims, *The migration of uranium through Clashach Sandstone: the role of low molecular weight organics in enhancing radionuclide transport.* Journal of Contaminant Hydrology, 1998. **35**(1-3): p. 235-248.
128. Nachtegaal, M. and D.L. Sparks, *Nickel sequestration in a kaolinite-humic acid complex.* Environmental Science & Technology, 2003. **37**(3): p. 529-534.
129. Bryce, A.L., et al., *Nickel Adsorption to Hydrous Ferric-Oxide in the Presence of Edta - Effects of Component Addition Sequence.* Environmental Science & Technology, 1994. **28**(13): p. 2353-2359.
130. Takahashi, Y., et al., *Comparison of adsorption behavior of multiple inorganic ions on kaolinite and silica in the presence of humic acid using the multitracer technique.* Geochimica Et Cosmochimica Acta, 1999. **63**(6): p. 815-836.
131. Schäfer, T. and U. Noseck, *Colloid/Nanoparticle formation and mobility in the context of deep geological nuclear waste disposal (Project KOLLORADO-1; Final Report)*, in *Wissenschaftliche Berichte/Forschungszentrum Karlsruhe*, T.N. Schäfer, U. , Editor 2010, Schäfer, T.; Noseck, U. (2010) Colloid/Nanoparticle formation and mobility in the context of deep geological nuclear waste disposal (Project KOLLORADO-1; Final Report), Wissenschaftliche Berichte/Forschungszentrum Karlsruhe, FZKA 7515, p77.
132. Villar, M.V., et al., *FEBEX bentonite: origin, properties and fabrication of blocks (full-scale engineered barriers experiment in crystalline host rock)*, 1998, Enresa (empresa nacional de residuos radiactivos, s.a.): Madrid, Spain.
133. ANSYS, *ANSYS FLUENT 12.1.4 User.* 2009.
134. Walther, C. and W. Hauser, *Influence of laser beam characteristics and focusing optics on optical laser-induced breakdown detection.* Applied Physics B-Lasers and Optics, 2009. **97**(4): p. 877-886.
135. Fernández, A.M., et al., *Analysis of the porewater chemical composition of a Spanish compacted bentonite used in an engineered barrier.* Physics and Chemistry of the Earth, Parts A/B/C, 2004. **29**(1): p. 105-118.
136. Elimelech, M., et al., *particle deposition & aggregation*1995, Woburn: Butterworth-Heinemann.
137. van Loenhout, M.T.J., et al., *Hydrodynamic flow induced anisotropy in colloid adsorption.* Colloids and Surfaces a-Physicochemical and Engineering Aspects, 2009. **342**(1-3): p. 46-52.
138. Mitchell, D.F., et al., *Film Thickness Measurements of Sio2 by Xps.* Surface and Interface Analysis, 1994. **21**(1): p. 44-50.
139. Lüttge, A., E.W. Bolton, and A.C. Lasaga, *An interferometric study of the dissolution kinetics of anorthite: The role of reactive surface area.* American Journal of Science, 1999. **299**(7-9): p. 652-678.

140. Fischer, C. and A. Luttge, *Converged surface roughness parameters - A new tool to quantify rock surface morphology and reactivity alteration.* American Journal of Science, 2007. **307**(7): p. 955-973.
141. Tong, M.P. and W.P. Johnson, *Excess colloid retention in porous media as a function of colloid size, fluid velocity, and grain angularity.* Environmental Science & Technology, 2006. **40**(24): p. 7725-7731.
142. Kline, T.R., G.X. Chen, and S.L. Walker, *Colloidal deposition on remotely controlled charged micropatterned surfaces in a parallel-plate flow chamber.* Langmuir, 2008. **24**(17): p. 9381-9385.
143. Ignasi, P., *Medusa: Program for calculation of chemical equilibrium*. p. http://progdist.ug.kth.se/public/freeware/medusa/windows/prog1.shtml.
144. Bradbury, M.H. and B. Baeyens, *Sorption of Eu on Na- and Ca-montmorillonites: Experimental investigations and modelling with cation exchange and surface.* Geochimica Et Cosmochimica Acta, 2002. **66**(13): p. 2325-2334.
145. Alonso, U., et al., *Bentonite colloid diffusion through the host rock of a deep geological repository.* Physics and Chemistry of the Earth, 2007. **32**(1-7): p. 469-476.
146. Alonso, U., et al., *Quantification of Au nanoparticles retention on a heterogeneous rock surface.* Colloids and Surfaces a-Physicochemical and Engineering Aspects, 2009. **347**(1-3): p. 230-238.
147. Filby, A., et al., *Interaction of latex colloids with mineral surfaces and Grimsel granodiorite.* Journal of Contaminant Hydrology, 2008. **102**(3-4): p. 273-284.
148. Fischer, C. and R. Gaupp, *Change of black shale organic material surface area during oxidative weathering: Implications for rock-water surface evolution.* Geochimica et Cosmochimica Acta, 2005. **69**(5): p. 1213-1224.
149. Elimelech, M., *Effect of Particle-Size on the Kinetics of Particle Deposition under Attractive Double-Layer Interactions.* Journal of Colloid and Interface Science, 1994. **164**(1): p. 190-199.
150. Elimelech, M. and C.R. Omelia, *Effect of Particle-Size on Collision Efficiency in the Deposition of Brownian Particles with Electrostatic Energy Barriers.* Langmuir, 1990. **6**(6): p. 1153-1163.
151. Huang, X.F., S. Bhattacharjee, and E.M.V. Hoek, *Is Surface Roughness a "Scapegoat" or a Primary Factor When Defining Particle-Substrate Interactions?* Langmuir, 2010. **26**(4): p. 2528-2537.
152. Hoek, E.M.V., S. Bhattacharjee, and M. Elimelech, *Effect of membrane surface roughness on colloid-membrane DLVO interactions.* Langmuir, 2003. **19**(11): p. 4836-4847.
153. Bhattacharjee, S., C.H. Ko, and M. Elimelech, *DLVO interaction between rough surfaces.* Langmuir, 1998. **14**(12): p. 3365-3375.
154. Hoek, E.M.V. and G.K. Agarwal, *Extended DLVO interactions between spherical particles and rough surfaces.* Journal of Colloid and Interface Science, 2006. **298**(1): p. 50-58.
155. Johnson, W.P., X.Q. Li, and G. Yal, *Colloid retention in porous media: Mechanistic confirmation of wedging and retention in zones of flow stagnation.* Environmental Science & Technology, 2007. **41**(4): p. 1279-1287.
156. Johnson, W.P. and M.P. Tong, *Observed and simulated fluid drag effects on colloid deposition in the presence of an energy barrier in an impinging jet system.* Environmental Science & Technology, 2006. **40**(16): p. 5015-5021.
157. Shen, C.Y., et al., *Predicting attachment efficiency of colloid deposition under unfavorable attachment conditions.* Water Resources Research, 2010. **46**: p. -.
158. Bradford, S.A. and S. Torkzaban, *Colloid transport and retention in unsaturated porous media: A review of interface-, collector-, and pore-scale processes and models.* Vadose Zone Journal, 2008. **7**(2): p. 667-681.
159. Burdick, G.M., N.S. Berman, and S.P. Beaudoin, *Describing hydrodynamic particle removal from surfaces using the particle Reynolds number.* Journal of Nanoparticle Research, 2001. **3**(5-6): p. 455-467.
160. Torkzaban, S., S.A. Bradford, and S.L. Walker, *Resolving the coupled effects of hydrodynamics and DLVO forces on colloid attachment in porous media.* Langmuir, 2007. **23**(19): p. 9652-9660.
161. Burdick, G.M., N.S. Berman, and S.P. Beaudoin, *Hydrodynamic particle removal from surfaces.* Thin Solid Films, 2005. **488**(1-2): p. 116-123.
162. Bergendahl, J. and D. Grasso, *Prediction of colloid detachment in a model porous media: hydrodynamics.* Chemical Engineering Science, 2000. **55**(9): p. 1523-1532.
163. Gregory, J., *Interaction of Unequal Double-Layers at Constant Charge.* Journal of Colloid and Interface Science, 1975. **51**(1): p. 44-51.

164. Sverjensky, D.A. and N. Sahai, *Theoretical prediction of single-site surface-protonation equilibrium constants for oxides and silicates in water.* Geochimica Et Cosmochimica Acta, 1996. **60**(20): p. 3773-3797.
165. Poehls, D.J. and J.S. Gregory, *Encyclopedic Dictionary of Hydrogeology*, 2009, Academic Press publications. p. 200.
166. Stumm, W., *Chemistry of the solid-water interface*, 1992, John Wiley and Sons Inc.: New York.
167. Stumpf, S., et al., *Sorption of Cm(III) onto different Feldspar surfaces: a TRLFS study.* Radiochimica Acta, 2006. **94**(5): p. 243-248.
168. Rath, R.K. and S. Subramanian, *Studies on adsorption of guar gum onto biotite mica.* Minerals Engineering, 1997. **10**(12): p. 1405-1420.
169. Rath, R.K. and S. Subramanian, *Surface chemical studies on mica and galena using dextrin.* Langmuir, 1998. **14**(15): p. 4005-4010.
170. Kosmulski, M., *The pH-dependent surface charging and the points of zero charge.* Journal of Colloid and Interface Science, 2002. **253**(1): p. 77-87.
171. Fischer, C., V. Karius, and A. Lüttge, *Correlation between sub-micron surface roughness of iron oxide encrustations and trace element concentrations* Science of the Total Environment, 2009. **407**: p. 4703-4710.
172. Fischer, C., et al., *Relationship between micrometer to submicrometer surface roughness and topography variations of natural iron oxides and trace element concentrations.* Langmuir, 2008. **24**(7): p. 3250-3266.
173. Suresh, L. and J.Y. Walz, *Effect of surface roughness on the interaction energy between a colloidal sphere and a flat plate.* Journal of Colloid and Interface Science, 1996. **183**(1): p. 199-213.
174. Martines, E., et al., *DLVO interaction energy between a sphere and a nano-patterned plate.* Colloids and Surfaces a-Physicochemical and Engineering Aspects, 2008. **318**(1-3): p. 45-52.
175. Darbha, G.K., et al., *Retention of Latex Colloids on Calcite as a Function of Surface Roughness and Topography.* Langmuir, 2010. **26**(7): p. 4743-4752.
176. Darbha, G., et al., *Deposition of Latex Colloids at Rough Mineral Surfaces: An Analogue Study Using Nanopatterned Surfaces.* Langmuir, 2012. **28**(16): p. 6606-6617.
177. Torkzaban, S., et al., *Hysteresis of Colloid Retention and Release in Saturated Porous Media During Transients in Solution Chemistry.* Environmental Science & Technology, 2010. **44**(5): p. 1662-1669.
178. Shen, C.Y., et al., *Kinetics of coupled primary- and secondary-minimum deposition of colloids under unfavorable chemical conditions.* Environmental Science & Technology, 2007. **41**(20): p. 6976-6982.
179. Bradford, S.A., S. Torkzaban, and S.L. Walker, *Resolving the coupled effects of hydrodynamics and DLVO forces on colloid attachment in porous media.* Langmuir, 2007. **23**(19): p. 9652-9660.
180. Elimelech, M. and Z.A. Kuznar, *Direct microscopic observation of particle deposition in porous media: Role of the secondary energy minimum.* Colloids and Surfaces a-Physicochemical and Engineering Aspects, 2007. **294**(1-3): p. 156-162.
181. Greenlan.Dj, *Interactions between Humic and Fulvic Acids and Clays.* Soil Science, 1971. **111**(1): p. 34-&.
182. Davis, J.M. and R.D. Duffadar, *Dynamic adhesion behavior of micrometer-scale particles flowing over patchy surfaces with nanoscale electrostatic heterogeneity.* Journal of Colloid and Interface Science, 2008. **326**(1): p. 18-27.
183. Fischer, C., et al., *Relationship between micrometer to submicrometer surface roughness and topography variations of natural iron oxides and trace element concentrations.* Langmuir, 2008. **24**(7): p. 3250-3266.
184. Fischer, C., V. Karius, and A. Luttge, *Correlation between sub-micron surface roughness of iron oxide encrustations and trace element concentrations.* Science of the Total Environment, 2009. **407**(16): p. 4703-4710.
185. Ryan, J.N. and M. Elimelech, *Colloid mobilization and transport in groundwater.* Colloids and Surfaces a-Physicochemical and Engineering Aspects, 1996. **107**: p. 1-56.
186. Torkzaban, S., et al., *Transport and fate of bacteria in porous media: Coupled effects of chemical conditions and pore space geometry.* Water Resources Research, 2008. **44**(4).
187. Boutt, D.F., et al., *Trapping zones: The effect of fracture roughness on the directional anisotropy of fluid flow and colloid transport in a single fracture.* Geophysical Research Letters, 2006. **33**(21): p. -.

188. Bhattacharjee, S. and J.A.L. Kemps, *Particle Tracking Model for Colloid Transport near Planar Surfaces Covered with Spherical Asperities.* Langmuir, 2009. **25**(12): p. 6887-6897.
189. Shellenberger, K. and B.E. Logan, *Effect of molecular scale roughness of glass beads on colloidal and bacterial deposition.* Environmental Science & Technology, 2002. **36**(2): p. 184-189.
190. Bergendahl, J.A. and D. Grasso, *Mechanistic basis for particle detachment from granular media.* Environmental Science & Technology, 2003. **37**(10): p. 2317-2322.
191. Chinju, H., et al., *Deposition behavior of polystyrene latex particles on solid surfaces during migration through an artificial fracture in a granite rock sample.* Journal of Nuclear Science and Technology, 2001. **38**(6): p. 439-443.
192. Möri, A. and I. Blechschmidt, *GTS Phase VI: CFM Experiment – Structural geological model. Arbeitsbericht NAB 06-18. Natonale Genossenschaft für die Lagerung radioaktiver Abfälle (NAGRA). Wettingen.* 2006.
193. Blechschmidt, I., et al., *GTS Phase VI: CFM Status Report on Field Work 2004 – 2005. Arbeitsbericht NAB 06-06. Natonale Genossenschaft für die Lagerung radioaktiver Abfälle (NAGRA). Wettingen.* 2006.
194. Lanyon, B. and I. Blechschmidt, *Hydraulic interference between CFM and LTD experiments. Arbeitsbericht NAB 08-11. Natonale Genossenschaft für die Lagerung radioaktiver Abfälle (NAGRA). Wettingen.* 2008.
195. Geckeis, H., T. Rabung, and T. Schäfer, *Actinide - Nanoparticle interaction: generation, stability and mobility*, in *Actinide Nanoparticle Research*, S.N. Kalmykov and M.A. Denecke, Editors. 2011, Springer-Verlag: Berlin, Heidelberg. p1-33.
196. Degueldre, C. and A. Benedicto, *Colloid generation during water flow transients.* Applied Geochemistry, 2012. **27**(6): p. 1220-1225.
197. Schäfer, T., D. Schenk, and H. Knoke. *Transport of particulate matter in groundwater depending on natural and anthropogenic hydraulic variations*. in *IAH: Gambling with groundwater- physical, chemical, and biological aspects of aquifer-stream relations*. 1998. Las Vegas, Nevada: American Institute of Hydrology, St. Paul, Minnesota.
198. Schäfer, T. and U. Noseck, *Colloid/ Nanoparticle formation and mobility in the context of deep geological nuclear waste disposal (Project KOLLORADO; Final report)*, ed. M. Bouby2010: Forschungszentrum Karlsruhe. 210.
199. Nelson, K.E. and T.R. Ginn, *New collector efficiency equation for colloid filtration in both natural and engineered flow conditions.* Water Resources Research, 2011. **47**: p. W05543.
200. Iijima, K., T. Tomura, and Y. Shoji, *Reversibility and modeling of adsorption behavior of cesium ions on colloidal montmorillonite particles.* Applied Clay Science, 2010. **49**(3): p. 262-268.
201. Bruno, J., et al., *Prediction of the solubility and speciation of RN in Febex and Grimsel waters*, 2000.
202. Huber, F., et al., *Sorption reversibility kinetics in the ternary system radionuclide–bentonite colloids/nanoparticles–granite fracture filling material.* Applied Geochemistry, 2011. **26**(12): p. 2226-2237.
203. NAGRA, *Aktennotiz AN / 07-, Draft CFM Modelling Task 1, Tracer Tests 09-01 and 10-01, 16.03-2010.* 2010.
204. Kalmykov, S.N.D.M.A. *Actinide nanoparticle research*. 2010; Available from: http://dx.doi.org/10.1007/978-3-642-11432-8.
205. Gaus, I. and P.A. Smith, *Modellers dataset for the Colloid Formation and Migration Project Status: End of CFM Phase 1*, 2008, NAGRA: Wettingen (Switzerland).
206. Kinzelbach, W.R.R., *Grundwassermodellierung : eine Einführung mit Ubungen*1995, Stuttgart [u.a.]: Bornträger.
207. Fein, E. and A. Schneider, *d³f – Ein Programmpaket zur Modellierung von Dichteströmungen. Abschlußbericht.* , 1999, Gesellschaft- für Anlagen- und Reaktorsicherheit (mbH) (GRS): Braunschweig.
208. Ingebritsen, S.E.S.W.E., *Groundwater in geologic processes*1998, Cambridge; New York, NY, USA: Cambridge University Press.
209. Tien, C.P.A.C., *Advances in deep bed filtration.* AICHE Journal, 1979. **25:5**: p. 737-759.
210. Yao, K.M., M.M. Habibian, and C.R. Omelia, *WATER AND WASTE WATER FILTRATION - CONCEPTS AND APPLICATIONS.* Environmental Science & Technology, 1971. **5**(11): p. 1105-&.
211. Ibaraki, M. and E.A. Sudicky, *Colloid-facilitated contaminant transport in discretely fractured porous media .1. Numerical formulation and sensitivity analysis.* Water Resources Research, 1995. **31**(12): p. 2945-2960.

212. Knabner, P., K.U. Totsche, and I. KogelKnabner, *The modeling of reactive solute transport with sorption to mobile and immobile sorbents .1. Experimental evidence and model development.* Water Resources Research, 1996. **32**(6): p. 1611-1622.
213. Fein, E., *Software Package r³t. Model for Transport and Retention in Porous Media. Final Report.*, 2004, Gesellschaft für Anlagen- und Reaktorsicherheit (mbH): Braunschweig.
214. GRAPE, *GRAPE Manual. Version 5.3. SFB 256*, 1999: University of Bonn.
215. Kinzelbach, W., *Numerische Methoden zur Modellierung des Transports von Schadstoffen im Grundwasser*1992, München u.a.: Oldenbourg.
216. De Marsily, G., *Quantitative hydrogeology*1986. Medium: X; Size: Pages: 464.
217. Flügge, J., et al. *Modeling colloid-bound radionuclide transport at the Grimsel Test Site*. in *International Groundwater Symposium by IAHR*. 2010. Valencia (Spain).
218. Kontar, K. and I. Blechschmidt, *GTS Phase VI – CFM Project: Radionuclide – Colloid/Conservative Tracer Test_Run CFM 12-02RN. Draft report. NAGRA/SOLEXPERTS. Unpublished.*, 2011.
219. POSIVA, *Safety Case for the Disposal of Spent Nuclear Fuel at Olkiluoto - Performance Assessment 2012, Report 2012-4. .* 2012.
220. Byegård, J., et al., *The interaction of sorbing and non-sorbing tracers with different Äspö rock types. Sorption and diffusion experiments in the laboratory scale. SKB Technical report TR-98-18*, 1998, Svensk Kärnbränslehantering AB, Stockholm, Sweden.
221. Enzmann, F. and M. Kersten, *X-ray computed micro tomography (µ-XRT) results of a granitic drill core*, in *1st Annual workshop Proceedings of IP FUNMIG, report CEA R-6122*, P. Reiller, et al., Editors. 2006, Commissariat a l'energie atomique (CEA): Gif sur Yvette (France). p. 211-215.
222. Hasselloev, M., et al., *Nanoparticle analysis and characterization methodologies in environmental risk assessment of engineered nanoparticles.* Ecotoxicology, 2008. **17**(5): p. 344-361.
223. Rameshwar, T., et al., *Determination of the size of water-soluble nanoparticles and quantum dots by field-flow fractionation.* Journal of Nanoscience and Nanotechnology, 2006. **6**(8): p. 2461-2467.
224. Mansel, A. and H. Kupsch, *Radiolabelling of humic substances with C-14 by azo coupling C-14 phenyldiazonium ions.* Applied Radiation and Isotopes, 2007. **65**(7): p. 793-797.
225. Torkzaban, S., et al., *Transport and deposition of functionalized CdTe nanoparticles in saturated porous media.* Journal of Contaminant Hydrology, 2010. **118**(3–4): p. 208-217.
226. Batchelor, G.K., *An Introduction to Fluid Dynamics*1967, Cambridge: Cambridge University Press.
227. Ertekin, T., J.H. Abou-Kaseem, and G.R. King, *Basic Applied Reservoir Simulation; SPE Text Book Series Vol. 7*. SPE Text Book Series Vol. 7, ed. S.o.P.E. (SPE)2001, Richardson, Texas.
228. Skjetne, E., A. Hansen, and J.S. Gudmundsson, *High-velocity flow in a rough fracture.* Journal of Fluid Mechanics, 1999. **383**: p. 1-28.
229. Cardenas, M.B., et al., *Effects of inertia and directionality on flow and transport in a rough asymmetric fracture.* J. Geophys. Res., 2009. **114**(B6): p. B06204.
230. ANSYS, *ANSYS FLUENT 12.1.4 User Guide*, 2009.
231. Detwiler, R.L., H. Rajaram, and R.J. Glass, *Solute transport in variable-aperture fractures: An investigation of the relative importance of Taylor dispersion and macrodispersion.* Water Resources Research, 2000. **36**(7): p. 1611-1625.
232. Caretto, L., et al., *Two calculation procedures for steady, three-dimensional flows with recirculation.* , in *Proceedings of the Third International Conference on Numerical Methods in Fluid Mechanics*, H. Cabannes and R. Temam, Editors. 1973, Springer Berlin / Heidelberg. p. 60-68.
233. Wang, J.H., C.V. Robinson, and I.S. Edelman, *SELF-DIFFUSION AND STRUCTURE OF LIQUID WATER .3. MEASUREMENT OF THE SELF-DIFFUSION OF LIQUID WATER WITH H-2, H-3, AND O-18 AS TRACERS.* Journal of the American Chemical Society, 1953. **75**(2): p. 466-470.
234. Einstein, A., *Über die von der molekularkinetischen Theorie der Wärme geforderte Bewegung von in ruhenden Flüssigkeiten suspendierten Teilchen.* Annalen der Physik, 1905. **322**(8): p. 549-560.
235. Tsang, C.F. and I. Neretnieks, *Flow channeling in heterogeneous fractured rocks.* Reviews of Geophysics, 1998. **36**(2): p. 275-298.
236. Bodin, J., F. Delay, and G. de Marsily, *Solute transport in a single fracture with negligible matrix permeability: 1. fundamental mechanisms.* Hydrogeology Journal, 2003. **11**(4): p. 418-433.

237. Moreno, L., et al., *Some anomalous features of flow and solute transport arising from fracture aperture variability.* Water Resources Research, 1990. **26**(10): p. 2377-2391.
238. Carrera, J., et al., *On matrix diffusion: formulations, solution methods and qualitative effects.* Hydrogeology Journal, 1998. **6**(1): p. 178-190.
239. Becker, M.W., P.W. Reimus, and P. Vilks, *Transport and attenuation of carboxylate-modified latex microspheres in fractured rock laboratory and field tracer tests.* Ground Water, 1999. **37**(3): p. 387-395.
240. Hinsby, K., et al., *Fracture aperture measurements and migration of solutes, viruses, and immiscible creosote in a column of clay-rich till.* Ground Water, 1996. **34**(6): p. 1065-1075.
241. McCarthy, J.F., L.D. McKay, and D.D. Bruner, *Influence of Ionic Strength and Cation Charge on Transport of Colloidal Particles in Fractured Shale Saprolite.* Environmental Science & Technology, 2002. **36**(17): p. 3735-3743.
242. Vilks, P. and D.B. Bachinski, *Colloid and suspended particle migration experiments in a granite fracture.* Journal of Contaminant Hydrology, 1996. **21**(1-4): p. 269-279.
243. James, S.C. and C.V. Chrysikopoulos, *Analytical solutions for monodisperse and polydisperse colloid transport in uniform fractures.* Colloids and Surfaces a-Physicochemical and Engineering Aspects, 2003. **226**(1-3): p. 101-118.
244. Hoshino, A., et al., *Physicochemical properties and cellular toxicity of nanocrystal quantum dots depend on their surface modification.* Nano Letters, 2004. **4**(11): p. 2163-2169.
245. Kosmulski, M., *pH-dependent surface charging and points of zero charge. IV. Update and new approach.* Journal of Colloid and Interface Science, 2009. **337**(2): p. 439-448.
246. Ryan, J.N. and M. Elimelech, *Colloid mobilization and transport in groundwater.* Colloids and Surfaces A: Physicochemical and Engineering Aspects, 1996. **107**(0): p. 1-56.
247. Chrysikopoulos, C.V. and A. Abdel-Salam, *Modeling colloid transport and deposition in saturated fractures.* Colloids and Surfaces A, 1997. **121**: p. 189 - 202.
248. Tufenkji, N. and M. Elimelech, *Correlation equation for predicting single-collector efficiency in physicochemical filtration in saturated porous media.* Environmental Science & Technology, 2004. **38**(2): p. 529-536.
249. Tufenkji, N. and M. Elimelech, *Deviation from the classical colloid filtration theory in the presence of repulsive DLVO interactions.* Langmuir, 2004. **20**(25): p. 10818-10828.
250. Yao, K.M., M.T. Habibian, and C.R. O'Melia, *Water and Wastewater Filtration: Concepts and Applications.* Environmental Science and Technology, 1971. **5**: p. 1105-1112.
251. Cirpka, O.A. and P.K. Kitanidis, *An advective-dispersive stream tube approach for the transfer of conservative-tracer data to reactive transport.* Water Resources Research, 2000. **36**(5): p. 1209-1220.
252. Kosakowski, G., *Anomalous transport of colloids and solutes in a shear zone.* Journal of Contaminant Hydrology, 2004. **72**(1-4): p. 23-46.
253. Artinger, R., et al., *Characterization of groundwater humic substances: influence of sedimentary organic carbon.* Applied Geochemistry, 2000. **15**(1): p. 97-116.
254. Buckau, G., et al., *Origin and mobility of humic colloids in the Gorleben aquifer system.* Applied Geochemistry, 2000. **15**(2): p. 171-179.
255. Buckau, G., et al., *14C dating of Gorleben groundwater.* Appl. Geochem., 2000. **15**: p. 583-597.
256. Schäfer, T., et al., *Origin and mobility of fulvic acids in the Gorleben aquifer system: implications from isotopic data and carbon/sulfur XANES.* Organic Geochemistry, 2005. **36**(4): p. 567-582.
257. Adamo, P., et al., *Distribution of trace elements in soils from the Sudbury smelting area (Ontario, Canada).* Water Air and Soil Pollution, 2002. **137**(1-4): p. 95-116.
258. Artinger, R., et al., *Humic colloid mediated transport of tetravalent actinides and technetium.* Radiochimica Acta, 2003. **91**(12): p. 743-750.
259. Artinger, R., et al., *A kinetic study of Am(III)/humic colloid interactions.* Environmental Science & Technology, 2002. **36**(20): p. 4358-4363.
260. Marquardt, C.M., et al., *The redox behaviour of plutonium in humic rich groundwater.* Radiochimica Acta, 2004. **92**(9-11): p. 617-623.
261. Blechschmidt, I., *CFM Phase 2. Presentation at the Poject Meeting 2011, Yteri Spa, Finland, 11 – 12 May 2011*, 2011.

6 Appendix

6.1 Variations of the model scale

For previously conducted model simulations for tracer test run 08-02 and the homologue test run 08-01 a smaller model geometry was employed, which is depicted in Figure 6.1. These simulations showed that transport paths are disconnected when the injection and extraction flow velocities become comparable (Figure 6.2), leading to spurious mass losses over virtual boundaries. Therefore, the height and the length of the model were doubled without changing any of the boundary conditions or the distance between the inflow and the outflow location for the simulations discussed here.

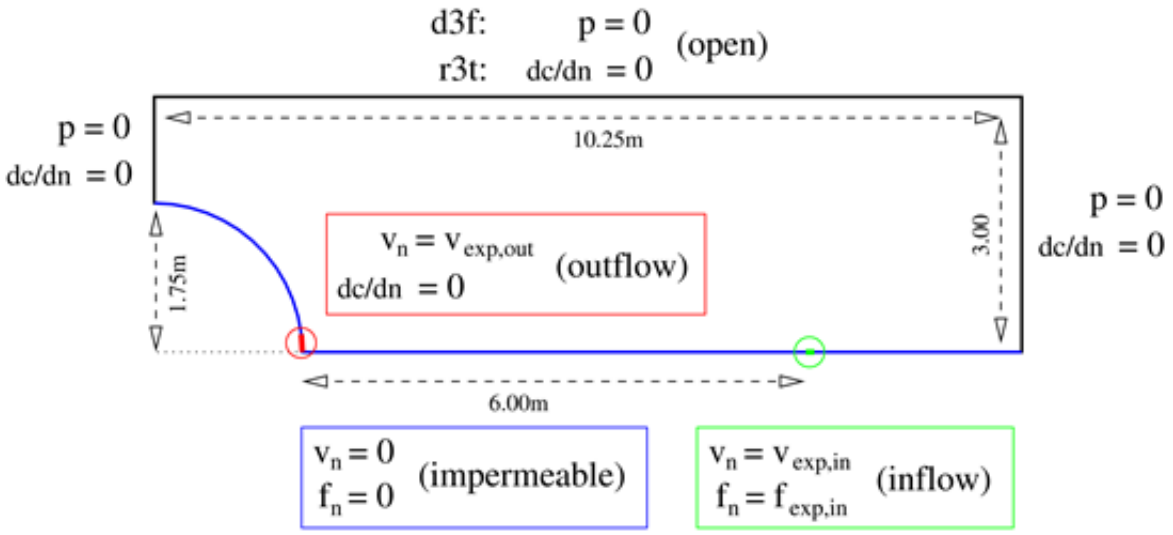

Figure 6.1: Geometry and hydrogeological/transport-related boundary conditions of the 2D computer model. For details about the given boundary conditions (colors) see chapter 3.1.2.

For the outflow rate of 50 ml min^{-1} and the larger model geometry, none of the transport pathways were disconnected from the outflow area as depicted in Figure 6.3. We ran additional comparative model simulations for the outflow rate of 50 ml min^{-1} as well as for 165 ml min^{-1} and determined the recovered mass fractions at the outflow. All simulations based on the large model geometry resulted in higher recovered mass fractions than those based on the smaller model geometry as is clarified in Figure 6.4 and Table 6.1. Only for the outflow rate of 165 ml min^{-1} the total injected tracer mass fraction is recovered at the outflow, but nevertheless for the outflow rate of 50 ml min^{-1} the recovered mass fraction was increased from approx. 65 % for the small model geometry to 95.7 % for the large model geometry, i.e. a nearly quantitative recovery.

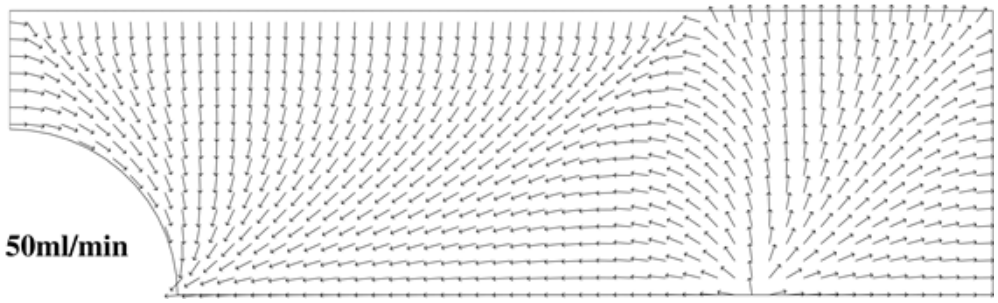

Figure 6.2: Steady-state velocity direction field at outflow rates of 50ml min^{-1} for the small model (ca. 10 m by 3 m). For illustration purposes, the length of the arrows is not scaled with the magnitude of the velocity.

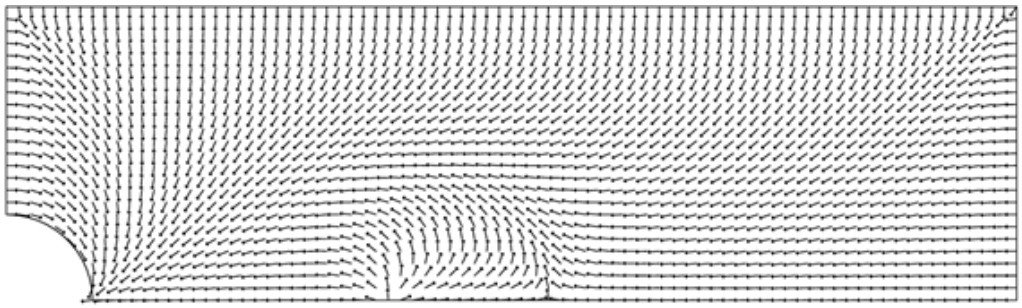

Figure 6.3: Steady-state velocity direction field at outflow rates of 50ml min^{-1} for the large model (ca. 20 m by 6 m). For illustration purposes, the length of the arrows is not scaled with the magnitude of the velocity.

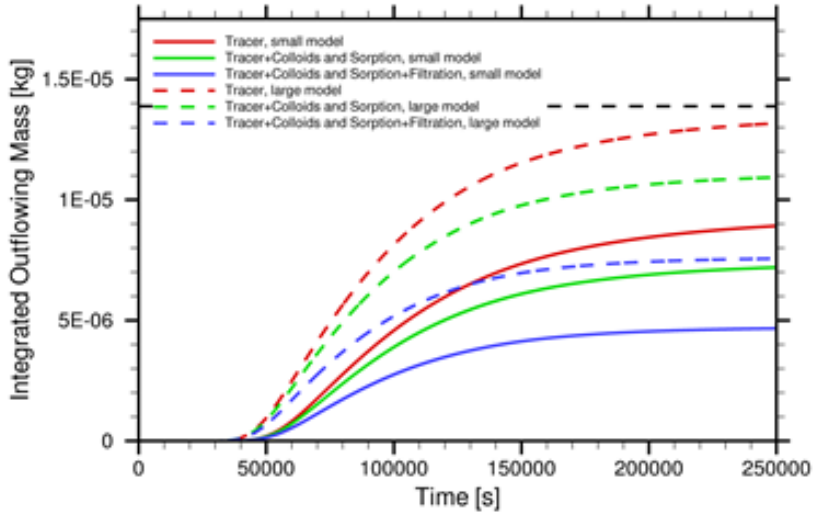

Figure 6.4: Time-dependent recovery of the injected pollutant mass for an extraction rate of 50 ml min^{-1}. The solid lines represent the model simulations for the small model geometry, the dashed lines represent the model simulations for the large model geometry. The dotted black line indicates the totally injected amount of the tracer.

Table 6.1: Recovered mass fractions for different simulation runs using different outflow rates and considering different processes, n.e. = not examined.

		small model		**large model**	
		[kg]	[%]	[kg]	[%]
10 ml	Tracer	$2.9 \cdot 10^{-6}$	21	$5.08 \cdot 10^{-6}$	36.8
	Tracer + Colloids and Sorption	$1.9 \cdot 10^{-6}$	14	n.e.	
	Tracer + Colloids and Sorption + Filtration	$7.6 \cdot 10^{-7}$	5.4	n.e.	
50 ml	Tracer	$8.9 \cdot 10^{-6}$	65	$1.32 \cdot 10^{-6}$	95.7
	Tracer + Colloids and Sorption	$7.2 \cdot 10^{-6}$	52	$1.09 \cdot 10^{-6}$	79.0
	Tracer + Colloids and Sorption + Filtration	$4.7 \cdot 10^{-6}$	34	$7.56 \cdot 10^{-6}$	54.8
165 ml	Tracer	$1.4 \cdot 10^{-5}$	99	$1.38 \cdot 10^{-5}$	99.9
	Tracer + Colloids and Sorption	$1.3 \cdot 10^{-5}$	91	n.e.	
	Tracer + Colloids and Sorption + Filtration	$1.0 \cdot 10^{-5}$	75	n.e.	

In contrast to this the enlargement of the model area almost had no impact on the recovered mass fractions in the simulation for 10 ml/min. Therefore, we expanded the model area to the size of 20.5 m by 20.5 m. Even this large model area does not prevent the transport pathways to be disconnected from the outflow location. Now, even at the left boundary the pathways are directed out of the model area (Figure 6.5). This implied that a complete recovery of the injected tracer mass at the outflow would only be achieved by a reduction of the inflow rate, if possible at all.

With these variations of the model scale, it was demonstrated that the model size has a strong impact on the flow and transport simulations as can be seen in the recovered mass fractions for the small and the large model.

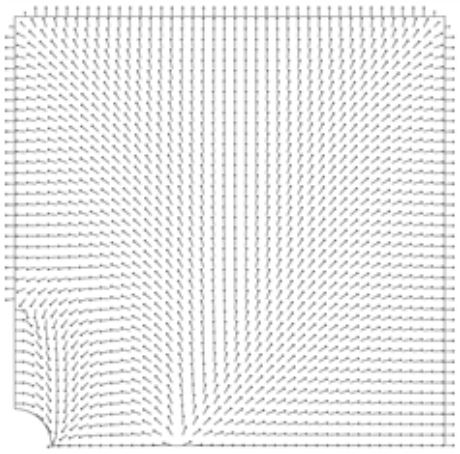

Figure 6.5: Steady-state velocity direction field at outflow rates of 10ml/min for the large model (20 m by 20 m). For illustration purposes, the length of the arrows is not scaled with the magnitude of the velocity.

6.2 Influence of the new observation boreholes and planned water extraction

CFM field experiments at the Grimsel test site were so far conducted at a dipole without any additional water extraction at observation boreholes. With regard to the integrated in situ experiment, which will be performed with a bentonite source emplaced in a shear zone interval, three additional boreholes were drilled in the direct vicinity of the injection borehole CFM 06.002. All three boreholes have a diameter of 56 mm, a length of more than 7 m, and a distance of approx. 4 cm to the injection borehole. The targeted extraction rate amounts to 50 µl/min for each observation borehole.

The aim of this work is to determine the potential influence of a continuous water abstraction in the three observation boreholes on the flow field and the tracer breakthrough at Pinkel for the experimental setup of the tracer experiment 10-01, where the dipol is characterized by an outflow rate of about 50 ml/min at the Pinkel /REF ?/.

6.2.1 Flow simulations

Flow and transport calculations at the dipole CFM06.002 – Pinkel have been carried out using the codes d³f [207]for flow simulations and r³t [213]for transport simulations. A description of the experimental setup and the background of the groundwater flow and transport model presented here is given in [53] and [217]. For previous model calculations, we only regarded a reduced model area due to the symmetry of the system. For this work, we maintained the model geometry. The three new observation boreholes were drilled radially around the

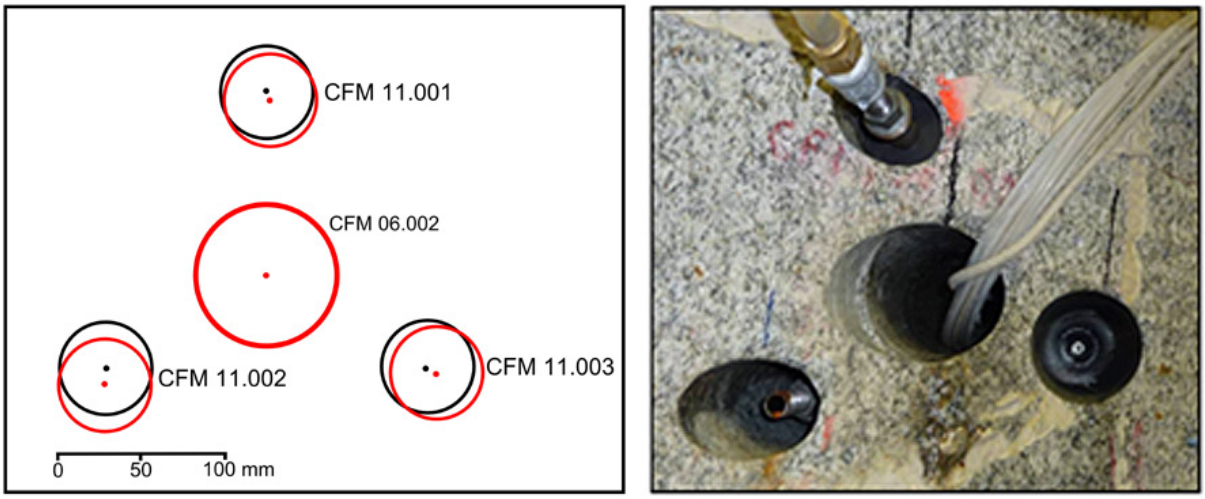

Figure 6.6: Borehole locations around the injection borehole CFM 06.002 [261].

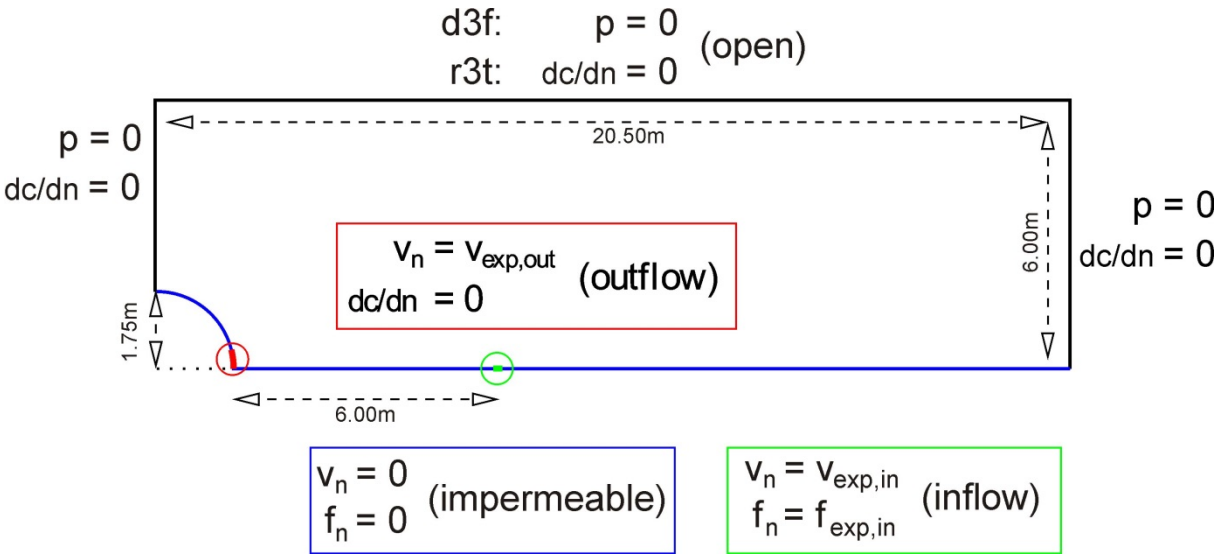

Figure 6.7: Geometry and hydrogeological/transport-related boundary conditions of the 2D computer model. Green: Inflow; Red: Outflow; Blue: Sealed tunnel wall and symmetry axis; Black: Permeable virtual boundaries within the shear zone. Notation: c = concentration; p = pressure; v = fluid velocity; f = pollutant mass flux; n is used either as a subscript to denote the normal component or in fractions in which n symbolizes the normal derivative of the respective variable.

injection borehole as depicted in Figure 6.6. To fit them into the reduced model geometry, we subsumed them to one borehole and assumed an abstraction rate Q of 150 µl/min as the sum of the three single extraction rates. The location of the single borehole is set to 4 cm distance to the inflow location at the lower boundary of the model domain, which is the direct connecting line between the injection (CFM 06.002) and the extraction (Pinkel) location and at the same time serves as the symmetry axis. The extraction of water is implemented by the

definition of a velocity boundary condition according to the extraction rate. The model geometry and the employed boundary conditions are depicted in Figure 6.7.

6.2.2 Results and discussion

Assuming the accumulated extraction rate of the three observation boreholes the water extraction has a minor influence on the tracer breakthrough in this model. The time of the maximum tracer concentration at Pinkel is shifted by 2,438 seconds from 117,187 seconds to 119,625 seconds, while the maximum tracer concentration is reduced by $1.54 \cdot 10^{-7}$ kg/m^3 (0.72 %) to $2.112366 \cdot 10^{-5}$ kg/m^3. The tracer recovery in both models amounts to 5 mg, which equals a recovery of 100 %.

To test the influence of higher or lower water extraction rates on the flow field and the tracer breakthrough, the value of the extraction rate was varied between 30 µl/min and 1500 µl/min. Results for the time of the tracer breakthrough and the concentration at the outflow are given in Table 6.2. The higher the extraction rate, the more perceivable is the decrease of the maximum concentration of the breakthrough curve and the more distinct is the delay of the maximum tracer concentration. This is due to the diverted flow paths between the inflow and outflow locations.

The breakthrough curves for the original model without the observation boreholes as well as for the model considering the extraction boreholes with both the realistic extraction rate and the increased extraction rate are given in Figure 6.8. The tracer recovery for the three model runs is depicted in Figure 6.9. It should be noted that all figures for the test run 10-01, where the model calculations achieved a tracer recovery of 100%, were scaled to 84 % to account for the mass losses during the experimental test.

Table 6.2: Time and concentration of the maximum of the breakthrough curves for different extraction rates in the observation boreholes (not scaled)**.**

	Time of maximum of the breakthrough curve [s]	Concentration of maximum of the breakthrough curve [kg/m^3]
Model, no sink	117,187	$2.127732 \cdot 10^{-5}$
Model, Q = 30 µl/min	117,883	$2.120977 \cdot 10^{-5}$
Model, Q = 150 µl/min	119,625	$2.112366 \cdot 10^{-5}$
Model, Q = 300 µl/min	122,217	$2.099886 \cdot 10^{-5}$
Model, Q = 750 µl/min	137,430	$2.023980 \cdot 10^{-5}$
Model, Q = 1500 µl/min	170,254	$1.833545 \cdot 10^{-5}$

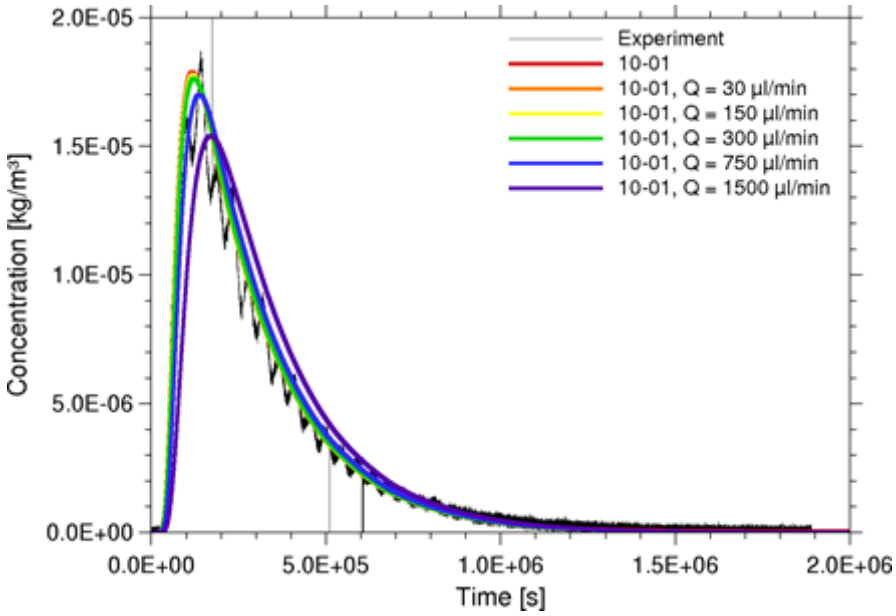

Figure 6.8: Tracer breakthrough curves for different model runs; (i) neglecting the three observation boreholes, (ii) regarding the realistic extraction rate of 150 µl/min, and (iii) variations regarding a decreased (30 µl/min) and increased extraction rates between 300 and 1500 µl/min.

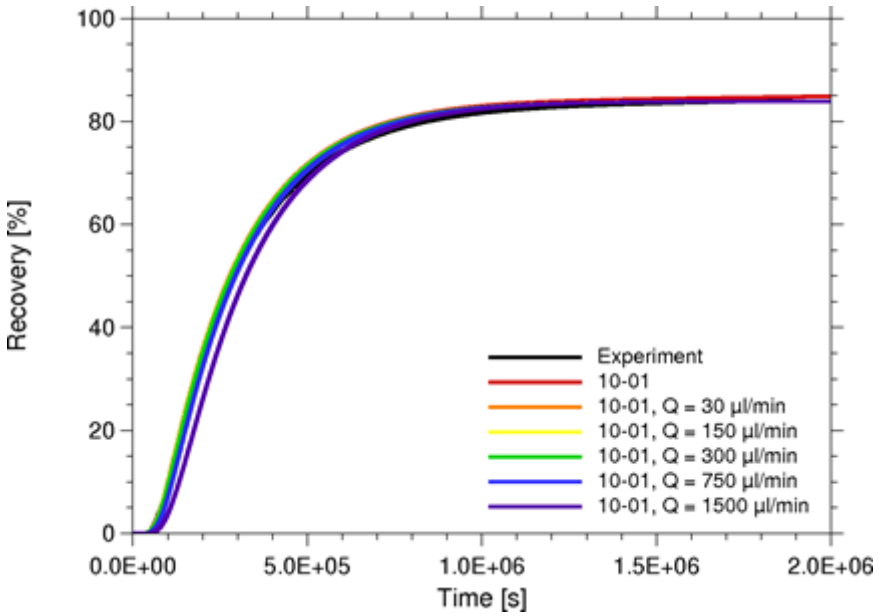

Figure 6.9: Tracer recovery for different model runs; (i) neglecting the three observation boreholes, (ii) regarding the realistic extraction rate of 150 µl/min, and (iii) variations regarding a decreased (30 µl/min) and increased extraction rates between 300 and 1500 µl/min.